

Centre Eau Terre Environnement

**A CLOSER LOOK AT THE RELATIVE TIMING AND NATURE OF GOLD  
MINERALIZATION OF THE BIF-ASSOCIATED TIRIGANIAQ DEPOSIT,  
MELIADINE DISTRICT, RANKIN INLET GREENSTONE BELT,  
NUNAVUT**

Par

Brayden St.Pierre

Thèse présenté pour l'obtention du grade de  
Maître ès Sciences (M.Sc.)  
en Sciences de la Terre

**Jury d'évaluation**

Président du jury et  
examineur interne

Dr. Benoît Dubé  
Commission géologique du Canada

Examineur externe

Prof. Chris Yakymchuk  
Earth and Environmental sciences  
University of Waterloo

Codirecteur de recherche

Patrick Mercier-Langevin  
Commission géologique du Canada

Codirecteur de recherche

Michel Malo  
INRS-ETE

## ACKNOWLEDGEMENTS

---

I gratefully acknowledge my supervisor, Dr. Patrick Mercier-Langevin, and my co-supervisor Dr. Michel Malo for providing me the opportunity to undertake such an interesting project. Their expertise, guidance, mentorship, and patience throughout this project is tremendously appreciated.

I thank Agnico-Eagle Mines' Meliadine division and the technical services department for providing me with employment for two summers, access to their properties, and support throughout my project. In particular I am grateful to Marjorie Simard, Olivier Côté-Mantha, Jean-Claude Blais, Guilhem Servelle, and Morgan Hjorth for many valuable discussions that enriched the quality of this thesis.

I thank the Geological Survey of Canada, as the bulk of the project was funded by the Targeted Geoscience Initiative 5 program. I am grateful to Benoit Dubé, Christopher Lawley, Sébastien Castonguay, Wouter Bleeker, Ian Honsberger, and Michel Houlé for several much-appreciated discussions about geology. Also, I am grateful to Kathleen Lauzière, for helping me with my posters. Additionally, I am grateful to Valerie Bécu for ensuring I always had field equipment, my samples were sent accordingly, and making me feel welcome in Québec City when I first arrived.

I would like to thank my fellow graduate students, Émile, Parham, Alexandre, Caroline, Sarah and Arnaud for their support and friendship throughout this experience. Also, a thank you is extended to a long-distance fellow graduate student Manon for her support, friendship, and for the many discussions on BIF-hosted/associated gold deposits we shared.

I would like to thank my current and past work colleagues for continuously encouraging me to finish my masters. Especially, Mike and Eugene, who have been valued mentors to me over the last couple of years.

A special thank you goes to my long-term friends: Adris, Andrew, Drake, Michael, Sahill, Taylor, and Tyler; many of which asked me on a frequent basis, "are you still not finished?" or "how long does it take to write about some rocks." Without this valuable emotional support, I surely would not have finished.

Lastly, but far from least, I am grateful for my tremendously supportive family. To my mother Beverly, father Randy, and sister Kaitlyn: there are not enough words to describe what you mean to me and how much I appreciate the support you have shown me in any endeavour I have undertaken.

## RÉSUMÉ

---

Le district aurifère de Meliadine est situé dans la ceinture de roches vertes archéennes polydéformées (environ 2660 Ma) de Rankin Inlet, au Nunavut. Le district comprend de nombreux gisements et zones aurifères d'intérêt qui sont spatialement associés à la faille Pyke et à des failles subsidiaires. Il s'agit notamment du gisement Tiriganiaq, actuellement en production, qui se trouve dans les turbidites dans le toit structural de la faille Lower, une structure est-ouest associée à la faille Pyke.

Les "séries filoniennes" 1150 et 1250 du gisement de Tiriganiaq forment une série de zones minéralisées aux géométries complexes. De nouvelles relations sur le terrain démontrent que la minéralisation aurifère dans les filons 1150 et 1250 est contrôlée par d'étroites zones de cisaillement  $D_2B$  inverses, à pendage nord, localisées dans un grauwacke à chlorite. Ces zones de cisaillement recoupent la foliation  $S_2A$  légèrement plus abrupte, transposée et inclinée vers le nord, qui est de plan axial aux plis  $F_2A$  transposés et serrés. Cette étude a également révélé l'importance des veines de quartz  $\pm$  ankérite d'extension  $D_2B$ , minéralisées, horizontales et à faible pendage vers le sud. Ces veines et les zones de remplacement des sulfures qui leur sont associées se développent de préférence dans des intervalles de formation de fer rubanée (FFR) au faciès d'oxyde-silicate et FFR pélitiques mineurs transposés et fortement plissés par les plis  $F_2A$ . Les FFR au faciès oxyde-silicate et pélitique sont relativement enrichies en Au par rapport aux lithologies de grauwacke à chlorite et de mudstone laminé, ce qui signifie qu'elles ont agi comme piège chimique et structural pour la minéralisation aurifère. Dans l'ensemble, les altérations à séricite, ankérite idioblastique, quartz et chlorite sont présentes dans les lithologies sédimentaires clastiques (grauwacke à chlorite, mudstone stratifié et certaines parties de la FFR pélitique), tandis que la FFR à oxyde-silicate et certaines parties de la FFR pélitique comprennent un assemblage d'altération dominant à quartz  $\pm$  chlorite  $\pm$  ankérite  $\pm$  sulfures.

L'or a été introduit au plus tôt au cours de la déformation  $D_2A$ , au plus tard au cours de la déformation syn- à tardi- $D_2B$ , et après le pic du métamorphisme. Le plissement et la formation de veines sont associés à la principale phase de déformation dans le secteur à l'étude, qui correspond à la deuxième phase ( $D_2$ ) de la déformation régionale. La déformation  $D_2$  du gisement de Tiriganiaq peut être subdivisée en deux phases principales continues: la première phase ( $D_2A$ ), est associée à un raccourcissement orienté nord-est–sud-ouest et à un plissement  $F_2A$  ; et la seconde phase ( $D_2B$ ), qui est associée à un raccourcissement nord-sud, à un plissement supplémentaire ( $F_2B$ ), ainsi qu'à un cisaillement inverse et à la formation de veines (veines

d'extension à faible pendage sud et veines de cisaillement à pendage modéré vers le nord). Ces zones présentent certaines des teneurs en or les plus élevées du gisement Tiriganiaq et soulignent ainsi l'importance des successions de FFR transposées, cisailées et plissées. Les plis F<sub>2</sub>A, plongent vers l'ouest et forment des zones à haute teneur contrôlées par la structure et la lithologie.

Le gisement de Tiriganiaq présente des caractéristiques communes à d'autres gisements aurifères de classe mondiale encaissés par des FFR ou associés à des FFR, tels que Lupin, Meadowbank, Amaruq et Homestake (États-Unis), notamment le contrôle lithologique exercé par les FFR au faciès silicate ± oxyde sur l'or et les zones de forte déformation. L'exploration de minéralisations aurifères similaires dans la ceinture de roches vertes de Rankin Inlet devrait se concentrer sur les zones de charnières de plis des successions de FFR épaissies par la tectonique et fortement plissées, recoupées par des structures secondaires et/ou des zones de forte déformation.

Mots-clés : Archéen ; or ; or encaissé dans formations de fer rubanées; gisement orogénique ; ceinture de roches vertes ; Nunavut.



## ABSTRACT

---

The Meliadine gold district is hosted within the Archean (ca. 2660 Ma) poly-deformed Rankin Inlet greenstone belt in Nunavut. The district comprises numerous gold deposits and prospects that are spatially associated with the Pyke Fault and its splays. This includes the currently producing Tiriganiaq deposit, which is hosted within the turbidite-dominated structural hanging wall of the Lower Fault, a west-trending splay of the Pyke Fault.

The 1150 and 1250 “lode series” within the Tiriganiaq deposit are a series of ore zones with complex geometries. New field relationships demonstrate gold mineralization in the 1150 and 1250 lodes are controlled by narrow, north-dipping, D<sub>2</sub>B reverse-dextral shear zones localized within chloritic greywacke. These shear zones overprint the slightly steeper, transposed north-dipping S<sub>2</sub>A foliation that is axial planar to transposed tight F<sub>2</sub>A folds. This study has also revealed the importance of horizontal to shallowly south-dipping ore-bearing D<sub>2</sub>B extensional quartz ± ankerite veins. These veins and their associated sulphide replacement zones are preferentially developed in transposed tightly F<sub>2</sub>A folded oxide-silicate facies BIF and minor pelitic BIF intervals. The oxide-silicate and pelitic BIF lithologies are relatively enriched in gold compared to the chloritic greywacke and the laminated mudstone lithologies signifying they acted as a chemical and structural trap for gold mineralization. Overall, sericite, idioblastic ankerite, quartz, and chlorite alteration are widespread in the clastic sedimentary lithologies (chloritic greywacke, laminated mudstone, and portions of the pelitic BIF) whereas the oxide-silicate BIF and portions of the pelitic BIF comprise a dominant quartz ± chlorite ± ankerite ± sulphides alteration assemblage.

Gold was introduced earliest during D<sub>2</sub>A deformation, latest syn- to- late D<sub>2</sub>B deformation, and post-peak metamorphism. Folding and veining are associated with the main phase of deformation in the deposit area, which corresponds to the second phase (D<sub>2</sub>) of regional deformation. The D<sub>2</sub> deformation at the Tiriganiaq deposit can be further subdivided into two main protracted phases: the first phase (D<sub>2</sub>A), which is associated with northeast-southwest-oriented shortening and F<sub>2</sub>A folding; and the second phase (D<sub>2</sub>B), which is associated with north-south shortening, further folding (F<sub>2</sub>B), and reverse shearing and veining (shallowly south-dipping extension veins and moderately north-dipping shear veins). These zones provide some of the highest gold grades within the Tiriganiaq deposit and thus highlight the importance of transposed west-plunging sheared and F<sub>2</sub>A folded BIF successions forming structurally and lithologically controlled high-grade zones.

The Tiriganiaq deposit shows features common with other world-class BIF-hosted/associated gold deposits such as Lupin, Meadowbank, Amaruq, and Homestake (USA), notably the lithological control of silicate ± oxide facies BIF on gold and strong deformation zones. Exploration for similar gold mineralization within the Rankin Inlet greenstone belt should focus on areas with hinge zones of tectonically thickened tightly folded BIF successions, intersected by secondary structures and/or high-strain zones are highly prospective.

Keywords : Archean; Gold; BIF-hosted gold; orogenic deposit; Greenstone Belt; Nunavut

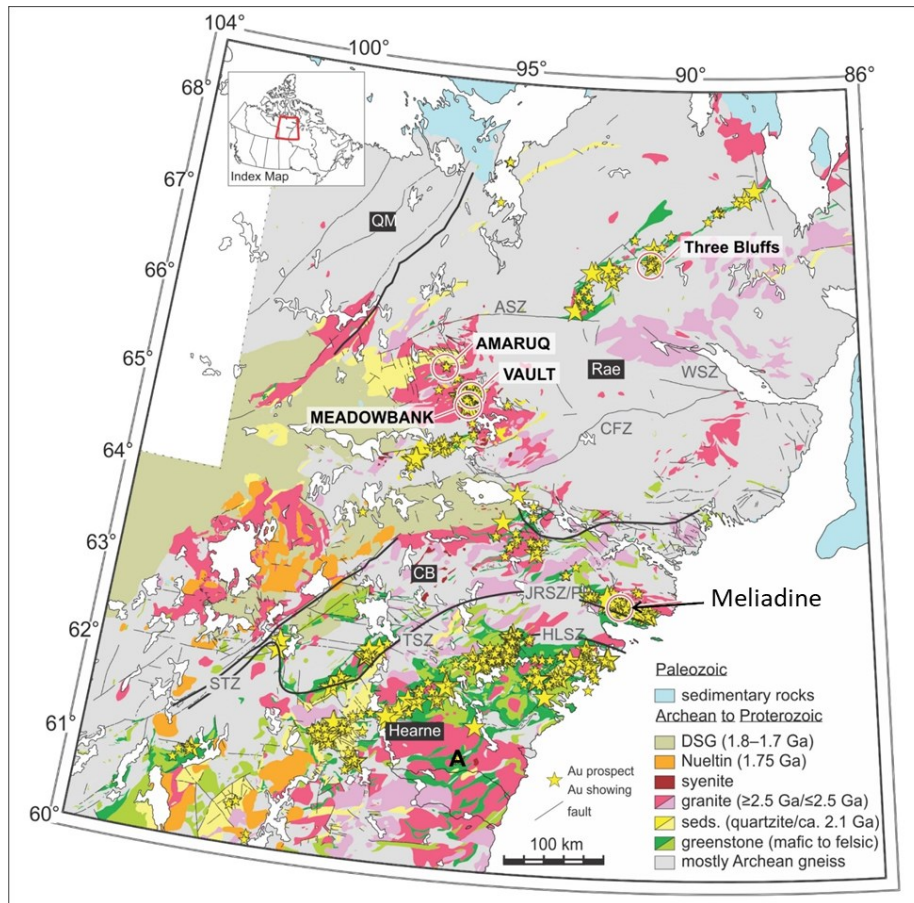
## SOMMAIRE RÉCAPITULATIF

---

### Chapitre 1 : Introduction

Le district aurifère de Meliadine (MGD, Meliadine Gold District), situé dans la ceinture de roches vertes de Rankin Inlet datée à environ 2 660 Ma, au Nunavut (Fig. 1), est l'un des plus importants districts aurifères émergents du Canada associés aux formations de fer rubanées (FFR) avec 3,65 millions d'onces (113,6 t) d'or en réserves prouvées et probables, 2,25 millions d'onces (69,9 t) d'or en ressources indiquées et 2,29 millions d'onces (71,3 t) d'or en ressources présumées en date du 31 décembre 2021 (Agnico Eagle Mines Limited, 2022). Le MGD comprend de nombreux gisements et indices aurifères orogéniques qui sont spatialement associés à la faille Pyke et la faille subsidiaire Lower (Fig. 2). Bon nombre de ces gisements d'or sont associés au FFR, notamment Tiriganiaq, le plus grand gisement du district. Le gisement Tiriganiaq (mine Meliadine) est entré en production à la mi-mai 2019 a produit 209,413 onces (6,5 t) d'or en 2020, et 370 000 onces (11,5 t) en 2021 (Agnico Eagle Mines limited, 2022).

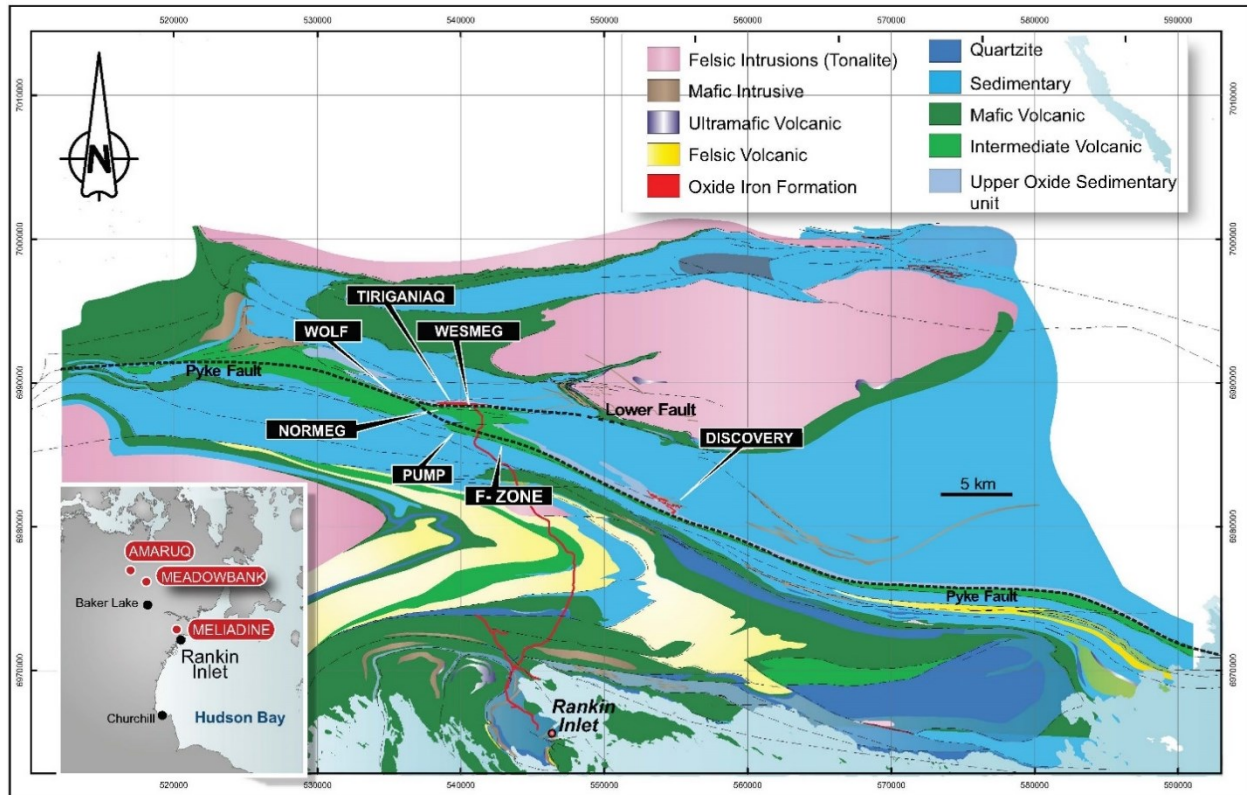
La chronologie de la minéralisation aurifère du gisement de Tiriganiaq et, plus largement, de la province de Churchill occidentale, n'a pas encore été établie avec précision. L'incertitude quant au moment de la mise en place de l'or est due en grande partie au manque d'exposition du substratum rocheux, à l'histoire relativement récente de l'exploration et de l'évaluation académique par rapport à d'autres districts miniers importants au Canada, ainsi qu'à une longue histoire de déformation et à la complexité géométrique qui en résulte. Néanmoins, la chronologie générale de l'introduction de l'or a été attribuée au remaniement et au métamorphisme pendant l'orogénèse trans-hudsonienne (1,9-1,8 Ga ; Carpenter et Duke, 2004 ; Carpenter et al., 2005 ; Lawley et al., 2015a, b, c, 2016). L'exploration et les recherches antérieures menées dans la région au cours des dernières décennies ont conduit à une compréhension de premier ordre des principales zones aurifères du gisement de Tiriganiaq (par exemple, Carpenter et Duke, 2004 ; Carpenter et al., 2005 ; Lawley et al., 2015a, b, c, 2016). Le modèle a toutefois été remis en question lorsque l'exploitation souterraine des " séries filoniennes " 1150 et 1250 a débuté, ce qui a mis en évidence des complexités structurales au sein des unités FFR plissées. Ces zones de minerai multi-déformés sont difficiles à modéliser en 3D, ce qui a un impact sur la production minière et les estimations de teneur et de tonnage. L'exploitation minière active a permis d'accéder aux expositions souterraines des séries filoniennes 1150 et 1250. Une cartographie géologique et structurale détaillée a été réalisée le long des galeries nouvellement développées qui exposent l'éponte supérieure structurale s'étendant au-delà de la série filonienne 1150.



**Figure 1** Carte géologique régionale de la province de Churchill occidentale montrant l'emplacement de la ceinture de roches vertes de Rankin Inlet (RIGB) et du district aurifère de Meliadine (MGD), ainsi que la distribution des autres gisements, gîtes et indices aurifères de la région. Abréviations : ASZ = zone de cisaillement Amer, CB = bloc Chesterfield, CFZ = zone de faille Chesterfield, DSG = super groupe Dubawant, HLSZ = zone de cisaillement Happy Lake, JRSZ = zone de cisaillement Josephine River, PF = faille Pyke, QM = bloc Queen Maud, STZ = zone tectonique Snowbird, TSZ = zone de cisaillement Tyrrell, TNO = Territoires du Nord-Ouest, WSZ = zone de cisaillement Wager. Modifié à partir de Lawley et al. (2016).

Cette situation n'est pas propre à Tiriganiaq et est commune à de nombreux gisements d'or encaissés/associés aux FFR, où de nombreux aspects structuraux et lithologiques exercent un contrôle important sur la distribution de l'or, ce qui rend difficile la modélisation des zones minéralisées et l'optimisation de la production. Tiriganiaq offre une occasion unique d'étudier les gisements d'or associés aux FFR, car plusieurs incertitudes sont associées à sa genèse et à l'importance relative des éléments lithologiques et structuraux clés à différents endroits du gisement. L'anisotropie des FFR hôtes a induit d'importantes complexités structurales tout au long de l'évolution de la minéralisation aurifère. La localisation et la cinématique des zones de cisaillement et du développement des veines aurifères et l'influence de ces complexités structurales sur la géométrie des zones aurifères sont essentielles pour optimiser les modèles d'exploration et le développement minier (Sherlock et al., 2004 ; Janvier et al., 2015 ; Oswald et

al., 2018 ; Tóth et al., 2019). L'histoire structurale de Tiriganiaq et le moment précis de l'introduction de l'or par rapport aux événements de déformation doivent encore être établis avec précision. Si elle est correctement comprise, elle conduira à une meilleure compréhension des contrôles géométriques et cinématiques sur l'or à l'échelle du gisement.



**Figure 2** Carte géologique du district aurifère de Meliadine, extraite de Anglo-Eagle Mines Ltd. Internal geology report).

Les trois questions principales abordées dans le cadre de cette étude sont :

1. Comment l'anisotropie des FFR hôtes a-t-elle affecté la cinématique, la géométrie et la localisation des zones de cisaillement et des veines aurifères ?
2. Quelle est l'histoire structurale précise du gisement d'or de Tiriganiaq ?
3. Quel est le moment précis de l'introduction de l'or par rapport aux événements de déformation du gisement d'or de Tiriganiaq ?

La documentation et la caractérisation des contrôles structuraux et lithologiques, ainsi que la définition de la chronologie relative des événements, permettront de répondre aux trois questions principales à Tiriganiaq, plus spécifiquement dans le contexte des séries filoniennes 1150 et

1250, ce qui conduira à une meilleure compréhension de certains aspects du contenu en or du MGD et permettra un développement minier plus précis et des stratégies d'exploration plus appropriées.

## Chapitre 2 : Roches hôtes des séries filoniennes 1150 et 1250

Les séries filoniennes 1150 et 1250 sont encaissées dans la Formation Upper Oxide, dans l'éponte supérieure (toit structural) de la faille Lower (Fig. 3 et 4). La Formation Upper Oxide se compose de grauwacke, de grès fin et d'argillite fortement lités et intercalés avec un faciès d'oxyde-silicate dominant et un FFR mineur amphibolitique (pélitique) qui ont été soumis à des conditions de métamorphisme au grade des schistes verts, à une déformation majeure et à une altération hydrothermale.

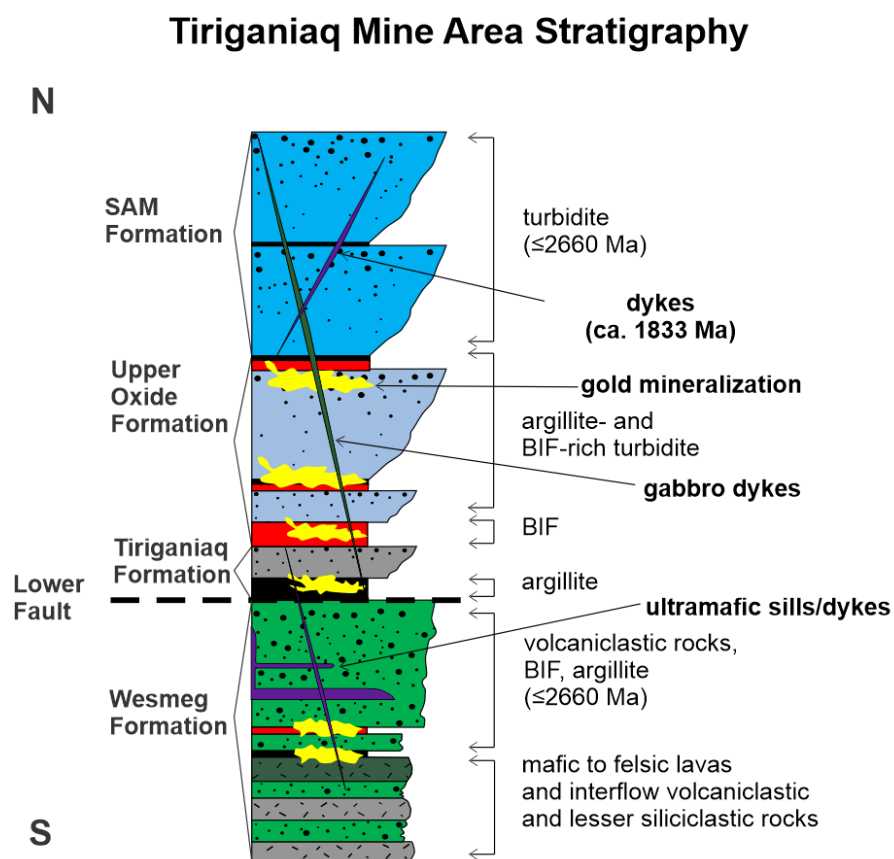


Figure 3 Colonne stratigraphique renversée du secteur Tiriganiaq.

Le grauwacke à chlorite comprend des grains de quartz et de feldspath fins à grossiers enveloppés d'un assemblage minéral dominant de muscovite ± chlorite qui définit la foliation principale (S<sub>2</sub>A). Le grauwacke est fortement affecté par la déformation principale et a été plissé et cisailé, présentant couramment des structures mylonitiques et fragiles-ductiles. Le grauwacke

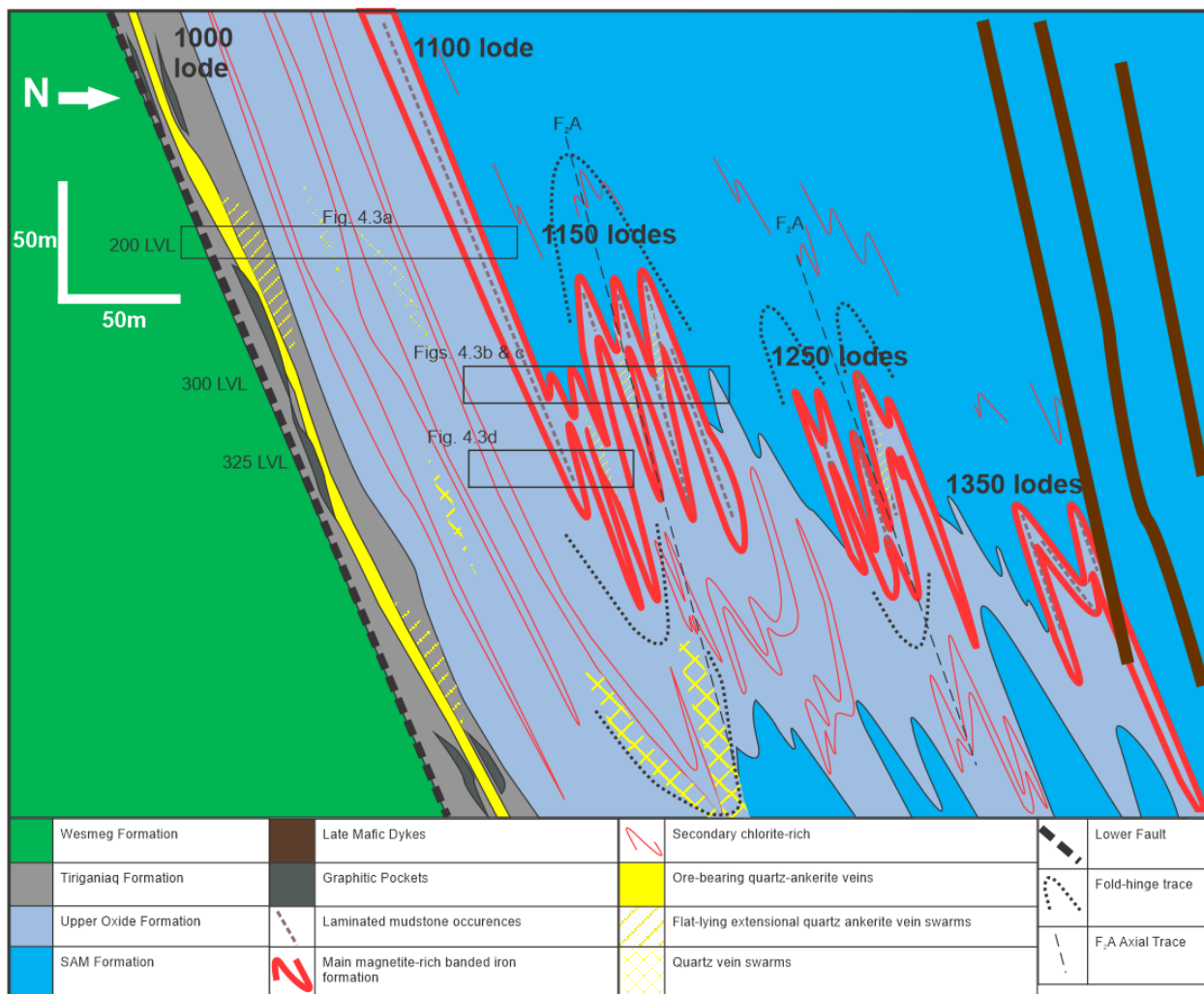
abrite des veines de cisaillement et d'extension minéralisées et a été fortement affecté par l'altération hydrothermale. Les lits individuels sont constitués de grauwacke massif quartzo-feldspathique ou de pélite à grain fin, riche en silt et en argile.

Le FFR à oxyde-silicate comprend un litage bien développé et consiste en une alternance de bandes semi-massives à massives de magnétite, de chert et de silicate. Cependant, des intervalles à litage mal défini, caractérisés par des bandes minéralogiques diffuses, sont également présents. Les lits de magnétite sont souvent bordés de grunerite aciculaire à grain fin. Les bandes riches en chert contiennent des quantités mineures de chlorite, de grunérite et de magnétite disséminée. Les bandes riches en silicates sont dominées par la chlorite et la grunérite avec de la magnétite à grain fin disséminée et une quantité mineure de quartz.

La FFR pélitique comprend un litage bien développé et consiste en une alternance de bandes de chlorite semi-massive à massive et de bandes dominées par la grunérite avec un peu de chert ou de bandes de pélite riche en silt et en phyllosilicate avec un peu de chert. La magnétite forme rarement des bandes cohérentes et est plus souvent disséminée dans le matériel pélitique. La FFR pélitique est localement fortement affectée par la déformation principale et a été plissée et cisailée, présentant couramment des structures mylonitiques et autres structures fragiles-ductiles, hébergeant des veines de cisaillement et d'extension minéralisées (se référer au chapitre 3 pour plus de détails) et a été localement fortement affectée par une altération hydrothermale.

L'argillite laminée comprend des couches fortement stratifiées, en alternance avec des couches de faible épaisseur quartzo-feldspathiques à grain très fin et riches en mudrock (avec de la chlorite à grain fin (<150 µm) sur les marges). Les couches d'argillite sont généralement à grain trop fin pour déterminer la minéralogie, à l'exception de la chlorite et de la séricite à grain très fin (<150 µm) formant des rubans riches en phyllosilicates. L'argillite laminée est affectée par la déformation principale et a été plissée et cisailée, présentant parfois des structures mylonitiques et fragiles-ductiles. Elle abrite localement des filons de quartz ± ankérite ± séricite ± sulfures minéralisés et parallèles à la foliation et a été affectée dans une certaine mesure par une altération hydrothermale.





**Figure 4** Coupe schématique du gisement de Tiriganiaq et de ses différentes zones de minerai (ou "filons"), en regardant vers l'ouest. La section montre la géométrie des différentes formations volcano-sédimentaires, la distribution des veines et l'emplacement des zones minéralisées (d'après St.Pierre et al., 2020 ; modifié d'après Agnico Eagle Mines Limited, rapports internes non publiés). Abréviations : BIF = formation de fer rubanée.

La composition chimique des roches hôtes des séries filoniennes 1150 et 1250 est très variable, ce qui démontre leur nature détritique et suggère que les sédiments proviennent largement des roches volcaniques et intrusives environnantes, de composition variée. La nature finement stratifiée des roches sédimentaires clastiques et chimiques dérivées de la Formation Upper Oxide qui abrite les séries de filons 1150 et 1250 montre une hétérogénéité distincte dans la composition pétrographique et géochimique. Cela est dû en partie à l'hétérogénéité des lits au sein des unités. Cependant, les principales variations de composition et de pétrographie entre et à l'intérieur des unités sont dues à l'altération hydrothermale. Malgré une sélection rigoureuse, la plupart des échantillons présentent des effets de l'altération hydrothermale associée aux zones minéralisées environnantes.



### **Chapitre 3 : Style et distribution de la minéralisation aurifère et empreinte hydrothermale associée**

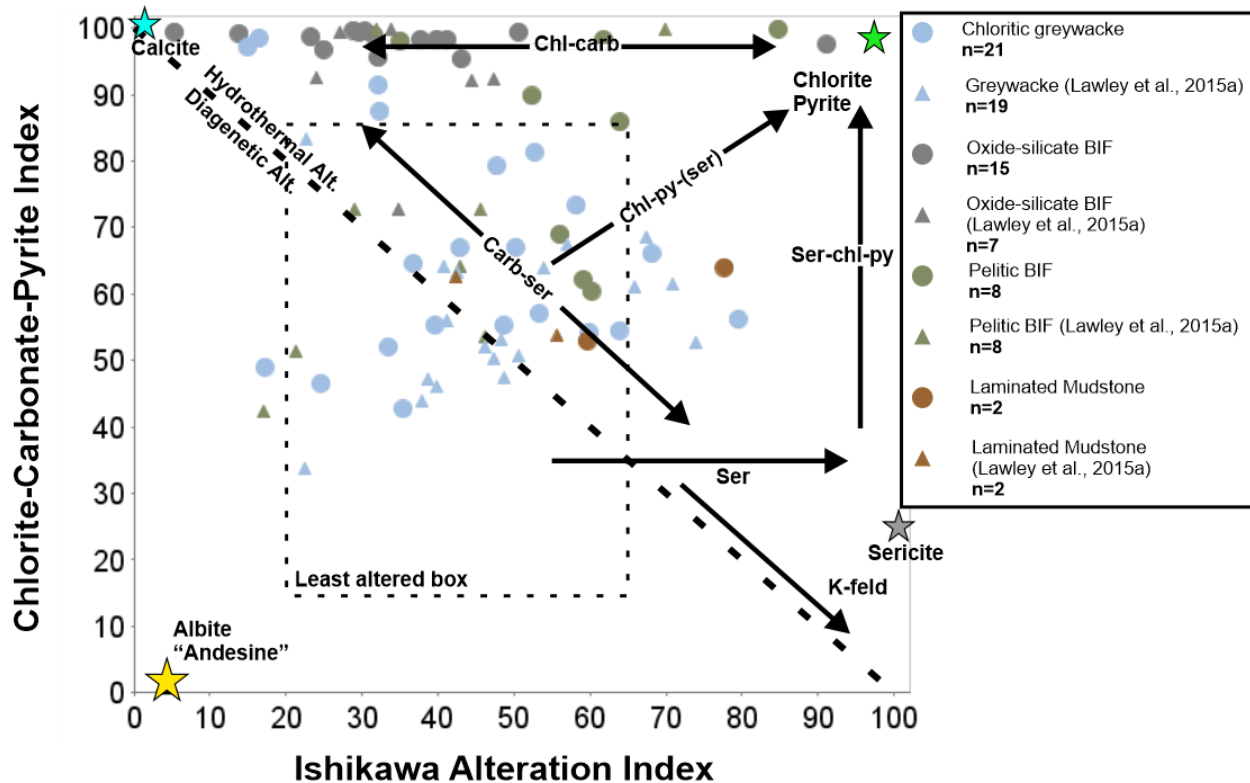
La minéralisation aurifère du gisement de Tiriganiaq est associée à une minéralisation de remplacement de type FFR, associée à des veines de quartz  $\pm$  ankérite aurifères qui se présentent sous la forme de zones minéralisées empilées et semi-continues appelées localement "*lodes*" ou *séries filoniennes*. Ces veines sont principalement composées de quartz  $\pm$  ankérite, avec des quantités variables de chlorite hydrothermale, de sulfures de fer et de quantités moindres de biotite, de magnétite et de monazite. L'or est paragénetiquement tardif et, à l'échelle microscopique, se retrouve dans des sites de microtextures présentant une déformation faible et dans des inclusions à l'intérieur de cristaux d'arsénopyrite variablement recristallisés et idiomorphiques.

En général, la FFR à oxyde-silicate est enrichie en pyrrhotite et en sulfures par rapport aux autres lithologies à l'étude. Les données pétrographiques montrent que la FFR à oxyde-silicate est relativement appauvrie en arsénopyrite par rapport aux pélites et au grauwacke à chlorite. Cependant, cela ne concorde pas avec d'autres observations de terrain qui montrent que l'arsénopyrite forme préférentiellement des zones de remplacement stratoïdes le long des couches riches en magnétite dans la FFR à oxyde-silicate.

Par comparaison, la FFR à oxyde-silicate est enrichie en Au, As, et S par rapport au grauwacke à chlorite et au mudstone ou argillite laminée mais appauvri par rapport à la FFR pélitique. Cependant, trois échantillons prélevés dans des veines de quartz  $\pm$  ankérite encaissées dans la FFR à oxyde-silicate présentent des valeurs enrichies en Au, As et S par rapport à toutes les lithologies à l'étude. Cette observation concorde avec les observations de Lawley et al. (2015a) qui affirme que la FFR à oxyde-silicate est enrichie en Au, As, et S par rapport à toutes les autres lithologies du gisement.

La plupart des roches hôtes des séries filoniennes 1150 et 1250 présentent des degrés variables d'altération hydrothermale, et les lithologies présentent des assemblages d'altération distincts. Dans l'ensemble, la séricite, l'ankérite idiomorphique, le quartz, l'altération à chlorite et les sulfures disséminés (principalement l'arsénopyrite) sont répandus dans les lithologies sédimentaires clastiques (grauwacke, argillite laminée et certaines parties de la FFR pélitique). Par contre, le faciès d'oxydes-silicates et certaines parties du faciès pélitique des FFR comprennent un assemblage d'altération dominant de quartz  $\pm$  chlorite  $\pm$  ankérite  $\pm$  sulfure, généralement associé dans l'espace à des veines de quartz  $\pm$  ankérite  $\pm$  chlorite  $\pm$  sulfure. Ces tendances sont clairement représentées lorsque les échantillons sont rapportés sur l'indice de chlorite-carbonate-

pyrite par rapport à l'indice d'altération de Hashimoto (Large et al., 2001, diagramme "box plot" ; Fig. 5).



**Figure 5** Diagramme «box plot» (Large et al., 2001) montrant l'indice chlorite-carbonate-pyrite  $[100(\text{Mg} + \text{FeO})/(\text{MgO} + \text{FeO} + \text{Na}_2\text{O} + \text{K}_2\text{O})]$  par rapport à l'indice d'altération de Hashimoto  $[100(\text{K}_2\text{O} + \text{MgO})/(\text{K}_2\text{O} + \text{MgO} + \text{Na}_2\text{O} + \text{CaO})]$  (Ishikawa et al., 1976) des roches hôtes des séries filoniennes 1150 et 1250, montrant le degré relatif d'altération et la minéralogie générale de l'altération.

Les profils multi-éléments normalisés aux chondrites présentés dans le chapitre 2 montrent systématiquement de grandes variations en Pb, Li, mais surtout en Sb. Le Sb a tendance à présenter de grandes anomalies positives dans toutes les lithologies. Les diagrammes montrent des degrés variables de corrélations positives entre l'or et les métaux As, Te, Sb, Se, Bi, Cu, Pb, mais une corrélation négative avec Zn. Cependant, l'As, le Sb et le Se semblent avoir les corrélations positives les plus fortes avec l'Au, suivis par le Bi et le Te. Les cartes à double tracé de l'analyse en composantes principales montrent les associations de métaux dans les zones d'altération (Fig. 6). Il semble y avoir deux événements distincts, une signature Au-As-Sb hydrothermale apparemment primaire, et une remobilisation Pb-Te-Se-Bi de certains des métaux traces (principalement avec la galène).

Ces résultats sont cohérents avec ceux de Lawley et al. (2015c) et Gourcerol et al. (2016), qui ont également démontré que les roches hydrothermales altérées et recoupées par des veines du district aurifère de Meliadine sont spatialement associées à des concentrations anormales en

éléments traces (Au-As-Se-Te-Bi-Sb-Ag) de 10 à 100 mètres de part et d'autre des zones de minéral.

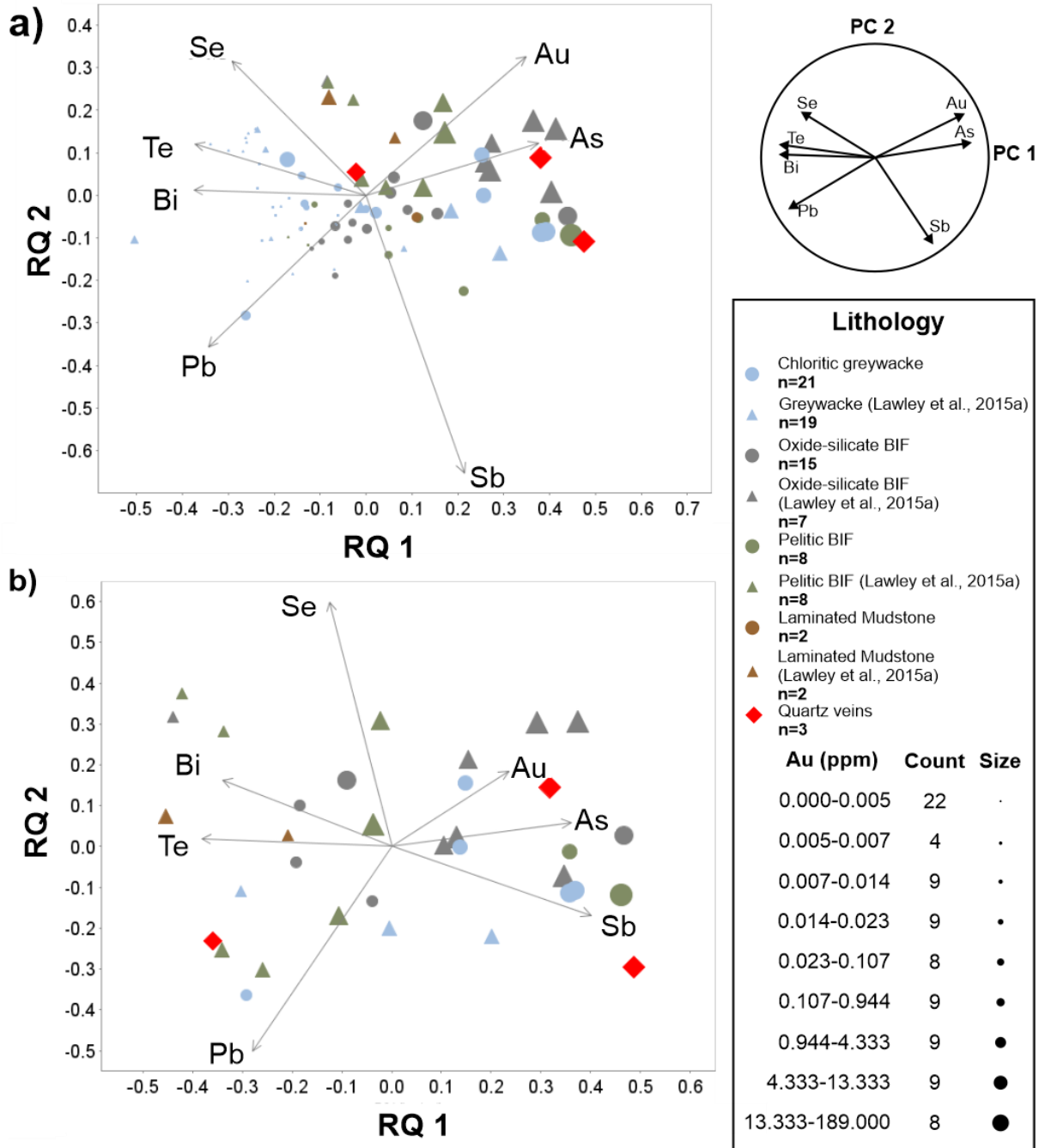


Figure 6 Carte de l'analyse des composantes principales, affichant les résultats de la composante principale 1 (a) et de la composante principale 2 (b), représentant statistiquement 78,2 % des données. b) ne comprend que les échantillons contenant 0,107ppm Au ou plus. (2015) représente les données de Lawley et al., 2015.

## Chapitre 4 : Analyse structurale des séries filoniennes 1150 et 1250

À l'échelle du gisement, on reconnaît trois phases de déformation (tableau 1). La première phase de déformation ( $D_1$ ) à Tiriganiaq, déduite d'observations à l'échelle régionale, s'est traduite par le chevauchement d'unités volcaniques sur des unités sédimentaires, impliquant probablement des plis isoclinaux le long de la faille Lower à pendage nord. Comme ailleurs dans la ceinture de roches vertes de Rankin Inlet, la phase  $D_1$  ne présente aucune fabrique identifiable.

La deuxième phase de déformation ( $D_2$ ) est un événement compressif prolongé qui peut être séparé en deux incréments de déformation sur la base d'observations détaillées faites sous terre du litage, de la foliation, du développement des plans de cisaillement et des relations de recoupement (St.Pierre et al., 2020). Dans ce modèle, la déformation  $D_2$  commence par un raccourcissement nord-est–sud-ouest ( $D_{2A}$ ) et une phase de plissement isoclinal  $F_{2A}$  parallèle aux couches des successions hôtes et le développement associé d'une foliation  $S_{2A}$  de plan axial et régionalement pénétrative. Cette phase a été suivie, ou a fait l'objet d'une transition, d'un léger changement d'orientation du raccourcissement vers le nord-sud ( $D_{2B}$ ), créant des plis en Z asymétriques cryptiques régionaux est-ouest (plis  $F_{2B}$  localement transposés) et une foliation composite  $S_{2A}$ - $S_{2B}$  (appelée  $S_{2B}$ ) transposée associée. Le plissement progressif a été associé à une déformation fragile-ductile ( $D_{2B}$ ) jusqu'à ce que les plis resserrés ne puissent plus accommoder le raccourcissement supplémentaire. La répartition préférentielle de la déformation le long des charnières de plis et plus particulièrement des membres, des unités relativement moins compétentes et des contacts lithologiques a conduit au développement de zones de cisaillement inverse. Des veines de cisaillement minéralisées ont été mises en place le long des plans de cisaillement  $D_{2B}$  qui ont entraîné la foliation  $S_{2A}$ . Les zones de cisaillement minéralisées et les veines d'extension associées ont pu débuté leur formation lors de l'épisode  $D_{2A}$  mais ont probablement été mises en place principalement pendant la phase de déformation  $D_{2B}$ .

La déformation  $D_3$  marque un événement de raccourcissement orienté E-O qui provoque de grands plis ouverts régionaux ( $D_4$  dans Carpenter et Duke 2004 et Carpenter et al., 2005 ;  $D_3$  dans Miller et al., 1995) entraînant un clivage local de crénulation  $S_3$  et des bandes de crénulation associées à l'échelle du gisement qui recoupent la foliation  $S_{2A}$  et les zones de cisaillement  $D_{2B}$ . Aucune perturbation significative des fabriques antérieures ou de la minéralisation n'est attribuée à l'événement  $D_3$ .

**Tableau 1 Résumé des événements structuraux à Tiriganiaq**

| Phase de déformation   | Description   | Structures associées  | Attitude principale des fabriques |
|--|---|---|-----------------------------------|
| <b>D<sub>1</sub></b>   | <b>D<sub>-1</sub></b> Juxtaposition initiale d'un ensemble volcanique mafique sur une séquence turbiditique le long d'un chevauchement ancestral orienté vers le nord ? | <b>S/S<sub>01</sub></b> ?   | ?                                 |
| <b>D<sub>2</sub></b>   | <b>D<sub>2A</sub></b> - Début du raccourcissement NNE-SSW entraînant un plissement parallèle des couches.   | <b>S<sub>2A</sub></b> - Foliation pénétrative régionale   | <b>268/65</b>                     |
|  |   | <b>F<sub>2A</sub></b> - Plis isoclinaux   | <b>10/268</b>                     |
|  | <b>D<sub>2B</sub></b> - Raccourcissement progressif N-S caractérisé par une déformation mixte fragile et ductile.   | <b>S<sub>2B</sub></b> – Foliation compisite ( <b>S<sub>2A</sub></b> transposée dans <b>S<sub>2B</sub></b> ) et plis d'orientation locale EW | <b>270/53</b>                     |
| <b>F<sub>2B</sub></b> - Plis en z asymétriques ( <b>plis F<sub>2A</sub> transposés</b> le long de la faille de Pyke)   |   | <b>10/268</b>   |                                   |
| <b>D<sub>2B</sub></b> - Développement d'un plan de cisaillement oblique et entraînant la foliation <b>S<sub>2A</sub></b> , indiquant un mouvement nord-sud dans les filons 1150 et 1250. |   | <b>270/53</b>   |                                   |
| <b>D<sub>3</sub></b>   | <b>D<sub>3</sub></b> - Un événement de raccourcissement orienté E-O.  | <b>S<sub>3</sub></b> - Clivage de crénulation N-NW affectant <b>S<sub>2A</sub></b> et <b>S<sub>2B</sub></b> .                               | <b>325/55</b>                     |

Les relations de terrain présentées dans ce projet de recherche documentent l'importance des veines d'extension de quartz ± ankérite **D<sub>2B</sub>** minéralisées, sub-horizontales à faiblement inclinées vers le sud. Les veines d'extension et les zones de remplacement des sulfures qui leur sont associées se développent de préférence dans des bandes de FFR d'épaisseur décimétrique à métrique, fortement plissées et transposées par des plis **F<sub>2A</sub>** parasitiques, de part et d'autre des zones de cisaillement inverse à pendage modéré vers le nord dans le grauwacke à chlorite (Fig. 7a-d ; St.Pierre et al., 2018, 2019, 2020). Ces zones fournissent certaines des plus hautes teneurs en or et des niveaux aurifères les plus épais au sein du gisement de Tiriganiaq, ce qui indique le contrôle significatif des charnières de plis **F<sub>2A</sub>** sur la distribution de l'or.

Deux tendances principales de zones à haute teneur ont été précédemment reconnues à Tiriganiaq (Lawley et al., 2016). La tendance la plus importante est coaxiale à la zone charnière **F<sub>2A</sub>** plongeant vers l'ouest du FFR étroitement plissé dans le toit du gisement. Les zones à haute teneur moins importantes et mal comprises, qui plongent vers le SE, correspondent probablement

à l'intersection de la faille Lower et des surfaces orientées NE-SW, comme la foliation régionale S<sub>2</sub>A.

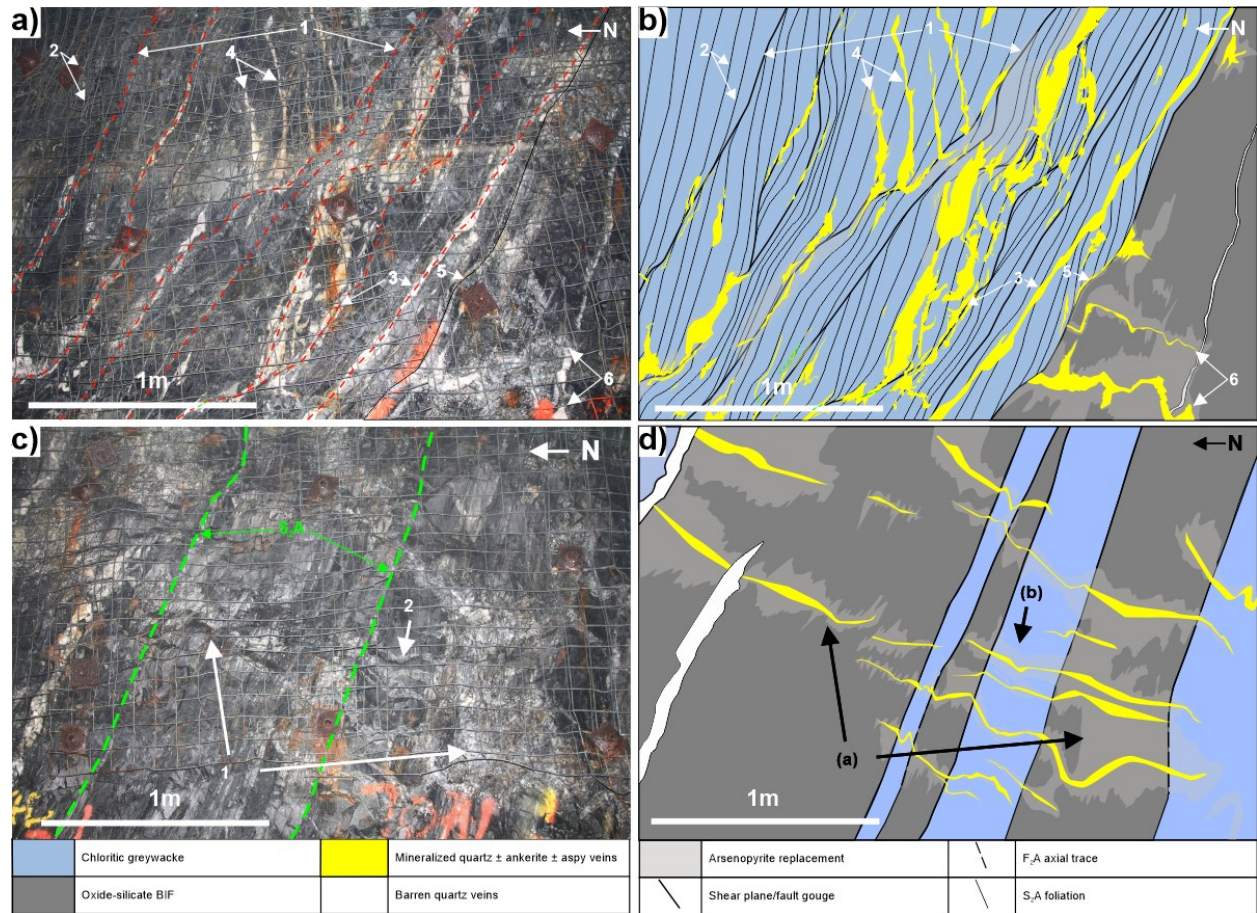
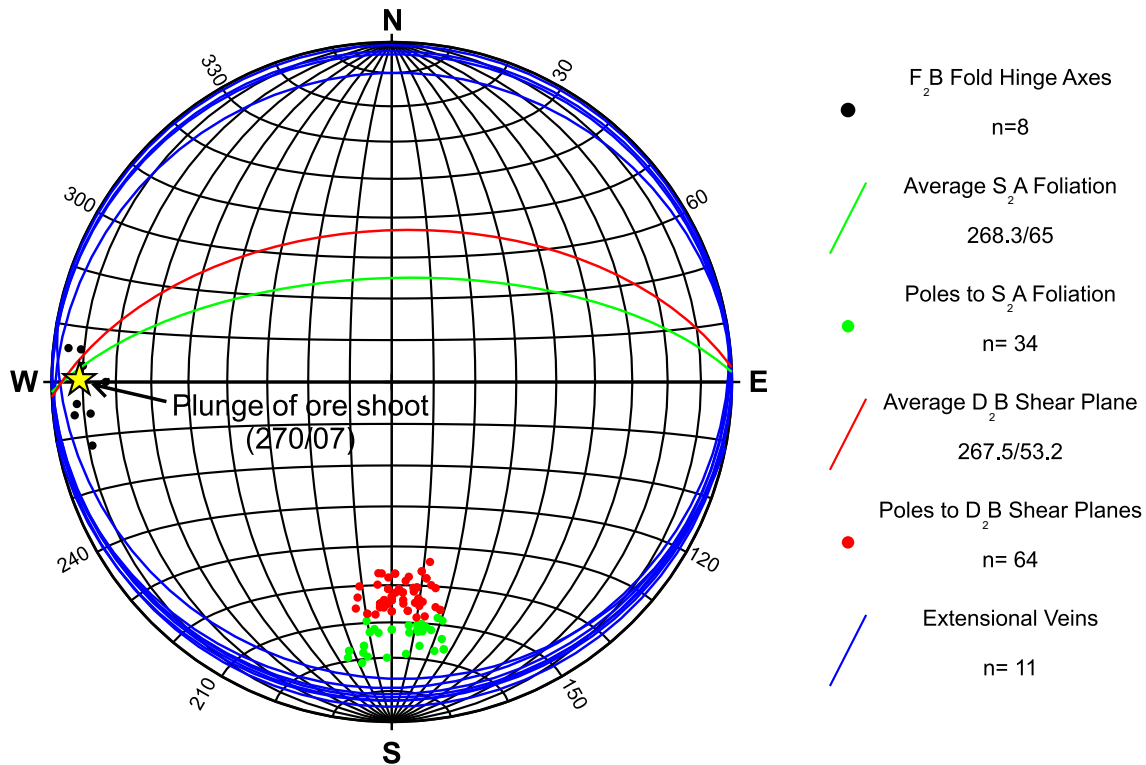


Figure 7

a) Photographie et schéma associé (b) de la zone 1150 dans la galerie CC300-152 (paroi est) montrant une zone de cisaillement localisée dans le grauwacke à chlorite, typique de la zone 1150, avec des indicateurs cinématiques de mouvement apparent inverse (entraînement de S<sub>2</sub>A), avec des plans de cisaillement discrets anastomosés (1) qui sont modérément inclinés (nord), c'est-à-dire plus superficiellement que la foliation principale, qui est entraînée sur les plans de cisaillement (2), ce qui indique une composante inverse du mouvement. Des veines de cisaillement bien développées de quartz ± ankérite ± arsénopyrite (3) se forment le long des plans de cisaillement et les veines d'extension associées (4) sont transposées vers le haut dans la foliation S<sub>2</sub>A. De plus, de minces veines de cisaillement parallèles au contact (5) se forment à la limite de la grauwacke à chlorite et du FFR. Des veines d'extension de quartz ± ankérite ± arsénopyrite (6) sub-horizontales à faiblement inclinées vers le sud, associées à la zone de cisaillement inverse, sont présentes dans le FFR et forment des zones de remplacement stratoïdes à arsénopyrite le long des marges des veines. c) Photographie et schéma associé (d) de la zone 1150 dans la coupe transversale CC300-152 (paroi est) montrant une série de veines de quartz ± arsénopyrite ± ankérite ± pyrrhotite D<sub>2</sub>B faiblement inclinées vers le sud et un remplacement du FFR parallèle au litage (1). Les veines qui s'étendent dans le siltstone ont tendance à contenir beaucoup moins de sulfure (2). Les veines qui coupent les roches sédimentaires moins compétentes et intensément foliées ont également tendance à être réfractées et transposées. Dans certains cas, les veines encaissées par le FFR ne s'étendent pas dans les bandes de siltstone à chlorite. Abréviations : FFR = formation de fer rubané.



À l'échelle des séries filoniennes 1150 et 1250, l'intersection de la foliation  $S_2A$  transposée et des plans de cisaillement  $D_2B$  avec les veines d'extension sub-horizontales plonge très peu (moins de 10 degrés) vers l'est et l'ouest (Fig. 8). La plongée moyenne de la charnière du pli  $F_2A$  est de  $N268/10$ , et correspond à l'intersection de la foliation  $S_2A$  et des plans de cisaillement  $D_2B$  avec les veines d'extension sub-horizontales (Fig. 8). Par conséquent, la géométrie du principal gisement de minerai à haute teneur correspond à la faible plongée, vers l'ouest, de la charnière du pli  $F_2A$  et à l'intersection de la foliation  $S_2A$ , des plans de cisaillement  $D_2B$  et des veines d'extension minéralisées subhorizontales. La nature des lithologies hôtes (composition et rhéologie) a également un effet important sur la distribution des zones riches en or dans les filons 1100, 1150 et 1250, ce qui génère également des zones de haute teneur de nature géométrique.



**Figure 8** Stéréonet des mesures structurales souterraines compilées prises dans les coupes transversales : CC300-152, CC300-153, et CC300-155, montrant la plongée du gisement de minerai des séries filoniennes 1150 et 1250 correspondant à la plongée de la charnière du pli  $F_2A$  et à l'intersection de la foliation  $S_2A$ , des plans de cisaillement  $D_2B$ , et des veines d'extension minéralisées sub-horizontales.

## Chapitre 5 : Discussion et conclusion

Tiriganiaq est un gisement d'or orogénique épigénétique, partiellement encaissé dans des FFR au faciès métamorphique des schistes verts. Les séries filoniennes 1150 et 1250 sont encaissées dans la Formation Upper Oxide, un ensemble plissé complexe de grauwacke, de grès et d'argillite à chlorite intercalés avec des niveaux de FFR au faciès oxyde-silicate dominant au faciès pélitique mineur. La minéralisation aurifère dans les séries filoniennes 1150 et 1250 est associée à une minéralisation de remplacement de type FFR, couplée à des veines et des veinules de quartz  $\pm$  ankérite aurifères. L'arsénopyrite et la pyrrhotite sont les phases sulfurées dominantes, avec des quantités mineures de chalcopyrite et de pyrite, et des traces de galène. Dans l'ensemble, la séricite, l'ankérite idioblastique, le quartz et l'altération en chlorite sont répandus dans les lithologies sédimentaires clastiques (grauwacke à chlorite, argillite laminée et certaines parties du faciès pélitique des FFR), alors que la FFR à oxyde-silicate et certaines parties de la FFR pélitique comprennent un assemblage d'altération dominant à quartz  $\pm$  chlorite  $\pm$  ankérite  $\pm$  sulfure.

La minéralisation aurifère dans les filons 1150 et 1250 est contrôlée par des zones de cisaillement étroites, à pendage nord,  $D_2B$  dextre-inverse, localisées dans le grauwacke à chlorite. Ces zones de cisaillement recoupent la foliation  $S_2A$  légèrement plus abrupte, transposée et à pendage nord, qui est planaire à l'axe des plis  $F_2A$  transposés et serrés. Plus important encore, cette étude a révélé l'importance des veines de quartz  $\pm$  ankérite minéralisées d'extension  $D_2B$  horizontales à faiblement inclinées vers le sud. Ces veines et les zones de remplacement des sulfures qui leur sont associées se développent de préférence dans des intervalles de FFR à faciès oxyde-silicate et de FFR pélitique mineur à plis  $F_2A$  serrés transposés. Les lithologies FFR à faciès oxyde-silicate et pélitique sont relativement enrichies en or par rapport aux lithologies de grauwacke chloritique et d'argillite laminée, ce qui signifie qu'elles ont agi comme un piège chimique et structural préférentiel pour la minéralisation aurifère.

Dans ce modèle, la déformation progressive  $D_2$  commence par un raccourcissement nord-est-sud-ouest ( $D_2A$ ) et une phase de plissement isoclinal  $F_2A$  parallèle aux couches des successions hôtes et le développement associé d'un clivage  $S_2A$  axial, régionalement pénétratif (Fig. 9). Le chevauchement et le couloir minéralisé le long des failles Pyke et Lower ont probablement commencé au début de l'événement de déformation  $D_2$  (c'est-à-dire  $D_2A$ ), tel que suggéré par Miller et al. (1995). Ce phénomène a été suivi d'un léger changement d'orientation, possiblement graduel, du raccourcissement vers le nord-sud ( $D_2B$ ). Cela a créé des plis en Z asymétriques cryptiques régionaux est-ouest (plis  $F_2A$  localement transposés) et une foliation  $S_2B$  axiale. La



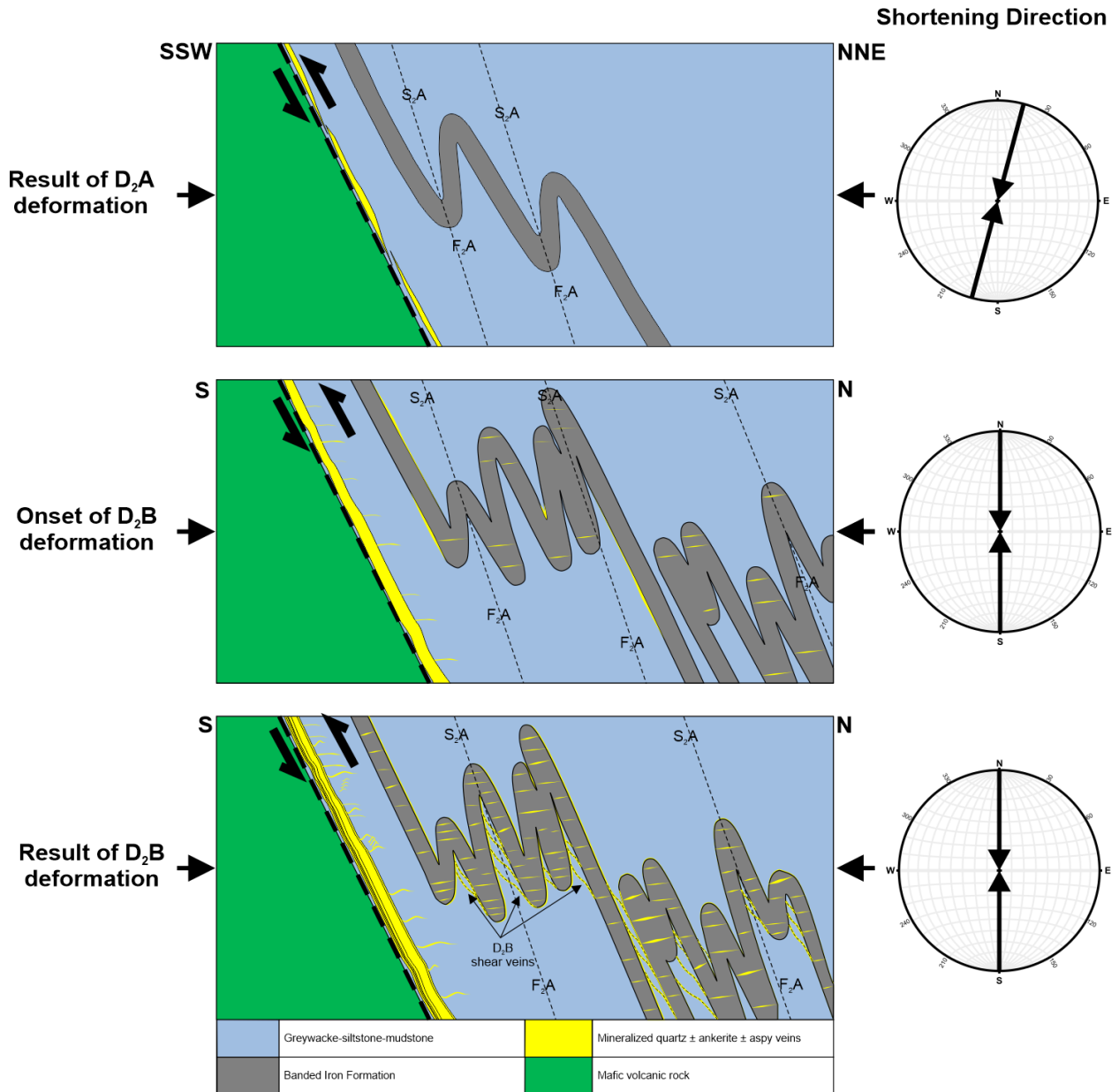
chronologie et le léger changement de l'orientation de l'axe de raccourcissement et de la fabrique pénétrative associée, ainsi que le cisaillement localisé peuvent avoir été influencés par : 1) la limite originale entre le bloc de Chesterfield et le craton de Hearne ; 2) la géométrie de la faille de Pyke en raison de la répartition des déformations et des contrastes de compétence à l'échelle régionale entre les roches métasédimentaires/volcaniques/volcanoclastiques et les plutons felsiques rigides ; et/ou 3) la mise en place d'intrusions telles que le monzogranite de Peter Lake ( $1856 \pm 10$  Ma) (Van Breemen et al, 2005 ; Berman et al., 2007). Le plissement progressif est associé à une déformation plus fragile-ductile ( $D_2B$ ) jusqu'à ce que les plis resserrés ne soient plus en mesure d'accommoder ce raccourcissement. Le partitionnement de la déformation le long des charnières de plis et plus particulièrement des membres, des unités relativement moins compétentes et des contacts lithologiques a conduit au développement de zones de cisaillement inverse. Des veines de cisaillement minéralisées ont été mises en place le long des plans de cisaillement  $D_2B$  qui ont entraîné la foliation  $S_2A$ . Les zones de cisaillement minéralisées et les veines d'extension associées ont donc été mises en place pendant la phase de déformation de la  $D_2B$  (Figs. 9 et 10).

Par conséquent, l'or a été introduit principalement pendant la déformation  $D_2B$  (bien qu'une partie moindre de l'or ait pu être introduite lors de la déformation  $D_2A$ ), après le pic du métamorphisme. Les contraintes de temps sur la déformation  $D_2$  peuvent être limitées par le début de l'événement métamorphique régional trans-hudsonien (1900-1850 Ma) et par le début de la déformation  $D_3$  vers 1850 Ma. La mise en place de l'or peut être limitée davantage par les résultats de datation U-Pb qui donnent un âge supérieur à  $1862 \pm 29$  Ma sur les veines minéralisées (Lawley et al., 2015b). Cela concorde avec un âge  $^{207}\text{Pb}/\text{Pb}^{206}$  monazite de  $1854 \pm 6$  Ma (Carpenter et al., 2005). De plus, la datation Re-Os suggère que les phases d'arsénopyrite-galène-ilménite associées au minerai se sont formées localement à  $\geq 1860$  Ma (Fig. 10).

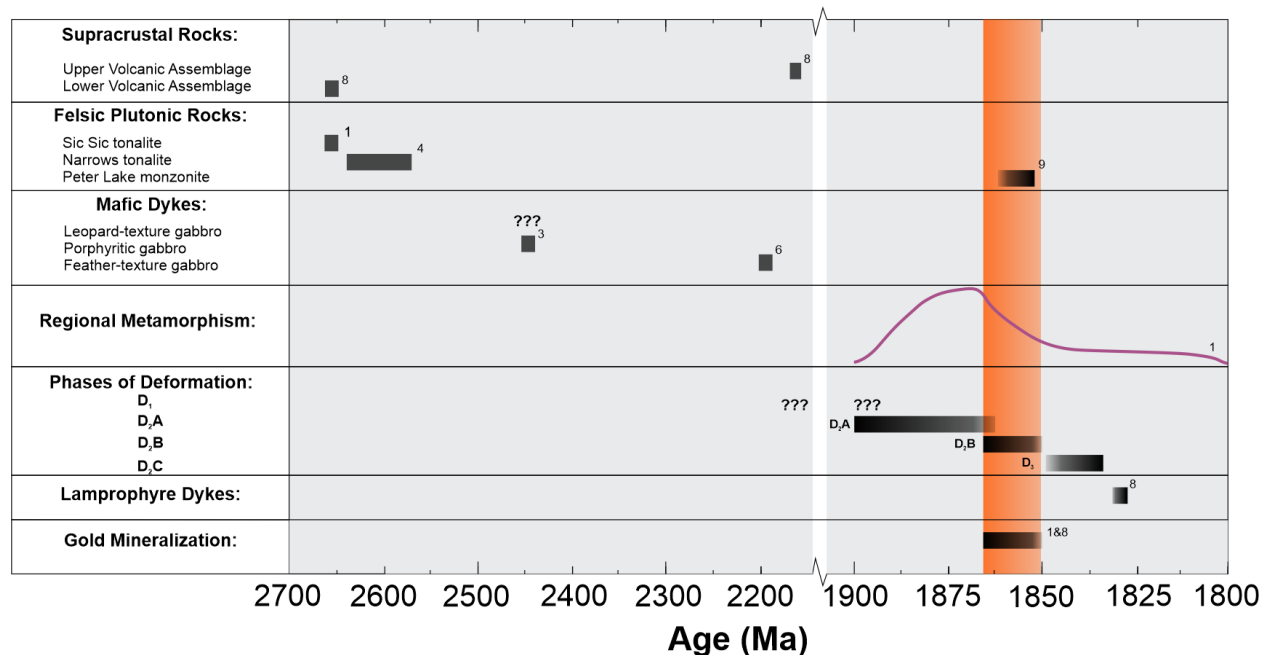
L'exploration pour une minéralisation aurifère similaire dans la ceinture de roches vertes de Rankin Inlet devrait se concentrer sur les zones avec des successions FFR larges qui ont subi une déformation polyphasée accompagnée de plissement et de cisaillement. Plus précisément, les zones de charnières des successions FFR épaissies par la tectonique et fortement plissées ( $F_2A$ ), recoupées par des structures secondaires et/ou des zones de forte contrainte, surtout celles qui sont transposées dans une orientation E-W comme à Tiriganiaq.

La cartographie géologique et structurale souterraine et le traitement des données géochimiques entrepris dans le cadre de cette étude ont permis d'améliorer les connaissances géologiques du gisement d'or de Tiriganiaq. Cette contribution comprend notamment : 1) une histoire structurale

mieux définie ; 2) une documentation détaillée des paramètres qui ont contrôlé la formation, la distribution et la géométrie de la minéralisation aurifère dans les séries filoniennes 1150 et 1250 ; et 3) une chronologie plus précise de l'introduction de l'or par rapport aux événements de déformation du gisement aurifère de Tirigniaq.



**Figure 9** Diagramme schématique montrant les éléments structuraux et la géométrie des veines minéralisées au cours de l'événement de déformation D<sub>2</sub> progressive. Aspy = arsénopyrite.



**Figure 10** Résumé de la chronologie relative et absolue des événements géologiques qui ont affecté le district aurifère de Meliadine. Contraintes d'âges isotopiques : 1) Carpenter et al. (2003), 2) Tella et al. (1996), 3) Heaman (1994), 4) Davis et al. (2000), 5) Peterson et al. (2002), 6) Sandeman et al. (2000b), 7) Roddick et Miller (1994), 8) Lawley et al. (2016) et 9) Van Breemen et al. (2005). Figure modifiée d'après Carpenter et al. (2003).

# TABLE OF CONTENTS

---

|  |               |
|--|---------------|
| <b>ACKNOWLEDGEMENTS</b> .....  | <b>I</b>      |
| <b>RÉSUMÉ</b> .....  | <b>II</b>     |
| <b>ABSTRACT</b> .....  | <b>IV</b>     |
| <b>SOMMAIRE RÉCAPITULATIF</b> .....  | <b>VI</b>     |
| <b>TABLE OF CONTENTS</b> .....   | <b>XXIII</b>  |
| <b>LIST OF FIGURES</b> .....   | <b>XXVI</b>   |
| <b>LIST OF TABLES</b> .....  | <b>XXVIII</b> |
| <b>1 INTRODUCTION</b> .....  | <b>1</b>      |
| 1.1    CONTEXT OF STUDY .....  | 1             |
| 1.1.1 <i>General Context</i> .....   | 1             |
| 1.1.2 <i>Orogenic Gold Deposits</i> .....  | 2             |
| 1.1.3 <i>Banded Iron Formations</i> .....  | 4             |
| 1.1.4 <i>BIF-Associated Gold Deposits</i> .....  | 5             |
| 1.1.5 <i>Structural Complexities of Orogenic Gold Deposits</i> .....   | 8             |
| 1.2    SPECIFIC PROBLEM .....  | 9             |
| 1.3    OBJECTIVES.....   | 10            |
| 1.4    METHODOLOGY .....   | 10            |
| 1.5    GEOLOGY .....   | 11            |
| 1.5.1 <i>Western Churchill Province Geology</i> .....  | 11            |
| 1.5.2 <i>The Rankin Inlet Greenstone Belt Geology</i> .....  | 13            |
| 1.5.3 <i>The Meliadine District Metallogeny</i> .....  | 16            |
| <b>2 GEOCHEMICAL AND PETROGRAPHIC CHARACTERIZATION OF THE 1150 AND 1250 LODE<br/>SERIES HOST ROCKS</b> ..... | <b>17</b>     |
| 2.1    CHLORITIC GREYWACKE .....   | 19            |
| 2.1.1 <i>Petrography</i> .....   | 20            |
| 2.1.2 <i>Geochemistry</i> .....  | 21            |
| 2.2    OXIDE-SILICATE BIF .....  | 26            |
| 2.2.1 <i>Petrography</i> .....   | 26            |
| 2.2.2 <i>Geochemistry</i> .....  | 27            |
| 2.3    PELITIC BIF.....  | 31            |
| 2.3.1 <i>Petrography</i> .....   | 31            |
| 2.3.2 <i>Geochemistry</i> .....  | 33            |
| 2.4    LAMINATED MUDSTONE .....  | 36            |
| 2.4.1 <i>Petrography</i> .....   | 36            |
| 2.4.2 <i>Geochemistry</i> .....  | 37            |

|          |   |           |
|----------|---|-----------|
| 2.5      | SUMMARY .....   | 41        |
| <b>3</b> | <b>STYLE AND DISTRIBUTION OF GOLD MINERALIZATION AND ASSOCIATED HYDROTHERMAL FOOTPRINT.....</b> | <b>47</b> |
| 3.1      | SULPHIDE MINERALOGY AND DISTRIBUTION OF GOLD, ARSENIC, AND SULPHUR .....                        | 49        |
| 3.1.1    | <i>Chloritic Greywacke</i> .....  | 49        |
| 3.1.2    | <i>Oxide-silicate BIF</i> .....   | 50        |
| 3.1.3    | <i>Pelitic BIF</i> .....  | 52        |
| 3.1.4    | <i>Laminated mudstone</i> .....   | 53        |
| 3.1.5    | <i>Summary</i> .....  | 55        |
| 3.2      | HYDROTHERMAL ALTERATION.....  | 58        |
| <b>4</b> | <b>STRUCTURAL ANALYSIS OF THE TIRIGANIAQ GOLD DEPOSIT .....</b>                                 | <b>65</b> |
| 4.1      | REGIONAL STRUCTURAL GEOLOGY .....   | 65        |
| 4.2      | TIRIGANIAQ STRUCTURAL GEOLOGY .....   | 67        |
| 4.3      | DETAILED UNDERGROUND MAPPING .....  | 70        |
| 4.3.1    | <i>Draw-point DP200-161</i> .....   | 74        |
| 4.3.2    | <i>Crosscut CC300-152</i> .....   | 74        |
| 4.3.3    | <i>Crosscut CC300-153</i> .....   | 74        |
| 4.3.4    | <i>Crosscut CC325-155</i> .....   | 74        |
| 4.4      | MICROSTRUCTURAL ANALYSIS.....   | 77        |
| 4.5      | GEOMETRY OF THE 1150 AND 1250 LODE SERIES .....   | 79        |
| <b>5</b> | <b>SYNTHESIS, DISCUSSION, AND CONCLUSIONS .....</b>   | <b>81</b> |
| 5.1      | SYNTHESIS OF DATA, RESULTS, AND INTERPRETATIONS .....   | 82        |
| 5.1.1    | <i>1150 and 1250 Lode Series Host Rocks</i> .....   | 82        |
| 5.1.2    | <i>Style and Distribution of Gold Mineralization and Associated Hydrothermal Footprint</i> .... | 82        |
| 5.1.3    | <i>Structural Analysis of the 1150 and 1250 Lode Series</i> .....                               | 84        |
| 5.2      | SEQUENCE OF EVENTS .....  | 86        |
| 5.3      | COMPARISON WITH OTHER BIF-ASSOCIATED GOLD DEPOSITS .....  | 92        |
| 5.3.1    | <i>Other ore zones in the Tiriganiaq deposit</i> .....  | 92        |
| 5.3.2    | <i>Other Deposits in the Meliadine Gold District</i> .....                                      | 93        |
| 5.3.3    | <i>Other BIF-hosted/associated Au deposits of the Churchill Province</i> .....                  | 95        |
| 5.3.4    | <i>Other type examples of BIF-hosted/associated Au deposits</i> .....                           | 98        |
| 5.3.5    | <i>Summary</i> .....  | 100       |
| 5.4      | IMPLICATIONS FOR MINE DEVELOPMENT AND EXPLORATION .....   | 100       |
| 5.5      | CONCLUSION .....  | 102       |
| 5.5.1    | <i>Main Contributions</i> .....   | 102       |
| 5.5.2    | <i>Outstanding questions</i> .....  | 103       |

|          |                           |            |
|----------|---------------------------|------------|
| <b>6</b> | <b>BIBLIOGRAPHY .....</b> | <b>105</b> |
| <b>7</b> | <b>ANNEX .....</b>        | <b>113</b> |

## LIST OF FIGURES

---

|             |  |    |
|-------------|--|----|
| Figure 1.1  | Inferred crustal levels of different gold deposit types. ....  | 4  |
| Figure 1.2  | Regional geologic map of the western Churchill Province.....   | 12 |
| Figure 1.3  | Cartoon cross section through the Rae-Hearne boundary .....  | 13 |
| Figure 1.4  | The Meliadine Gold District geology map .....  | 14 |
| Figure 1.5  | Lithostratigraphic column of the Rankin Inlet greenstone belt .....  | 15 |
| Figure 2.1  | Tiriganiaq mine area overturned stratigraphic column. ....   | 18 |
| Figure 2.2  | Representative photomicrographs of chloritic greywacke .....   | 20 |
| Figure 2.3  | Harker diagrams of chloritic greywacke samples. ....   | 24 |
| Figure 2.4  | Chondrite-normalized multi-element profile of chloritic greywacke samples.....   | 25 |
| Figure 2.5  | Representative photomicrographs of oxide-silicate BIF .....  | 26 |
| Figure 2.6  | Harker diagrams of oxide-silicate BIF samples .....  | 29 |
| Figure 2.7  | Chondrite-normalized multi-element profile of oxide-silicate BIF samples.....  | 30 |
| Figure 2.8  | Representative photomicrographs of pelitic BIF.....  | 31 |
| Figure 2.9  | Harker diagrams of pelitic BIF samples. ....   | 34 |
| Figure 2.10 | Chondrite-normalized multi-element profile of pelitic BIF samples .....  | 35 |
| Figure 2.11 | Representative photomicrographs of laminated mudstone .....  | 36 |
| Figure 2.12 | Harker diagram of laminated mudstone samples.....  | 39 |
| Figure 2.13 | Chondrite-normalized multi-element profile of laminated mudstone samples.....  | 40 |
| Figure 2.14 | Herron 1988 Geochemical classification diagram .....   | 43 |
| Figure 2.15 | Combined Zr / TiO <sub>2</sub> vs. Al <sub>2</sub> O <sub>3</sub> / TiO <sub>2</sub> geochemical discrimination diagram..... | 44 |
| Figure 2.16 | Winchester and Floyd (1977) classification diagram.....  | 45 |
| Figure 2.17 | Binary diagram Fe (III) tot / Ti vs Al / (Al + Fe (III) tot + Mn).....   | 46 |
| Figure 3.1  | Representative mineralization style of chloritic greywacke.....  | 49 |
| Figure 3.2  | Representative mineralization style of oxide-silicate BIF.....   | 51 |

|            |   |     |
|------------|---|-----|
| Figure 3.3 | Representative mineralization style of pelitic BIF.....   | 52  |
| Figure 3.4 | Representative mineralization style of laminated mudstone.....  | 54  |
| Figure 3.5 | Alteration indices box plot (Large et al., 2001). .....   | 59  |
| Figure 3.6 | Chloritic greywacke facies representative hydrothermal alteration.....  | 60  |
| Figure 3.7 | Oxide-silicate BIF facies representative hydrothermal alteration.....   | 61  |
| Figure 3.8 | Au vs. As-Sb-Se-Bi-Cu-Pb-Zn bi-plots.....   | 63  |
| Figure 3.9 | Metal associations principal component analysis bi-plot map .....   | 64  |
| Figure 4.1 | Schematic section of the Tiriganiaq deposit and its various ore zones.....  | 69  |
| Figure 4.2 | Photograph and associated schematic of a mineralized shear zone localized in chloritic greywacke typical of the 1150 zone. ....   | 71  |
| Figure 4.3 | Photograph and associated schematic of a sub-horizontal mineralized extensional veins forming stratabound sulphide replacement zones in BIF typical of the 1150 zone..... | 72  |
| Figure 4.4 | Representative photos of the Lower Fault, 1000 lode and 1100 lode.....  | 73  |
| Figure 4.5 | Detailed geological and structural maps of the underground workings of the 1000, 1100, and 1150 lodes at the Tiriganiaq deposit.....                                      | 77  |
| Figure 4.6 | Representative photomicrographs of the structural fabrics. ....   | 79  |
| Figure 4.7 | Stereonet projection of compiled underground structural measurements.....   | 80  |
| Figure 5.1 | Schematic diagram of the relative timing of events and structural features at Tiriganiaq in cross-section view looking west. ....   | 90  |
| Figure 5.2 | Schematic diagram of the orientation of the Pyke Fault during D <sub>2</sub> deformation .....  | 91  |
| Figure 5.3 | Summary of relative and absolute timing of geological events that affected the Meliadine gold district.....   | 92  |
| Figure 5.4 | Sketch showing the impact this study had on the geological modelling and stope design in the 1150 lode series.....  | 101 |



## LIST OF TABLES

---

|   |    |
|---|----|
| Table 2.1 Summary of chloritic greywacke gangue mineralogy (modal percent) .....                                | 21 |
| Table 2.2 Summary of chloritic greywacke major oxides composition .....   | 22 |
| Table 2.3 Summary of major oxide (wt. %) abundance for all lithologies .....                                    | 23 |
| Table 2.4 Summary of oxide-silicate BIF gangue mineralogy (modal percent) .....                                 | 27 |
| Table 2.5 Summary of oxide-silicate BIF gangue mineralogy .....   | 28 |
| Table 2.6 Summary of pelitic BIF gangue mineralogy modal percent .....  | 32 |
| Table 2.7 Summary of pelitic BIF major oxide .....  | 33 |
| Table 2.8 Summary of laminated mudstone gangue mineralogy (modal percent) .....                                 | 37 |
| Table 2.9 Summary of laminated mudstone major oxide (wt. %) .....   | 38 |
| Table 3.1 Summary of chloritic greywacke sulphide mineralogy modal percent .....                                | 50 |
| Table 3.2 Summary of gold, arsenic and sulphur content in chloritic greywacke .....                             | 50 |
| Table 3.3 Summary of oxide-silicate BIF sulphide mineralogy .....   | 51 |
| Table 3.4 Summary of gold, arsenic and sulphur content in oxide-silicate BIF .....                              | 51 |
| Table 3.5 Summary of pelitic BIF sulphide mineralogy .....  | 53 |
| Table 3.6 Summary of gold, arsenic and sulphur content in pelitic BIF .....                                     | 53 |
| Table 3.7 Summary of laminated mudstone sulphide mineralogy .....   | 54 |
| Table 3.8 Summary of gold, arsenic and sulphur content in laminated mudstone. ....                              | 54 |
| Table 3.9 Summary of sulphide assemblage (modal percentage) for all lithologies .....                           | 56 |
| Table 3.10 Summary of gold, arsenic and sulphur content for all lithologies .....                               | 57 |
| Table 4.1 Summary of Structural Events at the Rankin Inlet Greenstone Belt .....                                | 66 |
| Table 4.2 Summary of Structural Events at Tiriganiaq .....  | 68 |
| Table 5.1 Meliadine Gold District ore deposit characteristics summary .....                                     | 94 |
| Table 5.2 Comparison of key characteristics of the churchill province BIF-hosted/associated gold deposits ..... | 97 |

# 1 INTRODUCTION

---

## 1.1 Context of Study

### 1.1.1 General Context

Gold is consistently Canada's most valuable mined mineral by value of production annually, significantly contributing to Canada's GDP (Natural Resources Canada, 2021). Canada's gold resources are mainly related to mining districts located within Archean greenstone belts and most notably the Superior Province (Gosselin and Dubé, 2005; Percival, 2007; Oswald et al, 2018). In Archean greenstone belts, gold is most significant in terms of grade and abundance in orogenic quartz-carbonate-vein-type gold deposits, although gold has been concentrated and deposited in a variety of other geological settings including volcanogenic massive sulphides, intrusion-related, etc. (Poulsen et al., 2000; Golfarb et al., 2005; Robert and Poulsen., 2001; Dubé and Gosselin, 2007; Dubé and Mercier-Langevin, 2020).

Canada's north is largely underexplored and offers a massive geographic area that has the high potential to host orogenic quartz-carbonate vein-type gold deposits, as most Canada's north is underlain by Archean and Proterozoic rocks and numerous greenstone belts. These deposits are hosted within a variety of host rocks but mainly hosted in mafic volcanic rocks and intrusions, with only a minor portion hosted within banded-iron formation (BIF), referred to as BIF-associated or BIF-hosted gold deposits (Dubé et al., 2015). BIF-hosted gold deposits have the potential of being world-class gold deposits (e.g., Homestake deposit, South Dakota, 40 Moz Au; Caddey et al., 1991) and they represent an important exploration target in the greenstone belts of the Canadian Shield, especially in underexplored geographic areas such as Nunavut.

Over the past decade, Agnico-Eagle Mines limited has had tremendous success at acquiring district-scale advanced stage, and at discovering, BIF-associated gold projects and advancing them to operating mines within the Western Churchill Province of Nunavut. Agnico-Eagle Mines Meliadine Gold District (MGD), located within the Archean (>2.66 Ga) Rankin Inlet greenstone belt (RIGB) in Nunavut, is one of Canada's largest emerging gold districts with 3.65 million ounces (113.6 t) of gold in proven and probable reserves, 2.25 million ounces (69.9 t) of gold in indicated resources and 2.29 million ounces (71.3 t) of gold in inferred resources as of December 31, 2021 (Agnico Eagle Mines Limited, 2022). The MGD comprises numerous orogenic gold deposits, and prospects that are spatially associated with the crustal-scale Pyke Fault and its splays. Many of

these gold deposits are partly to dominantly hosted in BIF units, including the Tiriganiaq deposit, MGD's principal deposit, that has recently been put into commercial production (2019, Q2).

This thesis is based on detailed underground field work done as a contribution to graduate studies in Earth sciences at the Université du Québec-INRS-ETE, in conjunction with the Geological Survey of Canada Targeted Geoscience Initiative program gold projects, and Agnico Eagle Mines Ltd. This study is part of a larger thematic research project at the Geological Survey of Canada that aims at better understanding the controls on partly BIF-hosted gold deposits in general, and at unravelling the interplay between Archean and Paleoproterozoic events in forming the Churchill Province BIF-hosted gold deposits. The thesis integrates detailed structural and geological mapping, lithogeochemistry data, petrographic and microstructural analysis to provide a description of the structural and lithological controls on the distribution and nature of gold endowment within the Tiriganiaq gold deposit.

### **1.1.2 Orogenic Gold Deposits**

Orogenic gold deposits are epigenetic gold deposits present in granite-greenstone and slate belts that are formed during the late stages of orogeny. These deposits occur in deformed belts of all ages but are more common and significant in terms of gold content in Archean and Paleoproterozoic terranes (Goldfarb et al., 2005; Dubé and Gosselin, 2007).

Orogenic gold deposits are universally structurally controlled, at all scales ranging from the distribution of deposits to the internal textures and structures of the ore (Robert, 1994). These deposits are typically located adjacent to first-order deep crustal-scale fault zones, such as those marking convergent margins between major lithological and/or terrane boundaries. These crustal-scale fault zones show complex structural histories and can extend along strike for hundreds of kilometers and have widths of up to a few thousand meters (Robert, 1994; Goldfarb et al., 2005; Dubé and Mercier-Langevin, 2020).

Gold bearing fluid migration along these zones is thought to occur in a pulsative manner giving rise to crack and seal textures within ore-bearing veins (Sibson, 1986; Sibson et al., 1988; Cox, 1991). This seismic fluid-pressure cycling occurs during periods of seismic aftershock, as a result of orogeny, and focuses in the secondary and tertiary zones that remain active longer (Sheldon and Micklethwaite, 2007). Ore deposition is localized as vein fill of second- and third-order shears and faults, or associated fracture systems (Robert, 1994). Additionally, mineralization can be restricted to particular parts of faults or shear zones such as jogs or bends, and to fold-related structures such as saddle reefs. According to the continuum model, mineralization styles in

orogenic gold deposits vary from stockworks and breccias in shallow, brittle regimes, through laminated crack-seal veins and sigmoidal vein arrays in brittle-ductile crustal regions, to replacement- and disseminated-type orebodies in deeper, ductile environments (Goldfarb et al., 2005).

Most orogenic gold deposits occur in greenschist facies rocks, but significant orebodies can be present in both lower and higher-grade rocks. Deposits typically formed on retrograde portions of pressure-temperature-time paths and thus are discordant to metamorphic features within host rocks (Robert and Poulsen, 2001; Goldfarb et al., 2005).

World-class orebodies are generally 2 to 10 km long, about 1 km wide, and are mined downdip to depths of 2 to 3 km (Goldfarb et al., 2005; and references therein). Most orogenic gold deposits contain less than 5-10% percent sulphide minerals (Dubé and Gosselin., 2007), and have gold/silver ratios from 5 to 10 and gold fineness >900 (Goldfarb et al., 2005; and references therein). Arsenopyrite and pyrite are the dominant sulphide minerals, whereas pyrrhotite is more common in higher temperature ores; base metals are not highly anomalous. Alteration intensity, width, and assemblage vary with the host rock, but carbonates, sulphides, muscovite, chlorite, K-feldspar, biotite, tourmaline, and albite are generally present, except in high-temperature systems where alteration halos are dominated by skarn-like assemblages (Goldfarb et al., 2005; Dubé and Gosselin, 2007 and references therein).

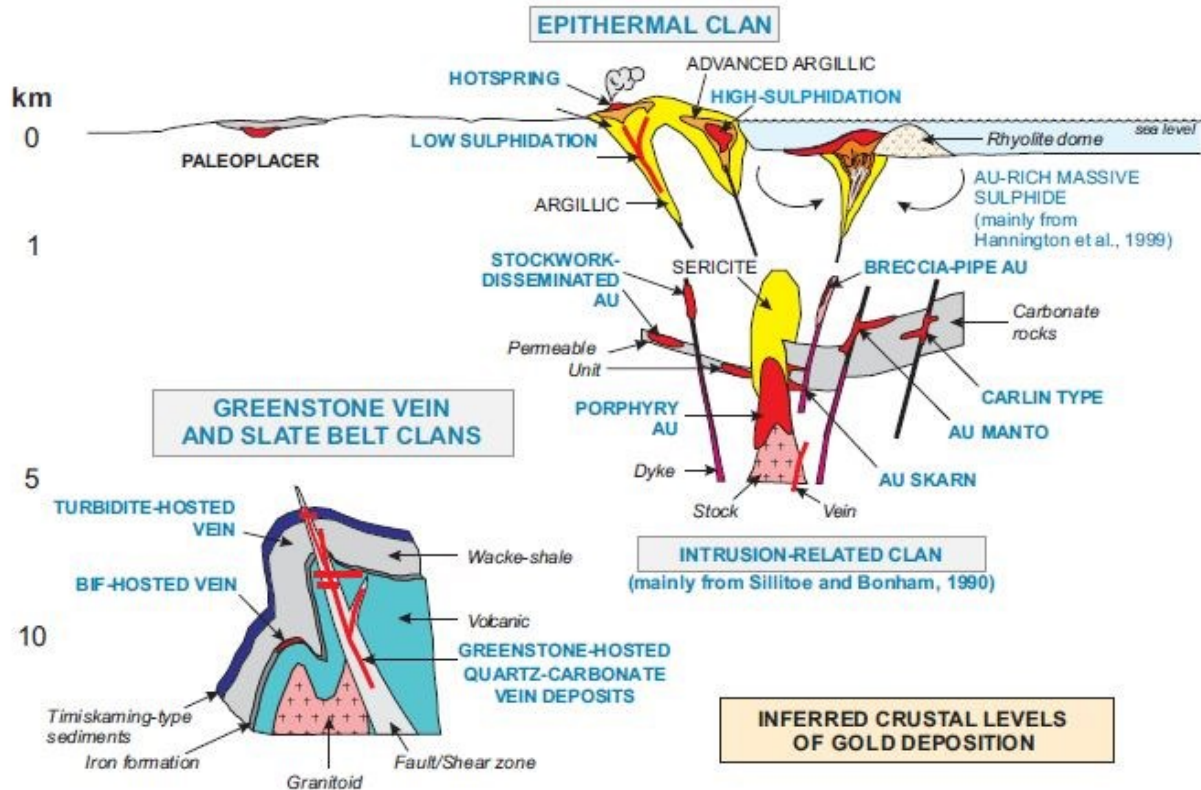


Figure 1.1 Inferred crustal levels of gold distribution showing the different deposit types and some of their characteristics (From Dubé and Gosselin, 2007).

Orogenic gold deposits typically form at depths greater than five km in a variety of different host rocks including BIF (Fig. 1.1). These deposits are considered a sub-type of orogenic gold deposits referred to as BIF-associated gold deposits (Poulsen et al., 2000; Dubé et al., 2015).

### 1.1.3 Banded Iron Formations

Banded iron formations (BIFs) host a significant volume of high-grade ore at Tiriganiaq, therefore understanding the characteristics of the BIF host rocks is an important component of this study. Special attention is given to the petrography and lithogeochemistry in chapter 2; the mineralization and hydrothermal alteration signature in host BIFs in chapter 3; and the relative competency contrasts between the BIFs and interlayered sedimentary rocks during deformation and their relationships with gold mineralization in chapter 4.

The term iron formation is restricted to stratigraphic units composed of layered, bedded, or laminated rocks that contain 15 percent or more iron, in which the iron minerals are commonly interlayered with quartz, chert, or carbonate; belonging to one of four iron formation facies, including: silicate, carbonate, oxide, and sulphide (James, 1954; Gross, 1980).

BIFs can be subdivided into three major types, mainly based on the inferred tectonic environments of the host stratigraphic sequence (Gross, 2009): Algoma, Superior and Rapitan types. Algoma-type BIFs are thinly bedded, chemical sedimentary rocks comprising alternating layers of iron-rich minerals and chert. They differ from Superior-type BIFs which represent extensive units, mainly Proterozoic in age, located in passive margin sedimentary successions and showing no specific association with volcanic units (e.g., Gross, 1980; Bekker et al., 2010). Rapitan BIFs are a minor younger type, specifically associated with glacial sedimentary deposits, usually formed of sandstone and conglomerate (Klein and Beukes, 1993). They commonly have a much more restricted extent compared to that of their host sequences (Bekker et al., 2010), which are mostly Cryogenian in age (e.g., Neoproterozoic; Klein, 2005).

#### **1.1.4 BIF-Associated Gold Deposits**

Algoma-type, and to some extent Superior-type BIFs represents an important host rock for a large number of world-class gold deposits, including the archetypical BIF-hosted Homestake mine, South Dakota, USA, which produced 40 million ounces (>1240 t) of gold (Bell, 2013). Other large BIF-hosted gold deposits include the Morro Velho mine in Minas Gerais, Brazil, which has produced over 15 million ounces (>465 t) of gold in almost 300 years of production (Vial et al., 2007) as well as past or currently producing Canadian mines (e.g., Lupin in Nunavut: Lhotka, 1988; Guesebroek and Duke, 2004, Meadowbank in Nunavut: Sherlock et al., 2004; Janvier, et al., 2017, Hardrock in Geraldton-Beardmore, Ontario: Tóth et al., 2019, Musselwhite in Ontario: Oswald et al., 2018, and Tiriganiaq in Nunavut: Carpenter and Duke., 2004).

The exceptional gold endowment of these deposits is due, at least in part, to the Fe-rich nature of the host rocks. Experimental geochemistry suggests that the solubility of gold within moderate temperature hydrothermal fluids is favoured by S-ligands. These S-Au complexes are destabilized during fluid:rock interaction with Fe-rich rocks (Phillips et al., 1984), which is reflected in the rock record by the ubiquitous association between gold and sulphide replacement zones (e.g., arsenopyrite, pyrite, pyrrhotite) at most BIF-hosted deposits. In addition, the host BIFs are relatively more competent than their surrounding sedimentary or volcanic rocks. These competency contrasts are responsible for preferential strain partitioning along the contacts of the BIF and surrounding rocks during deformation developing shear zones, which are optimal pathways for gold-rich fluids to migrate through, making BIFs an ideal physical trap for gold mineralization (Phillips et al., 1984; Colvine, 1989; Janvier et al., 2015).

Various classifications and genetic models have been proposed through time for BIF-hosted gold deposits, i.e. syngenetic/stratiform versus epigenetic/non-stratiform based on the dominant style of gold distribution (e.g., Fripp, 1976; Phillips et al., 1984). In non-stratiform deposits all of the gold occurs within or adjacent to secondary structures (veins, fractures, and/or shear zones) cutting the banded iron formation. Such deposits are clearly epigenetic products of localized sulphidation reactions in structurally and chemically favourable host rocks. In stratiform deposits much of the gold is uniformly disseminated in thin, laterally continuous units of sulphide-rich banded iron formation. The critical difference between the two principal types is the absence of stratiform ore in non-stratiform deposits (Kerswill, 1996).

At the Lupin gold mine in Nunavut, the stratiform syngenetic versus non-stratiform epigenetic model of formation has been debated in great detail (Kerswill, 1993; Gardiner, 1986; Kerswill et al., 1983, 1996; Lhotka, 1988; Ford, 1988; Gross, 1996; Colvine, 1989; Bullis, 1990, 1994). Most notably, Kerswill (1996) proposed a genetic model invoking a synsedimentary (diagenetic) concentration of much of the gold and sulphur in stratiform portions of the deposit, followed by localized remobilization or epigenetic introduction of some of the gold and sulphur immediately adjacent to late quartz veins throughout the deposit. This was mainly due to the seemingly historically consistent observations of heavily mineralized portions of the deposit being extensive, laterally continuous stratigraphic sulphide-rich BIF units (Kerswill, 1996; Bullis et al., 1994).

However, Ford and Duke (1993) and Guesebroek and Duke (2004) favour a more widely accepted metamorphic model of BIF-hosted ore genesis, with gold being critically linked to devolatilization accompanying prograde metamorphic reactions at the greenschist/ amphibolite recrystallization front. Guesebroek and Duke (2004) suggest a paragenetic history consistent with metamorphic pyrrhotite replacement of host silicate BIF and later shear-related hydrothermal löllingite/ arsenopyrite mineralization marginal to late quartz veins. Free gold most commonly occurs along the contacts of löllingite cores preserved within the late-growing arsenopyrite, suggesting that gold was initially fixed at higher temperatures (in löllingite) above the stability limit of arsenopyrite, and unmixed during the conversion of löllingite to arsenopyrite (Guesebroek and Duke, 2004).

The Homestake gold mine in South Dakota is dominantly hosted by carbonate-silicate-sulphide facies iron formation. The model of formation has been highly debated there as well. Based on Pb and S isotopic data, Rye et al. (1974) proposed a syngenetic sedimentary exhalative model for the origin of gold. This model suggests gold is being locally remobilized from, but originally syngenetic with, the host rock, was later adopted by others (e.g., Redden and French, 1989).

However, like Lupin, a more widely accepted model for Homestake is that it is non-stratiform epigenetic deposit and the stratabound character of the ore results from the iron formation being a favourable chemical trap for gold deposition when infiltrated by a hydrothermal fluid (e.g., Caddey et al. 1991; Frei et al. 2009). Groves et al. (1998), and Goldfarb et al. (2005) consider Homestake to be a typical “orogenic gold deposit” and recognize both the structural control on mineralization and the introduction of gold-bearing fluids at or after the initiation of peak regional metamorphism, as indicated by mineral assemblages from vein selvages in the deposit (Terry et al., 2003).

Dubé et al. (2015) distinguish two distinct groups of BIF-hosted gold deposits: 1) large deposits in which the ore is mainly hosted in Algoma-type BIF; and 2) deposits where only part of the mineralization is hosted in BIF. In both cases, they interpret gold as being a late component introduced in the BIF units during regional deformation along major structures.

Partly BIF-hosted gold deposits are generally hosted within lithotectonic settings where BIF units only constitute a minor component of the host sequence, but these settings can still be prospective for large BIF-hosted gold deposits. The ore-hosting BIF units are much thinner and discontinuous at deposit to district scales in comparison to BIF dominated deposits. Ultramafic flows appear sparse to minor in districts where BIFs represent a minor host (Dubé et al., 2015).

Mineralized zones within partly BIF-hosted gold deposits consist of orogenic greenstone-hosted quartz ± carbonate veins that tend to cluster along a major fault zone, and/or concentrated along thickened fold hinges and strongly attenuated limbs of shallow-plunging folds (syn- and/or post-ore) as well as second- and third order deformation zones (e.g., Lupin in Nunavut: Lhotka, 1988, Hardrock in Beardmore-Geraldton, Ontario: Tóth et al., 2019, Tiriganiaq in Nunavut: Carpenter and Duke, 2004).

On the other side of the spectrum, large deposits in which the ore is mainly hosted in Algoma-type BIF hosted within BIF-rich volcano-sedimentary basins. BIF units can be tens of meters thick and extend for thousands of metres in deposits dominantly hosted in BIF horizons, making them volumetrically and laterally much more important. Ultramafic flows form an essential part of the host stratigraphy in some dominantly BIF-hosted gold deposits (Dubé et al., 2015).

The Meadowbank deposit, a dominantly BIF-hosted gold deposit, contains significant gold mineralization within only one of multiple BIF units. This unit is interpreted to be located along the boundary between two distinct Archean assemblages that are possibly separated by long-lived fault(s) and splays. The presence of such a crustal boundary suggests that there is a large-scale



first order structural-control on gold and may explain why only this BIF is mineralized with gold and the other BIF units located away from that structure are barren (Janvier et al., 2015) but otherwise very similar compositionally (Janvier et al., 2015; Janvier, 2016; Gourcerol et al., 2016a, b). This suggests that such first-order fault zones are an equally important control on the formation and distribution of auriferous mineralized zones within BIF-hosted gold deposits just as they are in shear-hosted orogenic gold deposits. A somewhat similar context has been described at the Musselwhite mine (Oswald et al., 2015).

### **1.1.5 Structural Complexities of Orogenic Gold Deposits**

Orogenic gold deposits including those that are BIF-hosted are universally structurally controlled at all scales ranging from the distribution of deposits to the internal textures of the ore. There are three main factors that influence the geometry of orogenic gold deposits: 1) the stress regimes in which deposits were formed or deformed; 2) the presence of strength anisotropies and/or competency contrasts (BIF vs volcanic/siliciclastic/carbonate rocks), which influence the localization, geometry and kinematics of shear zones, and veins; and 3) the structural history of the deposits, which indicates whether a deposit is relatively undeformed or has been structurally overprinted (Robert, 1994).

Most gold districts are commonly associated with major crustal-scale fault or shear zones usually marking a major terrane boundary that are lithologically contrasting (volcanic, plutonic vs sedimentary lithologies). Within these gold districts, the bulk of gold mineralization most commonly occurs within third order shear zones being a few kilometers long and up to several meters wide. Third order shear zones tend to be oblique to first and second order shears and the district structural trend. These three orders of shear zones tend to intersect at a regional or deposit scale, being regarded as a district-scale plumbing system along which fluids infiltrated (Robert, 1994).

Establishing the mechanism(s) of formation of auriferous quartz veins is an important tool when trying to determine the structural controls and history of gold deposits. There are three main categories of veins: fault-fill veins, extensional veins, and stockwork and breccia veins. Fault-fill veins occupy faults and the central parts of shear zones, they are subparallel to their host structure and to the shear zone foliation. Extensional veins occur as planar veins in low strain rocks outside and between shear zones, or as arrays of sigmoidal veins within and bordering shear zones, typically at high angle with the local foliation. Stockwork and breccia veins consist of

superimposed multiple sets of veins and fractures, contrasting with fault-fill and extensional veins that typically consist of single fractures (Robert, 1994).

Ore shoots are higher grade mineralization trends within a deposit. Two broad categories of ore shoots have been recognized: 1) geometric; and 2) kinematic (Poulsen and Robert, 1989; Robert, 1994; Robert and Poulsen, 2001). Geometric ore shoots are controlled by the intersection of a structure (fault, or shear zone, or a vein) with a favourable lithological unit, like a BIF or another particularly reactive rock. The geometric ore shoot will be parallel to the line of intersection. Kinematic ore shoots are syn-deformation and syn-formation of the veins and are defined by the intersection of different sets of veins or contemporaneous structures. The plunge of kinematic ore shoots is commonly at high angle to the slip direction (Poulsen and Robert, 1989).

## **1.2 Specific Problem**

Tiriganiaq is classified as a partly BIF-hosted orogenic gold deposit (Dubé et al., 2015 and references therein). Exploration and previous research in the area in the last few decades has led to a good understanding of the main ore zones (e.g., Carpenter et al., 2004, Carpenter and Duke, 2005, Lawley et al., 2015a, b, c, 2016). The model was however challenged when underground development started, highlighting unexpected structural complexities that impacted on the recovery of gold, most notably in ore zones found in the hanging wall of the main ore-bearing structure. This is not unique to Tiriganiaq and common to many BIF-hosted/associated gold deposits where many structural and lithological aspects exert some control on gold distribution, making it difficult to model ore zones and optimize production. Tiriganiaq offers a unique opportunity to study BIF-hosted gold deposits, because there are several uncertainties associated with the controls on its ore zones genesis and the relative importance of key lithological and structural elements at different places in the deposit. The layer anisotropy of the host BIFs induced significant structural complexities throughout the evolution of gold deposition; localizing and affecting the kinematics of shear zones and auriferous vein development understanding these complexities is critical to optimize exploration models and mine development (Sherlock et al., 2004; Janvier et al., 2017; Oswald et al., 2018; Tóth et al., 2019). The structural history at Tiriganiaq, and the precise timing of gold introduction relative to the deformation events has yet to be precisely established. If correctly understood, it will lead to a better understanding of deposit scale geometric and kinematic ore-shoots.

The three main problems at Tiriganiaq are:

1. How has the layer anisotropy of the host BIFs affected the kinematics, geometry, and localization of shear zones and auriferous veins?
2. What is the precise structural history of the Tiriganiaq gold deposit?
3. What is the precise timing of gold introduction relative to the deformation events at the Tiriganiaq gold deposit?

Answering these questions will allow for more precise mine development and will aid in more precise exploration strategies.

### **1.3 Objectives**

The overarching objectives of this research project are to establish the relative timing of events, and to define the structural and lithological controls on ore formation and high-grade zones, by:

1. Documenting the geometry and structural style of the quartz-carbonate vein systems present at Tiriganiaq, including the satellite zones developed in the folded BIF units in the hanging wall of the main ore-controlling structure (Lower fault), with a focus on lode series 1150 and 1250;
2. Characterizing the different sets of quartz-carbonate veins based on their geometry, composition and timing of formation relative to the deformation event(s);
3. Identifying which system(s) or generation(s) of quartz-carbonate vein is/are related to gold;
4. Integrating the observations, results and interpretation in the overall metallogenic model for the district;
5. Help capture the observations and interpretations in the ongoing production and exploration models at the mine.

Documenting and defining the structural and lithological controls and defining the relative timing of events at Tiriganiaq will allow to answer the three main problems at Tiriganiaq, leading to a better understanding of some of the aspects of the gold endowment of the MGD.

### **1.4 Methodology**

Starting in early 2017, a delineation drill core campaign was undertaken and a number of new underground drifts crosscutting the deposit fabric exposing the ore at Tiriganiaq were developed, allowing for detailed documentation and targeted sampling providing the required information to try to tackle the main problems at Tiriganiaq.

Methods include:

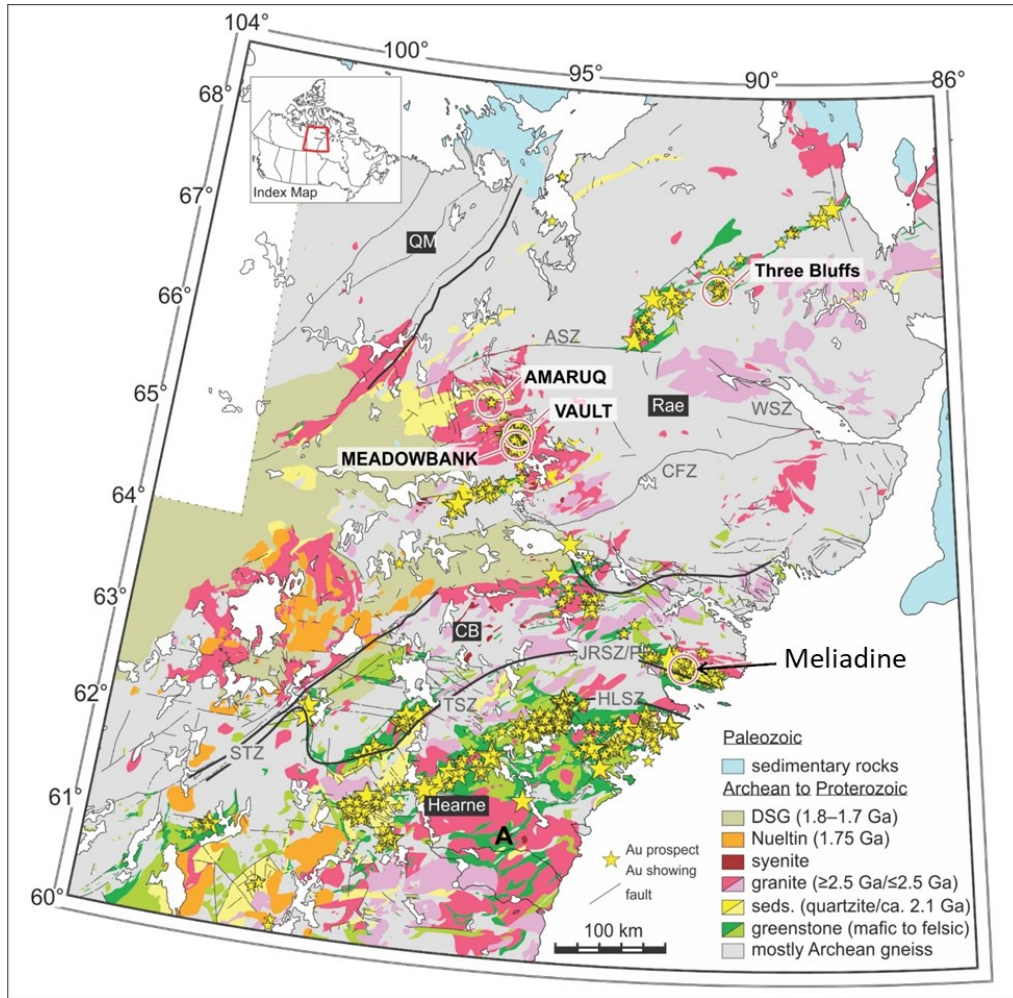
1. Detailed geological and structural underground mapping at drift scale (1:250 to 1:50) of developments (both walls, “back” or roof, and end wall) perpendicular to the strike of the ore exposing all relevant lodes, allowing for detailed documentation of the geometry of lithologies, kinematics of shear zones, and auriferous veins.
2. Study of delineation drill-cores that intersect the mineralized zones in vicinity of the mapped underground exposures and other areas to better understand the larger scale geometry of the lithologies and the structural and lithological controls on gold distribution in these areas.
3. Microstructural analysis of oriented samples and thin sections is used to better understand the relevant fabrics and components of the shears zones by analyzing stretching lineation(s), slickensides, intersection lineations, etc.
4. Whole-rock lithogeochemistry is used to help better understand the original protolith chemistry of each unit, the effect of hydrothermal alteration on, their signature and distribution, and their role in gold grade distribution in these zones
5. Slab sample analysis is used to observe structures and patterns within the veins to better understand the vein paragenesis and the interaction between veining and the host rock.
6. Data Compilation integrating the observations, results and interpretations from Agnico Eagle Mines Ltd. and previous studies. A review and integration of the data generated through the TGI-4 program (Lawley et al., 2015 a, b, c, 2016) and data from (Carpenter, 2004; Carpenter and Duke, 2005), was compiled to help further understand some of the structural complexities observed in BIF-hosted gold deposits, and to aid in unravelling MGD’s complex tectonic and metallogenic history.

## **1.5 Geology**

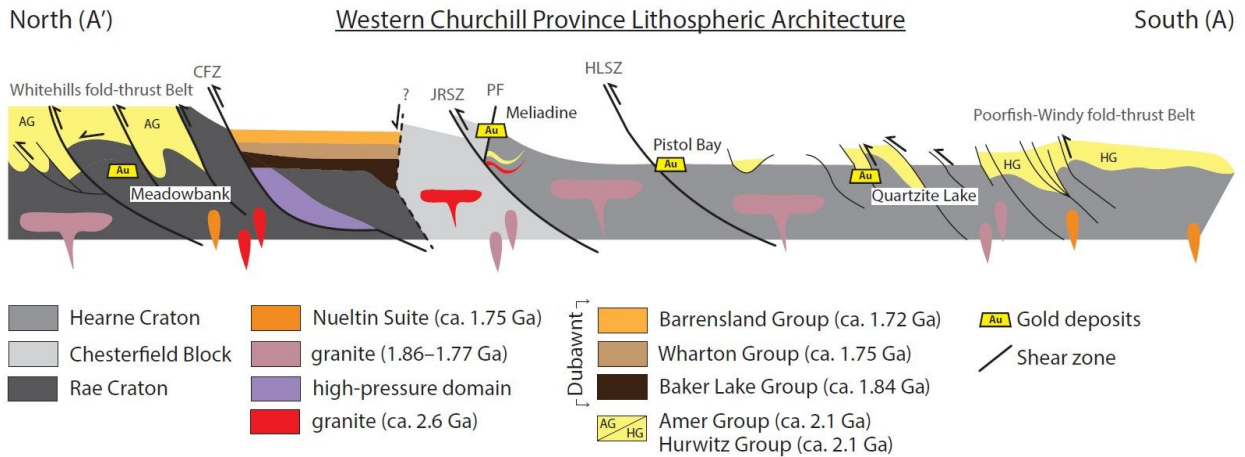
### **1.5.1 Western Churchill Province Geology**

The MGD is located within the Chesterfield block of the Western Churchill province, an understudied, remote region of eastern Nunavut (Fig. 1.2). It has a very complex geological and metallogenic history (Berman et al., 2007; Pehrsson et al., 2013; Lawley et al., 2015 a, b, c, 2016). Recent metamorphic and tectonic investigations of the Western Churchill Province have suggested that the traditional breakdown of the Western Churchill Province into the Rae and Hearne cratons is incomplete (Hoffman, 1988; Berman et al., 2007; Pehrsson et al., 2013;

Eglington et al., 2013). The MGD was initially assigned to the Hearne craton, but studies by Hoffman (1988), Berman et al. (2007), Eglington et al. (2013) and Pehrsson et al. (2013) suggest that a third domain should be included, referred to as the Chesterfield block.



**Figure 1.2** Regional geologic map of the western Churchill Province and distribution of gold prospects and showings. Note that Archean greenstone belts are cospatial with most gold occurrences, despite significantly predating gold. Abbreviations: ASZ = Amer shear zone, CB = Chesterfield block, CFZ = Chesterfield fault zone, DSG = Dubawnt Supergroup, HLSZ = Happy Lake shear zone, JRSZ = Josephine River shear zone, PF = Pyke Fault, QM = Queen Maud block, STZ = Snowbird tectonic zone, TSZ = Tyrrell shear zone, WSZ = Wager Bay shear zone. Modified from Pehrsson et al. (2013).

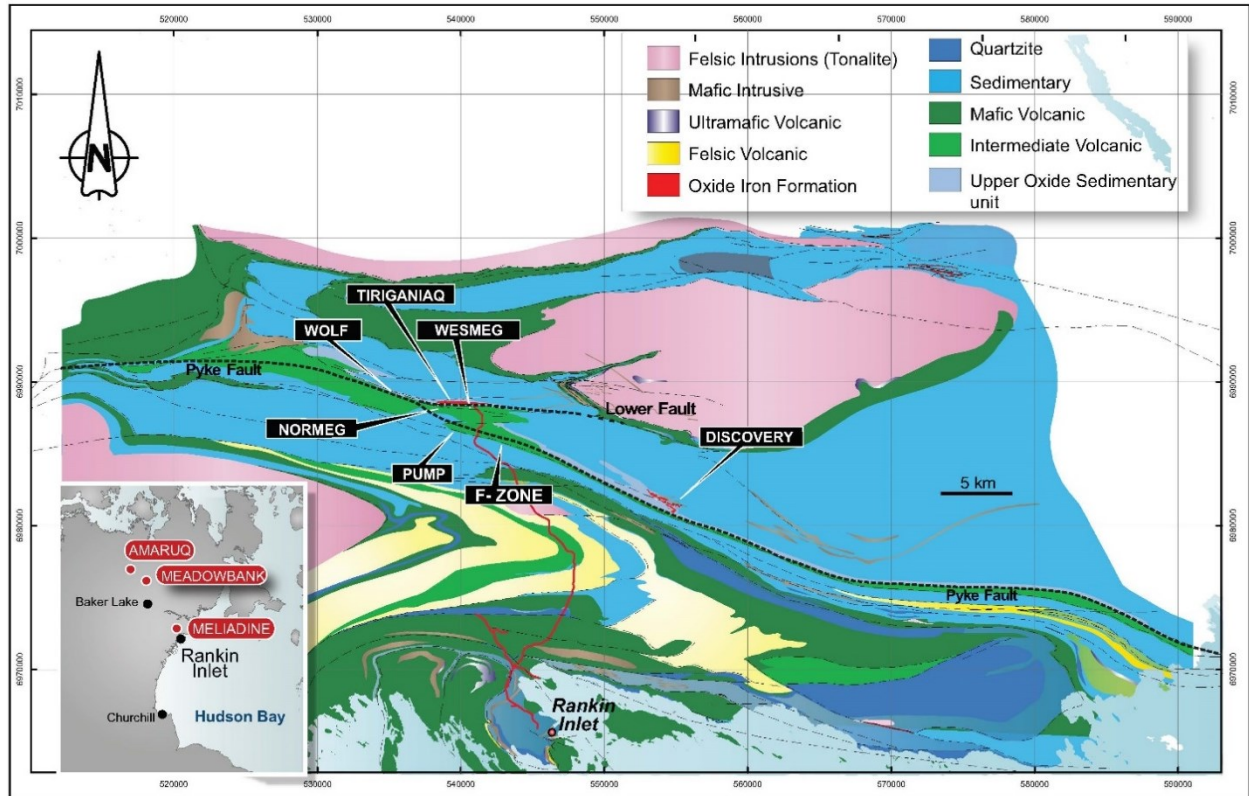


**Figure 1.3** *Cartoon cross section through the Rae-Hearne boundary zone* Major shear zones (CFZ = Chesterfield fault zone, HLSZ = Happy Lake shear zone, JRSZ = Josephine River shear zone, PF = Pyke Fault) and their relationship to important gold districts are shown for reference (Lawley et al., 2015b).

The northern boundary between the Rae craton and Chesterfield block is defined by the Snowbird tectonic zone (Lawley et al., 2016). The southern boundary of the Chesterfield block and the Hearne craton is largely inferred but is thought to have been defined by the W-trending Happy Lake shear zone, or more likely the composite SW-trending Tyrrell (MacLachlan et al., 2005) and W-trending Pyke Fault and Josephine River shear zone (Figs. 2 and 3) (Pehrsson et al., 2013). Although the major terrane boundary between the Hearne craton and Chesterfield block is largely inferred, this boundary likely played a key role in the formation of the MGD's gold deposits, acting as a locus for a first-order crustal-scale fault zone to form (Fig. 1.3) (Lawley et al., 2015 a, b, 2016) a crucial element in the formation of orogenic gold deposits. The Pyke Fault and associated gold deposits can be attributed to reworking during the 1.9 to 1.8 Ga metamorphism related to the Trans-Hudson Orogeny, which affected large swaths of the western Churchill Province, including the MGD (Berman et al., 2007; Berman, 2010; Lawley et al., 2015 b).

### 1.5.2 The Rankin Inlet Greenstone Belt Geology

The MGD is underlain by the RIGB, a Neoproterozoic supracrustal package that consists of mafic and minor ultramafic metavolcanic rocks, and metasedimentary rocks, which are crosscut by several episodes of Neoproterozoic and Proterozoic intrusions (Fig. 1.4) (Carpenter and Duke, 2004).

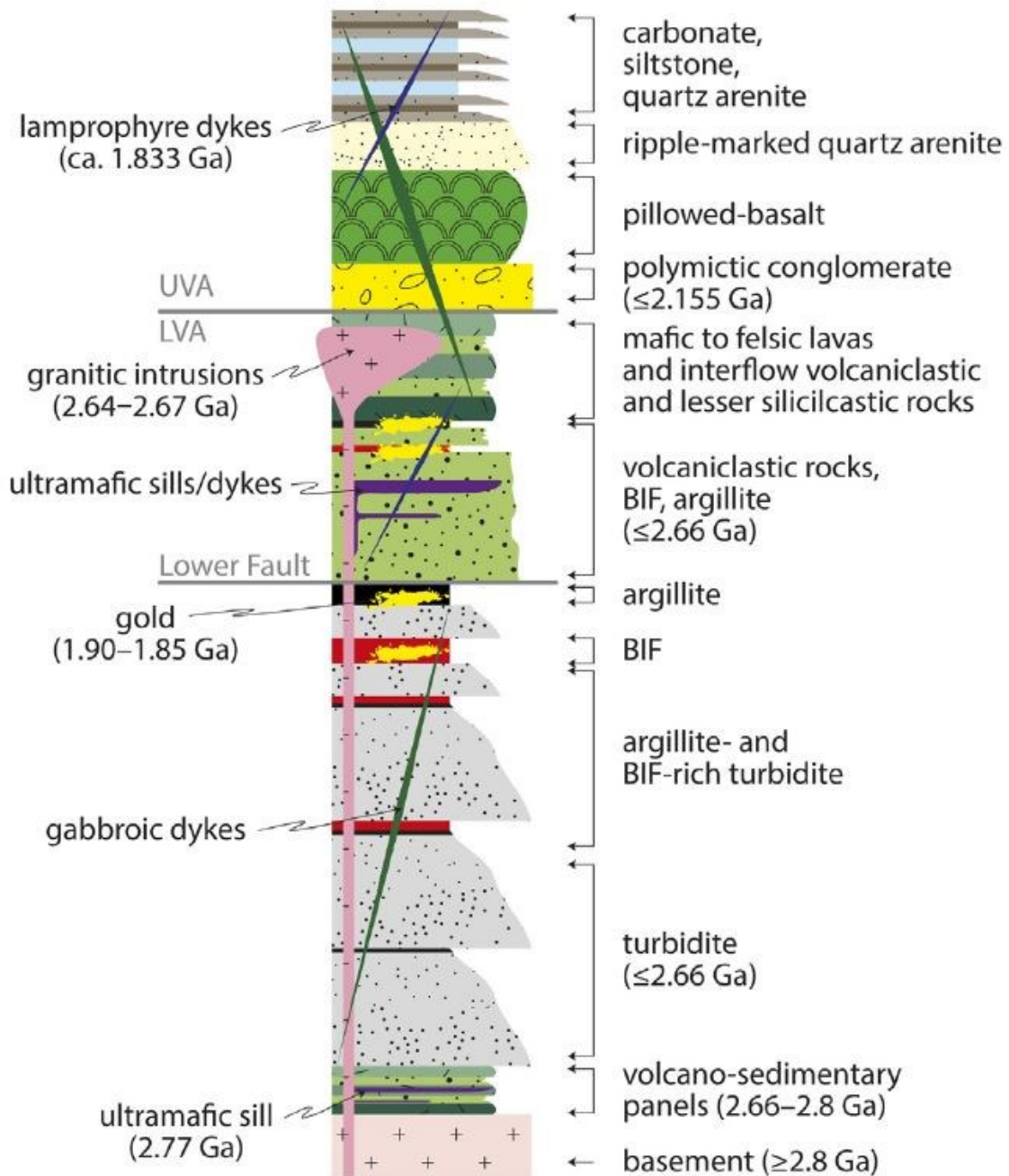


**Figure 1.4** *The Meliadine Gold District Geology Map, retrieved from Angico-Eagle Mines Ltd. Internal geology report).*

The RIGB comprises intercalated ca. 2.66 Ga predominately mafic volcanic and turbiditic successions deposited on an unexposed Meso- to Neoproterozoic substrate (Lawley et al., 2016). Neoproterozoic volcano-sedimentary panels are structurally bound by Paleoproterozoic conglomerate and basalt that are, in turn, unconformably overlain by pillowed-basalt and a distinct carbonate-siliciclastic sequence representing the remnants of Proterozoic basins (Fig. 1.5) (Lawley et al., 2016). Major stratigraphic units can be traced for tens of kilometers, with marked variations in structural geometry and metamorphic grade (Carpenter and Duke, 2004).



## Rankin Inlet Greenstone Belt Lithostratigraphy



**Figure 1.5** *Schematic lithostratigraphic column of the Rankin Inlet greenstone belt lithostratigraphy based on field relationships and zircon ages reported in Lawley et al., 2016.*

All supracrustal and intrusive rocks, except monzonite and lamprophyre dykes, have been regionally metamorphosed ranging from greenschist to amphibolite facies across the district (Carpenter and Duke, 2004). Additionally, the Peter Lake monzogranite has not been affected by regional metamorphism or structural overprinting. North of the MGD, peak metamorphism (6.3 kbar and 600°C; Berman et al., 2002) accompanied crustal shortening at ca. 1.90 Ga (Berman et



al., 2002, 2007), whereas peak metamorphic conditions (5.6 kbar and 585°C; Berman et al., 2002) south of the MGD and along the Happy Lake shear zone occurred at ca. 1.85 Ga (Lawley et al., 2015a, 2016). Based on  $^{40}\text{Ar}/^{39}\text{Ar}$  hornblende and biotite ages across the MGD, lower amphibolite to upper greenschist facies metamorphism likely continued until 1.81–1.73 Ga within the RIGB (Miller et al., 1995; Carpenter, 2003).

### **1.5.3 The Meliadine District Metallogeny**

The Meliadine Gold District hosts numerous orogenic gold deposits, and prospects that are spatially associated with the second order, potential crustal-scale Pyke Fault and its splays (Armitage et al., 1993; Miller et al., 1995; Lavigne et al., 1998b; Carpenter and Duke., 2004; Lawley et al., 2015a, b, c, 2016). High-grade gold intervals in these deposits and prospects are thought to occur as a series of sub-parallel and semi-continuous ore zones that are known locally as lodes. Most of these lodes correspond to folded, hydrothermally altered and veined BIF intervals which are intercalated and folded with turbidite (e.g., Tiriganiaq and Discovery) and volcanic successions (e.g., Normeg, Wesmeg, Pump, F Zone and Wolf) exposed along the surficial trace of the Pyke Fault (Fig. 1.4) (Lawley et al., 2016). In general, gold is cospatial with hydrothermally altered BIF- and shear-hosted quartz  $\pm$  ankerite veins at all of the major deposits and prospects in the district. Auriferous quartz  $\pm$  ankerite veins are, in turn, folded and transposed subparallel to the main deposit fabric (Lawley et al., 2015b).

## 2 GEOCHEMICAL AND PETROGRAPHIC CHARACTERIZATION OF THE 1150 AND 1250 LODGE SERIES HOST ROCKS

---

The Tiriganiaq deposit is hosted in an overturned west-trending, north-dipping turbidite-dominated sequence (Carpenter and Duke, 2004). This sequence has been subject to greenschist metamorphic conditions, major deformation and hydrothermal alteration; however, it has been separated into three distinct formations that comprise a diverse assemblage of clastic and chemically derived rocks (Fig. 2.1.). The Tiriganiaq Formation, the southernmost formation, is classified as a strongly bedded siltstone succession that transitions to a graphitic argillite lithology towards the faulted contact with the volcanic-dominated structural footwall of the Wesmeg Formation (Lawley et al., 2015a, c). The Upper Oxide Formation, the focus of this study, located further north, comprises a diverse assemblage of iron-rich clastic and chemically derived rocks (Carpenter and Duke, 2004). The Upper Oxide Formation consists of strongly bedded and graded chloritic greywacke-siltstone-mudstone interbedded with silicate facies dominated and minor amphibolite (pelitic) BIF (Carpenter and Duke, 2004; Lawley et al., 2015a, c). The northernmost formation, the SAM Formation, consists mainly of graded and bedded greywacke intervals, but does not host significant mineralization (Lawley et al., 2015a, c) and therefore will not be discussed further.

Previous studies have subdivided the Upper Oxide Formation into three main lithological facies that are intercalated with one another, predominantly consisting of chloritic greywacke, silicate facies BIF, and amphibolite (pelitic) BIF facies (Carpenter and Duke, 2004; Carpenter et al., 2005; Lawley et al., 2015a, b). Additionally, a distinct mudstone facies has been described by mine geologists and is characterized by a thinly laminated mudstone intercalated within larger BIF intervals. Because this study is focussed on the 1150 and 1250 lodes and their host rocks, the following sections of this chapter discuss the nature and composition of the Upper Oxide Formation lithologies.

The chloritic greywacke, a general term used to describe the diverse iron and chlorite-rich package of turbiditic siliciclastic rocks (greywacke-siltstone-mudstone), is intercalated with silicate and amphibolite facies BIF (Carpenter and Duke, 2004; Carpenter et al., 2005; Lawley et al., 2015a, c). The chloritic greywacke comprises strongly bedded, coarse quartz and plagioclase grains wrapped by the dominant muscovite  $\pm$  biotite  $\pm$  chlorite metamorphic mineral assemblage that defines the deposit main fabric (refer to chapter 4 for more information on deformation and associated fabrics). Individual beds consist of massive quartzo-feldspathic greywacke or fine-

grained, silt-rich pelite. Bedding thickness in greywackes and pelites ranges from centimeter-scale to meter-scale, and graded beds are typically tens of centimeters thick (Carpenter and Duke, 2004).

## Tiriganiaq Mine Area Stratigraphy

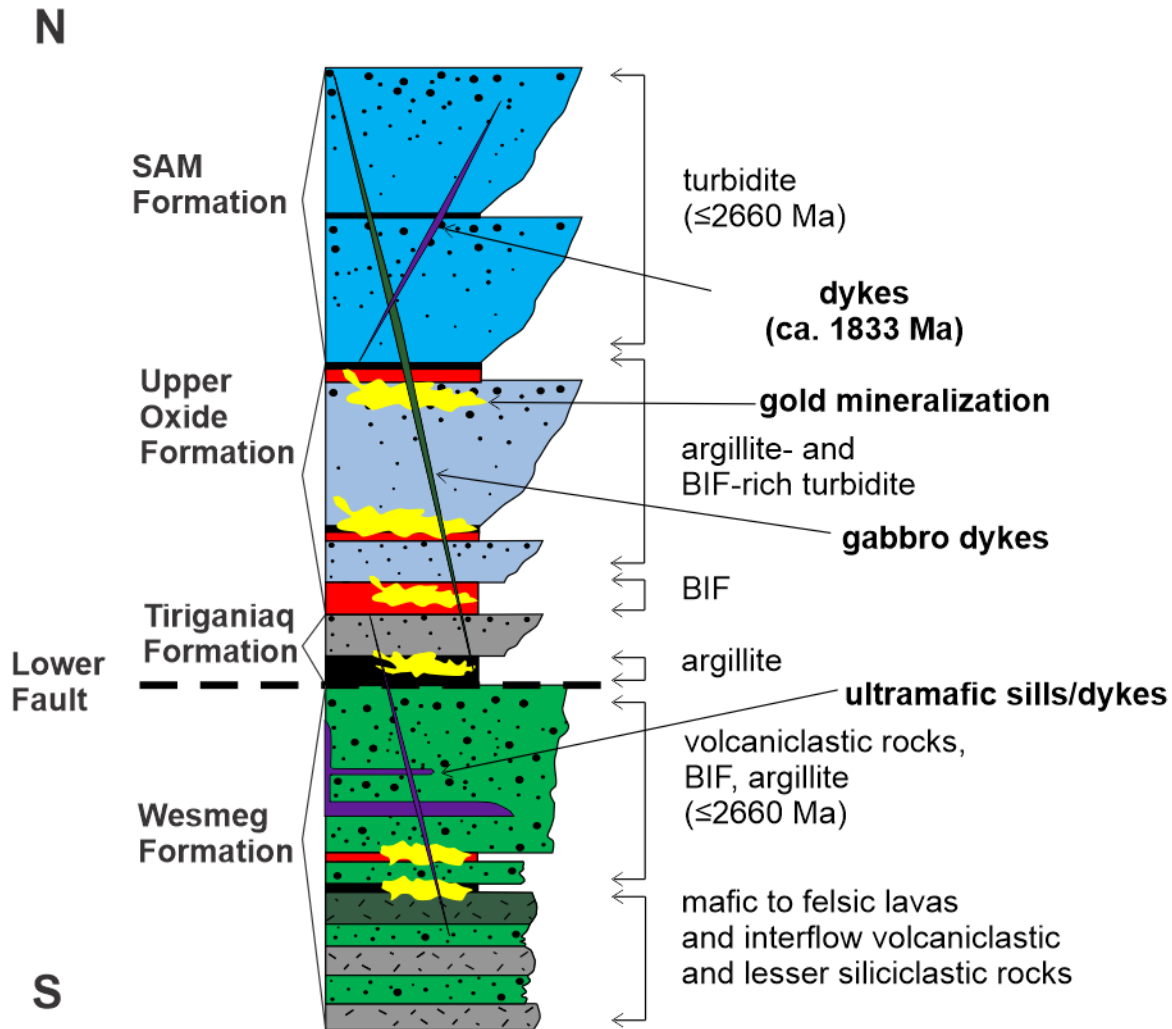


Figure 2.1 Tiriganiaq mine area overturned stratigraphic column.

The silicate facies BIF at Tiriganiaq comprises alternating magnetite- and chert-rich bands and siliciclastic rocks (Carpenter and Duke, 2004; Carpenter et al., 2005; Lawley et al., 2015a, c) and is referred to as oxide-silicate BIF in this study. Well-developed banding occurs at millimeter- to centimeter-scales and is preserved even within highly strained intervals where it probably represents metamorphic layering. Poorly banded and magnetite-rich intervals are also present (Carpenter and Duke, 2004; Carpenter et al., 2005).

Amphibolite (pelitic) facies BIF are characterized by abundant Fe-silicate minerals (e.g., grunerite, hornblende and chlorite) that occur at the margins of magnetite bands and radiate towards chert bands (Carpenter and Duke, 2005; Lawley et al., 2015c). Fe-silicates are also present in folded quartz veinlets and in late fractures, which suggest that at least some Fe-silicates may possess a hydrothermal, rather than metamorphic, origin (Lawley et al., 2015c).

In order to understand how the effects of hydrothermal alteration and deformation are expressed in the host lithologies of the study area and to evaluate the role that these lithologies have played on the nature and distribution of gold, this chapter describes the petrographic and geochemical characteristics of the host rocks of the Upper Oxide Formation hosting the 1150 and 1250 lode series of the Tiriganiaq deposit. The petrography (microscopic) description and the geochemical signature (major and trace elements) are presented for each lithology.

The petrographic documentation of the host rocks of the Tiriganiaq deposit are based on drill core descriptions, underground observations, and 80 thin sections from selected samples collected underground. A synthesis of detailed petrographic characteristics of the different lithologies from thin section analysis is available in Appendix I.

The geochemical composition of each of the host lithologies has been defined from processing a set of 49 representative whole-rock geochemistry samples and are compared to 38 whole-rock geochemistry samples from Lawley et al. (2015a) taken from the Upper Oxide Formation hosting the 1100 lode (series). The results of these analyses are available in Appendix II. The 87 rock samples retained are all metamorphosed to lower- to mid-greenschist facies and variably hydrothermally altered. The heterogenous nature of the beds in the siliciclastic and chemically derived sedimentary rocks explain part of the compositional variations in each lithology. However, hydrothermal alteration accounts for the bulk of compositional variations between and within lithologies, which could not be entirely avoided during sampling underground in a mine environment. Despite this, the use of different classification diagrams and mobile versus less mobile elements provides some indications on the primary nature of the host lithologies.

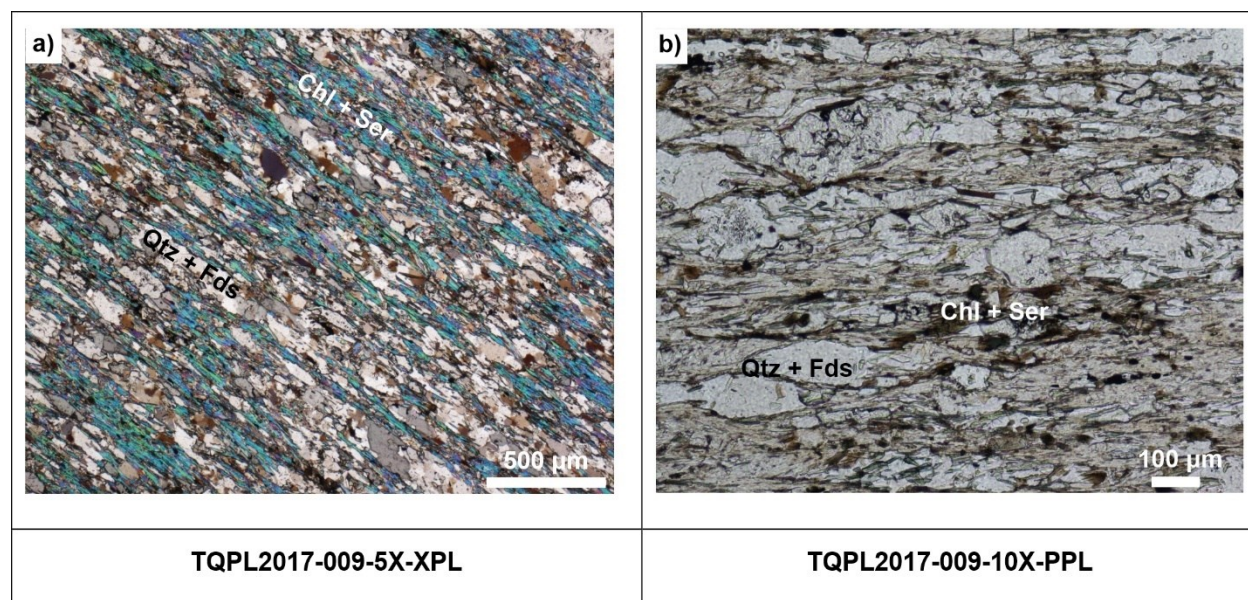
## **2.1 Chloritic Greywacke**

The description of the chloritic greywacke is mainly based on thin-section observations of 19 samples. The geochemical signature of the chloritic greywacke is based on 24 whole-rock geochemistry samples and are compared to 19 whole-rock geochemistry samples taken by Lawley et al. (2015a). All samples collected and analyzed for petrography and whole-rock

lithogeochemistry have been taken from underground crosscuts in high-strain zones within the 1150- and 1250- lode series. A summary of results is presented below.

### 2.1.1 Petrography

The chloritic greywacke comprises fine to coarse quartz and feldspar grains wrapped by the dominant muscovite  $\pm$  chlorite mineral assemblage that defines the foliation (the deposit main fabric, refer to chapter 4 for more details) (Fig. 2.2.). The chloritic greywacke is strongly affected by the main deformation and has been folded and sheared, commonly displaying mylonitic and other brittle-ductile structures; it hosts mineralized shear and extensional veins and has been strongly affected by hydrothermal alteration. Individual beds consist of massive quartzo-feldspathic greywacke or fine-grained, silt-rich to clay-rich pelite.



**Figure 2.2** Representative thin section photomicrographs of chloritic greywacke a) and b) fine to coarse-grained, deformed and elongated quartz and feldspar grains wrapped by the dominant chlorite (blue (a))  $\pm$  sericite metamorphic  $\pm$  hydrothermal mineral assemblage that defines the main foliation.

The general composition of the chloritic greywacke consists of 30–60 vol.% fine- to coarse-grained (50  $\mu\text{m}$  – 1300  $\mu\text{m}$ ) subhedral and irregular deformed quartz grains (Table 2.1.), some of which are very finely recrystallized equigranular grains. There is between 5 and 20 vol.% fine to medium grained (50  $\mu\text{m}$  – 1300  $\mu\text{m}$ ) anhedral to subhedral and irregular deformed feldspar grains. Between 5 and 35 vol.% fine-grained (30  $\mu\text{m}$  – 200  $\mu\text{m}$ ) subhedral chlorite grains aligned with foliation (Fig.2.2.) and locally displaying radiating texture proximal to quartz  $\pm$  ankerite veins.

Between 5 and 30 vol.% fine-grained (30  $\mu\text{m}$  – 200  $\mu\text{m}$ ) subhedral to euhedral sericite (fine-grained white mica) grains, regularly dominating initially clay-rich layers, is present along mylonitic fabrics and within and adjacent to quartz  $\pm$  ankerite veins. One sample contains up to 5 vol.% fine-grained (50  $\mu\text{m}$  – 150  $\mu\text{m}$ ) subhedral grunerite typically associated with fine-grained chlorite-rich clay-rich layers, although it may not be perfectly representative of this lithology as this sample may have been taken proximal to a pelitic BIF layer. The chloritic greywacke also contains trace subhedral to euhedral fine-grained (50  $\mu\text{m}$  – 350  $\mu\text{m}$ ) magnetite as well as other oxide minerals typically disseminated within the foliation. The chloritic greywacke contains 0.1-15 vol.% fine- to coarse-grained (50  $\mu\text{m}$  – 1300  $\mu\text{m}$ ) ankerite, typically finely disseminated but concentrated along foliation, mylonitic fabrics and along the margins of sulphide-bearing quartz  $\pm$  ankerite  $\pm$  sericite veins. Up to 10 vol.% anhedral to euhedral, very fine-grained to very coarse-grained (50  $\mu\text{m}$  – 5000  $\mu\text{m}$ ) euhedral sulphides, most commonly occurring within quartz  $\pm$  ankerite  $\pm$  sericite veins, but also disseminated along foliation and shear fabrics are present locally (refer to next chapter for more details).

**Table 2.1 Summary of chloritic greywacke gangue mineralogy (modal percent). n=19**

| Statistics | Qtz  | Fds  | Chl  | Ser  | Mag | Gru  | Ak  | Ox  | Sulph |
|------------|------|------|------|------|-----|------|-----|-----|-------|
| Average    | 48.8 | 10.4 | 15.9 | 14.4 | 0.1 | 0.69 | 7.4 | 0.1 | 2.3   |
| Minimum    | 30   | 5    | 5    | 5    | 0   | 0    | 0.1 | 0.1 | 0.1   |
| Maximum    | 60   | 20   | 35   | 30   | 0.1 | 5    | 15  | 0.1 | 10    |

Mineral abbreviations are as follows Quartz (Qtz); Feldspar (Fds); Chlorite (Chl); Sericite (Ser); Magnetite (Mag); Grunerite (Gru); Ankerite (Ak); Other oxides (Ox); Sulphides (Sulph).

### 2.1.2 Geochemistry

The chloritic greywacke has a very heterogeneous composition as indicated by highly variable major element contents, including  $\text{SiO}_2$  (51.3–78.8 wt.%),  $\text{Al}_2\text{O}_3$  (3.5–17.6 wt.%),  $\text{Fe}_2\text{O}_3$  (0.1–4.8%) and  $\text{K}_2\text{O}$  (0.24–5.15 wt.%) which are consistent with the greywacke samples collected by Lawley et al. (2015a) (Tables 2.2, and 2.3). The chloritic greywacke is however systematically enriched in  $\text{SiO}_2$ ,  $\text{CaO}$ , and  $\text{Na}_2\text{O}$  and depleted in  $\text{Fe}_2\text{O}_3$  relative to the BIFs (Table 2.9). The chloritic greywacke  $\text{SiO}_2$  content displays varying, but negative correlations with the other major oxides with exception of  $\text{Na}_2\text{O}$ , shown by the regression lines on the Harker diagram (Fig. 2.3) and mimic the greywacke samples taken from Lawley et al. (2015a), except for  $\text{Na}_2\text{O}$ .

The chondrite-normalized multi-element patterns of the chloritic greywacke (Fig. 2.4) are heterogeneous and show a range in relative abundances. The chloritic greywacke is light rare

earth element (LREE) enriched, but with distinct negative Ti, W, Mo, and P anomalies. The heavy rare earth elements (REEs) have slightly inclined to flat pattern however with distinct a negative Ti anomaly and positive Gd, and Li anomalies, and highly variable, majorly positive Sb anomaly.

**Table 2.2 Summary of of major oxide (wt. %) abundance for chloritic greywacke samples**

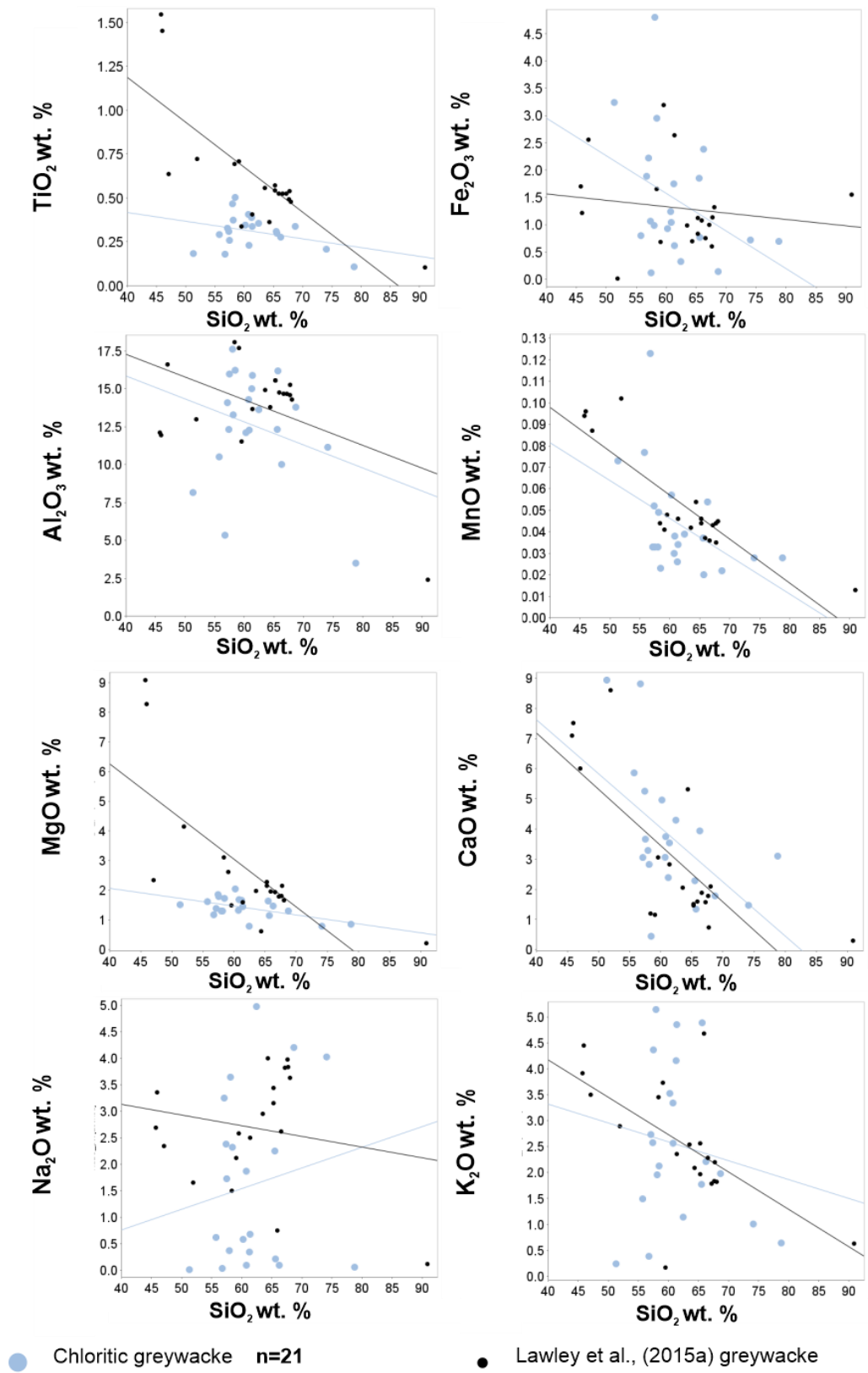
| <b>Chloritic greywacke n=21</b>    |                        |                        |                                    |                                    |            |            |            |                        |                       |                                   |
|------------------------------------|------------------------|------------------------|------------------------------------|------------------------------------|------------|------------|------------|------------------------|-----------------------|-----------------------------------|
|                                    | <b>SiO<sub>2</sub></b> | <b>TiO<sub>2</sub></b> | <b>Al<sub>2</sub>O<sub>3</sub></b> | <b>Fe<sub>2</sub>O<sub>3</sub></b> | <b>MnO</b> | <b>MgO</b> | <b>CaO</b> | <b>Na<sub>2</sub>O</b> | <b>K<sub>2</sub>O</b> | <b>P<sub>2</sub>O<sub>5</sub></b> |
| <b>Average</b>                     | 61.72                  | 0.31                   | 12.56                              | 1.45                               | 0.04       | 1.42       | 3.72       | 1.61                   | 2.53                  | 0.15                              |
| <b>Maximum</b>                     | 78.79                  | 0.50                   | 17.64                              | 4.80                               | 0.12       | 2.05       | 8.94       | 4.98                   | 5.15                  | 0.71                              |
| <b>Minimum</b>                     | 51.30                  | 0.11                   | 3.51                               | 0.12                               | 0.02       | 0.79       | 0.45       | 0.01                   | 0.24                  | 0.02                              |
| <b>(Lawley et al., 2015a) n=19</b> |                        |                        |                                    |                                    |            |            |            |                        |                       |                                   |
|                                    | <b>SiO<sub>2</sub></b> | <b>TiO<sub>2</sub></b> | <b>Al<sub>2</sub>O<sub>3</sub></b> | <b>Fe<sub>2</sub>O<sub>3</sub></b> | <b>MnO</b> | <b>MgO</b> | <b>CaO</b> | <b>Na<sub>2</sub>O</b> | <b>K<sub>2</sub>O</b> | <b>P<sub>2</sub>O<sub>5</sub></b> |
| <b>Average</b>                     | 62.18                  | 0.62                   | 13.96                              | 1.30                               | 0.05       | 2.69       | 3.04       | 2.69                   | 2.57                  | 0.29                              |
| <b>Maximum</b>                     | 63.25                  | 0.42                   | 15.85                              | 1.06                               | 0.06       | 1.22       | 4.70       | 4.44                   | 2.25                  | 0.12                              |
| <b>Minimum</b>                     | 45.75                  | 0.10                   | 2.42                               | 0.01                               | 0.01       | 0.22       | 0.30       | 0.11                   | 0.17                  | 0.01                              |

Table 2.3 Summary of major oxide (wt. %) abundance for all lithologies

| Chloritic greywacke n=21    |                  |                  |                                |                                |      |      |      |                   |                  |                               |
|-----------------------------|------------------|------------------|--------------------------------|--------------------------------|------|------|------|-------------------|------------------|-------------------------------|
|                             | SiO <sub>2</sub> | TiO <sub>2</sub> | Al <sub>2</sub> O <sub>3</sub> | Fe <sub>2</sub> O <sub>3</sub> | MnO  | MgO  | CaO  | Na <sub>2</sub> O | K <sub>2</sub> O | P <sub>2</sub> O <sub>5</sub> |
| Average                     | 61.72            | 0.31             | 12.56                          | 1.45                           | 0.04 | 1.42 | 3.72 | 1.61              | 2.53             | 0.15                          |
| Maximum                     | 78.79            | 0.50             | 17.64                          | 4.80                           | 0.12 | 2.05 | 8.94 | 4.98              | 5.15             | 0.71                          |
| Minimum                     | 51.30            | 0.11             | 3.51                           | 0.12                           | 0.02 | 0.79 | 0.45 | 0.01              | 0.24             | 0.02                          |
| (Lawley et al., 2015a) n=19 |                  |                  |                                |                                |      |      |      |                   |                  |                               |
|                             | SiO <sub>2</sub> | TiO <sub>2</sub> | Al <sub>2</sub> O <sub>3</sub> | Fe <sub>2</sub> O <sub>3</sub> | MnO  | MgO  | CaO  | Na <sub>2</sub> O | K <sub>2</sub> O | P <sub>2</sub> O <sub>5</sub> |
| Average                     | 62.18            | 0.62             | 13.96                          | 1.30                           | 0.05 | 2.69 | 3.04 | 2.69              | 2.57             | 0.29                          |
| Maximum                     | 63.25            | 0.42             | 15.85                          | 1.06                           | 0.06 | 1.22 | 4.70 | 4.44              | 2.25             | 0.12                          |
| Minimum                     | 45.75            | 0.10             | 2.42                           | 0.01                           | 0.01 | 0.22 | 0.30 | 0.11              | 0.17             | 0.01                          |
| Oxide-silicate BIF n=15     |                  |                  |                                |                                |      |      |      |                   |                  |                               |
|                             | SiO <sub>2</sub> | TiO <sub>2</sub> | Al <sub>2</sub> O <sub>3</sub> | Fe <sub>2</sub> O <sub>3</sub> | MnO  | MgO  | CaO  | Na <sub>2</sub> O | K <sub>2</sub> O | P <sub>2</sub> O <sub>5</sub> |
| Average                     | 51.72            | 0.10             | 4.04                           | 16.68                          | 0.05 | 1.23 | 2.85 | 0.02              | 0.30             | 0.24                          |
| Maximum                     | 74.45            | 0.32             | 12.94                          | 28.42                          | 0.07 | 2.57 | 6.02 | 0.07              | 0.85             | 0.40                          |
| Minimum                     | 33.39            | 0.01             | 0.61                           | 4.78                           | 0.02 | 0.13 | 0.31 | 0.01              | 0.01             | 0.06                          |
| (Lawley et al., 2015a) n=7  |                  |                  |                                |                                |      |      |      |                   |                  |                               |
|                             | SiO <sub>2</sub> | TiO <sub>2</sub> | Al <sub>2</sub> O <sub>3</sub> | Fe <sub>2</sub> O <sub>3</sub> | MnO  | MgO  | CaO  | Na <sub>2</sub> O | K <sub>2</sub> O | P <sub>2</sub> O <sub>5</sub> |
| Average                     | 45.62            | 0.12             | 4.60                           | 11.18                          | 0.06 | 1.07 | 2.56 | 0.63              | 0.59             | 0.19                          |
| Maximum                     | 52.62            | 0.27             | 10.26                          | 17.81                          | 0.07 | 1.44 | 3.79 | 2.43              | 1.88             | 0.27                          |
| Minimum                     | 36.54            | 0.03             | 1.56                           | 4.22                           | 0.03 | 0.64 | 1.20 | 0.02              | 0.03             | 0.13                          |
| Pelitic BIF n=8             |                  |                  |                                |                                |      |      |      |                   |                  |                               |
|                             | SiO <sub>2</sub> | TiO <sub>2</sub> | Al <sub>2</sub> O <sub>3</sub> | Fe <sub>2</sub> O <sub>3</sub> | MnO  | MgO  | CaO  | Na <sub>2</sub> O | K <sub>2</sub> O | P <sub>2</sub> O <sub>5</sub> |
| Average                     | 49.34            | 0.29             | 12.72                          | 6.98                           | 0.04 | 2.14 | 2.85 | 0.35              | 2.24             | 0.10                          |
| Maximum                     | 61.81            | 0.45             | 15.21                          | 19.12                          | 0.05 | 3.05 | 4.45 | 1.56              | 4.46             | 0.14                          |
| Minimum                     | 35.47            | 0.14             | 6.27                           | 0.79                           | 0.02 | 1.59 | 0.48 | 0.01              | 0.03             | 0.05                          |
| (Lawley et al., 2015a) n=8  |                  |                  |                                |                                |      |      |      |                   |                  |                               |
|                             | SiO <sub>2</sub> | TiO <sub>2</sub> | Al <sub>2</sub> O <sub>3</sub> | Fe <sub>2</sub> O <sub>3</sub> | MnO  | MgO  | CaO  | Na <sub>2</sub> O | K <sub>2</sub> O | P <sub>2</sub> O <sub>5</sub> |
| Average                     | 55.58            | 0.39             | 11.13                          | 4.36                           | 0.09 | 1.65 | 2.99 | 2.65              | 1.35             | 0.08                          |
| Maximum                     | 65.37            | 0.75             | 16.47                          | 8.21                           | 0.37 | 2.27 | 4.97 | 5.55              | 3.45             | 0.15                          |
| Minimum                     | 36.81            | 0.10             | 3.11                           | 0.01                           | 0.04 | 1.08 | 0.68 | 0.01              | 0.01             | 0.02                          |
| Laminated mudstone n=2      |                  |                  |                                |                                |      |      |      |                   |                  |                               |
|                             | SiO <sub>2</sub> | TiO <sub>2</sub> | Al <sub>2</sub> O <sub>3</sub> | Fe <sub>2</sub> O <sub>3</sub> | MnO  | MgO  | CaO  | Na <sub>2</sub> O | K <sub>2</sub> O | P <sub>2</sub> O <sub>5</sub> |
| Average                     | 61.47            | 0.43             | 17.14                          | 0.93                           | 0.02 | 1.70 | 1.50 | 1.32              | 4.15             | 0.10                          |
| Maximum                     | 62.06            | 0.46             | 17.49                          | 1.07                           | 0.02 | 1.71 | 1.85 | 2.08              | 4.18             | 0.11                          |
| Minimum                     | 60.88            | 0.40             | 16.79                          | 0.78                           | 0.02 | 1.68 | 1.14 | 0.55              | 4.12             | 0.09                          |
| (Lawley et al., 2015a) n=2  |                  |                  |                                |                                |      |      |      |                   |                  |                               |
|                             | SiO <sub>2</sub> | TiO <sub>2</sub> | Al <sub>2</sub> O <sub>3</sub> | Fe <sub>2</sub> O <sub>3</sub> | MnO  | MgO  | CaO  | Na <sub>2</sub> O | K <sub>2</sub> O | P <sub>2</sub> O <sub>5</sub> |
| Average                     | 58.27            | 0.53             | 13.86                          | 1.28                           | 0.09 | 1.46 | 4.96 | 0.40              | 3.71             | 0.14                          |
| Maximum                     | 58.99            | 0.59             | 15.95                          | 2.40                           | 0.11 | 1.64 | 5.65 | 0.42              | 4.58             | 0.14                          |
| Minimum                     | 57.54            | 0.47             | 11.76                          | 0.15                           | 0.06 | 1.27 | 4.27 | 0.38              | 2.83             | 0.13                          |

Values are rounded to two decimal places





**Figure 2.3** Harker diagrams displaying major oxide wt. % vs.  $\text{SiO}_2$  wt. % for the chloritic greywacke. Blue and black lines regression lines of respective sample populations.

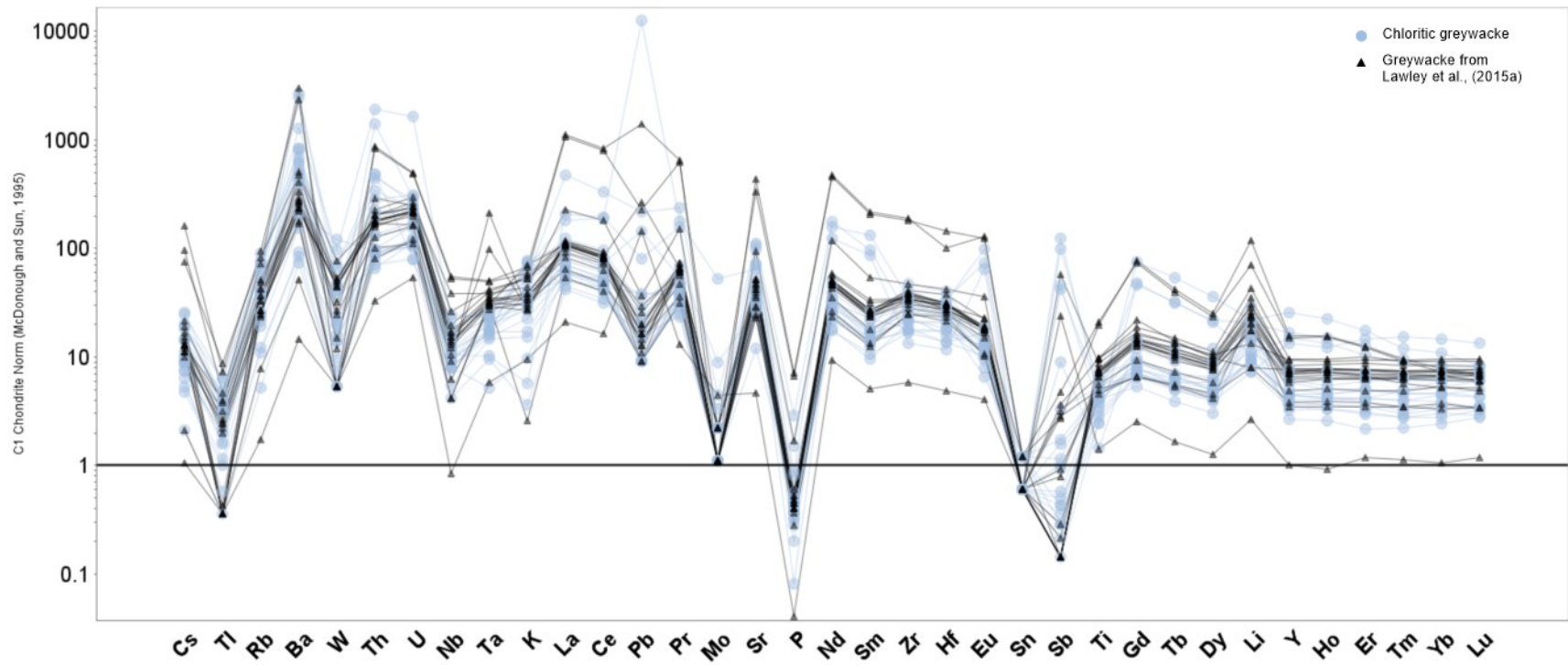


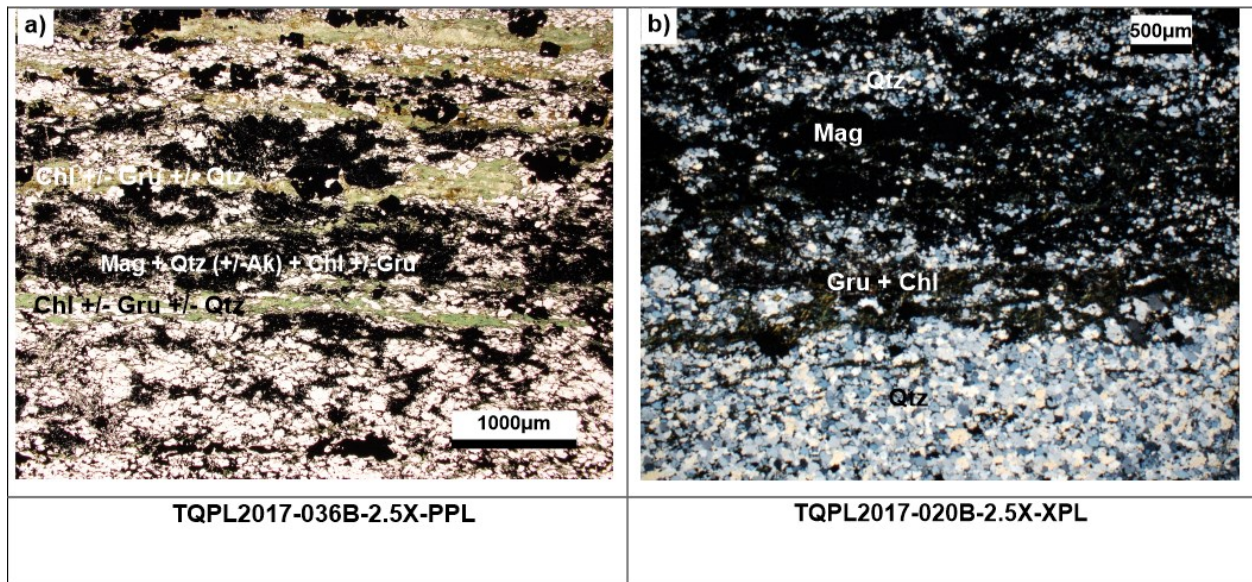
Figure 2.4 Chondrite-normalized multi-element profile for chloritic greywacke normalization values are from Sun and McDonough (1995).

## 2.2 Oxide-silicate BIF

The description to the oxide-silicate BIF is based on thin section observations from 10 samples. The geochemical signature of the oxide-silicate BIF is based on 15 whole-rock geochemistry samples and are compared to seven whole-rock geochemistry samples taken by Lawley et al. (2015a). All samples collected and analyzed for petrography and litho-geochemistry have been taken from underground crosscuts proximal to high-strain zones and contain varying amounts of mineralized veins within the 1150 and 1250 lode series. A summary of results is presented below.

### 2.2.1 Petrography

The oxide-silicate BIF comprises well-developed bedding and consist of alternating semi-massive to massive magnetite, chert, and silicate-rich bands. However, poorly bedded intervals, characterized by diffuse mineralogical banding, are also present. Magnetite beds are commonly rimmed by fine-grained, acicular grunerite. Chert-rich bands contain minor amounts of disseminated chlorite, grunerite and magnetite (Fig. 2.5a and b). Silicate-rich bands are dominated by chlorite and grunerite with disseminated fine-grained subhedral magnetite and minor quartz (Fig. 2.5a).



**Figure 2.5** Representative photomicrographs of oxide-silicate BIF a) alternating quartz-magnetite-chlorite +/- grunerite and magnetite-quartz-grunerite +/- chlorite layers b) magnetite dominated (intercalated with minor quartz + grunerite) and quartz dominated (intercalated with minor magnetite and grunerite) layers.

The oxide-silicate BIF consists of 20–61 vol.% microcrystalline to fine-grained (<10 µm – 250 µm), variably deformed quartz grains (Table 2.3). Microcrystalline quartz/chert bands are generally equigranular (Fig. 2.5a). Nine to 55 vol.% very fine to coarse-grained (50 µm – 1000 µm) anhedral to euhedral magnetite grains characterize the BIF layers. Magnetite commonly displays a pitted texture, some grains having been completely altered, with some partially to completely replaced by pyrrhotite and or arsenopyrite in the ore zones (see chapter 3 for more details). Up to 40 vol.% very fine- to fine-grained (50 µm – 150 µm) anhedral to euhedral chlorite grains, commonly define the main foliation, and locally form radiating acicular masses with grunerite (Fig. 2.5a). Up to 1 vol.% very fine- to fine-grained (50 µm – 150 µm) subhedral sericite grains aligned within the foliation or on the margins of quartz ± ankerite veining is present (see chapter 3 for more details). One to 15 vol.% very fine- to fine-grained (50 µm – 200 µm) subhedral grunerite is associated with chlorite-rich layers and magnetite. Locally up to 10 vol.% medium-grained (150 µm – 300 µm) subhedral amphibole grains, interstitial to chert and chlorite-grunerite layers. Up to 15 vol.% very fine- to coarse (50 µm – 1300 µm) subhedral to euhedral ankerite grains occur within cross-cutting quartz veins and or on the margins of veins within BIF layering (see chapter 3 for more details).

**Table 2.4 Summary of oxide-silicate BIF gangue mineralogy (modal percent). n=10**

| Statistics     | Qtz         | Mag         | Chl         | Gru        | Ser         | Amph     | Ak         | Sulph      |
|----------------|-------------|-------------|-------------|------------|-------------|----------|------------|------------|
| <b>Average</b> | <b>44.5</b> | <b>25.5</b> | <b>18.5</b> | <b>3.9</b> | <b>0.34</b> | <b>1</b> | <b>2.8</b> | <b>3.5</b> |
| <b>Minimum</b> | 20          | 9           | 0           | 1          | 0           | 0        | 0          | 0          |
| <b>Maximum</b> | 61          | 55          | 40          | 15         | 1           | 10       | 15         | 10         |

Mineral abbreviations are as follows Quartz (Qtz); Magnetite (Mag); Chlorite (Chl); Grunerite (Gru); Sericite (Ser); Amphibole (Amph); Ankerite (Ak); Sulphides (Sulph).

## 2.2.2 Geochemistry

The oxide-silicate BIF shows a wide range of concentration for some major elements, including SiO<sub>2</sub> (33.4–74.45 wt.%), Al<sub>2</sub>O<sub>3</sub> (0.61–12.94 wt.%), Fe<sub>2</sub>O<sub>3</sub> (4.78–28.42 wt.%), MgO (0.13–2.57 wt.%), and CaO (0.31–6.02 wt.%) (Table 2.5). By comparison, the oxide-silicate BIFs are enriched in Fe<sub>2</sub>O<sub>3</sub>, MnO, and P<sub>2</sub>O<sub>5</sub> and depleted in TiO<sub>2</sub>, Al<sub>2</sub>O<sub>3</sub>, MgO, Na<sub>2</sub>O, and K<sub>2</sub>O relative to the other lithologies (Table. 2.3). The oxide silicate BIFs SiO<sub>2</sub> content displays varying correlations with the other major oxides, and often disagree with samples taken from Lawley et al. (2015a); with exception for the relatively distinct negative correlation of Fe<sub>2</sub>O<sub>3</sub> versus SiO<sub>2</sub> and the positive correlation of CaO versus SiO<sub>2</sub> (Fig. 2.6).

Geochemical heterogeneity is to be expected in BIF due to the contrasted nature of the various layers present and having representative samples and analyses is difficult (e.g., Janvier, 2015). This makes it difficult to assess relative abundances of trace elements. Although, some relationships can be mentioned based on the shape of the multi-element profiles. The chondrite-normalized multi-element patterns of the oxide-silicate BIFs (Fig. 2.7) are generally sub-parallel but show a range in relative abundance. The oxide-silicate BIFs are light REE enriched, but with distinct negative Ti, W, Nb, K, Mo, and P anomalies. The heavy REE have a slightly negative slope to flat pattern however with distinct negative Sn, Ti anomalies, positive Gd anomaly, a variable with approximately half the samples showing negative and positive Li anomalies. Most notably a particularly variably but overall positive Sb anomaly (Fig. 2.7).

**Table 2.5 Summary of oxide-silicate BIF gangue mineralogy (modal percent)**

| <b>Oxide-silicate BIF n=15</b>    |                        |                        |                                    |                                    |            |            |            |                        |                       |                                   |
|-----------------------------------|------------------------|------------------------|------------------------------------|------------------------------------|------------|------------|------------|------------------------|-----------------------|-----------------------------------|
|                                   | <b>SiO<sub>2</sub></b> | <b>TiO<sub>2</sub></b> | <b>Al<sub>2</sub>O<sub>3</sub></b> | <b>Fe<sub>2</sub>O<sub>3</sub></b> | <b>MnO</b> | <b>MgO</b> | <b>CaO</b> | <b>Na<sub>2</sub>O</b> | <b>K<sub>2</sub>O</b> | <b>P<sub>2</sub>O<sub>5</sub></b> |
| <b>Average</b>                    | 51.72                  | 0.10                   | 4.04                               | 16.68                              | 0.05       | 1.23       | 2.85       | 0.02                   | 0.30                  | 0.24                              |
| <b>Maximum</b>                    | 74.45                  | 0.32                   | 12.94                              | 28.42                              | 0.07       | 2.57       | 6.02       | 0.07                   | 0.85                  | 0.40                              |
| <b>Minimum</b>                    | 33.39                  | 0.01                   | 0.61                               | 4.78                               | 0.02       | 0.13       | 0.31       | 0.01                   | 0.01                  | 0.06                              |
| <b>(Lawley et al., 2015a) n=7</b> |                        |                        |                                    |                                    |            |            |            |                        |                       |                                   |
|                                   | <b>SiO<sub>2</sub></b> | <b>TiO<sub>2</sub></b> | <b>Al<sub>2</sub>O<sub>3</sub></b> | <b>Fe<sub>2</sub>O<sub>3</sub></b> | <b>MnO</b> | <b>MgO</b> | <b>CaO</b> | <b>Na<sub>2</sub>O</b> | <b>K<sub>2</sub>O</b> | <b>P<sub>2</sub>O<sub>5</sub></b> |
| <b>Average</b>                    | 45.62                  | 0.12                   | 4.60                               | 11.18                              | 0.06       | 1.07       | 2.56       | 0.63                   | 0.59                  | 0.19                              |
| <b>Maximum</b>                    | 52.62                  | 0.27                   | 10.26                              | 17.81                              | 0.07       | 1.44       | 3.79       | 2.43                   | 1.88                  | 0.27                              |
| <b>Minimum</b>                    | 36.54                  | 0.03                   | 1.56                               | 4.22                               | 0.03       | 0.64       | 1.20       | 0.02                   | 0.03                  | 0.13                              |

Values are presented in weight % and rounded to two decimal places.

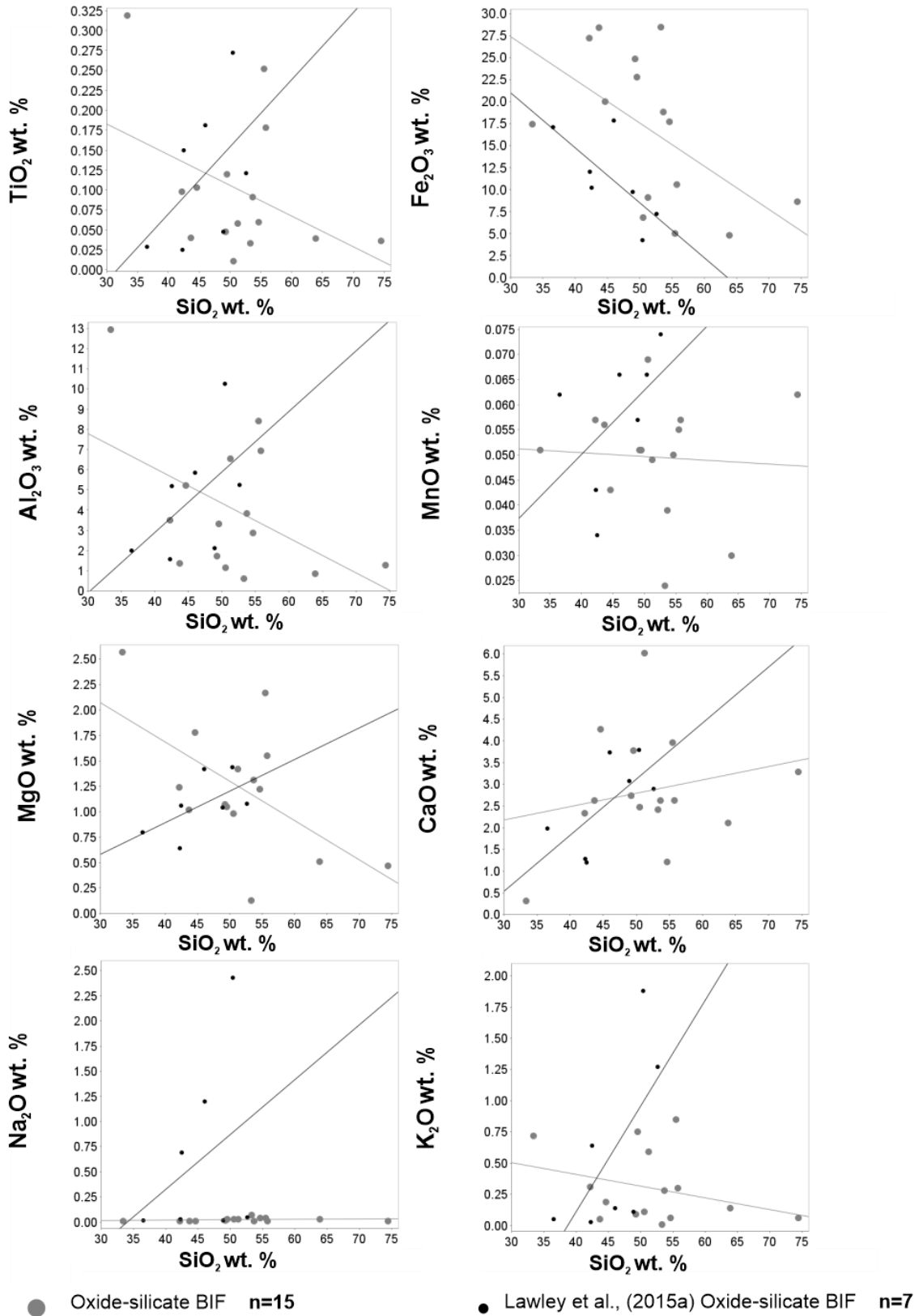


Figure 2.6 Harker diagrams displaying major oxide wt. % vs. SiO<sub>2</sub> wt. % of oxide-silicate BIF. Grey and black lines represent regression lines of respective sample populations.

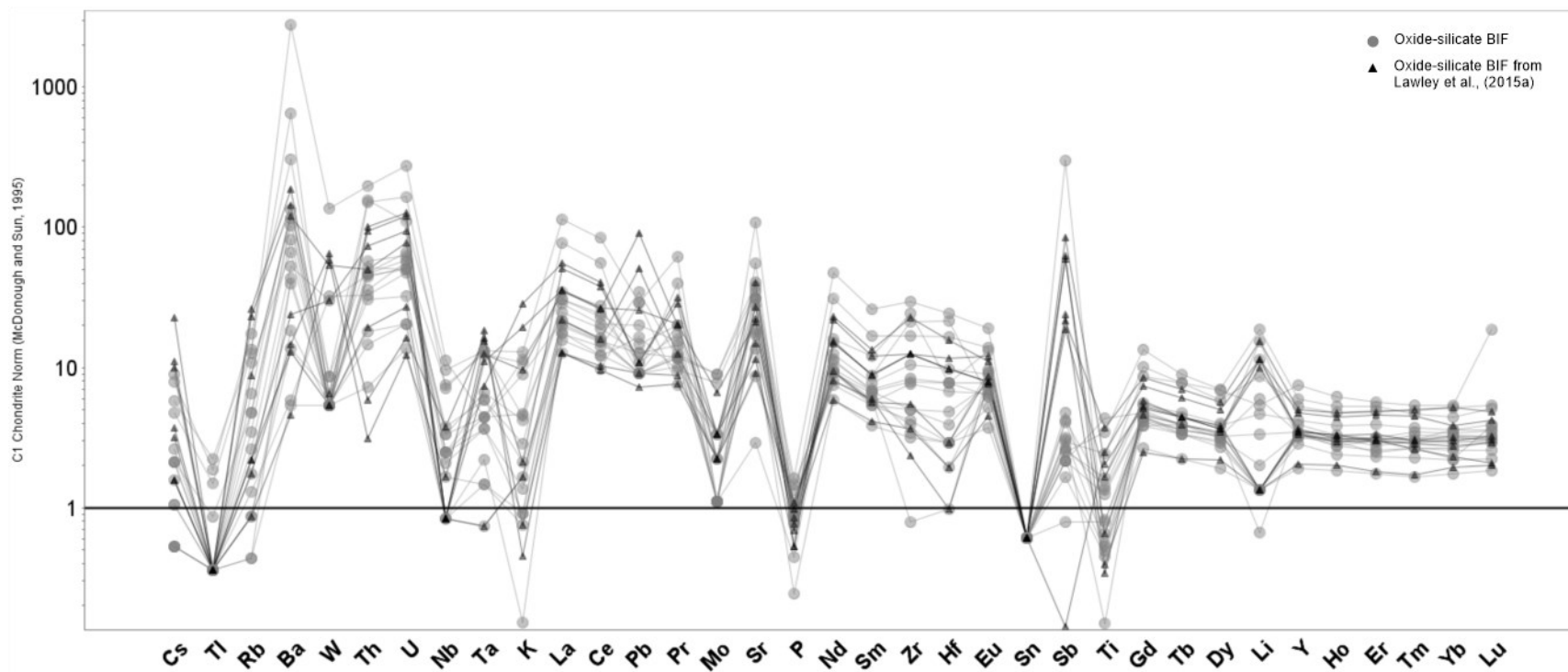


Figure 2.7 Chondrite-normalized multi-element profile for oxide-silicate BIF normalization values are from Sun and McDonough (1995).

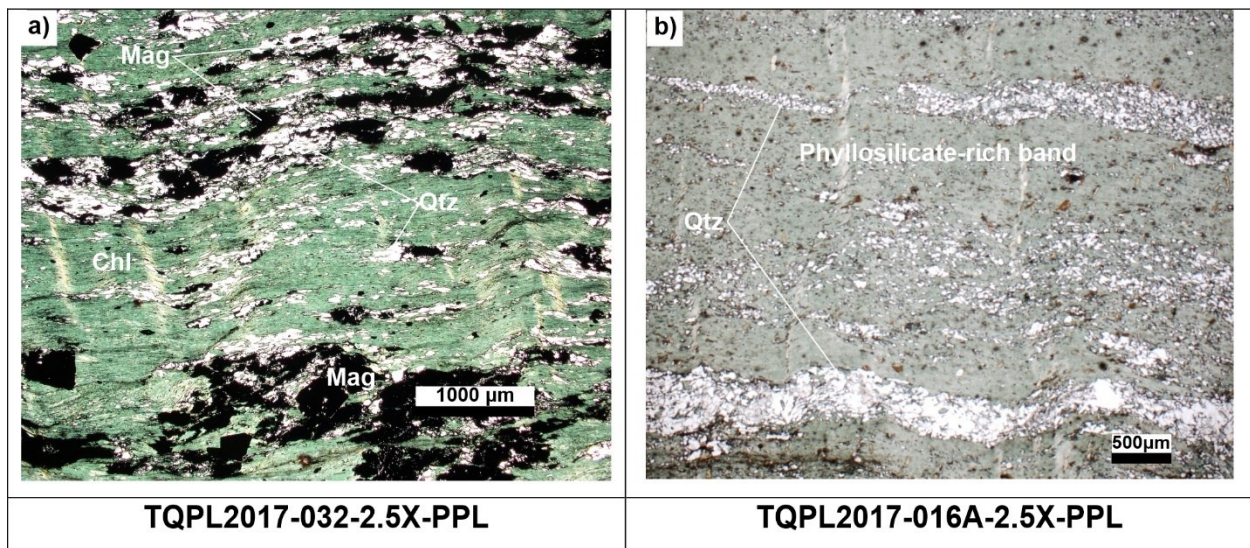


## 2.3 Pelitic BIF

The description of the pelitic BIF is based on the study of nine samples taken from underground workings. The geochemical signature of the pelitic BIF lithology is based on eight whole-rock geochemistry samples and are compared to eight whole-rock geochemistry samples taken by Lawley et al. (2015a). All samples collected and analyzed for petrography have been taken from underground crosscuts taken proximal to shear zones and containing varying amounts of mineralized veins. A summary of results is presented below.

### 2.3.1 Petrography

The pelitic BIF comprises well-developed bedding and consists of alternating beds of semi-massive to massive chlorite and grunerite-dominated layers with minor chert or silt-rich to phyllosilicate-rich pelite layers with minor chert (Fig. 2.8). Magnetite rarely forms coherent layers and is more commonly disseminated in the pelitic material (Fig. 2.8a). The pelitic BIF is locally strongly affected by the main deformation and has been folded and sheared, commonly displaying mylonitic and other brittle-ductile structures (refer to chapter 4 for more details), hosts mineralized shear and extensional veins (refer to chapter 3 for more details) and has been locally strongly affected by hydrothermal alteration.



**Figure 2.8** Representative photomicrographs of pelitic BIF a) very fine-grained chlorite-rich +/- grunerite +/- magnetite layers intercalated with quartz and magnetite-rich layers, b) phyllosilicate-rich band made up of predominantly very fine-grained chlorite intercalated with quartz-rich lenses.



The pelitic BIF is characterized by abundant very fine (50  $\mu\text{m}$  – 150  $\mu\text{m}$ ) anhedral to euhedral chlorite grains (30–55 vol.%: Table 2.6), generally making up the majority of phyllosilicate-rich layers and defining the main foliation; however, chlorite often forms local radiating acicular texture with fine grained (100  $\mu\text{m}$  – 300  $\mu\text{m}$ ) subhedral grunerite, comprising 1–15 vol.%. Very fine- to coarse-grained anhedral to euhedral disseminated magnetite grains comprise up to 15 vol.%, commonly display a pitted texture, some of which have been completely altered, and some partially to completely replaced by pyrrhotite and or arsenopyrite. Quartz-rich lenses comprising microcrystalline to fine-grained (<10  $\mu\text{m}$  – 200  $\mu\text{m}$ ), variably deformed quartz grains and minor feldspar, comprising 25–50 vol.% and up to 15% vol.%, respectively. Local traces of subhedral amphibole (unknown composition) grains occur disseminated in chlorite/grunerite dominated layers. Fine-grained (30  $\mu\text{m}$  – 150  $\mu\text{m}$ ) sericite (white mica) comprises 0–20 vol.% defining the main fabric and wrapping variably deformed quartz  $\pm$  feldspar grains, but also occurring along local mylonitic textures (see chapter 4) and the margins of quartz  $\pm$  ankerite  $\pm$  sericite  $\pm$  sulphide veins (refer to chapter 3 for more details). No distinction has been given to a hydrothermal and or metamorphic source for sericite.. However, the increase of sericite content on the margins of quartz  $\pm$  ankerite  $\pm$  sericite  $\pm$  sulphide veins and along mylonitic fabrics suggest a hydrothermal input. Varying sizes (50  $\mu\text{m}$  – 1300  $\mu\text{m}$ ) of subhedral to euhedral ankerite grains comprise up to 18 vol.% and the bulk of these grains are found within cross-cutting quartz veins and or on the margins of veins within BIF layering and along the main fabric, suggesting hydrothermal alteration. Local traces of very fine-grained (<50  $\mu\text{m}$ ) unidentifiable oxides occur disseminated throughout samples. All studied pelitic BIF samples contained between 0.1 and 5 vol.% sulphides, most sulphides commonly occurring within or along the margins of cross-cutting quartz  $\pm$  ankerite  $\pm$  sericite  $\pm$  sulphide veins, and/or replacing magnetite (refer to chapter 3 for more details).

**Table 2.6 Summary of pelitic BIF gangue mineralogy modal percent (n = 9)**

| Statistics     | Qtz         | Chl         | Gru        | Ser        | Mag        | Amph        | Fsp        | Cpx        | Ak         | Ox          | Sulph      |
|----------------|-------------|-------------|------------|------------|------------|-------------|------------|------------|------------|-------------|------------|
| <b>Average</b> | <b>33.3</b> | <b>41.9</b> | <b>4.2</b> | <b>6.5</b> | <b>3.4</b> | <b>0.01</b> | <b>4.9</b> | <b>1.1</b> | <b>2.5</b> | <b>0.08</b> | <b>2.1</b> |
| <b>Minimum</b> | 25          | 30          | 0          | 0          | 0          | 0           | 0          | 0          | 0          | 0           | 0          |
| <b>Maximum</b> | 50          | 55          | 10         | 20         | 15         | 0.1         | 15         | 10         | 18         | 0.5         | 5          |

Mineral abbreviations are as follows: Quartz (Qtz); Chlorite (Chl); Grunerite (Gru); Sericite (Ser); Magnetite (Mag); Amphibole (Amph); Feldspar (Fsp); Ankerite (Ak); Unknown oxides (Ox); Sulphides (Sulph).

### 2.3.2 Geochemistry

Like the other host lithologies, the pelitic BIF shows a wide range for some major element contents, including SiO<sub>2</sub> (35.47–61.81 wt.%), Al<sub>2</sub>O<sub>3</sub> (6.27–15.21 wt.%), Fe<sub>2</sub>O<sub>3</sub> (0.79–19.12 wt.%), MgO (1.59– 3.05 wt.%), CaO (0.48– 4.45 wt.%) and K<sub>2</sub>O (0.03– 4.46 wt.%) (Table 2.7.). However, by comparison, the pelitic BIF is enriched in MgO and depleted in SiO<sub>2</sub> relative to all the other lithologies and enriched in Fe<sub>2</sub>O<sub>3</sub>, relative to the chloritic siltstone and laminated mudstone (Table 2.3.). The pelitic BIFs SiO<sub>2</sub> content displays varying correlations with the other major oxides, and generally agree with samples taken from Lawley et al., 2015a, including a distinct negative correlation of Fe<sub>2</sub>O<sub>3</sub> and MgO vs SiO<sub>2</sub> and a distinct positive correlation with Na<sub>2</sub>O vs SiO<sub>2</sub> (Fig. 2.9.).

The chondrite-normalized multi-element profile patterns of the pelitic BIF (Fig. 2.10.) are generally sub-parallel with significant variations in some elements. The pelitic BIF is LREE enriched, but with distinct negative Ti, W, Nb, K, Mo, and P anomalies. The heavy REE have slightly declined to flat pattern with distinct negative Sn and Ti anomalies and a definite positive Li anomaly and a varying, but majorly distinct positive Sb anomaly (Fig. 2.10).

Table 2.7 Summary of pelitic BIF major oxide (wt. %)

| Pelitic BIF n=8            |                  |                  |                                |                                |      |      |      |                   |                  |                               |
|----------------------------|------------------|------------------|--------------------------------|--------------------------------|------|------|------|-------------------|------------------|-------------------------------|
|                            | SiO <sub>2</sub> | TiO <sub>2</sub> | Al <sub>2</sub> O <sub>3</sub> | Fe <sub>2</sub> O <sub>3</sub> | MnO  | MgO  | CaO  | Na <sub>2</sub> O | K <sub>2</sub> O | P <sub>2</sub> O <sub>5</sub> |
| <b>Average</b>             | 49.34            | 0.29             | 12.72                          | 6.98                           | 0.04 | 2.14 | 2.85 | 0.35              | 2.24             | 0.10                          |
| <b>Maximum</b>             | 61.81            | 0.45             | 15.21                          | 19.12                          | 0.05 | 3.05 | 4.45 | 1.56              | 4.46             | 0.14                          |
| <b>Minimum</b>             | 35.47            | 0.14             | 6.27                           | 0.79                           | 0.02 | 1.59 | 0.48 | 0.01              | 0.03             | 0.05                          |
| (Lawley et al., 2015a) n=8 |                  |                  |                                |                                |      |      |      |                   |                  |                               |
|                            | SiO <sub>2</sub> | TiO <sub>2</sub> | Al <sub>2</sub> O <sub>3</sub> | Fe <sub>2</sub> O <sub>3</sub> | MnO  | MgO  | CaO  | Na <sub>2</sub> O | K <sub>2</sub> O | P <sub>2</sub> O <sub>5</sub> |
| <b>Average</b>             | 55.58            | 0.39             | 11.13                          | 4.36                           | 0.09 | 1.65 | 2.99 | 2.65              | 1.35             | 0.08                          |
| <b>Maximum</b>             | 65.37            | 0.75             | 16.47                          | 8.21                           | 0.37 | 2.27 | 4.97 | 5.55              | 3.45             | 0.15                          |
| <b>Minimum</b>             | 36.81            | 0.10             | 3.11                           | 0.01                           | 0.04 | 1.08 | 0.68 | 0.01              | 0.01             | 0.02                          |

Values are presented in weight % and rounded to two decimal places.

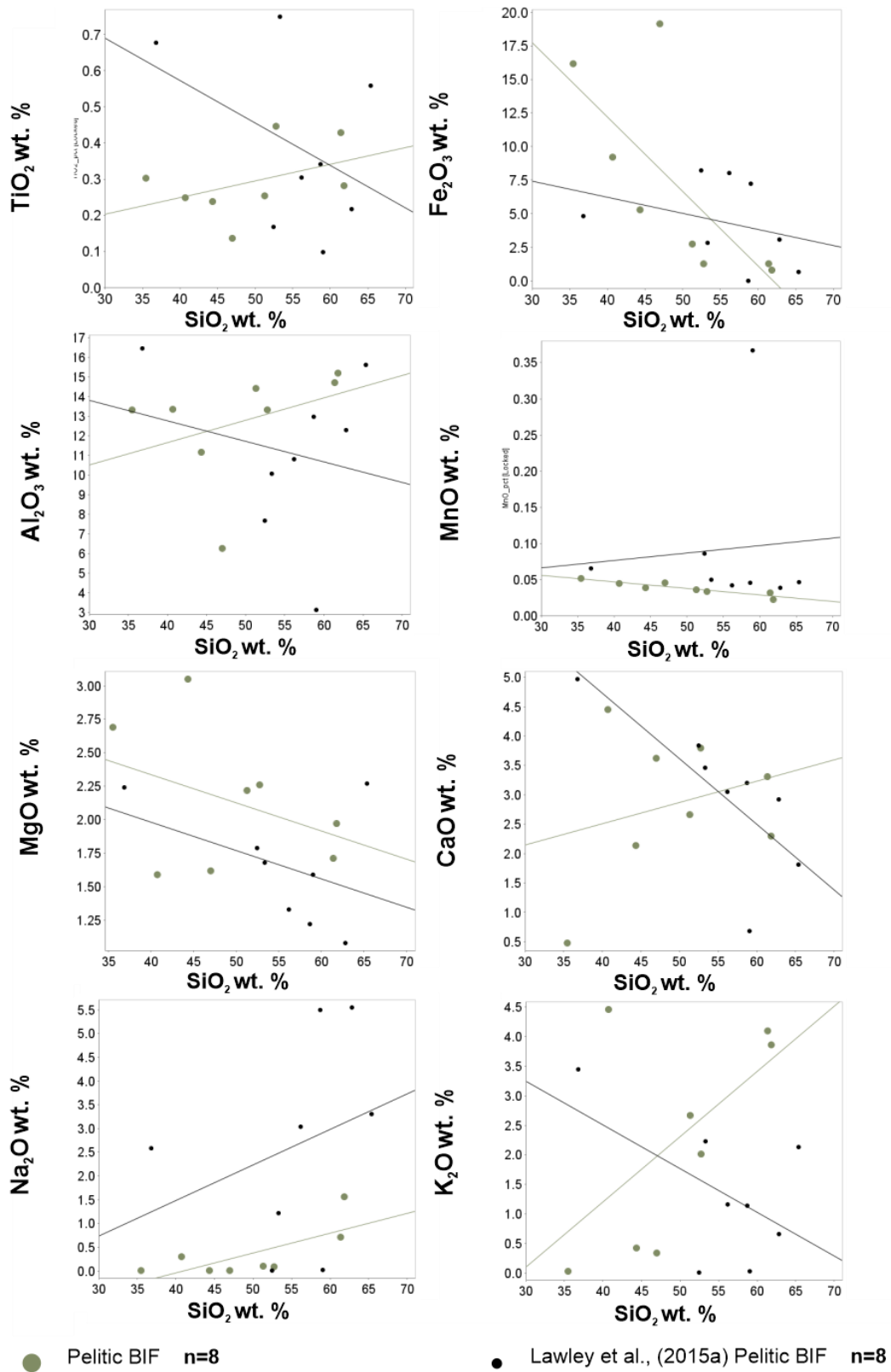


Figure 2.9 Harker diagrams displaying major oxide wt. % vs. SiO<sub>2</sub> wt. % of pelitic BIF. Green and black lines represent regression lines of respective sample populations.

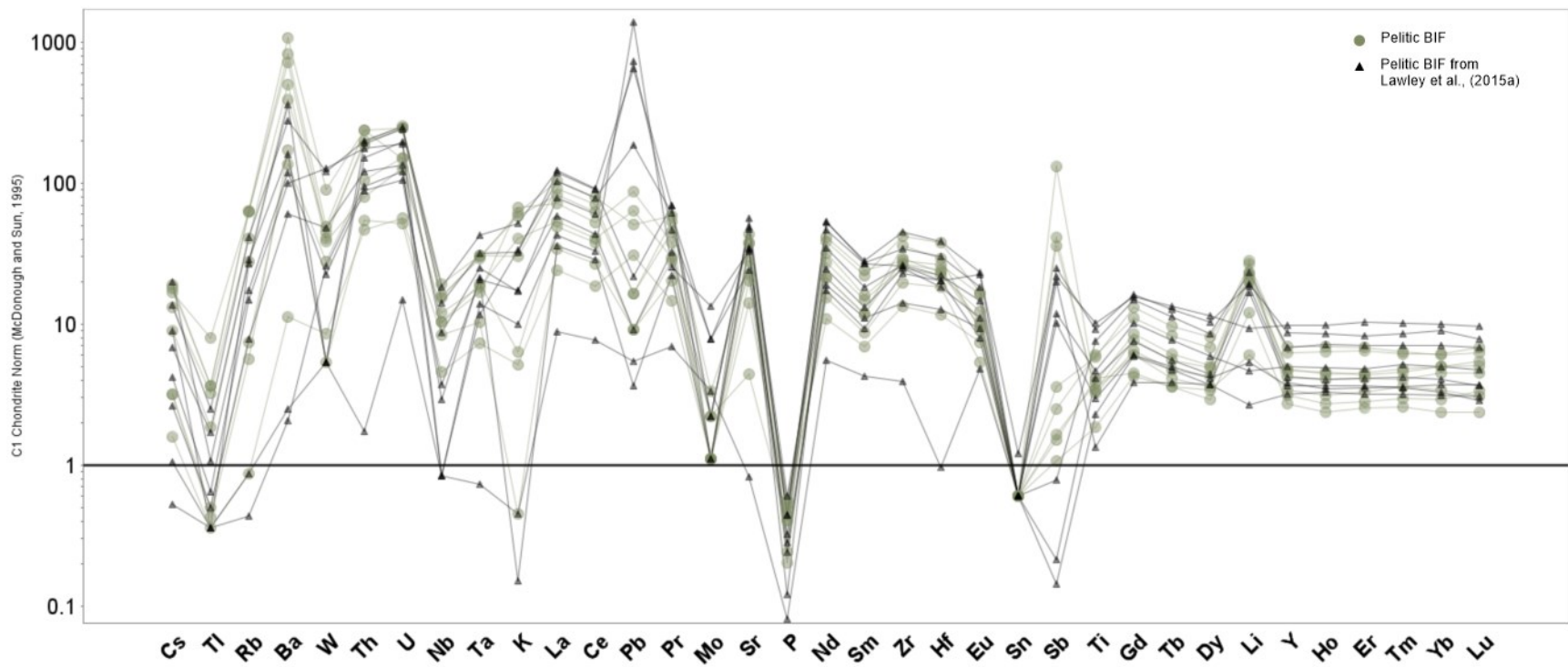


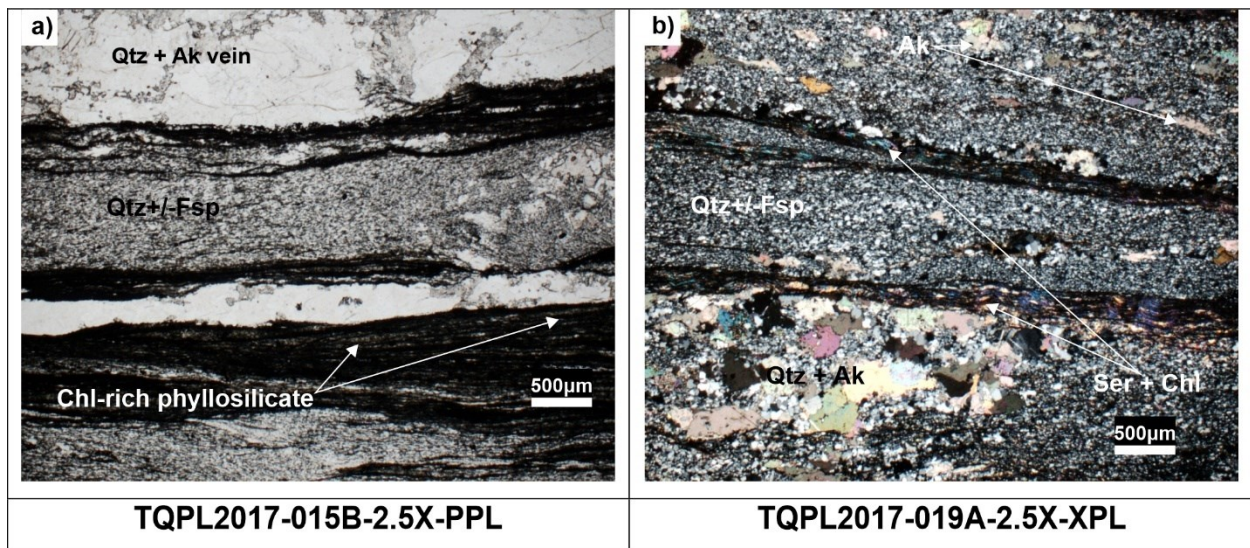
Figure 2.10 Chondrite-normalized multi-element profile for pelitic BIF normalization values are from Sun and McDonough (1995).

## 2.4 Laminated mudstone

The description of the laminated mudstone is based on two representative samples taken from underground workings.

### 2.4.1 Petrography

The laminated mudstone comprises strongly layered, alternating very fine-grained thin quartz-feldspathic and mudrock-rich layers (with fine-grained (<150  $\mu\text{m}$ ) chlorite on the margins). Mudrock layers are typically too fine-grained to determine individual mineralogy, except for very fine-grained (<150  $\mu\text{m}$ ) chlorite and sericite forming phyllosilicate-rich layers (Fig. 2.11a and b). The laminated mudstone is affected by the main deformation and has been folded and sheared, occasionally displaying mylonitic and other brittle-ductile structures. It locally hosts mineralized foliation-parallel quartz  $\pm$  ankerite  $\pm$  sericite  $\pm$  sulphide veins (Fig. 2.11.) (Refer to chapter 3 for more details) and has been affected to some degree by hydrothermal alteration.



**Figure 2.11** Representative photomicrographs of laminated mudstone a) alternating very fine-grained chlorite and sericite forming phyllosilicate-rich layers, deformed quartz-feldspar layers, and layer parallel quartz  $\pm$  ankerite veins parallel to foliation, b) fine grained quartz and chlorite intervals, with foliation parallel quartz  $\pm$  ankerite vein.

The composition of the laminated mudstone consists of 60–69 vol.% very fine-grained (30  $\mu\text{m}$  – 150  $\mu\text{m}$ ) subhedral and irregular deformed quartz grains, some of which are recrystallized equigranular grains (Fig. 2.11. b: Table 2.8). The samples contain approximately 10 vol.% fine-grained (50  $\mu\text{m}$  – 150  $\mu\text{m}$ ) anhedral to subhedral and irregular deformed feldspar grains. Very fine-grained (<150  $\mu\text{m}$ ) subhedral chlorite grains are sometimes recognizable within mudrock-rich

layers and comprise 5–10 vol.%. Very fine-grained (<150 µm) subhedral to euhedral sericite grains, commonly forming along the main fabric and within and adjacent to quartz ± ankerite veins make up 5–10 vol. %. Fine- to medium-grained (50 µm – 800 µm) ankerite comprises up to 10 vol. % of the laminated mudstone samples. Ankerite most commonly occurs along foliation and along the margins of foliation parallel sulphide-bearing quartz ± ankerite ± sericite ± sulphide veins and is attributed to hydrothermal alteration. Very fine grained (<50 µm) disseminated unidentifiable oxides are disseminated throughout samples. The laminated mudstone samples comprise 0.1-1 vol. % anhedral to euhedral very fine- to medium-grained (50 µm – 600 µm) euhedral sulphides, most commonly occurring within quartz ± ankerite ± sericite veins (refer to chapter 3 for more details), but also finely disseminated along foliation and shear fabrics.

**Table 2.8 Summary of laminated mudstone gangue mineralogy (modal percent)**

| Statistics | Qtz  | Fsp | Chl | Ser | Ak | Ox  | Sulph |
|------------|------|-----|-----|-----|----|-----|-------|
| Average    | 64.5 | 10  | 7.5 | 7.5 | 5  | 0.1 | 0.55  |
| Minimum    | 60   | 10  | 5   | 5   | 10 | 0.1 | 0.1   |
| Maximum    | 69   | 10  | 10  | 10  | 10 | 0.1 | 1     |

Mineral abbreviations are as follows Quartz (Qtz); Feldspar (Fsp); Chlorite (Chl); Sericite (Ser); Ankerite (Ak); Other oxides (Ox); Sulphides (Sulph).

## 2.4.2 Geochemistry

The geochemical characterization of the laminated mudstone is based on two whole-rock geochemistry samples and is compared with two whole-rock geochemistry taken by Lawley et al. (2015a), but likely does not represent the host lithology well.

The laminated mudstone shows consistent values for all major element contents, with a small range in Na<sub>2</sub>O content (0.55–2.08 wt.%: Table 2.8). By comparison, the laminated mudstone is enriched in SiO<sub>2</sub>, TiO<sub>2</sub>, Al<sub>2</sub>O<sub>3</sub>, and K<sub>2</sub>O and depleted in Fe<sub>2</sub>O<sub>3</sub> MnO, CaO, and P<sub>2</sub>O<sub>5</sub> relative to all other host lithologies (Table 2.3). In comparison, the laminated mudstone has a very similar major oxide composition compared to the two samples from Lawley et al. (2015a), except for the relative depletion in CaO (Table 2.3 and 2.9; Fig. 2.12).

The chondrite-normalized multi-element profile patterns of the laminated mudstone are generally sub-parallel (Fig. 2.13). The laminated mudstone is light REE enriched, but with relative distinct negative Ti, W, Nb, Mo, and P anomalies and variably Pb anomaly. The heavy REE have slightly declined to flat pattern however with a distinct negative Sn anomaly, positive Gd, and Li anomalies, and variably Sb anomaly (Fig. 2.13.).

Table 2.9 Summary of laminated mudstone major oxide (wt. %) (n = 2)

| Laminated mudstone n=2     |       |      |       |       |      |      |      |      |      |      |
|----------------------------|-------|------|-------|-------|------|------|------|------|------|------|
|                            | SiO2  | TiO2 | Al2O3 | Fe2O3 | MnO  | MgO  | CaO  | Na2O | K2O  | P2O5 |
| <b>Average</b>             | 61.47 | 0.43 | 17.14 | 0.93  | 0.02 | 1.70 | 1.50 | 1.32 | 4.15 | 0.10 |
| <b>Maximum</b>             | 62.06 | 0.46 | 17.49 | 1.07  | 0.02 | 1.71 | 1.85 | 2.08 | 4.18 | 0.11 |
| <b>Minimum</b>             | 60.88 | 0.40 | 16.79 | 0.78  | 0.02 | 1.68 | 1.14 | 0.55 | 4.12 | 0.09 |
| (Lawley et al., 2015a) n=2 |       |      |       |       |      |      |      |      |      |      |
|                            | SiO2  | TiO2 | Al2O3 | Fe2O3 | MnO  | MgO  | CaO  | Na2O | K2O  | P2O5 |
| <b>Average</b>             | 58.27 | 0.53 | 13.86 | 1.28  | 0.09 | 1.46 | 4.96 | 0.40 | 3.71 | 0.14 |
| <b>Maximum</b>             | 58.99 | 0.59 | 15.95 | 2.40  | 0.11 | 1.64 | 5.65 | 0.42 | 4.58 | 0.14 |
| <b>Minimum</b>             | 57.54 | 0.47 | 11.76 | 0.15  | 0.06 | 1.27 | 4.27 | 0.38 | 2.83 | 0.13 |

Values are presented in weight % and rounded to two decimal places.

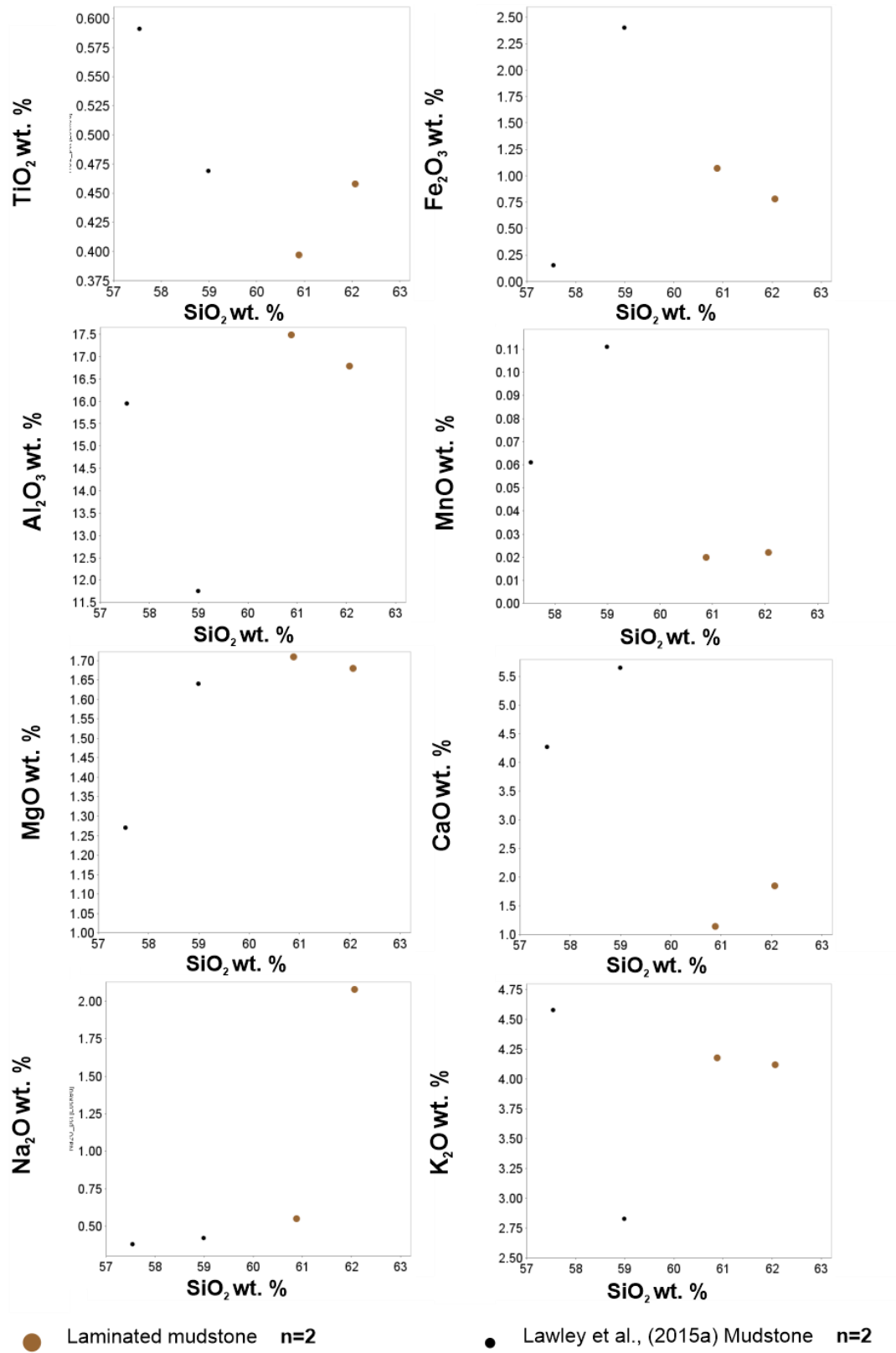


Figure 2.12 Harker diagram displaying major oxides (wt. %) vs. SiO<sub>2</sub> (wt. %) of laminated mudstone.



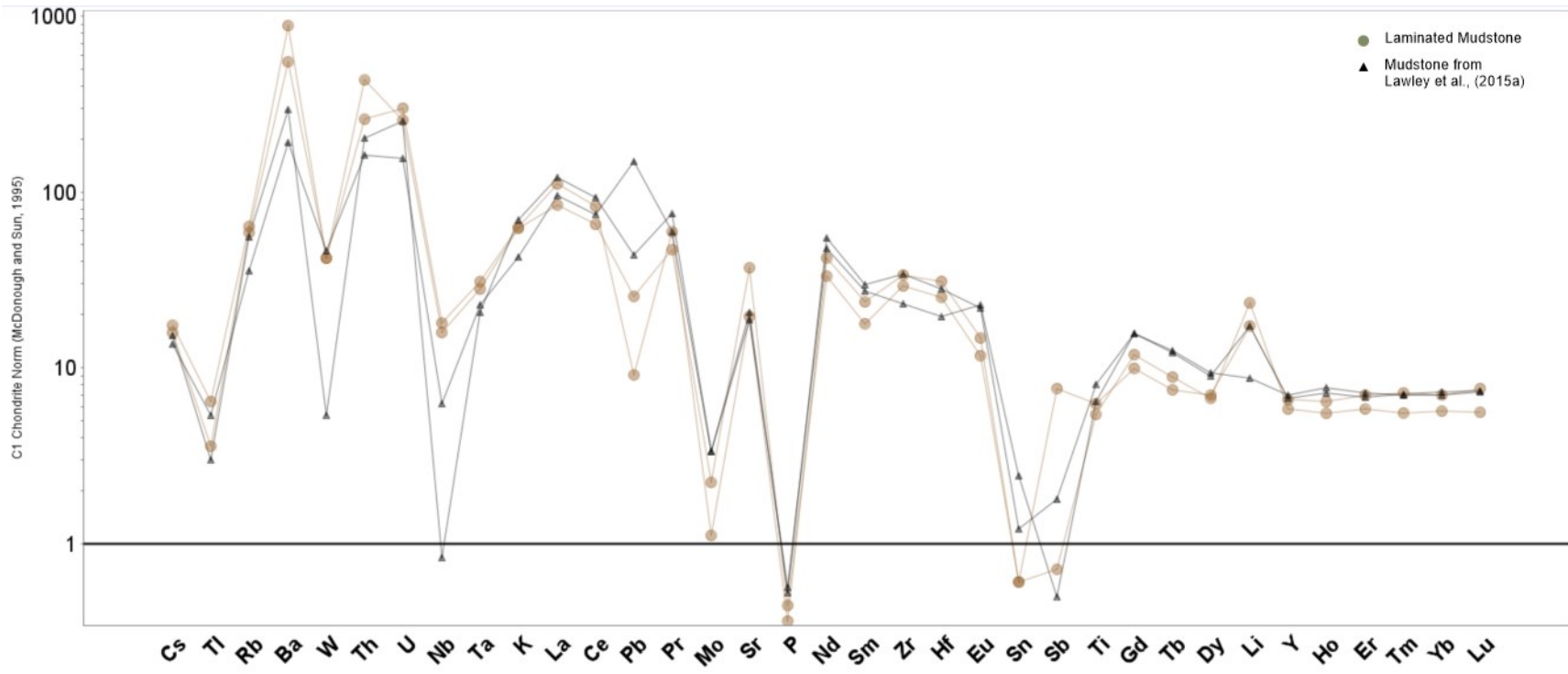


Figure 2.13 Chondrite-normalized multi-element profile of laminated mudstone normalization values are from Sun and McDonough (1995).

## 2.5 Summary

This section aims at summarizing the petrography observations and litho-geochemistry data to further classify the host lithologies.

Variations in the major element geochemistry of the metasedimentary host rocks of the 1150 and 1250 lode series are shown in summary (Table 2.3). When plotted on Harker diagrams, the samples and host rocks show variable correlations of SiO<sub>2</sub> against all major oxides (Figs. 2.3, 2.6, and 2.9). SiO<sub>2</sub> of the chloritic greywacke samples exhibit variable but negative correlations with all major oxides except Na<sub>2</sub>O, suggesting variations of the quartz to plagioclase ratio from bed to bed (e.g., sandstone versus arkose: Fig. 2.3). SiO<sub>2</sub> of the oxide-silicate BIF samples exhibits variable but negative correlations with TiO<sub>2</sub>, Fe<sub>2</sub>O<sub>3</sub>, Al<sub>2</sub>O<sub>3</sub>, MgO, and K<sub>2</sub>O, nearly flat correlations with MnO and Na<sub>2</sub>O, and variable but positive correlations with CaO, largely due to variations in the relative abundance of the chert component between samples (Fig. 2.6). SiO<sub>2</sub> of the pelitic BIF samples exhibit variable but positive correlations with TiO<sub>2</sub>, Al<sub>2</sub>O<sub>3</sub>, CaO, and K<sub>2</sub>O; and variable but negative correlations with Fe<sub>2</sub>O<sub>3</sub>, MnO, MgO, and Na<sub>2</sub>O (Fig. 2.9). Trend lines for laminated mudstone are not discussed as there are only two samples plotted.

The geochemical classification diagram of Herron (1988) is generally used to classify unmetamorphosed and unaltered sedimentary rocks, however it is shown here simply to illustrate the relative compositional range of the sampled sedimentary rocks (Fig. 2.14). The samples plot in a wide range that illustrates the diverse composition of the sampled lithologies and their heterogeneous (laminated) nature. The protolith of the chloritic greywackes can be compositionally discriminated as shale, greywacke, arkose, subarkose and Fe-sandstone. However, most samples plot in the greywacke field and straddle the arkose field, in agreement with their petrography. The oxide-silicate BIFs plot as Fe-sandstone, with one plotting as Fe-shale, in agreement with their very Fe-rich nature, and one plotting as quartz arenite (chert-rich end member). The pelitic BIF, because of wide variations in Fe content, plots in the greywacke, shale, Fe-shale and one Fe-sandstone fields. The laminated mudstone lithology plots low in the greywacke field, close the shale field.

The binary Zr/TiO<sub>2</sub> vs Al<sub>2</sub>O<sub>3</sub>/TiO<sub>2</sub>, which is generally used to broadly discriminate volcanic rocks based on their element ratios, is shown here simply to illustrate the compositional range of the sampled sedimentary rocks. As expected, the chemical composition of the 1150 and 1250 lode series host rocks is highly variable, demonstrating their detrital nature and suggesting that the

sediments have been widely sourced from the surrounding compositionally varied volcanic, sedimentary and intrusive rocks (Fig. 2.15).

All host rock samples cluster within two separate fields on Winchester and Floyd (1977) classification diagram: andesite and rhyodacite/dacite (Fig. 2.16), except for one pelitic BIF sample from Lawley et al. (2015a) plotting in the trachyte/andesite field. Overall indicating a bulk intermediate composition for most of the sedimentary lithologies.

The binary diagram  $\text{Fe (III) tot} / \text{Ti}$  vs  $\text{Al} / (\text{Al} + \text{Fe (III) tot} + \text{Mn})$  makes it possible to estimate the relative proportion of metalliferous sediments and clastic sediments input in all the samples (Fig. 2.17). This diagram assumes that Al and Ti originate from detrital sources while Fe and Mn are of hydrothermal or hydrolithic origin. The majority of the oxide-silicate BIF samples have a component of metalliferous sediments greater than 80% according to this diagram, a composition very similar to that of the iron sediments of the Red Sea (Bäcker, 1976) or that of the sediments of the East Pacific Rise (Cronan, 1976). However, a few samples of oxide-silicate BIF plot within the 60-80% range and one plots just below the 60% line of metalliferous sediment content. The pelitic BIF and chloritic greywacke samples show wide ranges of metalliferous sediment contents, however the pelitic BIF shows an approximate range of 10-85% of metalliferous sediment content and the chloritic greywacke displays an approximate range up to 65%. The laminated mudstone lithologies plot below the 20% metalliferous sediment content line (Fig. 2.17).

Part of the compositional variations between lithologies and within lithologies is due to hydrothermal alteration, which could not be entirely avoided during sampling underground in a mine environment. Despite careful selection, most samples exhibit effects of hydrothermal alteration associated with the nearby ore zones.

The chondrite normalized multi-element profiles consistently display large variations in Pb, Li, but most notably Sb, but commonly display positive anomalies within all lithologies overall (Figs. 2.4, 2.7, 2.10, and 2.13).

The finely layered nature of the clastic and chemically derived sedimentary rocks of the Upper Oxide Formation hosting the 1150 and 1250 lode series have shown distinct heterogeneity in petrographic and geochemical composition. This has been partly due to the heterogeneity of beds within the lithologies. However, major compositional and petrographic variations between and within lithologies are due to hydrothermal alteration. The nature of the lithologies and their role on alteration and mineralization will be discussed further in chapter 3.

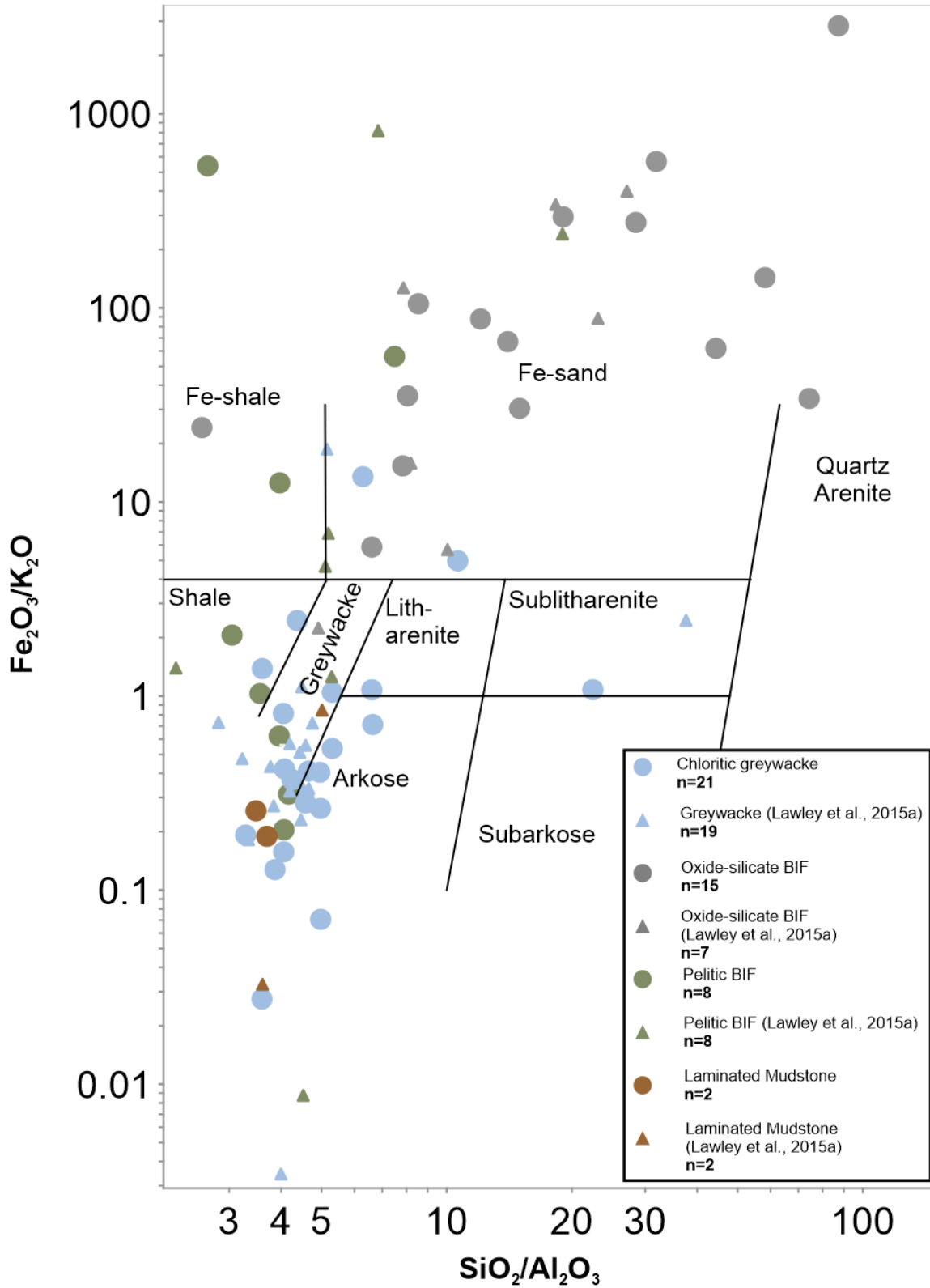


Figure 2.14 Geochemical classification of the 1150 and 1250 lode series host rocks using the log ( $\text{SiO}_2/\text{Al}_2\text{O}_3$ ) vs. log ( $\text{TFe}_2\text{O}_3/\text{K}_2\text{O}$ ) diagram (Herron, 1988).

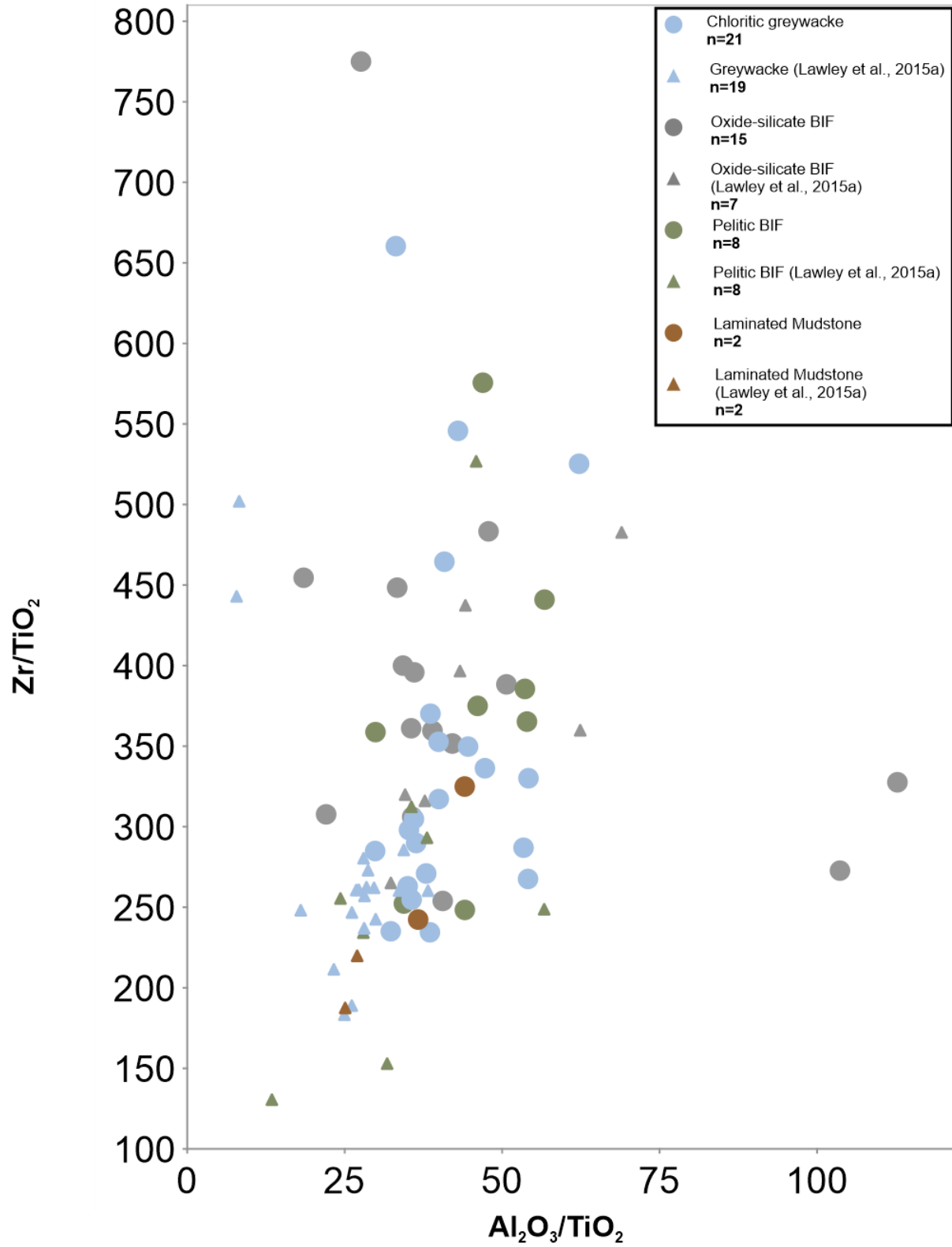
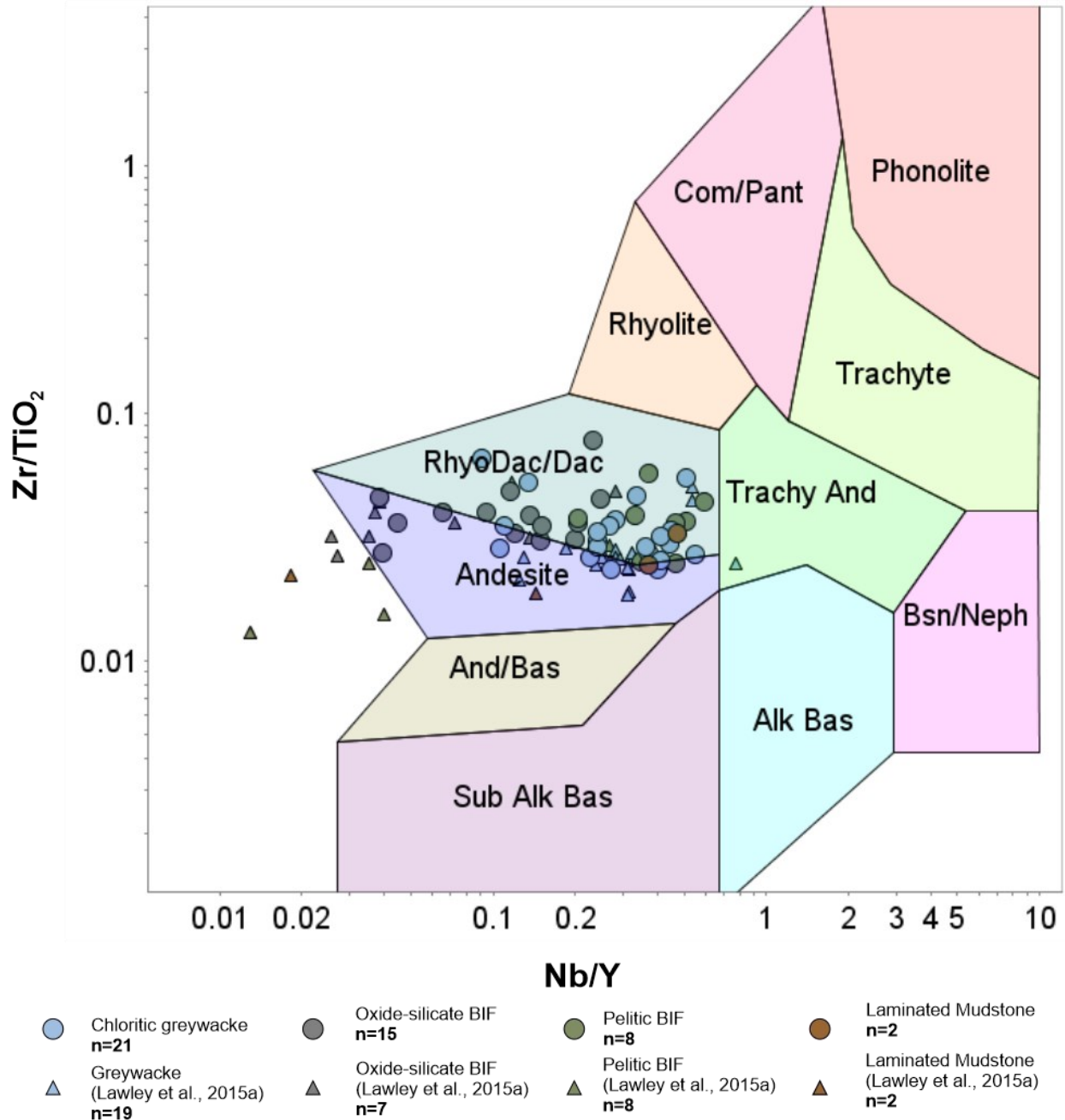


Figure 2.15 Combined Zr / TiO<sub>2</sub> vs. Al<sub>2</sub>O<sub>3</sub> / TiO<sub>2</sub> geochemical discrimination diagram for volcanic rocks but presented to give an approximation of the source of the Upper Oxide Formation sedimentary rocks.



**Figure 2.16** Winchester and Floyd (1977) classification diagram for volcanic rocks, presented here to give an idea of the bulk composition of the sampled lithologies.

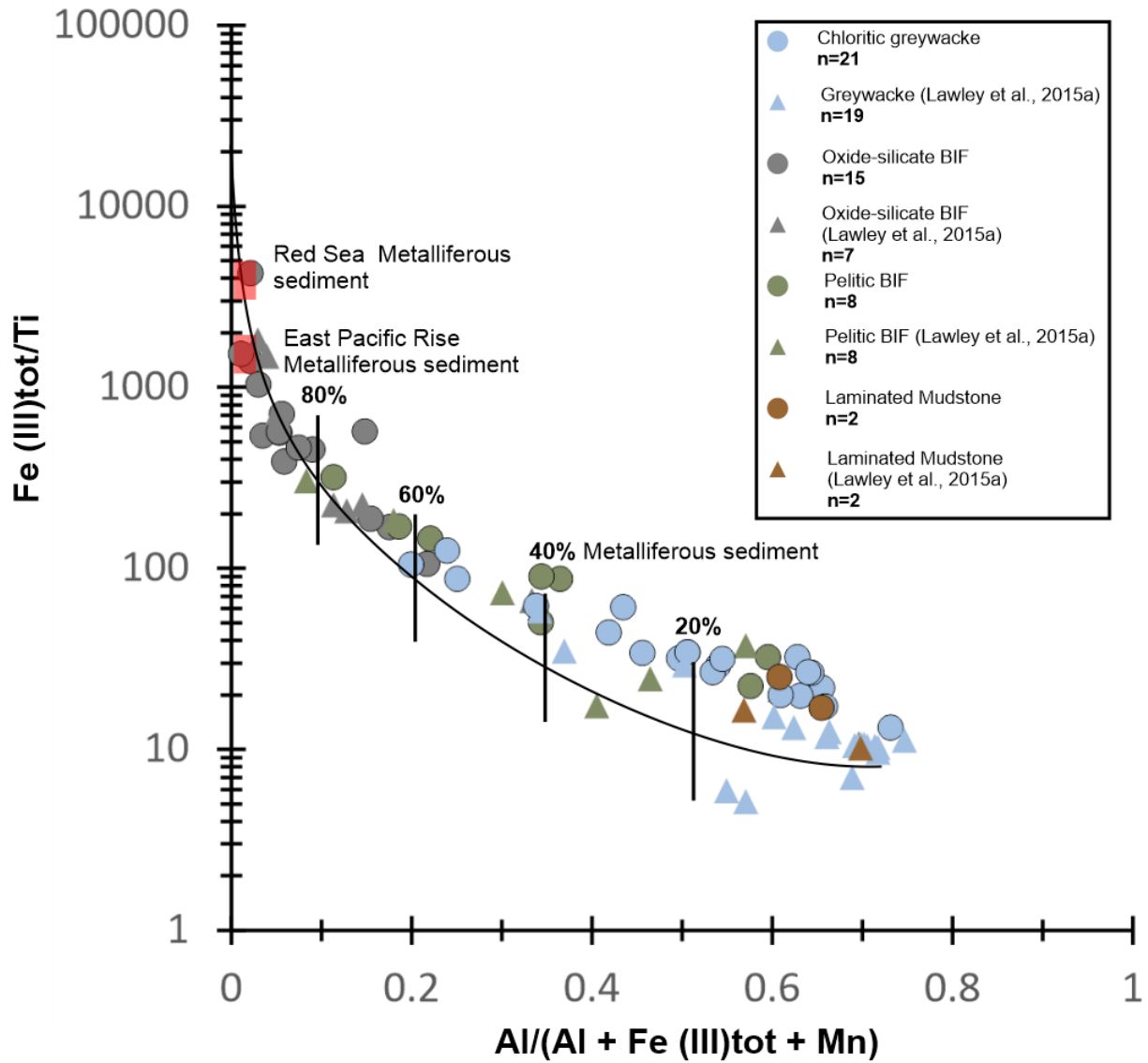


Figure 2.17 Binary diagram  $Fe(III)_{tot}/Ti$  vs  $Al/(Al + Fe(III)_{tot} + Mn)$  showing the relative proportion of metalliferous and clastic sediments of all samples compared to metalliferous sediments of the Red Sea (Bäcker, 1976) or those in the East Pacific Rise sector (Cronan, 1976).

### 3 STYLE AND DISTRIBUTION OF GOLD MINERALIZATION AND ASSOCIATED HYDROTHERMAL FOOTPRINT

---

Hydrothermal alteration and associated pathfinder elements associated with gold mineralization at Meliadine have been studied in detail previously (Carpenter, 2003; Carpenter and Duke, 2004; Carpenter et al., 2005; Lawley et al., 2015a, b, c, 2016) and therefore was not the focus of this study. However, some work aiming at confirming previous findings and demonstrating relationships with gold distribution, associated hydrothermal alteration, and host lithologies was completed.

Gold mineralization at the Tiriganiaq deposit is associated with BIF-hosted replacement-style mineralization, coupled with auriferous quartz  $\pm$  ankerite veins and selvages that occur as stacked, semicontinuous ore zones known locally as “*lodes*” (Lawley et al., 2015c). These veins are dominantly comprised of quartz and carbonate (ankerite and calcite), with variable amounts of hydrothermal chlorite, iron-sulphides, and lesser amounts of biotite, magnetite, and monazite (Carpenter and Duke, 2004). Gold is paragenetically late and, at the micro-scale, occurs within low-strain microtextural sites and clusters of inclusions within variably recrystallized and idiomorphic arsenopyrite crystals (Lawley et al., 2015c).

The Meliadine gold district shows a complex paragenetic sequence with potentially two generations of arsenopyrite that are mainly associated with gold mineralization. Lawley et al. (2015c) have shown that gold mineralization occurs in two forms associated with arsenopyrite, as inclusions within and fracture fills cutting arsenopyrite. Gourcerol et al. (2016) have shown that the Pump and F-zone mineralized Algoma-type BIFs also show a complex paragenetic sequence with two generations of arsenopyrite, identified as aspy1 and aspy2. Aspy1 occurs as strongly fractured, coarse euhedral that have a sieve-texture (along main fabric). In contrast, aspy2 is fine- to medium-grained and is unfractured and inclusion-free (Gourcerol et al., 2016).

The hydrothermal alteration associated with BIF-hosted replacement-style gold mineralization and auriferous quartz  $\pm$  ankerite veins comprising the 1150 and 1250 lode series accounts for major compositional and petrographic variations between and within units. Lawley et al. (2015a, c) studied the hydrothermal footprint of the Meliadine gold district’s BIF-hosted gold deposits, including the Tiriganiaq deposit, using field observations, whole-rock lithochemochemistry and portable x-ray fluorescence (pXRF) analyses. They identified key hydrothermal mineral assemblages at the margins of auriferous quartz  $\pm$  ankerite veins and in highly-strained intervals that typically truncate and overprint banding in the iron formation units and the main metamorphic



deposit fabric (discussed further in chapter 4). The hydrothermally altered and veined rocks are spatially associated with anomalous pathfinder element concentrations (Au, As, Te, Bi and Sb) and extend 10s to 100s meters adjacent to ore zones (Lawley et al., 2015c).

Coarse-grained and idiomorphic ankerite crystals, and associated calcite, sericite, quartz and arsenopyrite provide a visual indicator of gold ore. Geochemically, barren calcite bands and late quartz-calcite veins obscure the relationship between gold and carbonate alteration linked to auriferous quartz  $\pm$  ankerite veins. As a result, potassium enrichment is considered a useful proxy for this hydrothermal mineral alteration assemblage (Lawley et al., 2015c).

Coarse-grained, idiomorphic arsenopyrite and arsenian pyrite crystals provide the clearest visual proxy for elevated gold grades at Tiriganiaq, generally accompanied by a sulphide mineral assemblage comprising pyrrhotite along with lesser chalcopyrite, galena and sphalerite. Therefore, arsenic and sulphur anomalies provide a useful vector to gold ore (Lawley et al., 2015c).

Additionally, chlorite clots represent another good visual gold indicator and occur within auriferous quartz  $\pm$  ankerite veins and high-grade BIF intervals (Lawley et al., 2015a and c). Hydrothermal chlorite is paragenetically late compared to metamorphic chlorite in mudstone intercalated with BIF and is distinctly more Fe-rich relative to chlorite in metamorphosed pelitic and volcanic rocks (Carpenter, 2003; Lawley et al., 2015c). However, the ambiguity of Fe-rich alteration versus the Fe-rich nature of the protoliths makes it difficult to use Fe-enrichment as a geochemical proxy for gold mineralization. Ambiguous alteration zones with an uncertain relationship to gold also occur (e.g., magnetite porphyroblasts, acicular calcite needles and quartz–calcite banding, and epidote-rich domains: Lawley et al., 2015c).

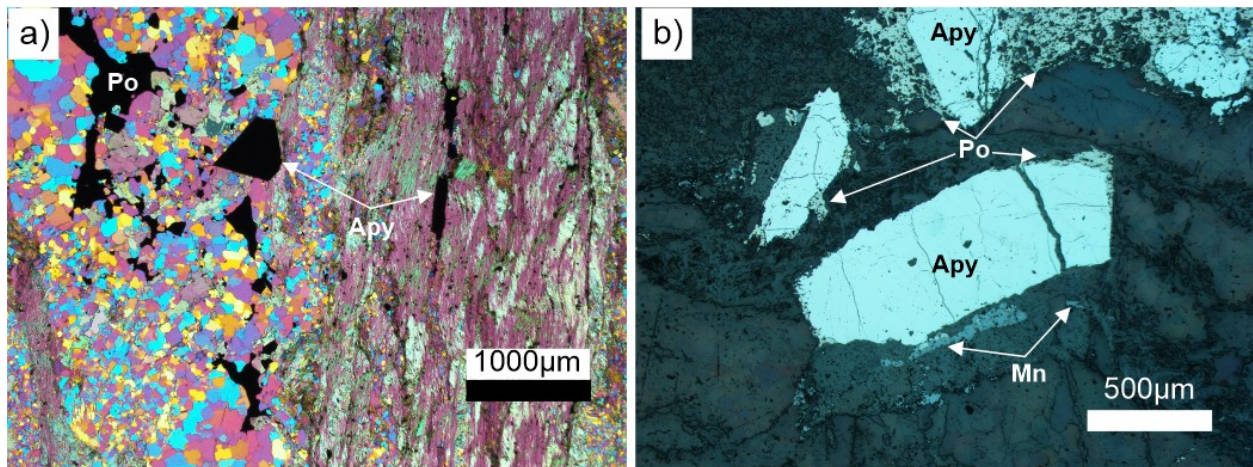
The style and distribution of gold mineralization and associated hydrothermal footprint within each host lithology of the 1150 and 1250 zones are presented in this chapter. This will help illustrate how the effects of hydrothermal alteration are expressed in the lithologies of the study area, and to evaluate the role that these lithologies have played on the nature and distribution of gold.

### 3.1 SULPHIDE MINERALOGY AND DISTRIBUTION OF GOLD, ARSENIC, AND SULPHUR

#### 3.1.1 Chloritic Greywacke

All chloritic greywacke samples taken contained up to 10 vol.% sulphides, including arsenopyrite generally concentrating along the main fabric, within or on the margins of quartz  $\pm$  ankerite  $\pm$  sericite veins (Table 3.1; Fig. 3.1a and b). Up to 2.5 vol.%, 50 – 20000 micrometers pyrrhotite, often occurring as irregular blebs disseminated throughout the sample or occurring within or on the margins of quartz  $\pm$  ankerite  $\pm$  sericite-veins, also occurs as partially or fully replacing arsenopyrite (Fig. 3.1b). Traces of 50 – 500 micrometers irregular blebs of chalcopyrite often associated with other sulphides occur on the margins of arsenopyrite or pyrrhotite. Up to 0.5 vol.% irregular galena grains occurring on the margin of an irregular grain of pyrrhotite hosted within a quartz  $\pm$  ankerite  $\pm$  sericite-vein was noted in one sample. Galena is much less abundant in lodes 1150 and 1250 than along the 1000 lode.

While the thin sections did not contain any visible gold grains the chloritic greywacke shows a wide range in Au (0.01–5.41 ppm), As (0.001–4.2 wt.%), and S (0.01–2.59 wt.%) (Table 3.2.).



**Figure 3.1** a) Photomicrograph of sample TQPL2017-040-2.5X-XPL, exhibiting a quartz ankerite vein with irregular anhedral to subhedral arsenopyrite and pyrrhotite grains with pervasive sericitic alteration halo. Sericite altered margin are intensely foliated and elongated arsenopyrite and pyrrhotite along fabrics; b) Photomicrograph of sample TQPL2018-007-2.5X-RL, revealing euhedral to subhedral arsenopyrite grains being partially replaced by pitted textured pyrrhotite in a quartz  $\pm$  ankerite  $\pm$  sericite  $\pm$  chlorite shear vein hosted in chloritic greywacke. Abbreviations: Apy = arsenopyrite, Mn = magnetite, Po = pyrrhotite.

**Table 3.1 Summary of chloritic greywacke sulphide mineralogy modal percent (n=19)**

| Statistics | Arsenopyrite | Pyrrhotite | Chalcopyrite | Pyrite | Galena |
|------------|--------------|------------|--------------|--------|--------|
| Average    | 1.80         | 0.54       | 0.01         | 0.00   | 0.03   |
| Minimum    | 0.10         | 0.00       | 0.00         | 0.00   | 0.00   |
| Maximum    | 10.00        | 2.50       | 0.10         | 0.00   | 0.50   |

**Table 3.2 Summary of gold, arsenic and sulphur content in chloritic greywacke**

| Chloritic greywacke n=21    |          |           |          |
|-----------------------------|----------|-----------|----------|
|                             | Au (ppm) | As (wt.%) | S (wt.%) |
| Average                     | 0.94     | 0.55      | 0.56     |
| Maximum                     | 5.41     | 4.20      | 2.59     |
| Minimum                     | 0.01     | 0.00      | 0.01     |
| (Lawley et al., 2015a) n=19 |          |           |          |
|                             | Au (ppm) | As (wt.%) | S (wt.%) |
| Average                     | 0.35     | 0.25      | 0.31     |
| Maximum                     | 4.16     | 2.99      | 1.57     |
| Minimum                     | 0.01     | 0.00      | 0.01     |

Values are rounded to two decimal places

### 3.1.2 Oxide-silicate BIF

All oxide-silicate BIF samples, most of which were carefully selected to avoid the most mineralized and sulphide bearing intervals, contained up to 10 vol.% sulphides (Fig. 3.2). Up to 6 vol.%, 50 µm–30 mm subhedral to euhedral arsenopyrite replaces magnetite grains. There is between 0.1 and 3 vol.%, 0.055 – 25 millimeters pyrrhotite, most commonly occurring as partially to fully replacing magnetite and arsenopyrite grains. Pyrrhotite also occurs as irregular blebs disseminated irregularly through samples, or within or at the margins of quartz ± ankerite ± sericite veins. Up to 1 vol.%, 50 – 500 micrometers very fine-grained irregular blebs of chalcopyrite associated with other sulphides occurs with arsenopyrite or pyrrhotite (Table 3.3).

The oxide-silicate BIF is variably endowed in Au, As, and S including Au (0.01–13.3 ppm), As (0.003–12 wt.%), and S (0.02–6.71 wt.%: Table 3.4).

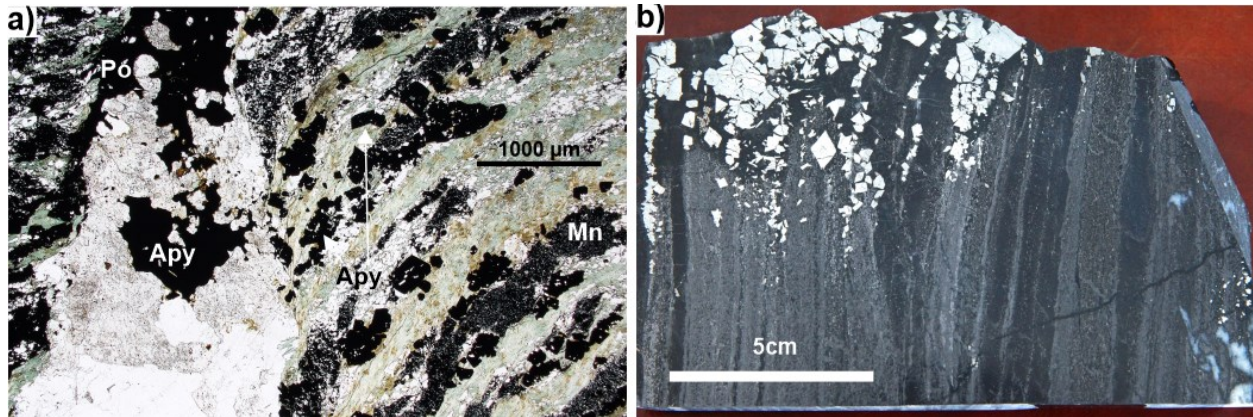


Figure 3.2 a) Photomicrograph of sample TQPL2017-036A-2.5X-PPL, showing mineralized oxide-silicate BIF comprising magnetite, chert, chlorite (with minor grunerite) dominated layers, cut by arsenopyrite + pyrrhotite bearing quartz ± ankerite vein. b) Slab sample of coarse, idiomorphic arsenopyrite replacement in BIF along a quartz ± ankerite vein selvage. Abbreviations: Apy = arsenopyrite, Mn = magnetite, Po = pyrrhotite.

Table 3.3 Summary of oxide-silicate BIF sulphide mineralogy (modal percent, n=10)

| Statistics | Arsenopyrite | Pyrrhotite | Chalcopyrite |
|------------|--------------|------------|--------------|
| Average    | 1.44         | 2.01       | 0.14         |
| Minimum    | 0.00         | 0.10       | 0.00         |
| Maximum    | 6.00         | 3.00       | 1.00         |

Table 3.4 Summary of gold, arsenic and sulphur content in oxide-silicate BIF

| Oxide-silicate BIF n=15   |          |            |          |
|---------------------------|----------|------------|----------|
|                           | Au (ppm) | As ( wt.%) | S (wt.%) |
| Average                   | 1.75     | 0.86       | 1.53     |
| Maximum                   | 13.30    | 12.00      | 6.71     |
| Minimum                   | 0.01     | 0.00       | 0.02     |
| (Lawley et al., 2015) n=7 |          |            |          |
|                           | Au (ppm) | As (wt.%)  | S (wt.%) |
| Average                   | 63.69    | 6.04       | 7.66     |
| Maximum                   | 189.00   | 11.20      | 15.80    |
| Minimum                   | 0.92     | 0.01       | 0.58     |

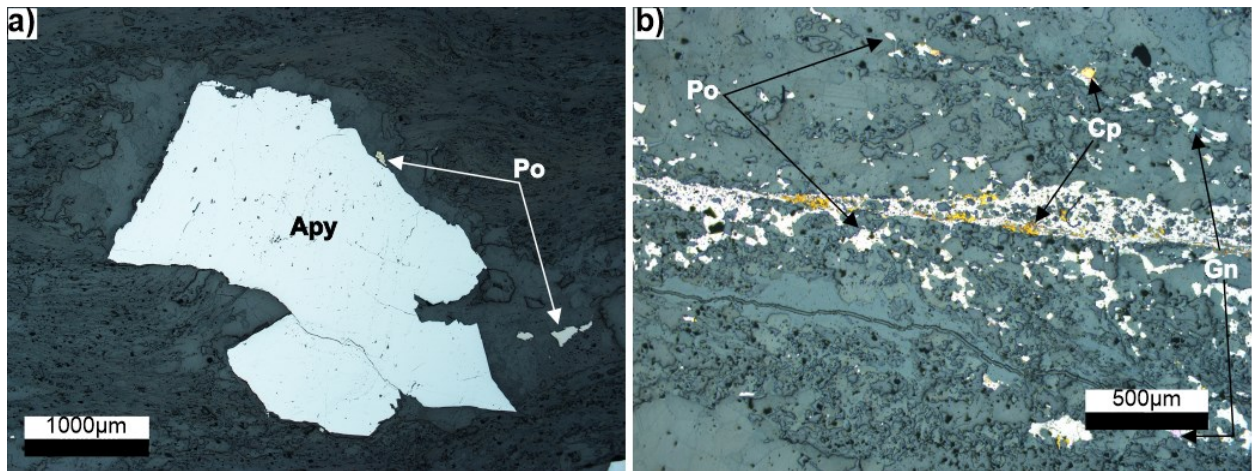
Values are rounded to two decimal places



### 3.1.3 Pelitic BIF

The representative sulphide assemblage of the pelitic BIF consists of up to 5 vol.%, 0.05– 25 millimeters subhedral to euhedral arsenopyrite typically replacing magnetite grains (Table 3.3; Fig. 3.3a). 0.1 to 1.5%, 0.05– 15 millimeters pyrrhotite most commonly occurs as partially to fully replacing magnetite and arsenopyrite grains and as irregular blebs or stringers disseminated irregularly through samples (Fig. 3.3b). Up to 0.5 vol.%, 25 – 50 micrometers very fine-grained irregular grains of galena commonly occur on the margins of or within irregular pyrrhotite stringers, and up to 0.1 vol.%, 25 – 50 micrometers irregular grains of chalcopyrite characteristically associated with other sulphides occur on the margins of arsenopyrite or pyrrhotite (Fig. 3.3b). Pyrite is present locally as 25 – 50 micrometers subhedral clusters associated with other sulphides, occurring on the margins of arsenopyrite or pyrrhotite.

The pelitic BIF shows a wide range of ore-associated elements such as Au (0.01–16.5 ppm), As (0.003–5.46 wt.%), and S (0.03–5.2 wt.%) (Table 3.5).



**Figure 3.3** a) Photomicrograph of sample TQPL2017-033-5X-RL, displaying subhedral arsenopyrite grains within quartz-rich strain fringe with minor irregular pyrrhotite. b) Photomicrograph of sample TQPL2017-043A-2.5X-RL, revealing irregular grains and stringers of pyrrhotite with local magnetite inclusions and very fine-grained irregular grains of galena and chalcopyrite occurring on the margins of and within irregular pyrrhotite stringers. Abbreviations: Apy = arsenopyrite, Cp = chalcopyrite, Gn = galena, Po = pyrrhotite.

**Table 3.5 Summary of pelitic BIF sulphide mineralogy (modal percent, n = 9)**

| Statistics     | Arsenopyrite | Pyrrhotite  | Chalcopyrite | Pyrite      | Galena      |
|----------------|--------------|-------------|--------------|-------------|-------------|
| <b>Average</b> | <b>1.90</b>  | <b>0.26</b> | <b>0.01</b>  | <b>0.01</b> | <b>0.05</b> |
| <b>Minimum</b> | 0.00         | 0.10        | 0.00         | 0.00        | 0.00        |
| <b>Maximum</b> | 5.00         | 1.50        | 0.10         | 0.10        | 0.50        |

Values are presented in weight % and rounded to two decimal places.

**Table 3.6 Summary of gold, arsenic and sulphur content in pelitic BIF**

| Pelitic BIF n=8            |          |           |          |
|----------------------------|----------|-----------|----------|
| Pelitic BIF n=8            | Au (ppm) | As (wt.%) | S (wt.%) |
| <b>Average</b>             | 2.37     | 1.22      | 1.55     |
| <b>Maximum</b>             | 16.50    | 5.46      | 5.20     |
| <b>Minimum</b>             | 0.01     | 0.00      | 0.03     |
| (Lawley et al., 2015a) n=8 |          |           |          |
|                            | Au (ppm) | As (wt.%) | S (wt.%) |
| <b>Average</b>             | 8.37     | 3.12      | 2.41     |
| <b>Maximum</b>             | 42.70    | 7.63      | 5.67     |
| <b>Minimum</b>             | 0.01     | 0.00      | 0.18     |

Values are rounded to two decimal places.

### 3.1.4 Laminated mudstone

Both laminated mudstone samples contain 0.1–1 vol.% sulphides (Table 3.7), including up to 0.1 vol.%, 0.05 – 5 millimeters subhedral to euhedral arsenopyrite concentrated along margins of foliation-parallel quartz ± ankerite ± sericite veins (Fig. 3.4a). Between 0.1 and 1 vol.%, 0.05 – 3 millimeters pyrrhotite is present, typically occurring on the margins of quartz ± ankerite ± sericite-veins or cross-cutting pyrrhotite stringers (Fig. 3.4b). Traces of irregular grains of chalcopyrite are locally associated with the pyrrhotite.

The laminated mudstone shows a narrow range in Au, As, and S, including Au (0.01–0.11 ppm), As (0.005–0.538 wt.%), and S (0.02–0.4 wt.%) (Table 3.8.).

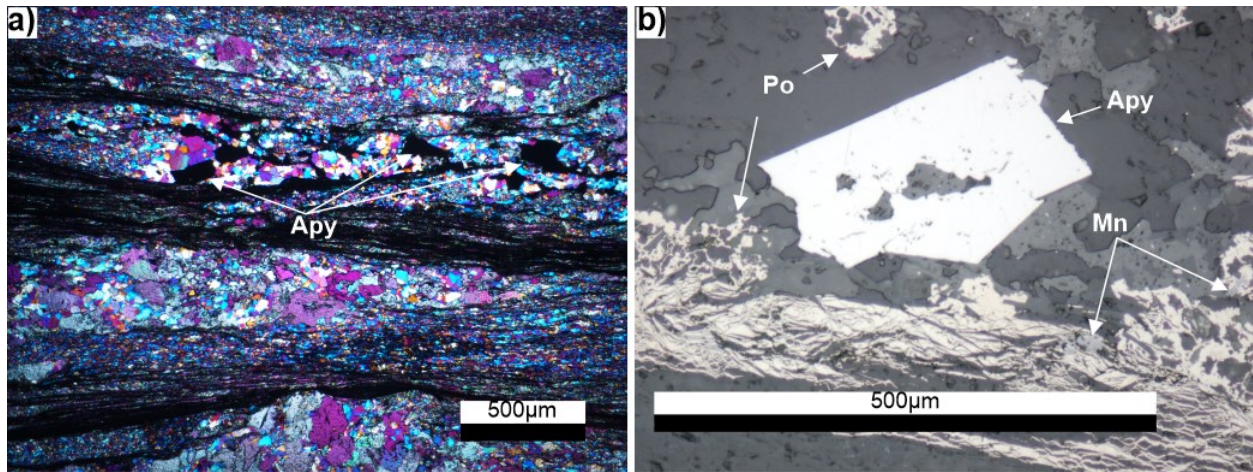


Figure 3.4 a) Photomicrograph of sample TQPL2017-019B-2.5X-XPL, displaying euhedral arsenopyrite grains within quartz ± ankerite ± sericite-vein. b) Photomicrograph of sample TQPL2017-019A-20X-RL, showing subhedral arsenopyrite grain and irregular blebs and stringers of pyrrhotite with local magnetite inclusions. Abbreviations: Apy = arsenopyrite, Mn = magnetite, Po = pyrrhotite.

Table 3.7 Summary of laminated mudstone sulphide mineralogy (modal percent, n=2)

| Statistics | Arsenopyrite | Pyrrhotite |
|------------|--------------|------------|
| Average    | 0.55         | 0.05       |
| Minimum    | 0            | 0.1        |
| Maximum    | 0.1          | 1          |

Table 3.8 Summary of gold, arsenic and sulphur content in laminated mudstone.

| Laminated mudstone n=2    |          |           |          |
|---------------------------|----------|-----------|----------|
|                           | Au (ppm) | As (wt.%) | S (wt.%) |
| Average                   | 0.06     | 0.27      | 0.21     |
| Maximum                   | 0.11     | 0.54      | 0.40     |
| Minimum                   | 0.01     | 0.00      | 0.02     |
| (Lawley et al., 2015) n=2 |          |           |          |
|                           | Au (ppm) | As (wt.%) | S (wt.%) |
| Average                   | 0.97     | 1.01      | 1.89     |
| Maximum                   | 1.31     | 1.66      | 2.17     |
| Minimum                   | 0.63     | 0.35      | 1.60     |

Values are rounded to two decimal places.

### 3.1.5 Summary

On average, the oxide-silicate BIF is enriched in pyrrhotite (2.01 mod.%) and total sulphide (3.50 mod.%) compared to all other lithologies (Table. 3.9). The petrography data shows the oxide-silicate BIF to be relatively depleted in arsenopyrite (1.44 mod.%) compared to the pelitic BIF (1.90 mod.%) and chloritic greywacke (1.80 mod.%) (Table. 3.9). However, this is not consistent with other field observations which show arsenopyrite to preferentially form stratabound replacement zones along magnetite-rich layers in the oxide-silicate BIF compared to other lithologies (Fig. 3.2). This is a factor of a small sample size and sample location of the selected thin sections.

The oxide-silicate BIF is variably endowed in Au, As, and S including Au (0.01–13.3 ppm), As (0.003–12 wt.%), and S (0.02–6.71 wt.%). By comparison, the oxide-silicate BIF is enriched in Au, As, and S compared to the chloritic greywacke and laminated mudstone but depleted relative to the pelitic BIF (Table 3.10). Although, three samples taken of quartz ± ankerite veins hosted within oxide-silicate BIF display enriched values of Au, As, and S compared to all lithologies. Additionally, the oxide-silicate BIF samples reported in Lawley et al. (2015a) are enriched in Au, As, and S compared to all other lithologies (Table 3.10).



Table 3.9 Summary of sulphide assemblage (modal percentage) for all lithologies

| Chloritic Greywacke n=19 |           |              |            |              |        |        |
|--------------------------|-----------|--------------|------------|--------------|--------|--------|
|                          | Sulphides | Arsenopyrite | Pyrrhotite | Chalcopyrite | Pyrite | Galena |
| <b>Average</b>           | 2.31      | 1.80         | 0.54       | 0.01         | 0.00   | 0.03   |
| <b>Maximum</b>           | 10.00     | 10.00        | 2.50       | 0.10         | 0.00   | 0.50   |
| <b>Minimum</b>           | 0.10      | 0.10         | 0.00       | 0.00         | 0.00   | 0.00   |
| Oxide-silicate BIF n=10  |           |              |            |              |        |        |
|                          | Sulphides | Arsenopyrite | Pyrrhotite | Chalcopyrite | Pyrite | Galena |
| <b>Average</b>           | 3.50      | 1.44         | 2.01       | 0.14         | 0.00   | 0.00   |
| <b>Maximum</b>           | 10.00     | 6.00         | 3.00       | 1.00         | 0.00   | 0.00   |
| <b>Minimum</b>           | 0.00      | 0.00         | 0.10       | 0.00         | 0.00   | 0.00   |
| Pelitic BIF n=9          |           |              |            |              |        |        |
|                          | Sulphides | Arsenopyrite | Pyrrhotite | Chalcopyrite | Pyrite | Galena |
| <b>Average</b>           | 2.13      | 1.90         | 0.26       | 0.01         | 0.01   | 0.06   |
| <b>Maximum</b>           | 5.00      | 5.00         | 1.50       | 0.10         | 0.10   | 0.50   |
| <b>Minimum</b>           | 0.00      | 0.00         | 0.10       | 0.00         | 0.00   | 0.00   |
| Laminated Mudstone n=2   |           |              |            |              |        |        |
|                          | Sulphides | Arsenopyrite | Pyrrhotite | Chalcopyrite | Pyrite | Galena |
| <b>Average</b>           | 0.55      | 0.05         | 0.55       | 0.05         | 0.00   | 0.00   |
| <b>Maximum</b>           | 1.00      | 0.10         | 1.00       | 0.10         | 0.00   | 0.50   |
| <b>Minimum</b>           | 0.10      | 0.00         | 0.10       | 0.10         | 0.00   | 0.00   |

Values are rounded to two decimal places.

Table 3.10 Summary of gold, arsenic and sulphur content for all lithologies

| <b>Chloritic greywacke n=21</b>    |                 |               |              |
|------------------------------------|-----------------|---------------|--------------|
|                                    | <b>Au (ppm)</b> | <b>As (%)</b> | <b>S (%)</b> |
| <b>Average</b>                     | 0.94            | 0.55          | 0.56         |
| <b>Maximum</b>                     | 5.41            | 4.20          | 2.59         |
| <b>Minimum</b>                     | 0.01            | 0.00          | 0.01         |
| <b>(Lawley et al., 2015a) n=19</b> |                 |               |              |
|                                    | <b>Au (ppm)</b> | <b>As (%)</b> | <b>S (%)</b> |
| <b>Average</b>                     | 0.35            | 0.25          | 0.31         |
| <b>Maximum</b>                     | 4.16            | 2.99          | 1.57         |
| <b>Minimum</b>                     | 0.01            | 0.00          | 0.01         |
| <b>Oxide-silicate BIF n=15</b>     |                 |               |              |
|                                    | <b>Au (ppm)</b> | <b>As (%)</b> | <b>S (%)</b> |
| <b>Average</b>                     | 1.75            | 0.86          | 1.53         |
| <b>Maximum</b>                     | 13.30           | 12.00         | 6.71         |
| <b>Minimum</b>                     | 0.01            | 0.00          | 0.02         |
| <b>(Lawley et al., 2015a) n=7</b>  |                 |               |              |
|                                    | <b>Au (ppm)</b> | <b>As (%)</b> | <b>S (%)</b> |
| <b>Average</b>                     | 63.69           | 6.04          | 7.66         |
| <b>Maximum</b>                     | 189.00          | 11.20         | 15.80        |
| <b>Minimum</b>                     | 0.92            | 0.01          | 0.58         |
| <b>Pelitic BIF n=8</b>             |                 |               |              |
|                                    | <b>Au (ppm)</b> | <b>As (%)</b> | <b>S (%)</b> |
| <b>Average</b>                     | 2.37            | 1.22          | 1.55         |
| <b>Maximum</b>                     | 16.50           | 5.46          | 5.20         |
| <b>Minimum</b>                     | 0.01            | 0.00          | 0.03         |
| <b>(Lawley et al., 2015a) n=8</b>  |                 |               |              |
|                                    | <b>Au (ppm)</b> | <b>As (%)</b> | <b>S (%)</b> |
| <b>Average</b>                     | 8.37            | 3.12          | 2.41         |
| <b>Maximum</b>                     | 42.70           | 7.63          | 5.67         |
| <b>Minimum</b>                     | 0.01            | 0.00          | 0.18         |
| <b>Laminated mudstone n=2</b>      |                 |               |              |
|                                    | <b>Au (ppm)</b> | <b>As (%)</b> | <b>S (%)</b> |
| <b>Average</b>                     | 0.06            | 0.27          | 0.21         |
| <b>Maximum</b>                     | 0.11            | 0.54          | 0.40         |
| <b>Minimum</b>                     | 0.01            | 0.00          | 0.02         |
| <b>(Lawley et al., 2015a) n=2</b>  |                 |               |              |
|                                    | <b>Au (ppm)</b> | <b>As (%)</b> | <b>S (%)</b> |
| <b>Average</b>                     | 0.97            | 1.01          | 1.89         |
| <b>Maximum</b>                     | 1.31            | 1.66          | 2.17         |
| <b>Minimum</b>                     | 0.63            | 0.35          | 1.60         |

Values are rounded to two decimal places.

## 3.2 HYDROTHERMAL ALTERATION

This section aims at classifying the hydrothermal alteration and associated pathfinder elements associated with gold mineralization and distribution among the host lithologies.

Most host rocks of the 1150 and 1250 lode series exhibit variable degrees of hydrothermal alteration when plotted on Chlorite-Carbonate-Pyrite Index versus Hashimoto Alteration Index (Large et al., 2001, box plot diagram). Although this diagram was developed to document alteration effects on volcanic rocks in a volcanogenic massive sulphide (synvolcanic seafloor) context, some of the trends shown here provide an idea of the chemical variations that may partly be due to alteration in the Upper Oxide Formation sedimentary host rocks, even though they cannot be used here to illustrate specific processes. The chloritic greywacke and laminated mudstone samples form two very rough “trends”. The first trend follows a diagonal path from the bottom left to the top right of the plot corresponding to chlorite, pyrite, sericite trend. The second trend is diagonal from the top left to the bottom right of the plot corresponding to sericite alteration. The oxide-silicate BIF samples form one clear trend across the top of the plot corresponding to chlorite-carbonate alteration and approaching the pyrite end member to the top right of the plot (Fig. 3.5). The pelitic BIF samples plot amongst the chloritic greywacke and oxide-silicate BIF samples, indicating a combination of the alteration assemblages can correspond to the pelitic BIF samples. This is in agreement with the petrographic observations made in Chapter 2 and presented below. The main difference is the dominant sulphide mineral observed in the host-rocks studied are arsenopyrite and pyrrhotite instead of pyrite.

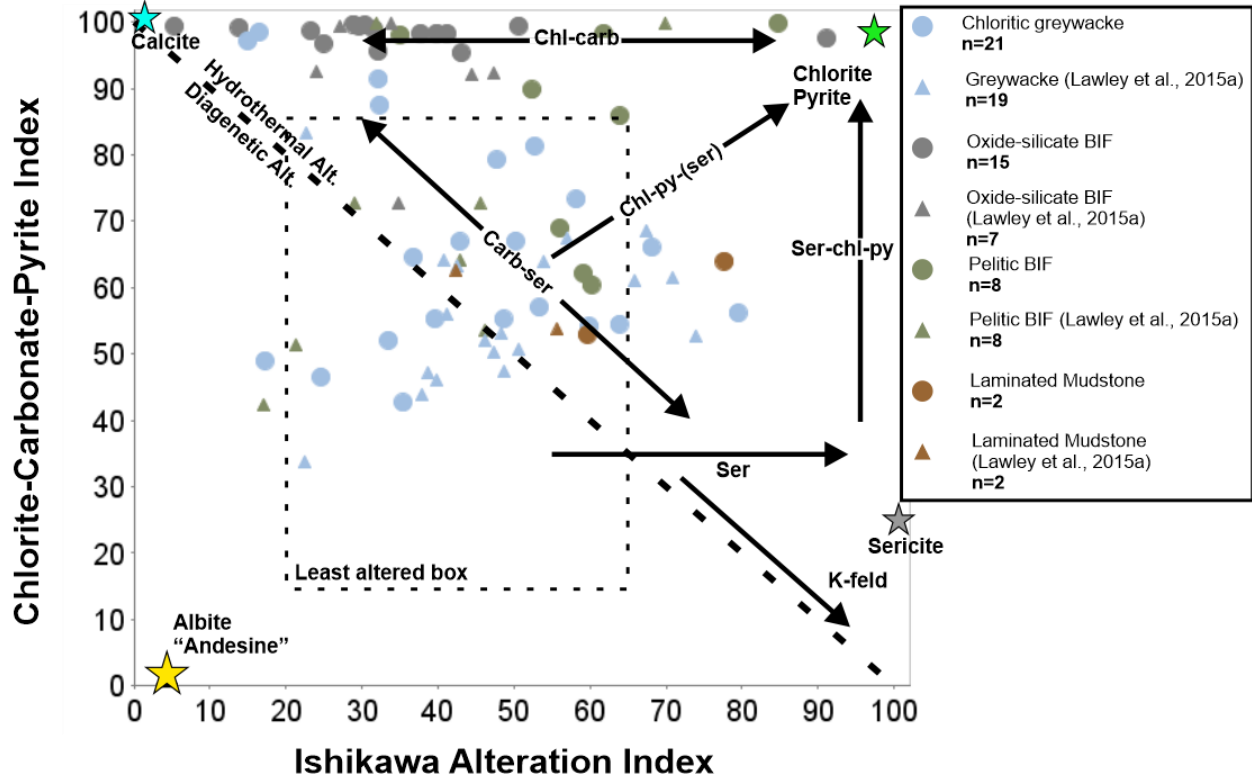
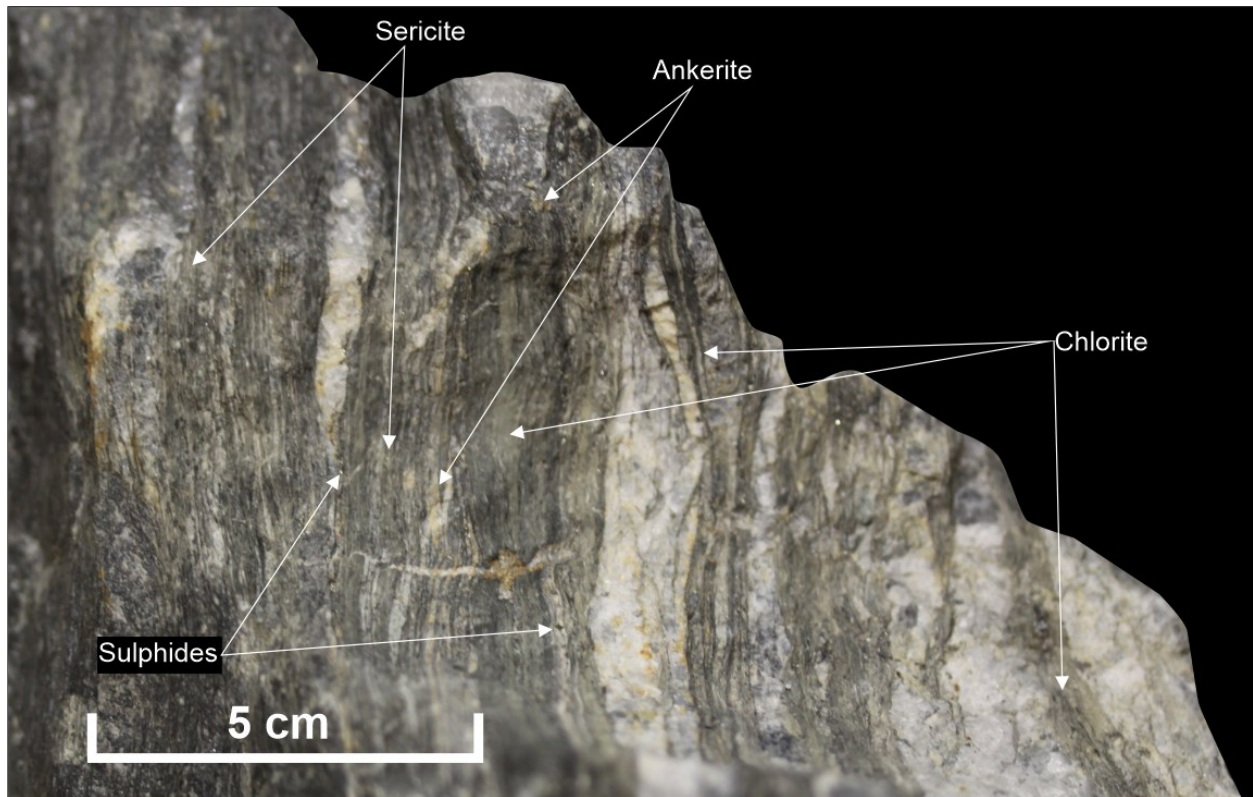


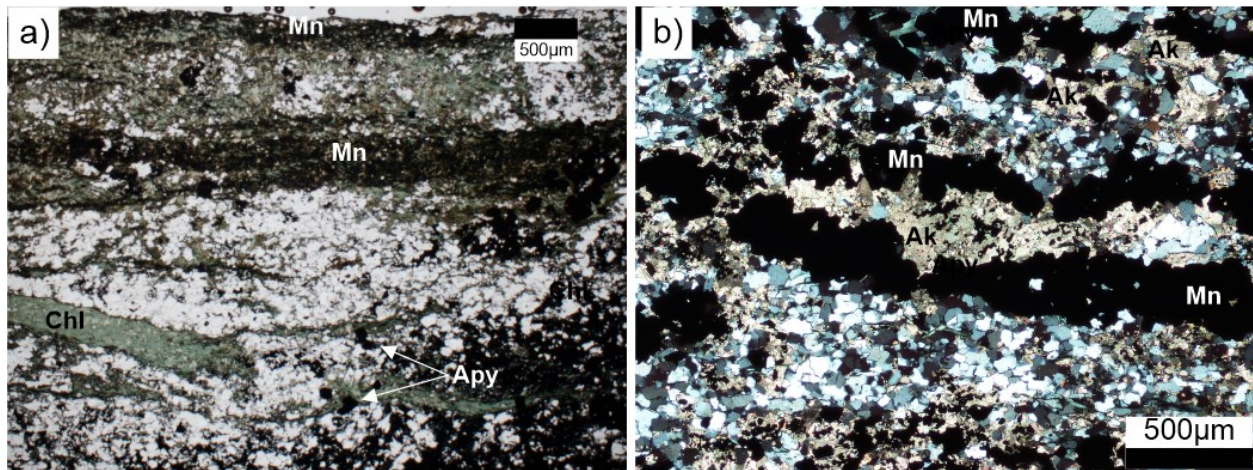
Figure 3.5 Box plot (Large et al., 2001) showing the Chlorite-Carbonate-Pyrite Index  $[100(\text{Mg} + \text{FeO})/(\text{MgO} + \text{FeO} + \text{Na}_2\text{O} + \text{K}_2\text{O})]$  versus Hashimoto Alteration Index  $[100(\text{K}_2\text{O} + \text{MgO})/(\text{K}_2\text{O} + \text{MgO} + \text{Na}_2\text{O} + \text{CaO})]$  (Ishikawa et al., 1976) of the host rocks of the 1150 and 1250 lode series, showing relative degree of alteration and general alteration mineralogy.

Overall, sericite, idiomorphic ankerite, quartz, chlorite alteration, and disseminated sulphides (mainly arsenopyrite) are widespread in the clastic sedimentary lithologies (chloritic greywacke, laminated mudstone, and portions of the pelitic BIF). However, a visual bleaching colour representing the alteration assemblage is spatially associated with high-strain zones and on the margins of quartz  $\pm$  ankerite  $\pm$  sericite  $\pm$  sulphide veins up to 10s of centimeters away from them (Fig. 3.6). Hydrothermal chlorite alteration can be distinguished from metamorphic chlorite, because it occurs as clots exclusively on the margins of or within quartz  $\pm$  ankerite  $\pm$  sericite  $\pm$  sulphide veins within high-strain zones.



**Figure 3.6** Representative hydrothermal alteration assemblage in highly strained intervals within the chloritic greywacke facies.

The Oxide-silicate BIF comprises a dominant quartz  $\pm$  chlorite  $\pm$  ankerite  $\pm$  sulphide alteration assemblage (Figs. 3.2a, b, 3.7a, b), generally spatially associated with cross-cutting quartz  $\pm$  ankerite  $\pm$  chlorite  $\pm$  sulphide veins. Hydrothermal chlorite alteration either occurs as chlorite clots or radial textured clusters within or on the margins of quartz  $\pm$  ankerite  $\pm$  chlorite  $\pm$  sulphide veins or along higher strained zones (Fig. 3.2a, b). Arsenopyrite replacement zones remain the easiest visual indicator of the gold-bearing hydrothermal alteration assemblage found in the oxide-silicate BIF facies. These replacement zones preferentially form on the margins of cross-cutting quartz  $\pm$  ankerite  $\pm$  chlorite  $\pm$  sulphide veins and extend up to 10s of centimeters away from the vein with the intensity of alteration decreasing away from the cross-cutting veins (Fig. 3.2a, b).



**Figure 3.7** a) Photomicrograph of sample TQPL2017-020A-2.5X-PPL, displaying minor arsenopyrite replacement of magnetite-rich layers in BIF, and Chlorite clots. b) Photomicrograph of sample TQPL2017-044B-5X-XPL, showing irregular disseminated ankerite alteration in a magnetite-quartz (chert)-rich portion of the oxide-silicate BIF. Abbreviations: Ak = ankerite, Apy = arsenopyrite, Chl = chlorite, Mn = magnetite.

The chondrite normalized multi-element profiles presented in chapter 2 consistently display large variations in Pb, Li, but most notably Sb. Antimony tends to display large positive anomalies within all lithologies (Figs. 2.4, 2.7, 2.10 and 2.13). The Au bi-plots in figure 3.8 display varying degrees of positive correlations with all elements except for the negative correlation with Zn. However, As, Sb, and Se seem to have the steepest positive correlations with Au.

The principal component analysis bi-plot maps display the main metal associations in alteration zones (Fig. 3.9a and b). The principal component 1 analysis bi-plot map displays a positive correlation between Au and As, as they are close to each other, and their arrows are pointed in a very similar direction (Fig. 3.9a). Au and Pb show a strong negative correlation as they are pointing in nearly the opposite direction (Fig 3.9a). The principal component 1 bi-plot map shows a rough trend of increasing gold grade concentration from the top left corner to the middle-right of the map by increasing symbol sizes, suggesting a positive correlation between increasing Au, As, and roughly Sb and a negative correlation with Pb-Te-Se-Bi (Fig. 3.9a). Figure 3.9b displays the principal component 2 bi-plot map, but only includes samples that have above 0.107 ppm Au. The principal component 2 bi-plot map displays a vague trend of increasing Au concentration from the left to the top right of the map by increasing symbol sizes. Again, Au, As, and Sb are closely associated with each other pointing in nearly the same direction and seem to be correlating with higher gold grade, whereas Pb-Te-Se-Bi are not as closely related with one another, but roughly represent a positive correlation with decreasing gold grade (Fig. 3.9b).

There seems to be two distinct temporal events, a seemingly primary Au-As-Sb signature, whereas the Pb-Te-Se-Bi suggests remobilization of some of the commonly most mobile trace metals (mostly with galena).

In general, these findings are consistent with Lawley et al. (2015c) and Gourcerol et al. (2016), which also demonstrated that the hydrothermal altered and veined rocks in the Meliadine gold district are spatially associated with anomalous pathfinder element concentrations (Au, As, Se, Te, Bi, Sb, and Ag), 10s to 100s meters adjacent to ore zones.

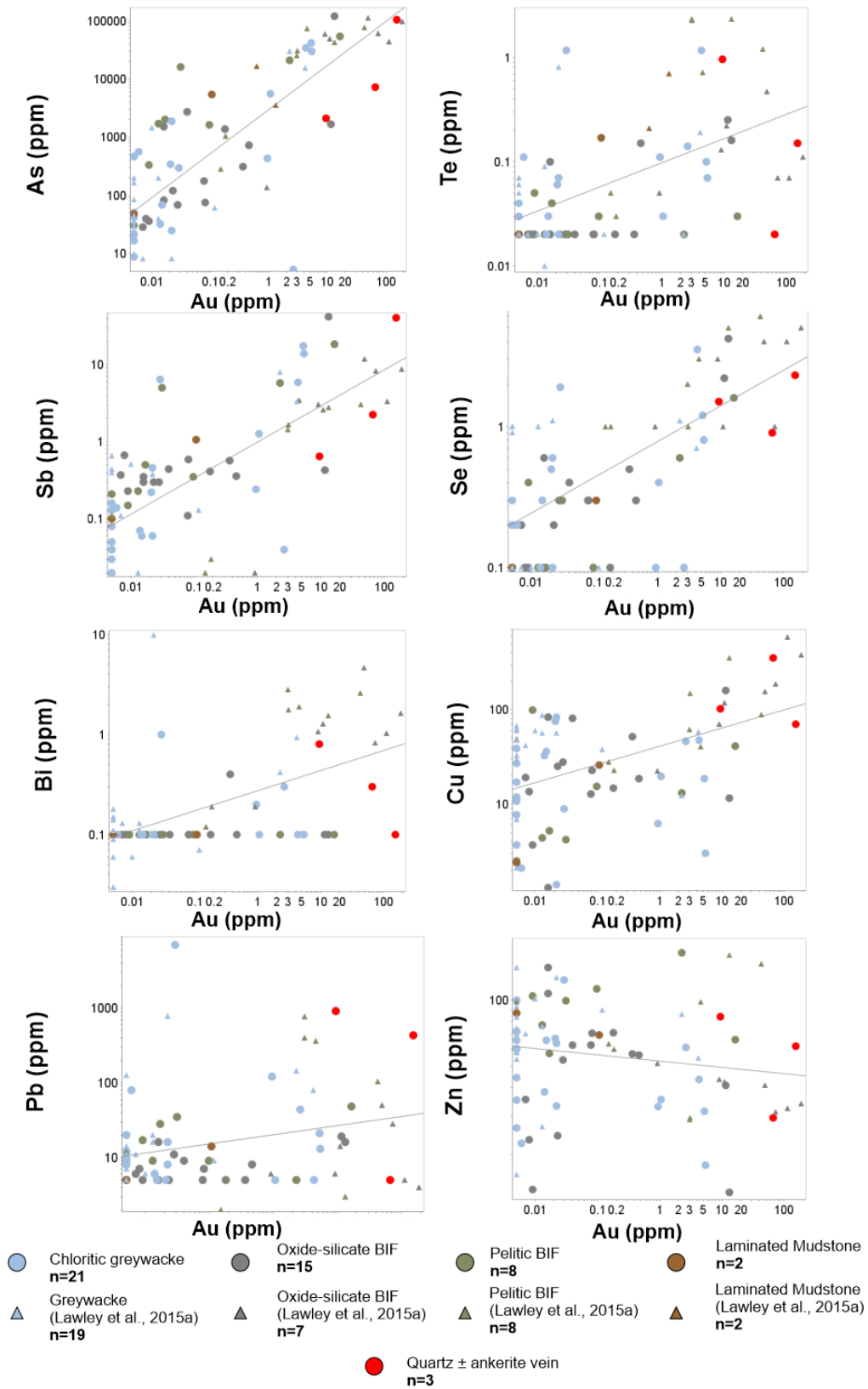


Figure 3.8 Au vs. As-Sb-Se-Bi-Cu-Pb-Zn bi-plots. Regression lines shown by grey lines represent total sample population.



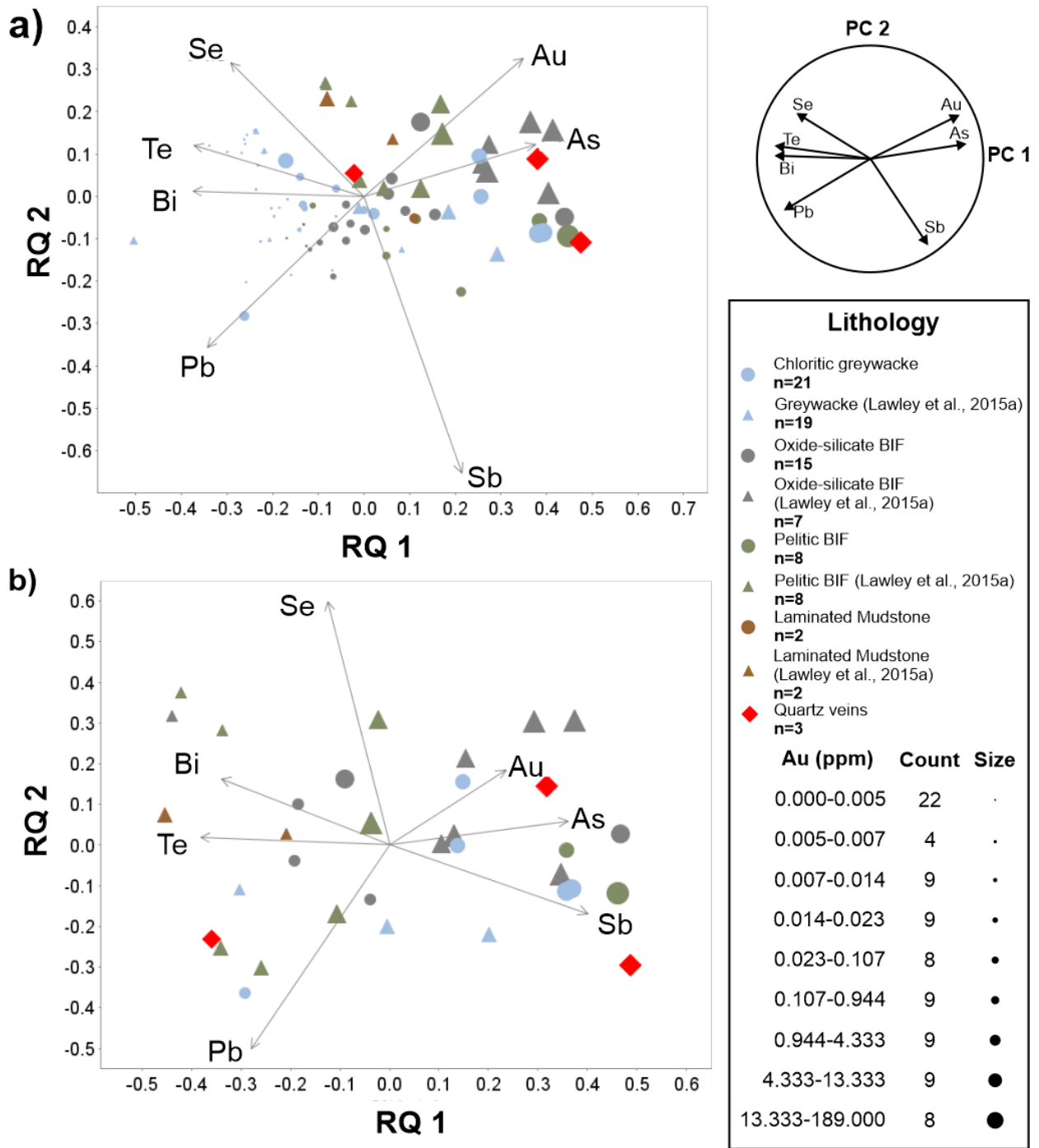


Figure 3.9 Principal component analysis bi-plot map, displaying results from principal component 1 (a) and principal component 2 (b), statistically representing 78.2% of the data. b) only includes samples with 0.107 Au ppm or greater.

## 4 STRUCTURAL ANALYSIS OF THE TIRIGANIAQ GOLD DEPOSIT

---

A detailed study of the structural controls on the mineralized veins of the Tiriganiaq deposit was recently published as part of this research project (St.Pierre et al., 2020). However, a revision of this work and supplementary data is presented here. Detailed drift-scale underground mapping, structural measurements, and interpretation of oriented thin sections will be presented in this chapter to better understand and refine the precise deposit-scale deformation history, structural style of mineralization and controls on gold mineralization within the 1150 and 1250 lodes.

### 4.1 REGIONAL STRUCTURAL GEOLOGY

The Rankin Inlet greenstone belt has undergone four phases of regional deformation (Table. 4.1) (Tella et al., 1986; Tella, 1994; Carpenter and Duke, 2004; Carpenter et al., 2005; Lawley et al., 2015a, b, c and 2016). The oldest phase of deformation ( $D_1$ ) lacks identifiable fabric, but likely represents layer parallel folding and thrusting and the initial juxtaposition of turbiditic and volcanic rock packages along an ancestral expression of what most probably now forms the Pyke Fault (Figs. 1.4 and 4.1: Carpenter and Duke, 2004; Carpenter et al., 2005; Lawley et al., 2015a,b,c, 2016). The second phase of deformation ( $D_2$ ) consisted of folding of the Archean successions by north-northeast–south-southwest shortening, which resulted in isoclinal  $F_2$  folds and a penetrative axial-planar  $S_2$  cleavage. The third phase of deformation ( $D_3$ ) consisted of a slight change of direction from northeast-southwest directed to north-south-directed shortening (Carpenter and Duke, 2004), forming Z-shaped regional scale folding pattern along the Pyke Fault and an associated locally apparent west-trending foliation. The fourth deformation ( $D_4$ ) marks an E-W oriented shortening event resulting in large NE trending open folds associated with small-scale kink bands and a locally well-developed north- to northwest-trending crenulation cleavage (Carpenter and Duke, 2004; Carpenter et al., 2005). The Rankin Inlet greenstone belt is interpreted as an east-dipping homocline that has been folded into a southeast-plunging upright  $F_2$  synform (Tella, 1994; Carpenter and Duke, 2004; Carpenter et al., 2005). At the Tiriganiaq deposit, there is one dominant foliation oriented at approximately N265/65, which has been interpreted by Miller et al. (1995) to represent the main regional  $S_2$  foliation that was transposed into a west-trending orientation during  $D_3$  deformation.

**Table 4.1 Summary of Structural Events at the Rankin Inlet Greenstone Belt**

| Phase of deformation | Description  | Associated Structures                              | Main Attitude of Fabrics           |
|----------------------|--|--|------------------------------------|
| <b>D<sub>1</sub></b> | Bedding-parallel thrusting and folding<br>Lacks identifiable cleavage<br>Initial juxtaposition of volcanic-sedimentary panels<br>Initiation of Pyke Fault and Tiriganiaq Lower Fault zone  | ?  | ?                                  |
| <b>D<sub>2</sub></b> | <b>D<sub>2A</sub></b> -Barclay (1991, 1992); Miller et al., (1995).<br><b>D<sub>2</sub></b> - Carpenter and Duke (2004), Carpenter et al. (2005).<br><br>NE–SW directed shortening<br>Bedding-parallel folding and thrusting<br>Penetrative cleavage development at 285/59N<br>Shearing along Pyke Fault and Tiriganiaq Lower Fault zone   | <b>F<sub>2A</sub></b><br><br><b>S<sub>2A</sub></b> | <b>285/59</b><br><br><b>285/59</b> |
|                      | <b>D<sub>2B</sub></b> -Barclay (1991, 1992); Miller et al., (1995).<br><b>D<sub>3</sub></b> - Carpenter and Duke (2004), Carpenter et al. (2005).<br>N–S directed shortening and localized E-W cleavage development<br>Shearing and re-activation of the Pyke Fault and Tiriganiaq Lower Fault zone<br>Development of middle Wesmeg Fault zone<br>Asymmetric Z-folding axial planar to E–W cleavage? | <b>F<sub>2B</sub></b><br><br><b>S<sub>2B</sub></b> | <b>276/52</b><br><br><b>276/52</b> |
| <b>D<sub>3</sub></b> | <b>D<sub>3</sub></b> - Barclay (1991, 1992); Miller et al., (1995).<br><b>D<sub>4</sub></b> - Carpenter and Duke (2004), Carpenter et al. (2005).<br>N–NW-trending crenulation cleavage<br>No significant disruption of earlier fabrics<br>Locally developed, tight angular NNW- and WSW- oriented kink banding<br>Well-preserved in fine-grained phyllosilicate-rich rocks                          | <b>S<sub>3</sub></b>                               | <b>325/55</b>                      |

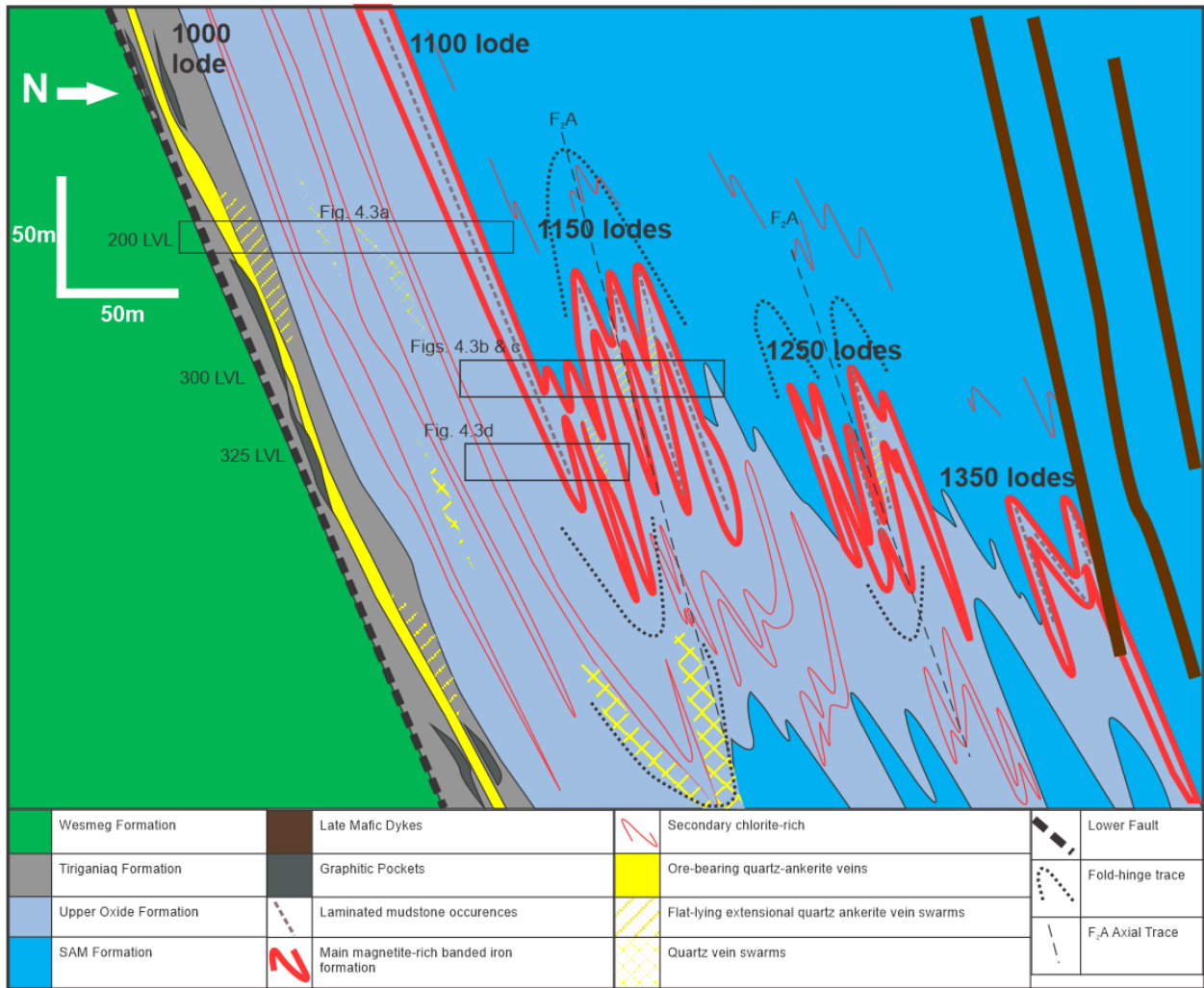
Modified and adapted from Carpenter and Duke (2004), Carpenter et al. (2005), Tella et al. (1986), Barclay (1991, 1992), Armitage et al. (1993), Balog (1993), Tella (1994), Brommecker et al. (1995), Miller et al. (1995).

## 4.2 TIRIGANIAQ STRUCTURAL GEOLOGY

At the deposit scale, three phases of deformation are recognized (Table 4.2). The earliest phase of deformation ( $D_1$ ) at Tiriganiaq, inferred from regional-scale observations, resulted in volcanic units being thrust on top of sedimentary units, likely involving layer parallel folding along the north-dipping Lower Fault. Like elsewhere in the belt,  $D_1$  lacks any identifiable fabric at Tiriganiaq. The second phase of deformation ( $D_2$ ) is a protracted compressional event that can be separated into two increments of deformation based on detailed underground observations of bedding, foliation, shear-plane development, and crosscutting relationships (St.Pierre et al., 2020). The first increment of the second phase of deformation ( $D_{2A}$ ) ( $D_2$  in Carpenter and Duke, 2004 and Carpenter et al., 2005;  $D_{2A}$  deformation in Miller et al., 1995) involved layer-parallel  $F_{2A}$  isoclinal folding of the host succession (e.g. Fig. 4.1) and the associated development of axial-planar, regionally penetrative  $S_{2A}$  foliation, as well as reverse displacements along the Pyke and Lower faults. The second increment of the second phase of deformation ( $D_{2B}$ ) ( $D_3$  in Carpenter and Duke, 2004 and Carpenter et al., 2005;  $D_{2B}$  in Miller et al., 1995) marks a slight change of shortening orientation to north-south, resulting in transpressional movement along the Lower-Fault, which locally transposed west trending  $F_{2A}$  folds creating a cryptic z-shaped pattern along the Lower Fault and associated west trending transposed  $S_{2A}$  axial planar foliation. Progressive folding was associated with more brittle-ductile deformation ( $D_{2B}$ ) until tightened folds could not accommodate further shortening. Preferential strain partitioning along fold hinges and more particularly limbs, relatively less competent units, and lithological contacts led to the development of west-trending decimetre- to metre-wide shear zones localized within chloritic-greywacke intercalated within decimetre to metre-wide transposed  $F_{2A}$  folded BIF (e.g. Figs. 4.2a, b, 4.3a, b, 4.5b-d). The  $D_{2B}$  shear planes have a slightly shallower dip than the  $S_{2A}$  foliation and dragging of the west trending  $S_{2A}$  foliation into the  $D_{2B}$  shears indicates a reverse-dextral (north-over-south) motion (Figs. 4.2a, b, 4.5b-d and 4.6a, d, f, g). Locally limbs of the transposed  $F_{2A}$  folded BIFs are transposed completely into the slightly shallower  $D_{2B}$  shear plane orientation and represent the  $S_{2B}$  foliation (Figs. 4.2a, b, 4.5b-d and 4.6a, d, f, g). The third phase of deformation ( $D_3$ ) marks an E-W oriented shortening event associated with small-scale kink bands and a locally well-developed north- to northwest-trending crenulation cleavage that overprints the transposed  $S_{2A}$  foliation and  $D_{2B}$  shear zones (Fig. 4.6b, c).

**Table 4.2 Summary of Structural Events at Tiriganiaq**

| Phase of deformation | Description   | Associated Structures   | Main Attitude of Fabrics |
|----------------------|---|---|--------------------------|
| <b>D<sub>1</sub></b> | <b>D<sub>1</sub></b> - Initial juxtaposition of mafic volcanic package on top of turbiditic sequence along ancestral north verging thrust?                            | <b>S<sub>0</sub>/S<sub>1</sub> ?</b>  | <b>?</b>                 |
| <b>D<sub>2</sub></b> | <b>D<sub>2A</sub></b> - Onset of NNE-SSW shortening resulting in layer parallel folding   | <b>S<sub>2A</sub></b> - foliation   | <b>268/65</b>            |
|                      |   | <b>F<sub>2A</sub></b> - Isoclinal folds   | <b>10/268</b>            |
|                      | <b>D<sub>2B</sub></b> - Progressive N-S shortening characterized by mixed brittle and ductile deformation   | <b>S<sub>2B</sub></b> – Locally transposed <b>S<sub>2A</sub></b> foliation parallel to D <sub>2B</sub> shear planes                     | <b>270/53</b>            |
|                      |   | <b>F<sub>2B</sub></b> – Asymmetric z-folds (transposed <b>F<sub>2A</sub></b> folds along the Pyke Fault)                                | <b>10/268</b>            |
|                      | <b>D<sub>2B</sub></b> - Shear plane development oblique to and dragging <b>S<sub>2A</sub></b> foliation indicating north over south motion within 1150 and 1250 lodes | <b>270/53</b>   |                          |
| <b>D<sub>3</sub></b> | <b>D<sub>3</sub></b> - E-W oriented shortening event  | <b>S<sub>3</sub></b> - Associated N-NW crenulation cleavage and kink bands overprinting <b>S<sub>2A</sub></b> and <b>S<sub>2B</sub></b> | <b>325/55</b>            |



**Figure 4.1** Schematic section of the Tiriganiaq deposit and its various ore zones (or “lodes”), looking west. The section shows the geometry of the different volcano-sedimentary formations, vein distribution, and the ore zone locations (From St.Pierre et al., 2020; Modified from Agnico Eagles Mines Limited, unpubl. internal reports). Abbreviation: BIF = banded iron formation.

### 4.3 DETAILED UNDERGROUND MAPPING

Approximately 75–80% of the ore at the Tiriganiaq deposit is hosted within the Upper Oxide Formation, including the 1100 lode, which is associated with the transposed long limb of a  $F_2A$  fold that affects the BIF succession (Figs. 4.1, 4.5a). Gold mineralization comprises contact-parallel and  $D_2B$  shear plane parallel quartz  $\pm$  ankerite shear veins, transposed quartz  $\pm$  ankerite extensional veins, and horizontal to shallowly south-dipping quartz  $\pm$  ankerite extension veins that are preferentially developed in BIF units. Coarse arsenopyrite and minor pyrrhotite replacement of magnetite-rich layers in BIF units often occur along the selvages of these veins (Fig. 4.2, 4.3, 4.5b–d).

Figures 4.2, 4.3 and 4.5 illustrate the main lithological and structural relationships observed in mapping the 1150 and 1250 lode series.  $D_2B$  mineralized reverse shear zones are localized within chloritic greywacke and contain mineralized quartz  $\pm$  ankerite  $\pm$  arsenopyrite  $\pm$  pyrrhotite veins along discrete anastomosing  $D_2B$  shear planes that drag the slightly steeper  $S_2A$  foliation consistently indicating a reverse (north over south) component of motion (Figs. 4.2 and 4.5b-d). Horizontal to shallowly south-dipping mineralized extensional veins, associated with the mineralized  $D_2B$  reverse shear zones, preferentially form within intercalated decimetre- to metre-wide  $F_2A$ -folded BIF (Figs. 4.3 and 4.5b-d). These horizontal to shallowly south-dipping extensional veins typically have coarse arsenopyrite and minor pyrrhotite replacement of magnetite-rich layers in BIF lithologies occurring along the selvages of these veins (Figs. 4.2, 4.3b-d).



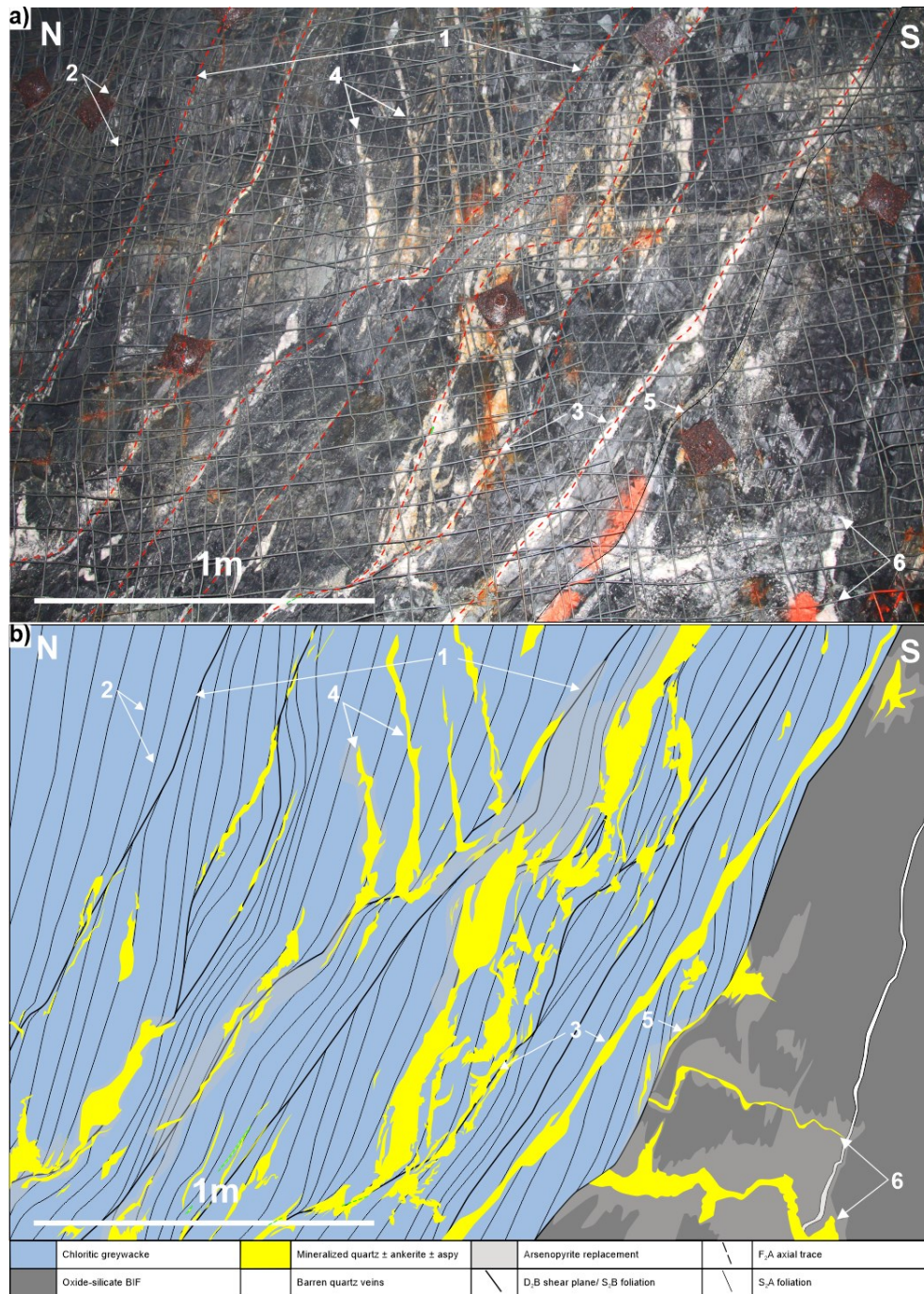
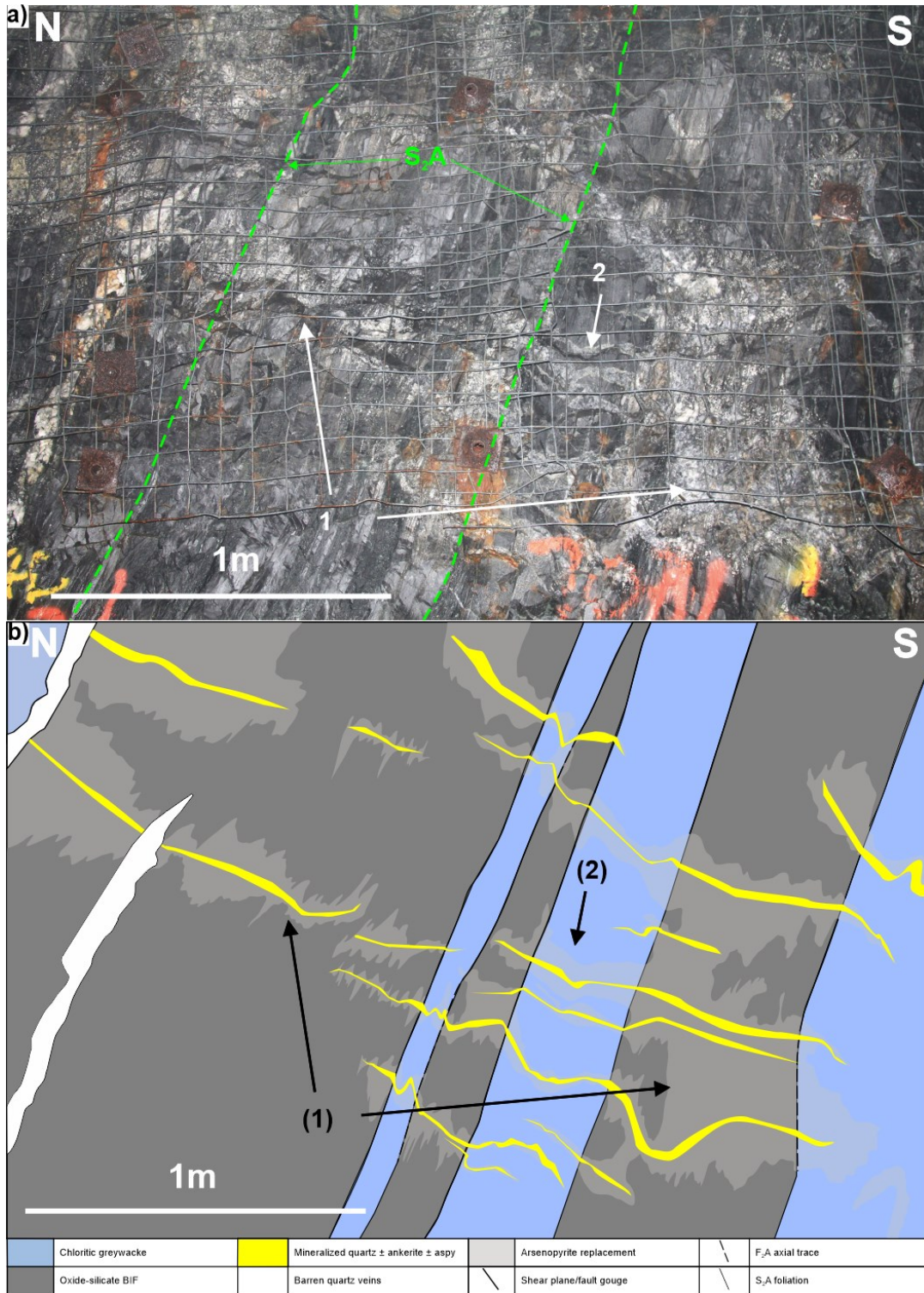


Figure 4.2

a) Photograph and associated schematic (b) of the 1150 zone in crosscut CC300-152 (East wall) showing a shear zone localized in chloritic greywacke, typical of the 1150 zone, with systematic reverse motion indicators, with discrete anastomosing shear planes (1) that are moderately dipping (north), i.e. more shallowly than the main foliation, which is dragged on the shear planes (2), indicating a reverse component of motion. Well developed quartz  $\pm$  ankerite  $\pm$  arsenopyrite shear veins (3) form along shear planes and associated extensional veins (4) are transposed up into the S<sub>2</sub>A foliation. Additionally, thin contact parallel quartz  $\pm$  ankerite shear veins (5) form at the boundary of the chloritic greywacke and BIF transposed into S<sub>2</sub>B orientation. Sub-horizontal to shallowly, south-dipping quartz  $\pm$  ankerite  $\pm$  arsenopyrite extensional veins (6), associated with the reverse shear zone, occur in BIF and form stratbound arsenopyrite replacement zones along vein margins.





**Figure 4.3** a) Photograph and associated schematic (b) of the 1150 zone in crosscut CC300-152 (East wall) showing a series of shallowly south-dipping D<sub>2</sub>B quartz ± arsenopyrite ± ankerite ± pyrrhotite veins and bedding-parallel BIF replacement (1). Veins that extend into siltstone tend to contain much less sulphide (2). Veins that cut the less competent and intensely foliated sedimentary rocks also tend to be refracted and transposed. In some cases, the BIF-hosted veins do not extend into chloritic siltstone bands. Abbreviations: BIF = banded iron formation, aspy = arsenopyrite.



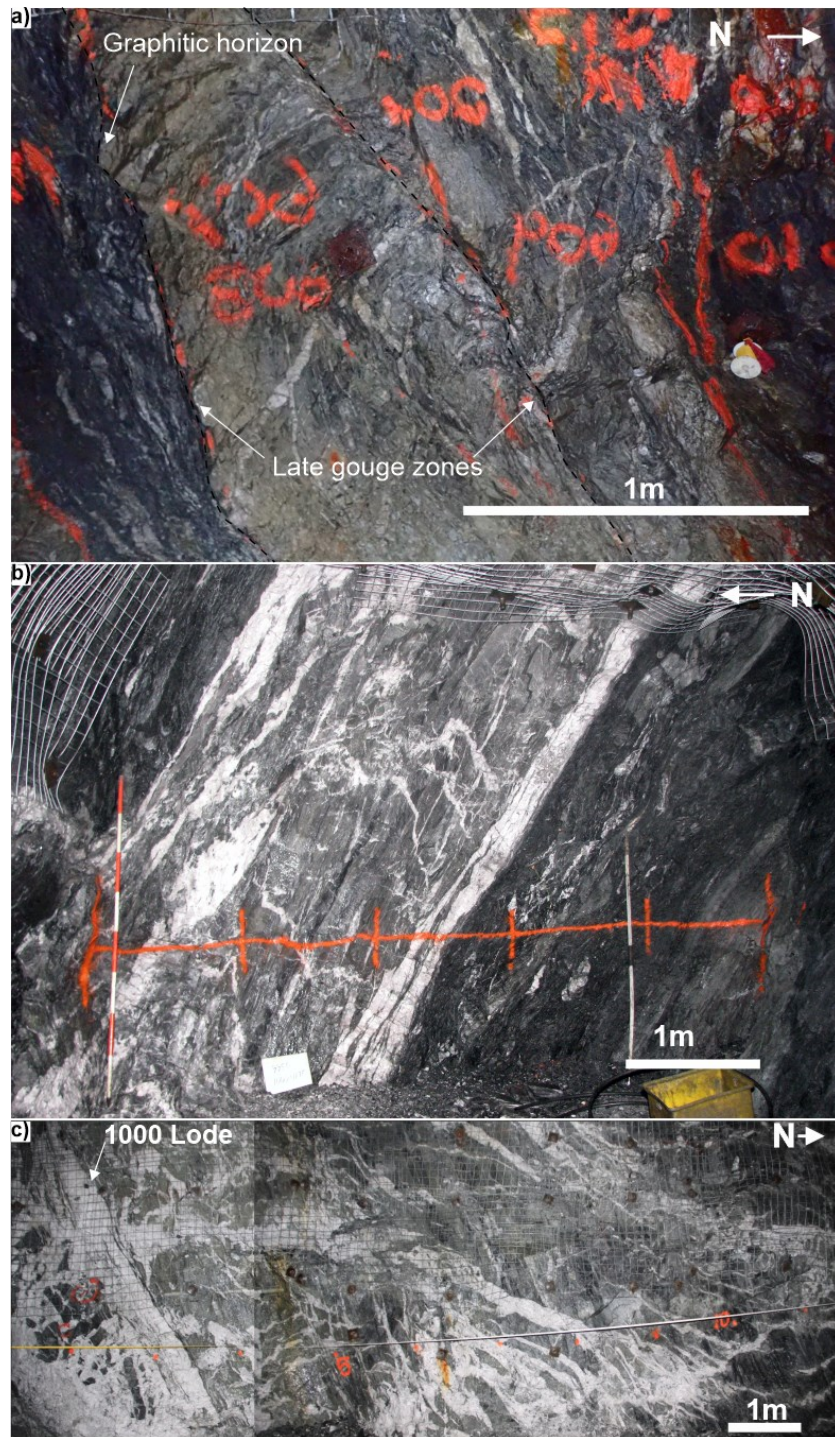


Figure 4.4

a) Photograph of the Lower Fault, looking west. The fault is characterized by overprinting fabrics and lineations with a late gouge zone. b) East wall of crosscut CC200-167 showing the shear-hosted 1000 lode main vein and the associated mineralization, alteration halo, and sulphidation. Photograph courtesy of Agnico Eagle Mines Limited. c) The West wall of crosscut CC200-157 showing the “interveining lodes” immediately north of the 1000 lode. The interveining lodes are represented by multiple generations of progressively deformed extensional vein arrays that are hosted by Tiriganiaq Formation sedimentary rocks. The extensional veins are predominantly sub-horizontal to shallowly north-dipping and are intensely transposed and folded.

#### **4.3.1 Draw-point DP200-161**

Draw-point DP200-161 (Fig. 4.5a) exposes the planar nature of the Lower Fault, the 1000 lode and the 1100 lode. The Lower Fault is parallel to the S<sub>2</sub>B foliation and D<sub>2</sub>B shear planes, which are slightly less steep than the surrounding dominant S<sub>2</sub>A foliation. The 1000 lode is defined by planar, laminated, composite quartz ± ankerite shear veins and intensely folded and transposed extensional veins spatially associated with Lower Fault (Fig. 4.5a). The 1100 lode, or ore zone, follows the planar geometry of the host stratigraphy and is further defined by contact-parallel shear veins and horizontal to shallowly south-dipping quartz ± ankerite extensional veins.

#### **4.3.2 Crosscut CC300-152**

Crosscut CC300-152 (Fig. 4.5b) exposes shear zones that are localized within chloritic siltstone, between tightly folded BIF intervals in the 1150 lodes. Quartz ± ankerite shear veins are coincident with D<sub>2</sub>B shear planes (Fig. 4.5a, b). Sub-horizontal to shallowly, south-dipping quartz ± ankerite extensional veins, associated with shear zones, occur in both the BIF and siltstone (Fig. 4.5a-d). The extensional veins are refracted in the BIF intervals and are weakly to strongly deformed in the intensely foliated siltstone. Stratabound arsenopyrite ± pyrrhotite replaces magnetite-rich layers within the BIF intervals where quartz ± ankerite vein selvages are present (Fig. 4.5a-d). These extensional veins and associated stratabound arsenopyrite ± pyrrhotite replacement zones are up to 50 centimeters thick in the BIF but generally less than 10 centimeters thick in the siltstone. In contrast, this pattern of alteration is largely absent in the siltstone intervals.

#### **4.3.3 Crosscut CC300-153**

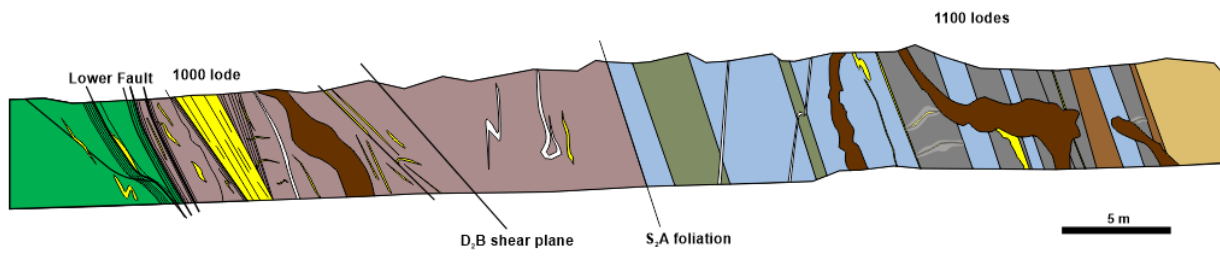
Crosscut CC300-153 (Fig. 4.5c), which is located approximately 15 meters east of crosscut CC300-152, exposes tighter folds, relative to those present in crosscut CC300-152. The 1150 lodes are well developed in this area, with shear veins that follow F<sub>2</sub>A fold limbs in BIF intervals and associated sub-horizontal to shallowly south-dipping extension veins with distinctive arsenopyrite replacement halos. The S<sub>2</sub>A foliation is axial planar to F<sub>2</sub>A folds and slightly steeper than the D<sub>2</sub>B shear zones.

#### **4.3.4 Crosscut CC325-155**

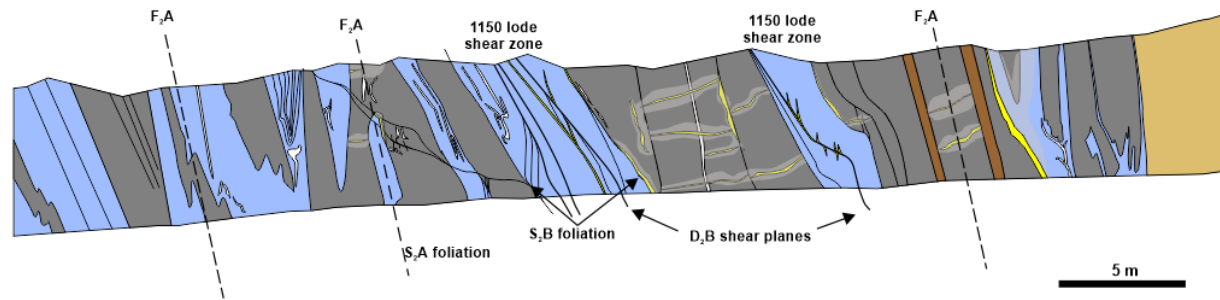
Crosscut CC325-155 (Fig. 4.5d) exposes a weakly deformed, subvertical, ore-bearing quartz ± ankerite vein with a weak sericite alteration halo that cuts BIF. Stratabound arsenopyrite and minor pyrrhotite replacement of magnetite-rich layers within the BIF are associated with the

selvages of this vein. A similar example of a subvertical partly rotated and attenuated ore-bearing quartz  $\pm$  ankerite is found in thin section, transposed up into the main D<sub>2</sub>B shear zone, in agreement with what we see at stope scale (Figs. 4.4a-b and 4.6g).

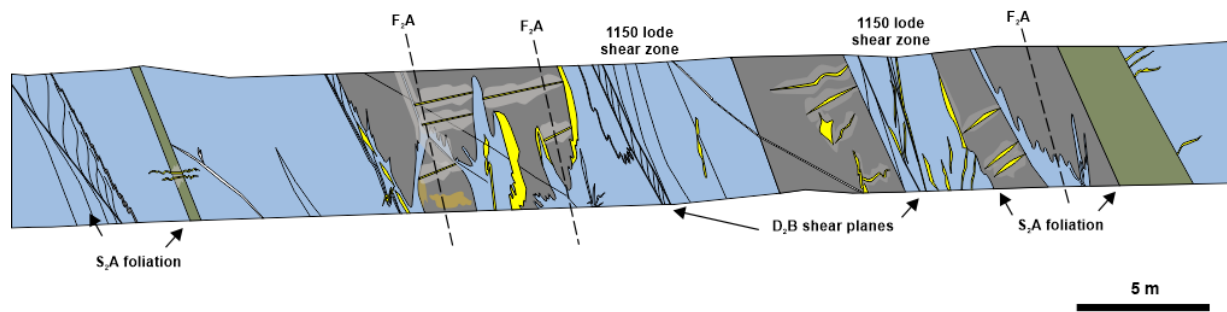
a)



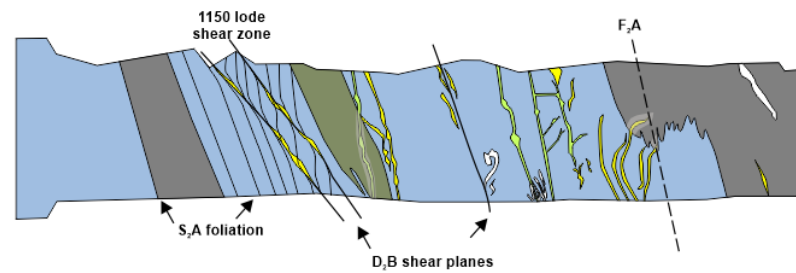
b)

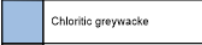
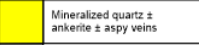
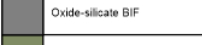
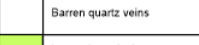
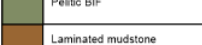
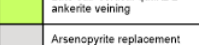
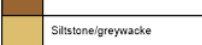
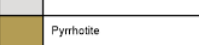
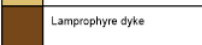

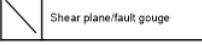


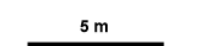


c)



d)



|   |                         |   |   |
|---|-------------------------|---|---|
|  | Chloritic greywacke     |  | Mineralized quartz ± ankerite ± aspy veins  |
|  | Oxide-silicate BIF      |  | Barren quartz veins                         |
|  | Pelitic BIF             |  | Late sub-vertical quartz ± ankerite veining |
|  | Laminated mudstone      |  | Arsenopyrite replacement                    |
|  | Siltstone/greywacke     |  | Pyrrhotite                                  |
|  | Lamprophyre dyke        |  | F, A axial trace                            |
|  | Shear plane/fault gouge |  | S, A foliation                              |

5 m

**Figure 4.5** a) Detailed geological and structural maps of the underground workings of the 1000, 1100, and 1150 lodes at the Tiriganiaq deposit. a) The West wall of draw-point DP200-161 (level 200, 200 m below surface). The section exposes the Wesmeg Formation in the structural footwall of the Lower Fault, with the 1000 lode in the hanging wall of the fault. It also shows late lamprophyre dykes that cut across folded units. Further to the north is the 1150 lode corridor that consists of F<sub>2</sub>A folded (long limbs exposed) and mineralized BIF units overprinted by moderately north-dipping D<sub>2</sub>B shears zones. b) The West wall of crosscut CC300-152 (level 300, 300 m below surface). The section shows transposed F<sub>2</sub>A folded BIF units (limbs and hinges are exposed) with narrow, weakly mineralized D<sub>2</sub>B shear veins along the limbs and shallowly south-dipping extension veins. c) The West wall of stope CC300-153, 15 m east of crosscut CC300-152. The section displays well preserved transposed F<sub>2</sub>A fold hinges and well developed D<sub>2</sub>B shear-parallel veins with localized extension veins in the BIF units. d) The West wall of crosscut CC325-155 (level 325, 325 m below surface). The section shows weakly mineralized, narrow D<sub>2</sub>B shear zones and a series of subvertical partly rotated and attenuated veins that are localized at the intersection with BIF units. Abbreviations: Ank = ankerite, Apy = arsenopyrite, BIF = banded iron formation, Qtz = quartz. From St.Pierre et al. (2020).

#### 4.4 MICROSTRUCTURAL ANALYSIS

Investigation of the oriented samples confirmed underground mapping observations and outlined additional important details regarding structure and mineralization. The oriented samples show the relationship of layer-parallel F<sub>2</sub>A isoclinal folding of S<sub>0</sub>/S<sub>1</sub> and the associated development of axial-planar, S<sub>2</sub>A foliation (Fig. 4.6e), which has now been transposed into the east-west orientation.

The oriented samples also confirmed distinct D<sub>2</sub>B shear bands cutting the main transposed S<sub>2</sub>A deposit foliation preferentially constrained to chloritic greywacke units, and better developed within phyllosilicate-rich layers (Fig. 4.6f, g). Kinematic indicators along the late shear bands are consistent with underground mapping, indicating a north over south reverse motion. In plan view thin sections also reveal distinct D<sub>2</sub>B shear bands cutting the main transposed S<sub>2</sub>A deposit foliation indicating a dextral shear sense (Fig. 4.6a).

Several euhedral arsenopyrite crystals disseminated along the transposed S<sub>2</sub>A foliation and associated shear fabrics show distinct asymmetric quartz-rich pressure fringes, many of which indicate dextral rotation in plan view (Fig. 4.6c, d). This indicates that the main deformation and its associated fabric have an oblique reverse dextral shear component, consistent with a major, syn- to late-ore, reverse component of motion in the deposit area (St.Pierre et al., 2019).

The already established transposed main deposit S<sub>2</sub>A foliation and D<sub>2</sub>B shear bands have been overprinted by the S<sub>3</sub> crenulation cleavage, which represents itself as a series of asymmetric microfolds with a Z-geometry (Fig. 4.6b, c).



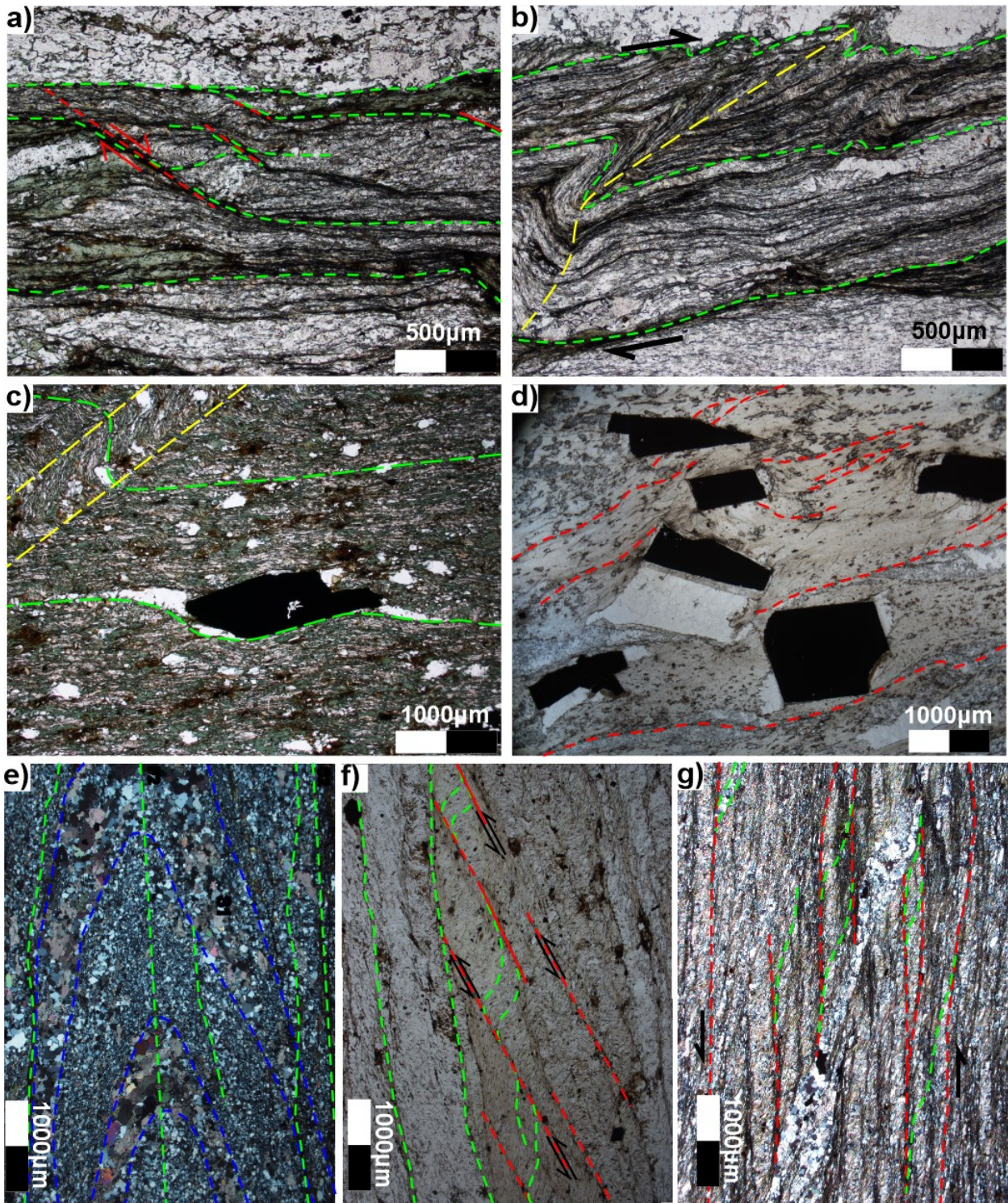




Figure 4.6 a) TQPL2017-021A-5X-PPL: Plan view of a chloritic greywacke sample displaying distinct D<sub>2</sub>B shear bands dragging S<sub>2</sub>A foliation representing a dextral shear sense; b) TQPL2017-019A-5X-PPL: Plan view of a chloritic greywacke sample displaying the transposed S<sub>2</sub>A foliation showing a series of asymmetric Z-shaped microfolds representing the S<sub>3</sub> crenulation cleavage; c) TQPL2017-028A-2.5X-PPL: Plan view of a chloritic greywacke sample displaying a euhedral arsenopyrite crystal disseminated along the transposed S<sub>2</sub>A foliation, which is locally folded by the S<sub>3</sub> crenulation cleavage, with an asymmetric quartz-rich strain fringe, displaying a dextral sense of rotation; d) TQPL2017-014A-10X-PPL: Plan view of a phyllosilicate-rich section of chloritic greywacke sample displaying distinct D<sub>2</sub>B shear bands and euhedral arsenopyrite crystals disseminated along the transposed S<sub>2</sub>A foliation, with asymmetric quartz-rich strain fringes, displaying a dextral sense of rotation; however not all arsenopyrite crystals have been rotated ; e) TQPL2017-040-2.5X-PPL: Section view (looking west) of a chloritic greywacke sample displaying layer-parallel F<sub>2</sub>A isoclinal folding of S<sub>0</sub>/S<sub>1</sub> and the associated S<sub>2</sub>A foliation ; f) TQPL2017-041B-2.5X-PPL: Section view (looking west) of chloritic greywacke sample displaying distinct D<sub>2</sub>B shear bands dragging S<sub>2</sub>A foliation representing a north over south reverse shear sense ; g) TQPL2017-025B-2.5X-PPL: Section view (looking west) of chloritic greywacke sample displaying distinct D<sub>2</sub>B shear bands dragging S<sub>2</sub>A foliation with a transposed sulphide-bearing sub-horizontal quartz ± ankerite vein.

#### 4.5 GEOMETRY OF THE 1150 AND 1250 LODE SERIES

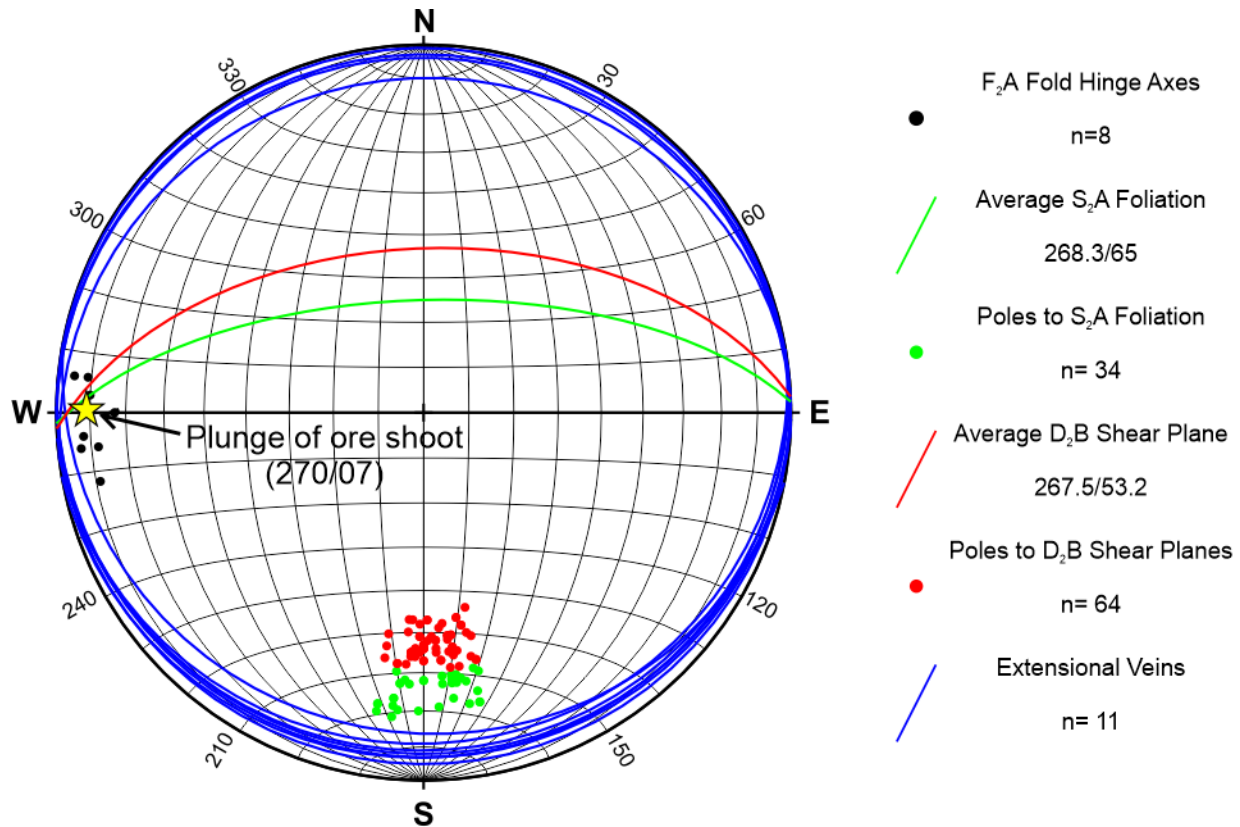
The field relationships presented in this research project document the importance of sub-horizontal to shallowly south-dipping ore-bearing D<sub>2</sub>B extensional quartz ± ankerite veins in the 1150 and 1250 lodes. The extensional veins and their associated sulphide replacement zones are preferentially developed in tightly F<sub>2</sub>A parasitic folded and transposed decimeter- to meter-thick BIF layers on both sides of the moderately north-dipping reverse shear zones localized in chloritic greywacke (Fig. 4.5b–d; St.Pierre et al., 2018, 2019, 2020). These zones provide some of the highest gold grades and thickest gold intervals within the Tiriganiaq deposit, indicating the significant control the transposed F<sub>2</sub>A fold hinges have on gold distribution.

Two high-grade ore shoot geometries have been previously recognized at Tiriganiaq (Lawley et al., 2016). The most prominent ore plunge is coaxial with the shallowly W-plunging F<sub>2</sub>A hinge zone of tightly folded BIF in the deposit hanging wall. The lesser and poorly understood moderately to steeply SE-plunging ore shoots correspond to the intersection of the Lower Fault and NE-SW-trending surfaces.

At the scale of the 1150 ore zone, the intersection of the S<sub>2</sub>A foliation and D<sub>2</sub>B shear planes with the sub-horizontal extensional veins plunge very shallowly (less than 10 degrees) to the east and west (Fig. 4.7.). The average plunge of the F<sub>2</sub>A fold hinge measurements are N268/10, and correspond with the intersection of the S<sub>2</sub>A foliation and D<sub>2</sub>B shear planes with the sub-horizontal extensional veins (Fig. 4.7). Therefore, the major high-grade ore shoot geometry corresponds with the shallow plunge, to the west, of the F<sub>2</sub>A fold-hinge and the intersection of S<sub>2</sub>A foliation,



D<sub>2</sub>B shear planes, and sub-horizontal ore-bearing extensional veins. The nature of the host lithologies (composition and rheology) also has a major effect on the distribution of gold-rich zones in lodes 1100, 1150 and 1250, which also generate geometric ore shoots, as discussed in detail in the next chapter.



**Figure 4.7** Stereonet projection of compiled underground structural measurements taken from crosscuts: CC300-152, CC300-153, and CC300-155, displaying the plunge of the ore shoot of the 1150 and 1250 lode series corresponding with the plunge of the F<sub>2</sub>A fold hinge and the intersection of S<sub>2</sub>A foliation, D<sub>2</sub>B shear planes, and sub-horizontal ore-bearing extensional veins.

## 5 SYNTHESIS, DISCUSSION, AND CONCLUSIONS

---

Exploration and previous research at Tiriganiaq in the last few decades has led to a good understanding of the main ore zones (e.g., Carpenter et al., 2004; Carpenter and Duke, 2005; Lawley et al., 2015a,b,c, 2016). The model was however challenged when underground development started, highlighting unexpected structural complexities that impacted on the recovery of gold, most notably in the partly BIF-hosted 1150 and 1250 ore zones found in the hanging wall of the main ore-bearing structure. These complexities have led to three main questions: 1) what is the precise structural history of the Tiriganiaq gold deposit?; 2) how has the layer anisotropy of the host BIFs affected the kinematics, geometry, and localization of shear zones and auriferous veins?; and 3) what is the precise timing of gold introduction relative to the deformation events at the Tiriganiaq gold deposit?

The previous chapters focused on providing key information from detailed geological underground mapping, delineation drill-cores, microstructure analysis of oriented samples, whole-rock litho-geochemistry, and data compilation, integrating the observations, results and interpretations from Agnico Eagle Mines limited and previous studies. Interpretations of the geological, structural, petrographic, geochemical, and metallogenic data are presented in this chapter to address the overarching objectives of this study: 1) establish the precise structural history of the Tiriganiaq gold deposit; 2) document the parameters that controlled the formation, distribution, and geometry of gold mineralization in the 1150 and 1250 lode series; and 3) define the precise timing of gold introduction relative to the deformation events at the Tiriganiaq gold deposit.

Data, results and interpretations of this study are summarized in section 5.1. The relative sequence of events is discussed in section 5.2. Section 5.3 compares the main characteristics of the 1150 and 1250 lode series of the Tiriganiaq deposit to other relevant BIF-hosted/associated gold deposits with the purpose of presenting the implications for exploration and mine development in the district in section 5.4. Finally, section 5.5 reviews the conclusions of this study and the outstanding questions to be addressed.

## 5.1 SYNTHESIS OF DATA, RESULTS, AND INTERPRETATIONS

### 5.1.1 1150 and 1250 Lode Series Host Rocks

The 1150 and 1250 lode series are hosted within the Upper Oxide Formation, in the structural hanging wall of the Lower Fault. The Upper Oxide Formation consists of strongly bedded and graded chloritic greywacke-siltstone-mudstone interbedded with oxide-silicate facies dominated and minor amphibolite (pelitic) BIF that have been subject to greenschist metamorphic conditions, major deformation and hydrothermal alteration.

The chemical composition of the 1150 and 1250 lode series host rocks is highly variable, demonstrating their detrital nature and suggesting that the sediments have been widely sourced from the surrounding, compositionally varied, volcanic and intrusive rocks. The finely layered nature of the clastic and chemically derived sedimentary rocks of the Upper Oxide Formation hosting the 1150 and 1250 lode series have shown distinct heterogeneity in petrographic and geochemical composition. This has been partly due to the heterogeneity of beds within units. However, major compositional and petrographic variations between and within units are due to hydrothermal alteration. Despite careful selection, most samples exhibit effects of hydrothermal alteration associated with the nearby ore zones.

### 5.1.2 Style and Distribution of Gold Mineralization and Associated Hydrothermal Footprint

Gold mineralization at the Tiriganiaq deposit is associated with BIF-hosted replacement-style mineralization, coupled with auriferous quartz  $\pm$  ankerite veins and selvages that occur as stacked, semicontinuous ore zones known locally as “*lodes*”. These veins are dominantly comprised of quartz  $\pm$  ankerite, with variable amounts of hydrothermal chlorite, iron-sulphides, and lesser amounts of biotite, magnetite and monazite. Gold is paragenetically late and, at the micro-scale, occurs within low-strain microtextural sites and clusters of inclusions within variably recrystallized and idioblastic arsenopyrite crystals.

On average, the oxide-silicate BIF is enriched in pyrrhotite, and total sulphides compared to all other lithologies. The petrography data shows the oxide-silicate BIF to be relatively depleted in arsenopyrite compared to the pelitic BIF and chloritic greywacke. However, this is not consistent with other field observations that show arsenopyrite to preferentially form stratabound replacement zones along magnetite-rich layers in the oxide-silicate BIF. This is a factor of a small sample size and sample location of the selected thin sections.

The oxide-silicate BIF is variably endowed in Au (0.01-13.3 ppm), As (0.003-12 wt. %) and S (0.02-6.71 wt. %). By comparison, the oxide-silicate BIF is enriched in Au, As, and S compared to the chloritic greywacke and laminated mudstone but depleted relative to the pelitic BIF. Although, three samples taken of quartz  $\pm$  ankerite veins hosted within oxide-silicate BIF display enriched values of Au, As, and S compared to all lithologies. Additionally, the oxide-silicate BIF samples reported in Lawley et al. (2015a) are enriched in Au, As, and S compared to all other lithologies.

Most host rocks of the 1150 and 1250 lode series exhibit variable degrees of hydrothermal alteration, and the lithologies display distinct alteration assemblages. Overall, sericite, idioblastic ankerite, quartz, chlorite alteration, and disseminated sulphides (mainly arsenopyrite) are widespread in the clastic sedimentary lithologies (chloritic greywacke, laminated mudstone and portions of the pelitic BIF) (Fig. 3.6). Whereas, the oxide-silicate BIF and portions of the pelitic BIF comprise a dominant quartz  $\pm$  chlorite  $\pm$  ankerite  $\pm$  sulphide alteration assemblage (Figs. 3.2a, b, 3.7a, b), generally spatially associated with cross-cutting quartz  $\pm$  ankerite  $\pm$  chlorite  $\pm$  sulphide veins. These trends are represented when samples are plotted on the Chlorite-Carbonate-Pyrite Index versus Hashimoto Alteration Index (Large et al., 2001, “box plot” diagram; Fig. 3.5).

The chondrite normalized multi-element profiles presented in chapter 2 consistently display large variations in Pb, Li, but most notably Sb. Antimony tends to display large positive anomalies within all lithologies (Figs. 2.4, 2.7, 2.10 and 2.13). The Au bi-plots in figure 3.5 display varying degrees of positive correlations with all elements except for the negative correlation with Zn. However, As, Sb, and Se seem to have the steepest positive correlations with Au.

The principal component analysis bi-plot maps display the main metal associations in alteration zones (Fig. 3.9a, b). There seems to be two distinct temporal events, a seemingly primary Au-As-Sb signature, and a Pb-Te-Se-Bi remobilization of some of the trace metals (mostly with galena). These findings are consistent with Lawley et al. (2015c) and Gourcerol et al. (2016), who also demonstrated that the hydrothermal altered and veined rocks in the Meliadine district are spatially associated with anomalous pathfinder element concentrations (Au-As-Se-Te-Bi-Sb-Ag) 10s to 100s meters adjacent to ore zones.

### 5.1.3 Structural Analysis of the 1150 and 1250 Lode Series

At the deposit scale, three phases of deformation are recognized. The earliest phase of deformation ( $D_1$ ) at Tiriganiaq, inferred from regional-scale observations, resulted in volcanic units being thrust on top of sedimentary units likely involving layer parallel folding along the north-dipping Lower Fault. Like elsewhere in the belt,  $D_1$  lacks any identifiable fabric.

The second phase of deformation ( $D_2$ ) is a protracted compressional event that can be separated into two increments of deformation based on detailed underground observations of bedding, foliation, shear-plane development, and crosscutting relationships (St.Pierre et al., 2020). In this model,  $D_2$  deformation starts with northeast-southwest shortening ( $D_{2A}$ ) and a phase of layer parallel  $F_{2A}$  isoclinal folding of the host successions and associated development of axial-planar and regionally penetrative  $S_{2A}$  foliation. This was followed by, or transitioned to, a slight change in shortening orientation to north-south ( $D_{2B}$ ) creating east-west regional cryptic asymmetric Z-folds (locally transposed  $F_{2A}$  folds) and associated transposed  $S_{2A}$  foliation. Progressive folding was associated with more brittle-ductile deformation ( $D_{2B}$ ) until tightened folds could not accommodate further shortening. Preferential strain partitioning along fold hinges and more particularly limbs, relatively less competent units, and lithological contacts led to the development of reverse shear zones. Ore-bearing shear veins were emplaced along  $D_{2B}$  shear planes that dragged the  $S_{2A}$  foliation. Mineralized shear zones and associated extensional veins were therefore emplaced during the  $D_{2B}$  increment of  $D_2$  deformation.

Horizontal to shallowly south-dipping extensional veins are preferentially developed in transposed tightly  $F_{2A}$  folded decimetre- to metre-thick BIF layers on both sides of the moderately north-dipping reverse shear zones localized within chloritic greywacke. Kinematic indicators within the late ( $D_{2B}$ ) shear planes are consistent with dextral shearing localized within the chloritic greywacke. This indicates that the second increment of the main deformation ( $D_{2B}$ ) and its associated ( $D_{2B}$ ) shear zones have an oblique reverse dextral shear component, consistent with a major, syn-ore, reverse component of motion in the deposit area (St.Pierre et al., 2019, 2020).

$D_3$  deformation marks an E-W oriented shortening event causing large regional open folds ( $D_4$  in Carpenter and Duke, 2004 and Carpenter et al., 2005;  $D_3$  in Miller et al., 1995) resulting in local  $S_3$  crenulation cleavage and associated kink bands at deposit scale that overprint the  $S_{2A}$  foliation and  $D_{2B}$  shear zones. No significant disruption of earlier fabrics or mineralization are attributed to the  $D_3$  event.

The field relationships presented in this research project document the importance of sub-horizontal to shallowly south-dipping ore-bearing D<sub>2</sub>B extensional quartz ± ankerite veins. The extensional veins and their associated sulphide replacement zones are preferentially developed in tightly F<sub>2</sub>A parasitic folded and transposed, decimetre- to metre-thick BIF layers on both sides of the moderately north-dipping reverse shear zones in chloritic greywacke (Fig. 4.3b–d; St.Pierre et al., 2018, 2019, 2020). These zones provide some of the highest gold grades and thickest gold intervals within the Tiriganiaq deposit, indicating the significant control the F<sub>2</sub>A fold hinges have on gold distribution.

Two high-grade ore shoot trends have been previously recognized at Tiriganiaq (Lawley et al., 2016). The most prominent ore plunge is coaxial with the W-plunging F<sub>2</sub>A hinge zone of tightly folded BIF in the deposit hanging wall. The lesser and poorly understood SE-plunging ore shoots, likely correspond to the intersection of the Lower Fault and NE-SW-trending surfaces, such as the regional S<sub>2</sub>A foliation.

At the scale of the 1150 and 1250 lode series, the intersection of the transposed S<sub>2</sub>A foliation and D<sub>2</sub>B shear planes with the sub-horizontal extensional veins plunges very shallowly (less than 10 degrees) to the east and west (Fig. 4.5.). The average plunge of the F<sub>2</sub>A fold hinge measurements are N268/10, and correspond with the intersection of the S<sub>2</sub>A foliation and D<sub>2</sub>B shear planes with the sub-horizontal extensional veins (Fig. 4.5). Therefore, the major high-grade ore shoot geometry corresponds with the shallow plunge, to the west, of the F<sub>2</sub>A fold-hinge and the intersection of the transposed S<sub>2</sub>A foliation, D<sub>2</sub>B shear planes, and sub-horizontal ore-bearing extensional veins. The nature of the host lithologies (composition and rheology) also has a major effect on the distribution of gold-rich zones in lodes 1100, 1150 and 1250, which also generates geometric ore shoots.

## 5.2 SEQUENCE OF EVENTS

Gold mineralization at the Tiriganiaq deposit has previously been attributed to reworking and metamorphism during the Trans-Hudson Orogeny (1900–1800 Ma: Carpenter and Duke, 2004; Carpenter et al., 2005; Lawley et al., 2015 a, b, c, 2016). Reworking and metamorphism during the Trans-Hudson Orogeny has been previously attributed to D<sub>2</sub>-D<sub>4</sub> deformation (D<sub>2</sub> and D<sub>3</sub> in this study).

The best evidence for an early, pre-1900 Ma phase of deformation (D<sub>1</sub>) comes from pre-F<sub>2</sub> mineral lineations, and stratigraphic and structural facing reversals within the upper volcanic cycle (Tella et al., 1986; Tella, 1994; Carpenter and Duke, 2004; Carpenter et al., 2005). However, this potentially early event can be constrained by a D<sub>2</sub>-deformed Paleoproterozoic conglomeratic unit (<2155 Ma; Davis et al., 2008) at the base of the Upper Volcanic assemblage. Additionally, Re-Os arsenopyrite model ages that range from 2270 to 1800 Ma provide evidence for a formerly unrecognized, pre-Trans-Hudson hydrothermal event(s) (Lawley et al., 2015b). Although this range of Re-Os ages may reflect isotopic disturbance and samples that yielded the oldest ages were gold-poor, a pre-1860 Ma gold-bearing hydrothermal event(s) is now considered likely (Lawley et al., 2015b; Mercier-Langevin et al., 2018).

The interpretation of a late gold event (syn- to late D<sub>2</sub>B in Carpenter et al., 2005) drove exploration models for many years in the Meliadine district, based, in large part, on previously reported 1854 ± 6 Ma Pb-Pb monazite ages that were inferred to date the introduction of gold (Carpenter and Duke, 2004; Carpenter et al., 2005). Carpenter et al. (2005) documented weakly deformed quartz ± ankerite veins that crosscut the S<sub>2</sub>A foliation and the importance of relatively late (D<sub>2</sub>B) shear zone development and associated reactivation of the S<sub>2</sub>A foliation as further support for a late gold event. Idioblastic arsenopyrite crystals, which represent a good gold indicator and share a close spatial relationship to high-grade gold ore, were interpreted to postdate the S<sub>2</sub>A foliation at Tiriganiaq (Carpenter et al., 2005). Consequently, gold exploration focused on late D<sub>2</sub>B structures (Z folds and W-trending shear zones) that transect the regional S<sub>2</sub>A (NW-trending) foliation trend. Earlier F<sub>2</sub>A folds and other D<sub>2</sub>A structures were thought to be separate and predate gold and therefore were considered not to be prospective.

Lawley et al. (2015 a, b, c, 2016) documented slightly different relationships between quartz veining and deformation. For example, they noted that the main 1000 lode quartz ± ankerite vein system is locally folded, boudinaged, and transposed parallel to the transposed S<sub>2</sub>A foliation (Lawley et al., 2015b). They also noted that randomly oriented and idioblastic arsenopyrite crystals are concentrated within the selvages of these deformed veins, but at the microscale are

commonly wrapped by the main  $S_2A$  foliation and possess strain fringes. These field relationships imply that quartz  $\pm$  ankerite veining and sulphides predate or are synchronous with the main deposit  $S_2A$  foliation at Tiriganiaq.

In fact, in both cases, these observations are for the most part accurate. New underground and microstructural observations presented in this study demonstrate that the more geometrically and structurally complex 1150 and 1250 lode series, which are located in the structural hanging wall of the 1000 lode, are controlled by narrow, north-dipping,  $D_2B$  mineralized reverse shear zones localized within chloritic greywacke. The 1150 and 1250 lodes contain mineralized quartz  $\pm$  ankerite veins along  $D_2B$  shear planes that drag the  $S_2A$  foliation. Horizontal to shallowly south-dipping extensional veins, associated with the shear zones and related fault-fill veins, are preferentially developed in tightly folded decimetre- to metre-thick magnetite-rich BIF layers around the moderately north-dipping oblique reverse dextral shear zones. These and other underground observations, which are developed at different scales, all agree with a major syn-ore incremental compressional – minor transpressional deformation event ( $D_2$ ).

In this model,  $D_2$  deformation likely starts with northeast-southwest shortening ( $D_2A$ ) and a phase of layer parallel  $F_2A$  isoclinal folding of the host successions and associated development of axial-planar and regionally penetrative  $S_2A$  cleavage (Fig. 5.1). Thrusting and mineralized veining along the Pyke and Lower faults likely started at the onset of the  $D_2$  deformation event (i.e.  $D_2A$ ), as suggested in Miller et al. (1995). This was followed by, or transitioned to, a slight change in shortening orientation to north-south ( $D_2B$ ). This created east-west regional cryptic asymmetric Z-folds (locally transposed  $F_2A$  folds) and locally axial planar composite  $S_2A/S_2B$  foliation. The timing and slight change in the orientation of the shortening axis and associated localized shearing may have been influenced by: 1) the geometry of the Pyke-Fault during progressive deformation due to strain partitioning and regional-scale competency contrasts between metasedimentary/ volcanic/ volcanoclastic vs. rigid felsic plutons; or 2) the emplacement of intrusions such as the  $1856 \pm 10$  Ma Peter Lake monzogranite (Van Breemen et al., 2005; Berman et al., 2007), and/or a combination of the two. Progressive folding was associated with more brittle-ductile deformation ( $D_2B$ ) until tightened folds could not accommodate further shortening. Preferential strain partitioning along fold hinges and more particularly limbs, relatively less competent units, and lithological contacts led to the development of  $D_2B$  reverse dextral shear zones. Ore-bearing shear veins were emplaced along  $D_2B$  shear planes that dragged the  $S_2A$  foliation. Mineralized shear zones and associated extensional veins were therefore emplaced during the  $D_2B$  deformation phase (Fig. 5.1).



Regionally, the evolution of formation and interplay between D<sub>2</sub>A and D<sub>2</sub>B foliations remains up for debate. However, it is evident that strain has been distributed unevenly throughout the Rankin Inlet greenstone belt due to the anisotropic and heterogeneous nature of the belt. This is a primary function of pre-deformational anisotropy and/or competency contrasts of the rocks (Rigid felsic plutons, and anisotropic BIFs vs. surrounding metasedimentary/volcanic/volcaniclastic rocks) and secondarily of structures that form during deformation, i.e. the Pyke Fault. In particular, once a weak fault or shear zone forms it continues to localize the simple shear component while the surrounding more competent rock volume preferentially accommodates coaxial components of the deformation (Fossen., 2010). Therefore it is also possible that the D<sub>2</sub> deformation is a progressive north-south shortening event where F<sub>2</sub>A isoclinal folding and associated axial-planar regionally penetrative S<sub>2</sub>A cleavage was initially oriented east-west. This transitioned to the Pyke Fault progressively changing orientation to NW-SE, transposing the S<sub>2</sub>A foliation along it, and forming the locally apparent oblique (E-W) S<sub>2</sub>B (S<sub>3</sub> in Carpenter and Duke, 2004 and Carpenter et al., 2005; S<sub>2</sub>B in Miller et al., 1995) foliation in segments transposed in an NW-SE orientation. This is in response to the Pyke Fault progressively localizing shearing and mimicking the boundaries of the surrounding more competent large-scale rigid felsic intrusions. This progressive event caused the cryptic F<sub>2</sub>B asymmetric Z-folding along the Pyke Fault during the progressive D<sub>2</sub>B shortening (Fig. 5.2).

The Peter Lake monzogranite is the only known felsic intrusive rock at Meliadine that has not obviously been affected by regional metamorphism or structural overprinting. However, Van Breemen et al. (2005) described an exposure of this monzogranite as medium-grained, equigranular with a faint relict foliation defined by aligned biotite. He however did not indicate the orientation of that faint fabric, but it could potentially be linked to late D<sub>2</sub>B shortening. A highly discordant upper intercept U-Pb zircon age of  $2395.2 \pm 4.4$  Ma is reported in Carpenter et al. (2005) for this intrusion. Additionally, a Pb-Pb age of  $2676 \pm 10$  Ma was obtained by Van Breemen et al. (2005). Both ages are not believed to be igneous crystallization ages because they have a zero probability of fit on the Concordia diagrams, and the analyzed zircons have variable morphologies, U concentrations, and Th/U ratios. These ages are instead considered inherited, which is rather characteristic of the volcanic belt into which the granite was emplaced. The weighted mean of the two Proterozoic <sup>207</sup>Pb/<sup>206</sup>Pb ages at  $1856 \pm 10$  Ma is however interpreted to represent igneous crystallization of the intrusion, because of the zircon overgrowth morphology, low Th/U ratios, and mineralogical and textural similarities with other ca. 1830 Hudsonian monzonite intrusions (Peterson and Van Breemen., 1999; Peterson et al., 2000, 2002; Van Breemen et al., 2005). As indicated above, the emplacement of this granite body could have

played a key role in the timing and change in orientation of the developing penetrative fabrics and localized shearing transitioning from D<sub>2</sub>A to D<sub>2</sub>B deformation.

D<sub>3</sub> deformation marks an E-W oriented shortening event causing large regional open folds (D<sub>4</sub> in Carpenter and Duke 2004 and Carpenter et al., 2005; D<sub>3</sub> in Miller et al., 1995) resulting in local S<sub>3</sub> crenulation cleavage and associated kink bands at deposit scale that overprint the S<sub>2</sub>A foliation and D<sub>2</sub>B shear zones. No significant disruption of earlier fabrics or mineralization are attributed to the D<sub>3</sub> event. The D<sub>3</sub> event can be constrained by the lower limit of gold mineralization at ca. 1850 Ma and by undeformed 1830 Ma lamprophyre dykes (Lawley et al., 2016).

Therefore, D<sub>2</sub> deformation can be constrained by the onset of the regional Trans-Hudsonian metamorphic event at ca. 1900–1850 Ma and by the onset of the D<sub>3</sub> deformation ca. 1850 Ma. Gold emplacement can be constrained further with U-Pb xenotime results that yield an upper intercept concordia age at  $1862 \pm 29$  Ma on mineralized veins (Lawley et al., 2015b). This agrees with a  $^{207}\text{Pb}/^{206}\text{Pb}$  monazite age of  $1854 \pm 6$  Ma (Carpenter et al., 2005). Additionally, Re-Os dating suggests that ore-associated arsenopyrite-galena-ilmenite phases locally formed at  $\geq 1860$  Ma (Lawley et al., 2015a, b) (Fig. 5.3).

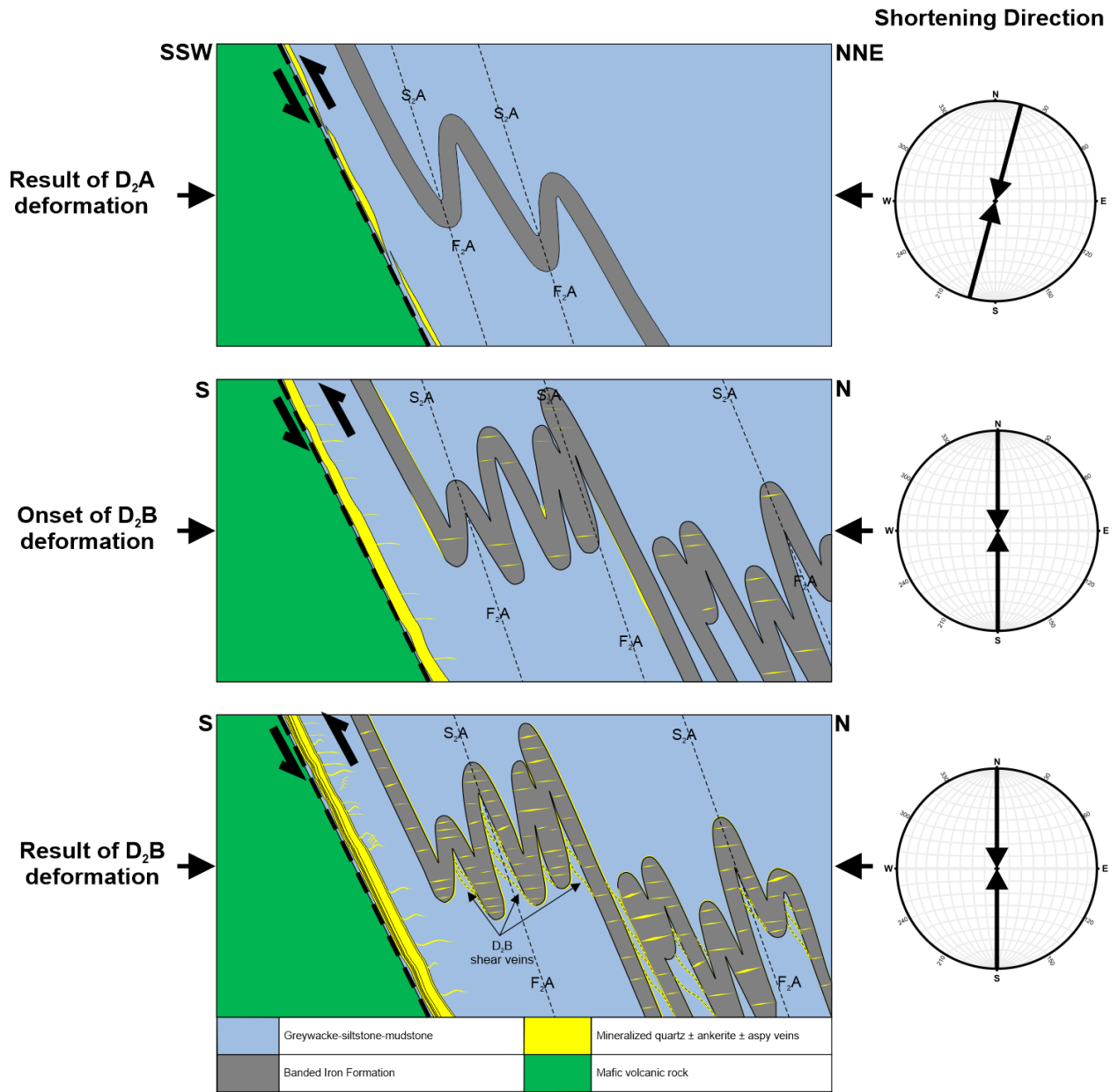
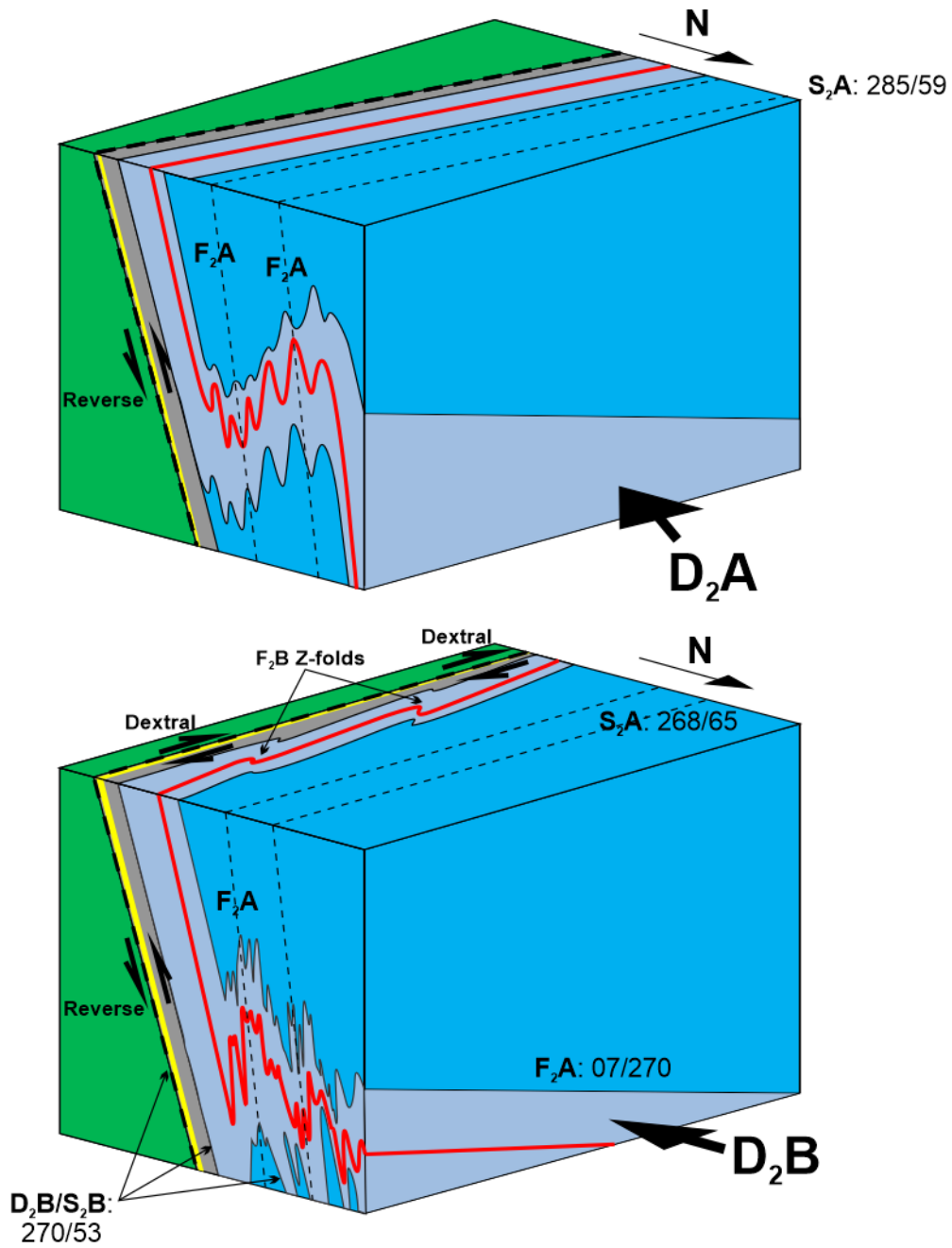
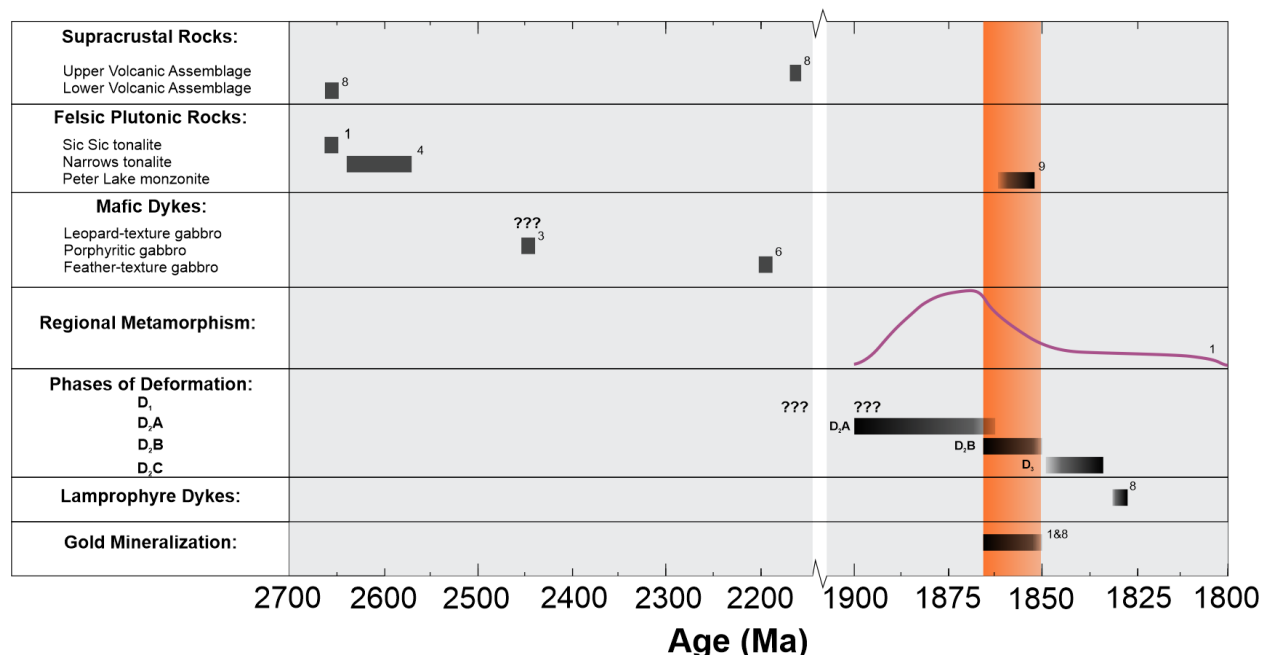


Figure 5.1 Schematic diagram of the relative timing of events and structural features at Tiriganiaq in cross-section view looking west.



|  |                       |       |                                   |
|--|-----------------------|-------|-----------------------------------|
|  | Wesmeg Formation      | ↻     | Main magnetite-rich banded iron   |
|  | Tiriganiaq Formation  |       | Ore-bearing quartz-ankerite veins |
|  | Upper Oxide Formation | - - - | F <sub>2</sub> A Axial Trace      |
|  | SAM Formation         | / \   | Lower Fault                       |

Figure 5.2 Schematic diagram of the orientation of the Pyke Fault during D<sub>2</sub> deformation



**Figure 5.3** Summary of relative and absolute timing of geological events that affected the Meliadine gold district. Isotopic age constraints :1) Carpenter et al. (2003), 2) Tella et al. (1996), 3) Heaman (1994), 4) Davis et al. (2000), 5) Peterson et al. (2002), 6) Sandeman et al. (2000b), 7) Roddick and Miller (1994), 8) Lawley et al. (2016) and 9) Van Breemen et al. (2005). Figure modified from Carpenter et al. (2003).

## 5.3 COMPARISON WITH OTHER BIF-ASSOCIATED GOLD DEPOSITS

### 5.3.1 Other ore zones in the Tiriganiaq deposit

The 1000 lode is a composite laminated quartz ± ankerite shear vein up to four meters wide (Fig. 4.4b, c) spatially associated with the Lower Fault. The 1000 lode is hosted in the Tiriganiaq Formation, classified as a strongly bedded siltstone succession that transitions to a graphitic argillite lithology towards the faulted contact with the volcanic-dominated structural footwall of the Wesmeg Formation (Lawley et al., 2015a and c). The Tiriganiaq Formation can be distinguished from the Upper Oxide Formation, which hosts the 1150 and 1250 lode series, because it contains much less iron, and therefore, much less chlorite, disseminated magnetite, and no interbedded BIFs. However, the dominant alteration assemblage found on the margins of the 1000 lode vein is similar with a sericite, ankerite, chlorite, and disseminated sulphides-dominated assemblage that is constrained in the chloritic greywacke along the margin of quartz ± ankerite veins and high-strain zones of the 1150 and 1250 lode series. Comparatively, the 1000 lode is much more planar than the geometrically complex 1150 and 1250 lode series and mimics the planar nature of the Lower Fault. However, just like the 1150 and 1250 lode series, the 1000 lode and associated

zones of deformed, horizontal to shallowly north-dipping auriferous quartz  $\pm$  ankerite extensional veins display horizontal vein tips and suggest they were also formed syn- to late D<sub>2</sub>B.

The 1100 lode is also relatively planar as it is associated with the transposed long limb of a F<sub>2</sub>A fold that affects the BIF succession. Like the 1150 and 1250 lode series, the 1100 lode is hosted in the upper oxide formation, however gold mineralization is constrained to contact-parallel shear veins and horizontal to shallowly south-dipping quartz  $\pm$  ankerite extension veins that are developed in BIF units. The 1100 lode contains the same chlorite-ankerite dominant alteration assemblage found on the margins of crosscutting quartz  $\pm$  ankerite veins replacing magnetite-rich layers in BIF lithologies, as in the 1150 and 1250 lode series.

### **5.3.2 Other Deposits in the Meliadine Gold District**

The MGD comprises numerous orogenic gold deposits and prospects that are spatially associated with the Pyke Fault and its splays. A summary of the deposit characteristics is displayed in table 5.1. High-grade gold intervals occur as a series of sub-parallel and semi-continuous ore zones that are known locally as lodes at all prospects. Like Tiriganiaq, most of these lodes correspond to folded, hydrothermally altered and veined BIF intervals, which are intercalated and folded with turbidite (e.g., Tiriganiaq and Discovery) and mafic volcanic successions (e.g., Normeg, Wesmeg, Pump, F Zone and Wolf). The BIFs intercalated with mafic volcanic-dominated rocks however are oxide-facies BIFs, rich in chert and magnetite. In general, there is a common sulphide assemblage throughout the MGD consisting of arsenopyrite  $\pm$  pyrrhotite  $\pm$  chalcopyrite  $\pm$  pyrite  $\pm$  sphalerite  $\pm$  galena associated with BIF replacements zones, quartz  $\pm$  ankerite veins and/or high strain zones in the surrounding metasedimentary or volcanic/volcanoclastic rocks. Additionally, silica flooding  $\pm$  sulphidation  $\pm$  chlorite clots  $\pm$  sericitization  $\pm$  carbonatization (mainly ankerite) are the dominant alteration assemblage associated with gold mineralization across the MGD and are consistent with Tiriganiaq. All of the gold deposits and prospects in the MGD are metamorphosed to upper greenschist facies, with the exception of the Discovery deposit, which is metamorphosed to lower amphibolite facies (Table. 5.1.). Importantly, Tiriganiaq, Normeg and Wesmeg are the only deposits transposed in an E-W orientation. In summary, these deposits are associated with D<sub>2</sub>B shearing along the transposed limbs of F<sub>2</sub>A folds (D<sub>2</sub>B; Carpenter and Duke, 2004) that structurally thicken prospective BIF horizons along the least transposed segments of the Pyke Fault.

**Table 5.1 Meliadine Gold District ore deposit characteristics summary (modified from Lawley et al., 2015c).**

| <b>Deposit</b>    | <b>Lithofacies</b>  | <b>BIF type</b>                   | <b>Metamorphic grade</b> |
|-------------------|---|-----------------------------------|--------------------------|
| <b>Tiriganiaq</b> | Turbidite (hanging wall)<br>BIF (ore zone)<br>Volcanic (footwall) | Silicate facies<br>Pelitic facies | Upper greenschist        |
| <b>Normeg</b>     | Volcanic (hanging wall<br>and footwall)<br>BIF (ore zone)         | Oxide Facies                      | Upper greenschist        |
| <b>Wesmeg</b>     | Volcanic (hanging wall<br>and footwall)<br>BIF (ore zone)         | Oxide Facies                      | Upper greenschist        |
| <b>F Zone</b>     | Volcanic (hanging wall<br>and footwall)<br>BIF (ore zone)         | Oxide Facies                      | Upper greenschist        |
| <b>Pump</b>       | Volcanic (hanging wall<br>and footwall)<br>BIF (ore zone)         | Oxide Facies                      | Upper greenschist        |
| <b>Discovery</b>  | Turbidite (hanging wall<br>and footwall)<br>BIF (ore zone)        | Silicate facies                   | Lower amphibolite        |

### 5.3.3 Other BIF-hosted/associated Au deposits of the Churchill Province

Many of the characteristics of the Tiriganiaq deposit are similar to other BIF-hosted gold deposits located in Western Churchill Province. Table 5.2 summarizes the main characteristics of the Tiriganiaq deposit and other BIF-hosted gold deposits (Meadowbank, Amaruq, and Three Bluffs) in the Churchill Province.

All these deposits are part of Archean greenstone belts and are affected by Paleoproterozoic deformation. Like the Upper Oxide Formation at Tiriganiaq, the host stratigraphy of the Central Domain of the Whale Tail deposit and the Middle Sedimentary Sequence of the Three Bluffs deposit are dominated by clastic sedimentary rocks intercalated with silicate  $\pm$  oxide BIFs (Davies et al., 2010; Valette et al., 2020). However, the Middle Sedimentary Sequence at Three Bluffs also contains a minor concordant felsic volcanic unit. Contrastingly, the host stratigraphy at Meadowbank differs significantly as it is dominated by intermediate  $\pm$  mafic to felsic volcanoclastic rocks and ultramafic and mafic volcanic rock intercalated with meters- to 10s of meters-thick oxide facies BIFs (Janvier et al., 2015).

In all of these deposits, the dominant part of gold mineralization is hosted in BIFs. Gold mineralization in BIF is consistently associated with stratabound and/or crosscutting sulphide replacement along Fe-rich layers in BIF (generally magnetite) commonly on the margins of quartz  $\pm$  carbonate veins. However, at Meadowbank the sulphide replacement in BIF is related to high-strain zones rather than quartz veining, although a second style of mineralization consists of gold-bearing quartz-pyrrhotite  $\pm$  pyrite veins hosted by intermediate to felsic volcanoclastic rocks. Similarly, at Amaruq and Tiriganiaq, a portion of gold mineralization is hosted in rocks intercalated with BIFs in the form of quartz veining in high-strain zones. Additionally, one of the main mineralization styles unique to Amaruq, Meadowbank, and the Three Bluffs deposits are zones of “silica flooding” in BIF (Davies et al., 2010; Janvier et al, 2015; Valette et al., 2020; Lebeau and Mercier-Langevin, 2021).

Although each of these deposits share very similar mineralization styles, they contain unique dominant sulphide assemblages (Table. 5.2.). The sulphide assemblage at Amaruq and Tiriganiaq are dominated by arsenopyrite ( $\pm$  löllingite at Amaruq) and pyrrhotite with minor amounts of pyrite and local galena, and as the case at Tiriganiaq minor chalcopyrite, rare chalcopyrite and galena. Contrarily, the sulphide assemblage at the Three Bluffs deposit and Meadowbank are dominated by pyrrhotite and pyrite with only minor amounts of arsenopyrite ( $\pm$  löllingite at Three Bluffs), and chalcopyrite.



These deposits are all metamorphosed to different metamorphic facies. Meadowbank and Three Bluffs are on the transition zone between greenschist and amphibolite facies. Amaruq is metamorphosed to amphibolite facies and Tiriganiaq is metamorphosed to greenschist facies.

All the deposits mentioned in this section are structurally-controlled and high-grade zones are associated with ductile-to- brittle-ductile shear zones characteristically along geological contacts and/or constrained to relatively less competent units. Additionally high-grade gold mineralization is localized within the hinge zones and limbs of  $F_2$  folded BIFs at all deposits, which provide zones of tectonic thickening, and are ideal sites for brittle fracturing and intense gold bearing quartz veining to develop.

The BIF deposits of the Churchill province have very complex geological and metallogenic history (Berman et al., 2007; Pehrsson et al., 2013; Lawley et al., 2015 a, b, c, 2016; Lebeau and Mercier-Langevin, 2021). All deposits are hosted in poly-deformed and poly-metamorphosed Archean greenstone belts. Multiple deformation and metamorphic episodes make it difficult to understand the relative timing of the introduction of gold. Consequently, there is disagreement as to which event(s) is believed to be responsible for the introduction of gold. Preliminary Re-Os analyses on ore associated arsenopyrite from the Amaruq deposit suggest a major time span with the youngest model ages at ca. 2250 and the oldest at ca. 2650 Ma (Mercier-Langevin et al., 2018). Similar results were obtained at the Meliadine district where arsenopyrite Re-Os ages range from 2300 Ma to 1800 Ma (Lawley et al., 2015c). However, all deposits show evidence of a Paleoproterozoic age for mineralization between 1900 and 1800 Ma, generally post-peak metamorphism. Although, Re-Os dating of gold-rich arsenopyrite at Meadowbank yielded an age of ca. 1899 Ma (Janvier, 2016) and is thought to have occurred early or during peak metamorphism.

**Table 5.2 Comparison of key characteristics of the churchill province BIF-hosted/associated gold deposits.**

|   | <b>Tiriganiaq</b>   | <b>Meadowbank</b>  | <b>Amaruq (Whale Tail)</b>   | <b>Three Bluffs</b>  |  |
|---|---|--|--|--|--|
| <b>Geological province</b>                          | Western Churchill Province  | Western Churchill Province   | Western Churchill Province   | Western Churchill Province   |  |
| <b>Surrounding rocks</b>                            | BIF interbedded with graywacke/mudstone   | BIF interbedded with mafic to felsic volcaniclastic rocks ± ultramafic and mafic volcanic rock   | BIF interbedded with greywacke and argillite ± mafic to ultramafic volcanic rock (North Domain)  | BIF interbedded with psammatic wacke ± felsic volcanic rock  |  |
| <b>Ore host rocks</b>                               | BIF + greywacke   | BIF ± volcanoclastic   | BIF + greywacke  | BIF  |  |
| <b>Age of host rocks</b>                            | ≤ 2660 Ma   | 2711 Ma  | 2730–2630 Ma   | 2706 Ma  |  |
| <b>Metamorphic facies</b>                           | Greenschist   | Transition at greenschist to amphibolite   | Amphibolite  | Lower to upper amphibolite   |  |
| <b>Type of BIF</b>                                  | Oxide-silicate + pelitic BIF  | Oxide (± silicate) BIF   | Silicate (± oxide) BIF   | Oxide + silicate BIF   |  |
| <b>Alteration mineralogical assemblages</b>         | <b>BIF</b>  | Ankerite, chlorite   | Chlorite, grunerite, biotite, garnet, ferro-hornblende   | Chlorite, cummingtonite/grunerite, Fe-actinote, tremolite and stilpnomelane                          | Muscovite, actinolite, garnet, biotite, hornblende     |
|   | <b>Surrounding rocks</b>  | Ankerite, sericite, chlorite   | Muscovite, chlorite ± calcite, (epidote, biotite, ferro-hornblende, garnet ± staurolite, actinolite)   | Chlorite, biotite ± muscovite  | Biotite, muscovite, staurolite ± cordierite and garnet |
| <b>Sulphides</b>                                    | Apy ± Po ± Py ± Cp ± Gal ± rare sphalerite  | Po-Py ± Apy ± Cp   | Apy (± Lö) -Po ± Py  | Po-Py ± Apy (+Lö) - Cp   |  |
| <b>Mineralization Style</b>                         | Quartz ± ankerite veins with coarse idioblastic Apy ± Po / Stratabound Apy ± Po replacement along Mn-rich layers in BIF/ Disseminated Apy in high strain zones in greywacke | Sulphides clusters and/or stockwork and/or veinlets parallel to the S <sub>p</sub> /S <sub>0</sub> or intersecting the S <sub>0</sub> rare veins of quartz ± rich in sulphides | Stratabound and locally discordant sulphide replacement in chert-poor silicate-facies BIF/ silica flooding zones associated with sulphides in chert-rich silicate - facies BIF | Stratabound and crosscutting sulphides<br>Strong silicification zones and sulphide-poor quartz veins |  |
| <b>Structural control on mineralization</b>         | D <sub>2</sub> B brittle-ductile shear zones localized in chloritic greywacke/ transposed F <sub>2</sub> A fold-hinge   | D <sub>1</sub> faults and/or proximal to D <sub>2</sub> fault/shear zones along sheared F <sub>2</sub> fold limbs  | Ductile shear zones localized along geological contacts/ F <sub>2</sub> fold-hinge   | Zone of strong brittle ductile deformation and F <sub>2</sub> fold-hinge                             |  |
| <b>Mineralization relative to peak metamorphism</b> | Pre?<br><b>Syn- to- post</b>  | Pre-peak metamorphism?   | Pre- and post- peak metamorphism?  | Post-peak metamorphism   |  |
| <b>Age of mineralization</b>                        | 2270Ma<br>2140-2060Ma<br>1900Ma<br><b>mh: 1854±6Ma</b><br><b>xe: 1856±10Ma</b>  | Pre-1899Ma?<br>1899Ma  | 2250 - 2650 Ma   | 1822±21 Ma<br>1813.8±8.7 Ma  |  |

Dating methods: \* Re-Os on arsenopyrite; M U/Pb on hydrothermal monazite; MH U/Pb on hydrothermal monazite in a gold-bearing quartz vein; Xe U/Pb on xenotime. (Modified from Janvier et al., 2016). Abbreviations: Apy = arsenopyrite, Lö = löllingite, Po= pyrrhotite, Cp = chalcopyrite, Gn = galena, Po = pyrrhotite, and Mn = magnetite.

### 5.3.4 Other type examples of BIF-hosted/associated Au deposits

#### Lupin Gold Mine

The former Lupin gold mine is located in the Slave Province, Nunavut, Canada. It is hosted in the Neoproterozoic Contwoyto Formation of the Yellowknife Supergroup (Lhotka and Nesbitt, 1989). Although distinct in some ways, the Lupin and Tiriganiaq deposits show common features that deserve attention as they suggest similar ore-forming processes.

Like Tiriganiaq, the host stratigraphy of the Lupin deposit is dominated by clastic sedimentary rocks intercalated with silicate and pelitic BIFs (Kerswill., 1993; Bullis et al., 1994; Geusebroek and Duke, 2004). Although both are considered silicate facies BIFs, the main amphibolitic BIF at Lupin is dominated by grunerite and quartz rather than quartz and magnetite like the oxide-silicate BIF at Tiriganiaq (Bullis et al., 1994; Geusebroek and Duke., 2004). Like Tiriganiaq, Lupin contains thin discontinuous pelitic BIFs. However, the pelitic BIF at Lupin is dominated by garnet, rather than chlorite at Tiriganiaq, likely in response to amphibolite grade metamorphism at Lupin. Like Tiriganiaq, the silicate facies BIF is relatively enriched in gold compared to the pelitic BIF at Lupin.

At Lupin, two sets of auriferous veins have been identified. The first set consists of early quartz veins accompanying sulphidization/calc-silicate alteration of BIF, which are tightly folded and sheared. The second set, a later undeformed ladder quartz veins are restricted to, and consistently form at high angles to the contacts of amphibolitic BIF units with associated chlorite almandine arsenopyrite-rimmed löllingite selvages. While resulting in a much higher gold endowment, this late stage of As-rich mineralization is comparable to the D<sub>2</sub>B sub-horizontal quartz ± ankerite ± arsenopyrite ± pyrrhotite veins documented at Tiriganiaq, which also form at high-angle to BIF contacts and form stratabound arsenopyrite ± pyrrhotite ± chlorite ± ankerite selvages. At Lupin, free gold is most commonly sited along the contacts of löllingite cores preserved within the late-growing arsenopyrite in response to retrograde metamorphic reactions from amphibolite grade metamorphism (Bullis et al., 1994; Ford and Duke, 1993; Geusebroek and Duke, 2004). At Tiriganiaq visible gold is most commonly found at the border or in late fractures of arsenopyrite crystals and other low-strain microtextural sites.

At Lupin, ductile D<sub>2</sub> folding and brittle-ductile D<sub>3</sub> folding and shearing have produced a dome and basin fold interference pattern. D<sub>2</sub> and D<sub>3</sub> deformation documented at Lupin have a comparable structural and metallogenic significance of the D<sub>2</sub>A and D<sub>2</sub>B events at Tiriganiaq. Timing of first

gold introduction is interpreted to have occurred during latest-D<sub>2</sub> to earliest-D<sub>3</sub> deformation concentrated within F<sub>2</sub> fold structures in BIF, and along D<sub>3</sub> chloritic shear zones (Geusebroek and Duke, 2004). Though, unlike Tiriganiaq, D<sub>2</sub> and D<sub>3</sub> deformation and associated mineralization at Lupin are Archean.

### **Homestake Gold Mine**

The archetypal Homestake mine, the largest known BIF-hosted gold deposit, is located in the Black Hills of South Dakota and has produced over 40 Moz of gold (Caddey et al., 1991). The Homestake gold mine is underlain by Paleoproterozoic carbonaceous black shales and turbidites intercalated with carbonate-silicate-sulphide facies BIF (Caddey et al., 1991; Bell, 2013).

The BIFs at Homestake mainly consists of a chert-siderite carbonate-silicate facies, and a minor chert-grunerite silicate facies. The bulk of gold mineralization is hosted in the carbonate-silicate facies BIF of the Homestake Formation, and the bulk of the ore consists of arsenopyrite-pyrrhotite ± pyrite replacement in BIF, with associated quartz ± siderite ± chlorite alteration (Caddey et al., 1991). The breccia vein mineralization documented at Homestake refers to foliation/shear parallel quartz veining, and sub-horizontal (high-angle to BIF contacts) quartz veining and associated sulphide replacement in BIF. The distribution of the ore is controlled by the hinge zone of folds where dilatational segments developed during late-stage brittle-ductile shearing (Bell, 2013).

The Homestake deposit is located at the transition between greenschist and amphibolite facies along a folded garnet isograd (Caddey et al., 1991). A large part of the deposit is hosted in amphibolite facies rocks. Gold mineralization is interpreted to postdate peak metamorphism because the alteration assemblage associated with gold mineralization overprints the peak metamorphic minerals (Caddey et al., 1991; Bell, 2013).

Many characteristics of the Homestake deposit are similar with the Tiriganiaq deposit as they are both typical late- to post-metamorphic gold deposits occurring near the greenschist-amphibolite transition zones. Although, the surrounding host rocks and BIFs that host gold mineralization are different (carbonate-silicate vs. oxide-silicate ± pelitic), both deposits show clear evidence for sharing the same strong lithological (BIF rheology) and structural (thickened/tight fold hinges) controls on high-grade gold mineralization. Additionally, both deposits share a nearly identical sulphide and alteration assemblages related to gold mineralization (arsenopyrite + pyrrhotite + chlorite + carbonate).

### 5.3.5 Summary

The comparison of other well documented major BIF-hosted/associated gold deposits allows for documenting the common characteristics that lead to the formation of these deposits, which can be used as potential exploration vectors. All deposits discussed display similar features, most of which are typical of orogenic gold deposits (Poulsen et al., 2000; Goldfarb et al., 2005; Dubé and Gosselin, 2007), such as: mineralization associated with quartz veins, systematic association between gold mineralization and sulphides, and structural control of mineralization by zones of shearing and folding (St.Pierre et al., 2020).

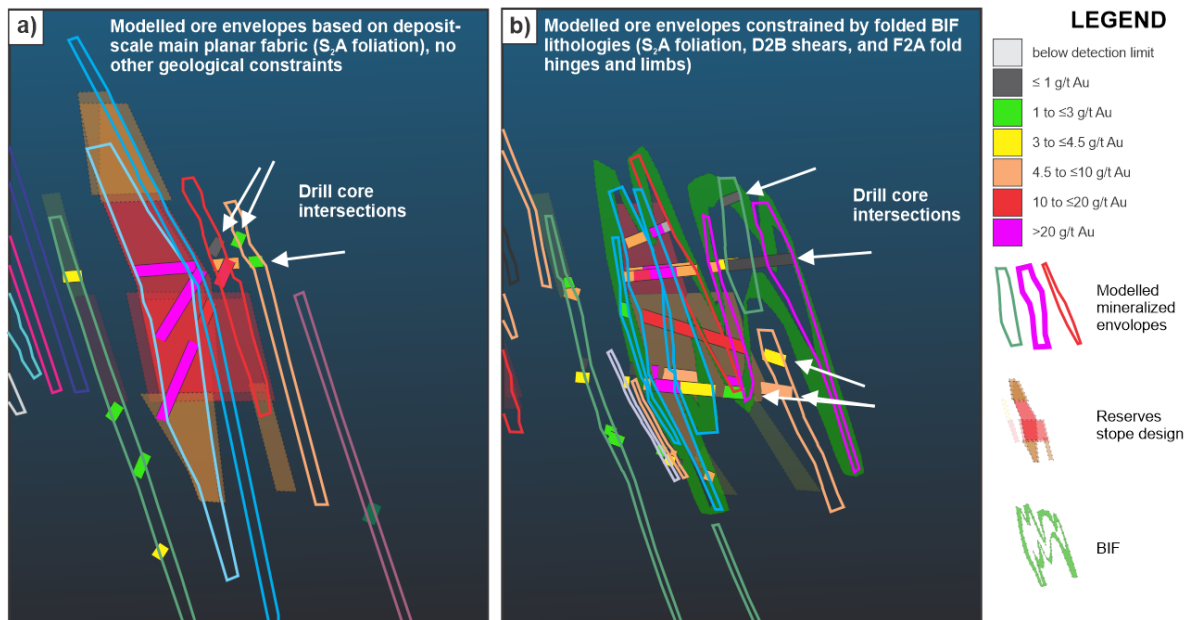
## 5.4 IMPLICATIONS FOR MINE DEVELOPMENT AND EXPLORATION

New underground and microstructural observations presented in this study demonstrate that the geometrically and structurally complex 1150 and 1250 lode series are controlled by narrow, north-dipping, D<sub>2</sub>B reverse shear zones that overprint the slightly steeper, north-dipping S<sub>2</sub>A foliation that is axial planar to tight F<sub>2</sub>A folds. More importantly, this study has revealed the importance of horizontal to shallowly south-dipping ore-bearing D<sub>2</sub>B extensional quartz ± ankerite veins. These veins and their associated sulphide replacement zones are preferentially developed in tightly transposed F<sub>2</sub>A folded oxide-silicate and minor pelitic facies BIF intervals. The oxide-silicate and pelitic BIF lithologies are relatively enriched in gold compared to the chloritic greywacke and the laminated mudstone lithologies signifying they acted as a chemical and structural trap for gold mineralization. The 1150 and 1250 lodes provide an excellent example of the type of geometric complexities of ore-bearing veins found within shallowly west-plunging transposed F<sub>2</sub>A folded BIF successions.

These zones provide some of the highest gold grades and thickest gold intervals within the Tiriganiaq deposit and thus represent excellent exploration targets for both within the Tiriganiaq deposit as well as regionally within the Rankin Inlet greenstone belt. However, the orientation of these ore-bearing veins and their associated hydrothermal alteration zones were difficult to document in the absence of oriented drill core. Access to the 1150 lodes underground and their detailed documentation and study at drift scale as part of the current study helped understand the controls and geometry of these gold-rich zones.

This information significantly aided in stope design, 3-D modelling, and resource estimation. The revised understanding of the structural controls at play at the Tiriganiaq deposit based on the results of this study provide excellent criteria for targeting near-mine and regional exploration by highlighting: 1) the importance of F<sub>2</sub>A fold hinge zones, preferably transposed in an E-W

orientation, and their effect on the generation of favourable traps (thickened BIF intervals); and 2) the development of narrow shears along the limbs (D<sub>2</sub>B) and the development of associated extensional veins in the BIF. Figure 5.4 illustrates how a better understanding of the geometry of the host BIF unit and the structural controls on the ore-bearing veins of the 1150 lodes impacted modelling results and grade and tonnage estimates. Updated modelling of these ore zones now includes the folded geometry of the host BIF units (favourable host), the distribution of the veins along the sheared limbs (shear veins), and the development of shallowly dipping mineralized veins within the hinge zones of thickened BIF layers.



**Figure 5.4** Sketch showing two models of the Tiriganiaq deposit, the first using knowledge before this study and the second using knowledge gained through this study. a) Modelling of typical ore zones based on drillhole intersections and the assumption that gold intersections are continuous and can be interpolated and extrapolated parallel to the main fabric. b) A revised model using information gained through this study and a better understanding of the combined structural and lithological controls on gold, which now integrates the folding and geometry of the BIF units and the presence of BIF-bound ore intervals, such as shallowly south-dipping extensional veins. Simplified from material provided by Agnico Eagle Mines Limited. Abbreviation: BIF = banded iron formation. From St Pierre et al. (2020).

## 5.5 CONCLUSION

### 5.5.1 Main Contributions

Underground geological and structural mapping and geochemical data processing undertaken in this study has improved the geological knowledge of the Tiriganiaq gold deposit. This contribution notably includes: 1) better constrained structural history; 2) detailed documentation of the parameters that controlled the formation, distribution, and geometry of gold mineralization in the 1150 and 1250 lode series; and 3) a more refined timing of gold introduction relative to the deformation events at the Tiriganiaq gold deposit.

Tiriganiaq is an epigenetic, partly BIF-hosted greenschist-facies orogenic gold deposit. The 1150 and 1250 lode series are hosted in the Upper Oxide Formation, a complexly folded package of chloritic greywacke-siltstone-mudstone interbedded with oxide-silicate facies dominated and minor pelitic BIF. Gold mineralization in the 1150 and 1250 lode series are associated with BIF-hosted replacement-style mineralization, coupled with auriferous quartz  $\pm$  ankerite veins and selvages. Arsenopyrite and pyrrhotite are the dominant sulphide phases, with minor chalcopyrite and pyrite, and trace galena. Overall, sericite, idioblastic ankerite, quartz, and chlorite alteration are widespread in the clastic sedimentary lithologies (chloritic greywacke, laminated mudstone, and portions of the pelitic BIF), whereas the Oxide-silicate BIF and portions of the pelitic BIF comprise a dominant quartz  $\pm$  chlorite  $\pm$  ankerite  $\pm$  sulphide alteration assemblage.

Gold mineralization in the 1150 and 1250 lodes are controlled by narrow, north-dipping, D<sub>2</sub>B reverse-dextral shear zones localized within chloritic greywacke. These shear zones overprint the slightly steeper, transposed north-dipping S<sub>2</sub>A foliation that is axial planar to transposed tight F<sub>2</sub>A folds. More importantly, this study has revealed the importance of horizontal to shallowly south-dipping ore-bearing D<sub>2</sub>B extensional quartz  $\pm$  ankerite veins. These veins and their associated sulphide replacement zones are preferentially developed in transposed tightly F<sub>2</sub>A folded oxide-silicate facies BIF and minor pelitic BIF intervals. The oxide-silicate and pelitic BIF lithologies are relatively enriched in gold compared to the chloritic greywacke and the laminated mudstone lithologies signifying they acted as a chemical and structural trap for gold mineralization. The 1150 and 1250 lodes provide an excellent example of the type of geometric complexities of ore-bearing veins found within shallowly west-plunging transposed F<sub>2</sub>A folded BIF successions.

Gold was introduced earliest during D<sub>2</sub>A deformation, latest syn- to- late D<sub>2</sub>B deformation, and post-peak metamorphism. D<sub>2</sub> deformation can be constrained by the onset of the regional Trans-Hudsonian metamorphic event at ca. 1900–1850 Ma and by the onset of the D<sub>3</sub> deformation ca.

1850 Ma. Gold emplacement can be constrained further with U-Pb xenotime results that yield an upper intercept concordia age at  $1862 \pm 29$  Ma on mineralized veins (Lawley et al., 2015b). This agrees with a  $^{207}\text{Pb}/^{206}\text{Pb}$  monazite age of  $1854 \pm 6$  Ma (Carpenter et al., 2005). Additionally, Re-Os dating suggests that ore-associated arsenopyrite-galena-ilmenite phases locally formed at  $\geq 1860$  Ma.

The Tiriganiaq deposit shows features common with other BIF-hosted/associated gold deposits such as Lupin, Meadowbank, Amaruq, and Three Bluffs in Nunavut, and Homestake in South Dakota, notably the lithological control of silicate BIF on gold and strong deformation zones. Exploration for similar gold mineralization within the Rankin Inlet greenstone belt should focus on areas with major BIF successions that have experienced polyphase folding and shearing. More specifically hinge zones of tectonically thickened, tightly  $F_2$ A folded BIF successions intersected by secondary structures and/or high-strain zones are highly prospective, especially ones which are transposed in an E-W orientation like Tiriganiaq.

### **5.5.2 Outstanding questions**

This was the first study that used geological and structural mapping of the new underground development at the Tiriganiaq mine to try and understand structural complexities that impacted on the recovery of gold. However, only a small portion of the mine has been documented in this study, and other geological and structural complexities will likely be uncovered with the expansion of underground and open pit development.

Similar studies must be undertaken at all deposits and prospects to highlight and document all zones adequately, in order to get a more complete understanding of the gold mineralization in the Tiriganiaq deposit and greater Meliadine district.

Analysis of the larger scale geometry of the ore zones and high-grade gold intercepts in 3-D is necessary in order to better understand the geometry of the host succession and high-grade ore-shoots, especially the poorly constrained and poorly understood SE-plunging ore shoots.





## 6 BIBLIOGRAPHY

---

- Agnico Eagle, 2018. Agnico Eagle Mines Limited Detailed Mineral Reserves and Resources Data: As of December 31, 2017; Agnico Eagle Mines Limited. <[https://www.agnicoeagle.com/English/operations and development projects/ reserves and resources/default.aspx](https://www.agnicoeagle.com/English/operations%20and%20development%20projects/reserves%20and%20resources/default.aspx)> [accessed January 23, 2019]
- Armitage, A.E., Tella, S., and Miller, A.R. (1993) Iron-formation-hosted gold mineralization and its geological setting, Meliadine Lake area, District of Keewatin, Northwest Territories. In *Current Research, Part C; Geological Survey of Canada, Paper 93-1C*. p. 187-195.
- Bäcker H (1976) Fazies und chemische Zusammensetzung rezenter Ausfällungen aus Mineralquellen im Roten Meer. *Geol Jahrb D* 17: 151-172.
- Balog, M.J. (1993) The 1993 exploration report and geological compilation of the Meliadine Property, N.W.T. Volume 1 of 5. Internal report for Comaplex Minerals Corp., Calgary, Alberta.
- Bannatyne, M.J., 1958. The geology of the Rankin Inlet area and North Rankin Nickel Mines Limited, Northwest Territories; unpublished M.Sc. thesis, University of Manitoba, Winnipeg, Canada, 83 p.
- Barclay, W.A. (1991) Report on structural mapping and analysis, and recommendations for exploration on the Meliadine River Project. Internal Report, Asamera Minerals Inc. 37p.
- Barclay, W.A. (1992) Report on inspection of selected drill core and reconnaissance regional mapping for the Meliadine River Project. Internal Report, Asamera Minerals Inc. 51p.
- Barham, B., 2010. Geological map of the Meliadine gold property, interpretation and compilation – Nov. 2009; Comaplex Minerals Corp. internal report.
- Bekker A., Slack J.F., Planavsky N., Krapez B., Hofmann A., Konhauser K.O. & Rouxel J. (2010) Iron formations: The sedimentary product of a complex interplay among mantle, tectonic, oceanic, and biospheric processes. *Economic Geology*, 105:467-508.
- Bell C. (2013) Structural controls on gold mineralization at the Homestake Mine and their implications for the geology of the Black Hills. Ph.D. thesis, James Cook University, 232 p.
- Berman, R., Davis, W.J., and Pehrsson, S., (2007) Collisional Snowbird tectonic zone resurrected: Growth of Laurentia during the 1.9 Ga accretionary phase of the Hudsonian orogeny; *Geology*, v. 35, p. 911–914.
- Berman, R.G., Davis, W.J., Ryan, J.J., and Brown, N. (2002) In situ SHRIMP U-Pb geochronology of Barrovian facies-series metasedimentary rocks in the Happy Lake and Josephine River supracrustal belts: Implications for the Paleoproterozoic architecture of the northern Hearne Domain, Nunavut: Radiogenic age and isotopic studies: Report 15: Geological Survey of Canada, Current Research 2002-F4, 14 p.
- Breemen, O., Peterson, T.D. Sandeman., Hamish. (2005) U-Pb zircon geochronology and Nd isotope geochemistry of Proterozoic granitoids in the western Churchill Province: Intrusive age pattern and Archean source domains. *Canadian Journal of Earth Sciences*. 42. 339-377.
- Brommecker, R., Margeson, B., Campbell, J., Goodwin, T., Tykajilo, R. and Daniels, A. (1995) WMC International Limited report on the Meliadine Mining Venture. Internal WMC Report. 44p.
- Bullis H.R, Hureau R.A. & Penner B.D. (1994) Distribution of gold and sulfides at Lupin, Northwest Territories. *Economic Geology*, 89:1217-1227.

Bullis H.R. (1990) Geology of the Lupin Deposit, N.W.T. In: Padgham W.A. & Atkinson D. (Eds.) Mineral Deposits of the Slave Province, Northwest Territories, 8th International Association on the Genesis of Ore Deposits Symposium, Field Trip Guidebook, Field Trip 13, Geological Survey of Canada, Open File 2168, pp. 115-125.

Caddey S.W., Bachman R.L., Campbell T.J., Reid R.R. & Otto R.P. (1991) The Homestake Gold Mine, an early Proterozoic iron-formation-hosted gold deposit, Lawrence county, South Dakota. In: Shawe D.R., Ashley R.P. & Carter L.M.H. (Eds.) Geology and resources of gold in the United States, U.S. Geological Survey Bulletin 1857, pp. J1-J67.

Carpenter, R.L. (2003) Relative and absolute timing of supracrustal deposition, tectonothermal activity and gold mineralization, West Meliadine region, Rankin Inlet greenstone belt, Nunavut, Canada: Unpublished

Carpenter, R.L. and Duke, N.A., (2004) Geological setting of the West Meliadine gold deposits, Western Churchill Province, Nunavut, Canada; *Exploration and Mining Geology Journal*, v. 13, p. 49–65.

Carpenter, R.L., Duke, N.A., Sandeman, H.S., and Stern, R., (2005) Relative and absolute timing of gold mineralization along the Meliadine trend, Nunavut, Canada: Evidence for Paleoproterozoic gold hosted in an Archean greenstone belt; *Economic Geology*, v. 100, p. 567–576.

Colvine, A.C. (1989) An empirical model for the formation of Archean gold deposits: Products of final cratonization of the Superior Province, Canada. In *The Geology of Gold Deposits: The Perspective in 1988*. Edited by R.R. Keays, W.R.H. Ramsey and D.I. Groves. *Economic Geology Monograph*, 6, p. 37-53.

Cox, S.F., Etheridge, M.A., Cas, R.A.F., Clifford, B.A. (1991) Deformational style of the Castlemaine area, Bendigo-Ballararat Zone—implications for evolution of the crustal structure across southeast Australia. *Aust. J. Earth Sci.* 38, 151–170.

Creaser, R.A., McNicoll, V.J., Grondin-Leblanc, P., St.Pierre, B., Lauzon, M.-C., Malo, M., Côté-Mantha, O., and Simard, M., (2018) Lithologic controls on Paleoproterozoic BIF-hosted/associated gold : overview of Re-Os geochronology and Pb isotopes preliminary results; in *Targeted Geoscience Initiative 2017 Report of Activities volume I*, (ed.) N. Rogers; Geological Survey of Canada Open File 8358, p. 147-152.

Cronan D.S. (1976) Basal metalliferous sediments from the eastern Pacific. *Geological Society of America Bulletin* 87(6): 928-934.

Davies, T., Richards, J.P., Creaser, R.A., Heaman, L.M., Chako, T., Simonetti, A., Williamson, J., and McDonald, D.W. (2010) Paleoproterozoic age relationships in the Three Bluffs Archean iron formation-hosted gold deposit, Committee Bay greenstone belt, Nunavut, Canada: *Exploration and Mining Geology*, v. 19, p. 55–80.

Davis, W.J., Hanmer, S., Aspler, L., Sandeman, H., Tella, S., Zaleski, E., Relf, C., Berman, R. and Maclachlan, K. (2000) Regional differences in the Neoproterozoic crustal evolution of the western Churchill Province: Can we make sense of it? *GeoCanada 2000 Meeting*, May, 2000, Calgary, Alberta. Abstract #864 (CD format).

Davis, W.J., Ryan, J.J., Sandeman, H.A., and Tella, S. (2008) A Paleoproterozoic detrital zircon age for a key conglomeratic horizon within the Rankin Inlet area, Kivalliq region, Nunavut: Implications for Archean and Proterozoic evolution of the area; *Geological Survey of Canada, Current Research 2008-08*, 8 p.

Dubé, B., and Gosselin, P. (2007) Greenstone-hosted quartz carbonate vein deposits, In: Mineral deposits of Canada: A synthesis of major deposit types, district metallogeny, the evolution of geological provinces, and exploration methods, (ed.) W.D. Goodfellow; Geological Association of Canada, Mineral Deposits Division, Special Publication no. 5, p. 49–83.

Dubé, B., Mercier Langevin, P., Castonguay, S., McNicoll, V.J., Bleeker, W., Lawley, C.J.M., De Souza, S., Jackson, S.E., Dupuis, C., Gao, J. F., Bécu, V., Pilote, P., Goutier, J., Beakhouse, G.P., Yergeau, D., Oswald, W., Janvier, V., Fontaine, A., Pelletier, M., Beauchamp, A. M., Katz, L.R., Kontak, D.J., Tóth, Z., Lafrance, B., Gourcerol, B., Thurston, P.C., Creaser, R.A., Enkin, R.J., El Goumi, N., Grunsky, E.C., Schneider, D.A., Kelly, C.J., and Lauzière, K., (2015) Precambrian lode gold deposits — a summary of TGI 4 contributions to the understanding of lode gold deposits, with an emphasis on implications for exploration, In: Targeted Geoscience Initiative 4: Contributions to the understanding of Precambrian lode gold deposits and implications for exploration, (eds.) B. Dubé and P. Mercier Langevin; Geological Survey of Canada, Open File 7852, p. 1–24.

Eglinton, B.M., Pehrsson, S.J., Ansdell, K.M., Lescuyer, J.-L., Quirt, D., Milesi, J.-P., Brown, P. (2013) A domain-based digital summary of the evolution of the Paleoproterozoic of north America and Greenland and associated unconformity-related uranium mineralization. *Precambrian Res.* 232, 4–26.

Ford R.C. & Duke N.A. (1993) Concentration of gold during retrograde metamorphism of Archean banded iron formations, Slave Province, Canada. *Canadian Journal of Earth Science*, 30:1566-1581.

Ford, R.C. (1988) Comparative Geology of Gold-bearing Archean Iron-formation, Slave Structural Province, Northwest Territories. M.Sc. thesis, University of Western Ontario, London, 137 p.

Fossen H. (2010) Structural Geology. Cambridge University Press, 463 p.

Frei R., Dahl P.S., Frandsson M.M., Jensen L.A., Hansen T.R., Terry M.P. & Frei K.M. (2009) Lead-isotope and trace-element geochemistry of Paleoproterozoic metasedimentary rocks in the Lead and Rochefort basins (Black Hills, South Dakota, USA): Implications for genetic models, mineralization ages, and sources of leads in the Homestake gold deposit. *Precambrian Research*, 172:1-24.

Fripp R.E.P. (1976) Stratabound gold deposit in Archean banded iron-formation, Rhodesia. *Economic Geology*, 71:58-75.

Gardiner J.J. (1986) Structural geology of the Lupin gold mine, Northwestern Territories. M.Sc. thesis, Acadia University, 206 p.

Geusebroek P.A. & Duke N.A. (2004) An update on the geology of the Lupin Gold Mine, Nunavut, Canada. *Canadian Institute of Mining, Metallurgy and Petroleum, Exploration Mining Geology*, 13(1-4):1-13.

Goldfarb R.J., Baker T., Dubé B., Groves D.I., Hart C.J.R. & Gosselin P. (2005) Distribution, character, and genesis of gold deposits in metamorphic terranes. In: Hedenquist J.W., Thompson J.F.H., Goldfarb R.J. & Richards J.P. (Eds.) *Economic Geology 100th Anniversary Volume*, pp. 407-450.

Gosselin P. & Dubé B. (2005) Gold deposits and gold districts of the world. Geological Survey of Canada, Open File 4893, 1 map.

Gourcerol, B., Kontak, D., Thurston, P., Duparc, Q. (2016a) Do magnetite layers in Algoma-type BIF preserve their primary geochemical signature: A case study of samples from three Archean BIF-hosted gold deposits? *The Canadian Mineralogist*.

- Gourcerol, B., Thurston, P., Kontak, D., Côté-Mantha, O., Biczok, J. (2016b) Depositional Setting of Algoma-type Banded Iron Formation. *Precambrian Research*.
- Gross G.A. (1980) A classification of iron formations based on depositional environments. *The Canadian Mineralogist*, 18(2):215-222.
- Gross G.A. (1996) Stratiform iron. In: Eckstrand O.R., Sinclair W.D. & Thorpe R.I. (Eds.) *Geology of Canadian Mineral Deposit Types. The Geology of North America, Geological Society of America* (also Geological Survey of Canada, *Geology of Canada*, No. 8), P1:41-80.
- Gross G.A. (2009) Iron formation in Canada, genesis and geochemistry. Geological Survey of Canada, Open File 5987, 164 p.
- Groves, D.I., Goldfarb, R.J., Gebre-Mariam, M., Hagemann, S.G., Robert, F. (1998) Orogenic gold deposits: a proposed classification in the context of their crustal distribution and relationship to other gold deposit types. *Ore Geol. Rev.* 13, 7–27.
- Heaman, L.M. (1994) 2.45 Ga. Global mafic magmatism: Earth's oldest superplume? In Eighth International Conference on Geochronology, Cosmochronology and Isotope Geology. United States Geological Survey, Circular 1107, p.132 (Abstract).
- Herron, M. (1988) Geochemical Classification of Terrigenous Sands and Shales from Core or Log Data. *Journal of Sedimentary Research*.
- Hoffman, P.F. (1988) United plates of America, the birth of a craton: Early Proterozoic assembly and growth of Laurentia. *Annual Reviews of Earth and Planetary Science* 16, 543–603.
- Ishikawa, Y., Sawaguchi, T., Iwaya, S., and Horiuchi, M. (1976) Delineation of prospecting targets for Kuroko deposits based on modes of volcanism of underlying dacite and alteration halos; *Mining Geology*, v. 26, p. 105–117.
- James H.L. (1954) Sedimentary facies of iron-formation. *Economic Geology* 49: p. 235-293.
- Janvier, V. (2016) *Geologie du gisement d'or encaissé dans des formations de fer rubanées Meadowbank, Nunavut, Canada*. Unpublished Ph.D. thesis, Institut national de la Recherche scientifique – Centre Eau, Terre et Environnement, Quebec City, 472 p., 1 CD-ROM.
- Janvier, V., Castonguay, S., Mercier-Langevin, P., Dubé, B., Malo, M., McNicoll, V.J., Creaser, R.A., de Chavigny, B., Pehrsson, S.J. (2015) Geology of the banded iron formation-hosted Meadowbank gold deposit, Churchill Province, Nunavut, In: Targeted Geoscience Initiative 4: Contributions to the Understanding of Precambrian Lode Gold Deposits and Implications for Exploration, (ed.) B. Dubé and P. Mercier-Langevin. Geological Survey of Canada Open File 7852: 255-269.
- Kerswill J.A. (1993) Models for iron-formation-hosted gold deposits. In: Kirkham R.V., Sinclair W.D., Thorpe R.I. & Duke J.M. (Eds.) *Mineral Deposit Modeling*. Geological Association of Canada, Special Paper 40, pp. 171-199.
- Kerswill, J.A. (1996) Iron-formation-hosted stratabound gold. in *Geology of Canadian Mineral Deposit Types*, (ed.) O.R. Eckstrand, W.D. Sinclair, R.I. Thorpe. Geological Survey of Canada, *Geology of Canada* 8: 367-382.
- Kerswill, J.A., Woolett, G.N., Strachan, D.M. and Gardner, J. (1983) Geological setting and gold distribution at the Lupin gold deposit, Contwoyto Lake area, N.W.T. *Canadian Institute of Mineralogy Bulletin*, 76, p. 38.
- Klein, C. (2005) Some Precambrian banded iron-formations (BIFs) from around the world: Their age, geologic setting, mineralogy, metamorphism, geochemistry, and origin. *American Mineralogist*, 90:1473-1499.

Klein, C., Beukes, N.J. (1993) Sedimentology and geochemistry of the glaciogenic Late Proterozoic Rapitan iron-formation in Canada. *Economic Geology*, 88:542-565.

Large, R., Gemmill, B., Paulick, H., Huston, D. (2001) The Alteration Box Plot: A Simple Approach to Understanding the Relationship between Alteration Mineralogy and Litho-geochemistry Associated with Volcanic-Hosted Massive Sulfide Deposits. *Economic Geology*. 96. 957-971.

Lavigne, J., Podetz, C., Sexton, A. and Brommecker, R. (1998b) Report on drill holes M97-126, M97-144, M97-172, M97-174, M97-178, MB97-01, MB97-02 and MS97-03 on the Wesmeg Claims, Meliadine West Property, Kivalliq Region, Nunavut. Department of Indian Affairs and Northern Development (DIAND), Nunavut Regional Office, Iqaluit, Nunavut. Assessment Report #084037.

Lawley, C.J.M., Creaser, R.A., Jackson, S., Yang, Z., Davis, B., Pehrsson, S., Dubé, B., Mercier Langevin, P., and Vaillancourt, D., (2015b) Unravelling the Western Churchill Province Paleoproterozoic gold metallotect: Constraints from Re-Os arsenopyrite and U-Pb xenotime geochronology and LA-ICP-MS arsenopyrite trace element chemistry at the BIF-hosted Meliadine gold district, Nunavut, Canada; *Economic Geology*, v. 110, p. 1425–1454.

Lawley, C.J.M., Dubé, B., Mercier Langevin, P., Kjarsgaard, B.A, Knight, R., and Vaillancourt, D. (2015c) Defining and mapping hydrothermal footprints at the BIF-hosted Meliadine gold district, Nunavut, Canada; *Journal of Geochemical Exploration*, v. 155, p. 33–55.

Lawley, C.J.M., Dubé, B., Mercier Langevin, P., McNicoll, V.J., Creaser, R.A., Pehrsson, S., Castonguay, S., Blais, J.-C., Simard, M., Davis, W.J., and Jackson, S.E. (2015a) Setting, age, and hydrothermal footprint of the emerging Meliadine gold district, Nunavut, In: *Targeted Geoscience Initiative 4: Contributions to the understanding of Precambrian lode gold deposits and implications for exploration*, (eds.) B. Dubé and P. Mercier Langevin; Geological Survey of Canada, Open File 7852, p. 99–111.

Lawley, C.J.M., McNicoll, V.J., Sandeman, H., Pehrsson, S., Simard, M., Castonguay, S., Mercier Langevin, P., and Dubé, B. (2016) Age and geological setting of the Rankin Inlet greenstone belt and its relationship to the gold endowment of the Meliadine gold district, Nunavut, Canada; *Precambrian Research*, v. 275, p. 471–795.

Lebeau, L., and Mercier-Langevin, P. (2021) Review of banded iron formation-hosted gold deposits in Nunavut and preliminary data on a new prospect: Canada-Nunavut Geoscience Office, Summary of Activities 2020, p. 1-18.

Lhotka P.G. & Nesbitt B.E. (1989) Geology of unmineralized and gold-bearing iron formation, Contwoyto Lake-Point Lake region, Northwest Territories, Canada. *Canadian Journal of Earth Sciences*, 26(1):46-64.

Lhotka, P.G. (1988) Geology and Geochemistry of Goldbearing Iron-formation in the Contwoyto Lake Region, Northwest Territories, Canada. Ph.D. thesis, University of Alberta, Edmonton, p. 223.

MacLachlan, K., Davis, W.J., and Relf, C. (2005) Paleoproterozoic reworking of an Archean thrust fault in the Hearne Domain, Western Churchill Province: U-Pb geochronological constraints; *Canadian Journal of Earth Science*, v. 42, p. 1313–1330.

Mercier-Langevin, P., Valette, M., De Souza, S., Creaser, R.A., McNicoll, V., Grondin-Leblanc, P., St-Pierre, B., Lauzon, M.- C., Malo, M., Côté-Mantha, O., and Simard, M. (2018) Lithologic controls on Paleoproterozoic BIF-hosted/associated gold: Overview of Re-Os geochronology and Pb isotopes preliminary results; in *Targeted Geoscience Initiative: 2017 report of activities*, volume 1, (ed.) N. Rogers; Geological Survey of Canada, Open File 8358, p. 147–152.

- Miller, A.R., Balog, M.J. and Tella, S. (1995) Oxide iron formation hosted lode gold, Meliadine Trend, Rankin Inlet Group, Churchill Province, Northwest Territories; Geological Survey of Canada, Current Research 1995 C, p. 163–174.
- Oswald, W. (2018) Geology of the Musselwhite banded iron formation-hosted gold deposit, Superior Province, Ontario, Canada; Ph.D. thesis, Institut national de la recherche scientifique – Centre Eau Terre Environnement, Québec, Quebec, 475 p.
- Oswald, W., Castonguay, S., Dubé, B., McNicoll, V.J., Biczok, J., Malo, M., Mercier-Langevin, P. (2015) Geological setting of the world-class Musselwhite gold mine, Superior Province, northwestern Ontario: implications for exploration, In: Targeted Geoscience Initiative 4: Contributions to the Understanding of Precambrian Lode Gold Deposits and Implications for Exploration, (ed.) B. Dubé and P. Mercier-Langevin Geological Survey of Canada, Open File Open File 7582: 69-84.
- Pehrsson, S., Berman, R., and Davis, W. (2013) Paleoproterozoic orogenesis during Nuna aggregation: A case study of reworking of the Rae craton, Woodburn Lake, Nunavut; Precambrian Research, v. 232, p. 167–188.
- Percival J.A. (2007) Geology and metallogeny of the Superior Province, Canada. In: Mineral Deposits of Canada: A Synthesis of Major Deposit-Types, District Metallogeny, the Evolution of Geological Provinces, and Exploration Methods. Geological Association of Canada, Mineral Deposits Division, Special Publication, 5:903-928.
- Peterson, T.D. and van Breeman, O. (1999) Review and progress report of the Proterozoic granitoid rocks of the western Churchill Province, Northwest Territories (Nunavut). In Current Research 1999-C; Geological Survey of Canada, p. 119-127.
- Peterson, T.D., van Breeman, O., Sandeman, H. and Cousens, B. (2002) Proterozoic (1.85 – 1.75 Ga) igneous suites of the Western Churchill Province: granitoid and ultrapotassic magmatism in a re-worked Archean hinterland. Precambrian Research, 119, p. 73-100.
- Peterson, T.D., van Breeman, O., Sandeman, H. and Rainbird, R.H. (2000) Proterozoic (1.85 – 1.75 Ga) granitoid plutonism and tectonics of the Western Churchill Province. GeoCanada2000 Meeting, May 2000, Calgary, Alberta. Abstract# 539 (CD format).
- Phillips, G.N., Groves D.T. & Martyn J.E. (1984) An epigenetic origin for Archean banded iron-formation-hosted gold deposits. Economic Geology, 79:162-171.
- Poulsen, K.H., & Robert, F. (1989) Shear zones and Gold: practical examples from the southern Canadian shield. In Mineralization and Shear Zones, edited by J.T. Bursnsnall, Geological Association of Canada, Short Course Notes v. 6, p. 239-266.
- Poulsen, K.H., Robert, F., and Dubé, B. (2000) Geological classification of Canadian gold deposits; Geological Survey of Canada, Bulletin 540, 106 p.
- Redden, J.A. & French, G. (1989) Geologic setting and potential exploration guides for gold deposits, Black Hills, South Dakota. US Geological Survey Bulletin 1857-B:B45–B72
- Robert, F. & Poulsen, K.H. (2001) Vein formation and deformation in greenstone gold deposits. Reviews in Economic Geology, 81: 578-592.
- Robert, F. (1994) Timing relationships between Cu-Au mineralization, dykes, and shear zones in the Chibougamau camp, northwestern Abitibi subprovince, Quebec, In: Current Research 1994-C; Geological Survey of Canada, p. 287–294.
- Robert, F., Poulsen, K.H., and Dubé, B. (1994) Structural analysis of lode gold deposits in deformed terranes; Geological Survey of Canada, Open File 2850, p. 5–17.

- Roddick, J.C., Miller, A.R. (1994) An  $^{40}\text{Ar}/^{39}\text{Ar}$  age from REE-enriched Enekatsha ultrapotassic intrusive suite and implications for timing of ultrapotassic magmatism in the Churchill Structural Province, N.W.T. In Radiogenic Age and Isotopic Studies, Report 8. Geological Survey of Canada, Current Research 1994-F, p. 1-31.
- Rye, D.M. & Rye, R.O. (1974) Homestake Gold Mine, South Dakota: I. Stable Isotope Studies. *Economic Geology*, 69:293-317.
- Sandeman, H.A., Cousens, B., Peterson, T., Hemmingway, C., Davis, W., Hanmer, S., Tella, S., Ryan, J. and Aspler, L.B. (2000b) Petrochemistry and Nd isotopic evolution of Proterozoic mafic rocks of the Western Churchill Province, Nunavut and their implications for the evolution of the lithospheric mantle. GeoCanada2000 Meeting, May 2000, Calgary, Alberta. Abstract #808. (CD format).
- Sheldon, H. A., & Micklethwaite, S. (2007) Damage and permeability around faults: implications for mineralization. *Geology*, 35(10), 903-906.
- Sherlock, R.L., Pehrsson, S.J., Logan, A.V., Hrabi R.B., Davis W.J. (2004) Geological Setting of the Meadowbank Gold Deposits, Woodburn Lake Group, Nunavut. *Exploration and Mining Geology* 13: 67-107.
- Sibson, R.H. (1986) Brecciation processes in fault zones: inferences from earthquake rupturing. *PAGEOPH*, v. 124, p. 191-213.
- Sibson, R.H., Robert, F., Poulsen, K.H. (1988) High-angle reverse faults, fluid-pressure cycling, and mesothermal gold-quartz deposits. *Geology* 16(6): 551-555.
- St.Pierre, B., Mercier-Langevin, P., Blais, J.-C., Servelle, G., Simard, M., Côté-Mantha, O., and Malo, M. (2020) Structural controls and relative timing of gold mineralization of the banded iron formation-associated Tiriganiaq deposit, Meliadine district, Rankin Inlet greenstone belt, Nunavut; in Targeted Geoscience Initiative 5: Contributions to the Understanding of Canadian Gold Systems, (ed.) P. Mercier-Langevin, C.J.M. Lawley, and S. Castonguay; Geological Survey of Canada, Open File 8712, p. 237–250.
- St.Pierre, B., Mercier Langevin, P., Simard, M., Côté Mantha, O., Malo, M., and Servelle, G. (2018) Structural and lithologic controls on the nature and distribution of gold in the BIF associated 1150 and 1250 lode series at Tiriganiaq, Meliadine district, Rankin Inlet greenstone belt, Nunavut, In: Targeted Geoscience Initiative: 2017 report of activities, volume 1, (ed.) N. Rogers; Geological Survey of Canada, Open File 8358, p. 157–161.
- St.Pierre, B., Mercier Langevin, P., Simard, M., Côté Mantha, O., Malo, M., and Servelle, G. (2019) Structural and lithological controls on the nature and distribution of gold at the Tiriganiaq deposit, Meliadine district, Rankin Inlet greenstone belt, Nunavut, In: Targeted Geoscience Initiative: 2018 report of activities, volume 1, (ed.) N. Rogers; Geological Survey of Canada, Open File 8549, p. 77–82.
- Sun S.-S. & McDonough W.F. (1995) The composition of the Earth. *Chemical Geology*, 120:223-253.
- Tella, S. (1994) *Geology, Rankin Inlet (55K/16), Falstaff Island (55J/13) and Quartzite Island (55J/11), district of Keewatin, Northwest Territories*; Geological Survey of Canada, Open File 2968, 2 sheets; 1 CD-ROM.
- Tella, S., Annesley, I.R., Borradaile, G.J., Henderson, J.R. (1986) Precambrian Geology of Parts of Tavani, Marble Island, and Chesterfield Inlet Map Areas, District of Keewatin: A Progress Report. Geological Survey of Canada Paper 86-13, 20 pp.



Tella, S., Mikkel, S., Armitage, A.E., Seemayer, B.E., and Lemkow, D. (1992) Precambrian geology and economic potential of the Meliadine Lake-Barbour Bay region, district of Keewatin, Northwest Territories; Geological Survey of Canada, Current Research, Part C, Paper 92-1C, p. 1–11.

Tella, S., Roddick, J.C., and van Breemen, O. (1996) U-Pb zircon age for a volcanic suite in the Rankin Inlet Group, Rankin Inlet map area, district of Keewatin, Northwest Territories; Geologic Survey of Canada, Radiogenic Age and Isotopic Studies Report 9, p. 11–15.

Tóth, Z. (2019) The geology of the Beardmore-Geraldton belt, Ontario, Canada: geochronology, tectonic evolution and gold mineralization; Ph.D. thesis, Laurentian University, Sudbury, Ontario, 303 p.

Valette, M., De Souza, S., Mercier-Langevin, P., Côté-Mantha, O., Simard, M., Wodicka, N., McNicoll, V.J., and Barbe, P. (2020) Lithological and tectonic controls on banded iron formation-associated gold at the Amaruq deposit, Churchill Province, Nunavut, and implications for exploration; in Targeted Geoscience Initiative 5: Contributions to the Understanding of Canadian Gold Systems, (ed.) P. Mercier-Langevin, C.J.M. Lawley, and S. Castonguay; Geological Survey of Canada, Open File 8712, p. 251–266.

Vial, D.S., deWitt, E., Lobato, L.M., and Thorman, C.H. (2007) The geology of the Morro Velho gold deposit in the Archean Rio das Velhas greenstone belt, Quadrilátero Ferrífero, Brazil; *Ore Geology Reviews*, v. 32, p. 511–542.

Winchester, J.A. and Floyd, P.A. (1977) Geochemical discrimination of different magma series and their differentiation products using immobile elements; *Chemical Geology*, v. 20, p. 325–343.

## **7 ANNEX**

---

Appendices I to V in separate files.